Chronology and Faunal Evolution of the Middle Eocene Bridgerian North American Land Mammal "Age": Achieving High Precision Geochronology

Kaori Tsukui

Submitted in partial fulfillment of the
requirements for the degree of
Doctor of Philosophy
in the Graduate School of Arts and Sciences

COLUMBIA UNIVERSITY

2016

ABSTRACT

Chronology and Faunal Evolution of the Middle Eocene Bridgerian North American Land Mammal "Age": Achieving High Precision Geochronology

Kaori Tsukui

The age of the Bridgerian/Uintan boundary has been regarded as one of the most important outstanding problems in North American Land Mammal "Age" (NALMA) biochronology. The Bridger Basin in southwestern Wyoming preserves one of the best stratigraphic records of the faunal boundary as well as the preceding Bridgerian NALMA. In this dissertation, I first developed a chronological framework for the Eocene Bridger Formation including the age of the boundary, based on a combination of magnetostratigraphy and U-Pb ID-TIMS geochronology. Within the temporal framework, I attempted at making a regional correlation of the boundary-bearing strata within the western U.S., and also assessed the body size evolution of three representative taxa from the Bridger Basin within the context of Early Eocene Climatic Optimum. Integrating radioisotopic, magnetostratigraphic and astronomical data from the early to middle Eocene, I reviewed various calibration models for the Geological Time Scale and intercalibration of $^{40}Ar/^{39}Ar$ data among laboratories and against U-Pb data, toward the community goal of achieving a high precision and well integrated Geological Time Scale.

In Chapter 2, I present a magnetostratigraphy and U-Pb zircon geochronology of the Bridger Formation from the Bridger Basin in southwestern Wyoming. The ~560 meter composite section spans from the lower Bridger B to the Bridger E, including the Bridgerian/Uintan NALMA boundary in the uppermost part of the section. Analysis of

samples from 90 sites indicates two paleomagnetic reversals that are correlated to an interval spanning Chrons C22n, C21r, and C21n by comparison to the Geomagnetic Polarity Time Scale (GPTS). This correlation places the Bridgerian/Uintan faunal boundary within Chron C21n, during the initial cooling phase following the peak of the Early Eocene Climatic Optimum. Based on the bio- and magnetostratigraphic correlation, I provide correlation of other Bridgerian/Uintan boundary-bearing sections to the GPTS, demonstrating that in the western North America, the Bridgerian/Uintan boundary occurs everywhere in Chron C21n. In addition, U-Pb zircon geochronological analyses were performed on three ash beds from the Bridger Formation. High-precision U-Pb dates were combined with the paleomagnetic polarity data of the same ash beds as well as the integrative chronostratigraphy of the basin to assess prior calibration models for the Eocene part of the GPTS. The data from the Bridger Formation indicate that the Option 3 age model of Westerhold et al. (2008) best reconciles the geochronological data from all of the ash beds except for one. Thus I favor this Option 3 model, which indicates the ages of 56.33 Ma and 66.08 Ma for the Paleocene-Eocene Thermal Maximum and Cretaceous/Paleogene boundary, respectively.

In Chapter 3, the body size evolution of three mammalian taxa from the Bridgerian NALMA was analyzed within the context of Bergmann's Rule, which poses a correlation between the size of endotherms and climate (latitude). The Bridgerian NALMA is from a time of global cooling following the peak of the Early Eocene Climatic Optimum, thus according to Bergmann's Rule, the Bridgerian mammals are expected to increase in size. This hypothesis is tested among *Notharctus*, *Hyopsodus*, and *Orohippus*, using the size of molar dentition as a proxy for their body size. These taxa

represent three different ecomorphs, and I investigated if these taxa showed a pattern of body size change consistent with the prediction made by Bergmann's Rule, and how their ecological adaptation may have affected their response to the climate change. Prior to analyzing the body size evolution, specimens of *Notharctus* and *Hyopsodus* were identified to species based on dental characters. This practice differs from previous studies in which species identification relied on relative size of the individuals and stratigraphic levels of origin. Within the new framework of morphologically determined species identification, five species of *Notharctus* were recognized, among which, *N. pugnax*, *N. robustior* and *N.* sp. indet. exhibited statistically significant body size increase in the time span of interest. Based on morphological analyses of *Hyopsodus* dentition, I recognized five species. Dentition-based body size analysis showed that *H. lepidus* and *H. despiciens* exhibited a statistically significant change towards larger size within the sampled interval. When analyzed at the generic level, a statistically significant increase was observed for both *Notharctus* and *Hyopsodus*. Finally, a genus-level analysis of *Orohippus* showed a lack of statistically significant size increase over the study interval. Thus, among the three taxa from the Bridgerian, Bergmann's Rule is supported by *Notharctus* and *Hyopsodus*, at least at the genus level, but not by *Orohippus*, although the patterns are more variable at the intraspecific level.

In Chapter 4, $^{40}Ar/^{39}Ar$ dates were obtained from sanidines from the middle Eocene Henrys Fork tuff and Upper Carboniferous Fire Clay tonstein, with the goal of making highly precise measurements of these two samples, keyed to the Fish Canyon monitor standard. Analytically, both samples were well characterized, as had been shown previously. The irradiation disk was arranged such that there would have been control

from the Fish Canyon surrounding each of the unknown pits. However, due to several complications in the lab during the course of the experiment, only the analyses from one run disk (Disk 677) were of the quality needed for the goals of the study. As a result, the Fish Canyon sanidine standards that were irradiated near the center of the irradiation disk had to be discarded, and thus, the neutron fluence could not be mapped out precisely across the entire disk. The $^{40}Ar/^{39}Ar$ age relative to Fish Canyon sanidines is 47.828 ± 0.205 Ma and 311.937 ± 1.282 Ma for the Henrys Fork tuff and Fire Clay tonstein, respectively (1σ, including error on the age of the monitor). Because the ages were both offset about the same amount, I explored the option of using the U-Pb ID-TIMS ages of the Henrys Fork tuff and Fire Clay tonstein to test the agreement in the chronometers. The Henrys Fork tuff was dated at 48.260 ± 0.107 Ma (1σ, including error on the age of the monitor) using the Fire Clay sanidines and assuming its age is the U-Pb zircon age. The Fire Clay tonstein was dated at 314.593 ± 0.699 Ma (1σ, including error on the age of the monitor), using the Henrys Fork sanidines and assuming its age is the U/Pb zircon age. Although the complications encountered render these data unpublishable, they show great promise as the ages of each sanidine sample, tied to the other ash using the other ash's U-Pb age, give results that are in close agreement between the two chronometers on the same sample (e.g., 314.593 ± 0.699 Ma vs. 314.554 ± 0.020 Ma at 1σ for sanidine and zircon respectively from the Fire Clay tonstein, and 48.260 ± 0.107 Ma vs. 48.265 ± 0.008 Ma 1σ for sanidine and zircon respectively from the Henrys Fork tuff).

TABLE OF CONTENTS

MAGNETOSTRATIGRAPHY AND U-PB GEOCHRONOLOGY OF THE MIDDLE EOCENE BRIDGER FORMATION (WYOMING, USA): IMPLICATIONS FOR THE AGE AND CORRELATION OF THE BRIDGERIAN/UINTAN NALMA BOUNDARY AND CALIBRATION OF THE GEOMAGNETIC POLARITY TIME SCALE

Chapter 4

^{40}AR/^{39}AR SANIDINE GEOCHRONOLOGY OF THE HENRYS FORK TUFF (MIDDLE EOCENE) AND FIRE CLAY TONSTEIN (UPPER CARBONIFEROUS) – CRITICAL OBSERVATIONS FROM ONE LABORATORY ON INTER-LABORATORY CALIBRATION AND BIASES

Chapter 5

LIST OF TABLES

Chapter 2

Chapter 3

Chapter 4

LIST OF FIGURES

Chapter 1

Chapter 2

Chapter 3

Chapter 4

Acknowledgements

First and foremost, I would like to thank my advisors, John Flynn and Sidney Hemming for the opportunity to work on this research project and all the support they have given me throughout the years. Through them and this program in general, I was privileged to have had access and opportunities that I would not have had elsewhere. For this I am truly grateful.

I have been helped by a great number of people at LDEO and the AMNH, some of whom I would like to specially thank here for their help and generosity. First, I would like to thank Meng Jin for his interest in my study and acting as a committee member. I am indebted to the members of AGES lab at LDEO, especially, Elizabeth Pierce, Joel Gombiner, Guleed Ali, Gary Mesko and Karen Benedetto, for teaching me everything I now know about working in a radioisotopic lab. Dennis Kent and Chris Lepre from Paleomagnetics Lab at LDEO generously allowed me to use their facility for measurement, and simultaneously offered kind support. Morgan Hill and Henry Towbin from AMNH Microscopy and Imaging Facility were very helpful with collecting data on SEM.

I would like to thank Walter Pitman and Nick Christie-Blick for kindly serving on my Orals Committee, and Paul Olsen and Sam Bowring on my defense committee. I feel honored to have had opportunities to talk with all these people about my research. Their insightful comments and wisdom allowed me to look at my project in a new light.

In addition to my fortune to have known the world-class scientists and state-of-the-art facilities in New York, I was extremely privileged to learn U-Pb geochronology in

Sam Bowring's lab at MIT. I would like to thank everyone in Dr. Bowring's lab, especially Sam Bowring, Jahan Ramezani, Robert Buchwaldt, Matt Rioux, Noah McLean, Erin Shea, Seth Burgess, and Terry Blackburn, for sharing with me their exhaustive knowledge in high-precision U-Pb geochronology and their lab/office space. I would like to thank Paul Murphey for showing me around the Bridger Basin to teach me about fossil localities and detailed stratigraphy. Special thanks goes to Malka Machlus for the wonderful time we had in the field. Some of the specimens I used in my research were housed in the collection at the University of Colorado – Boulder, and I would like to thank Toni Culver for facilitating my visit.

Outside the lab setting, I am equally grateful for the extraordinary administrative staff whose help made it all possible for me to stay in the program and focus on my research. I am indebted especially to Mia Leo, Carol Mountain, Missy Pinckert, Jean Leote, Sally Odland, Robbie Simpson (LDEO), Maria Rios, Anna Manuel, and Adam Kashuba (AMNH-RGGS). All of you have always greeted me with warm smiles and had answers for all of my questions to which I had been clueless.

I would like to show my utmost gratitude to Columbia University, Lamont-Doherty Earth Observatory (Climate Center Grant) and Richard Gilder Graduate School at the American Museum of Natural History (Theodore Roosevelt Committee) for funding my research. Here is my testament to everyone who has taken part in my Ph.D journey in whatever capacity and role, that I will always remember the help you have given me and the lessons you taught me. You have inspired me to continue to grow as a scientist and a person.

Lastly, I want to thank my family, especially my parents and my husband, for their patience, support, and love. You are the true rock of my life.

Chapter 1

Introduction

INTRODUCTION

No doubt the study of Earth history plays an important role in our understanding of the present-day Earth system and acts as the intellectual basis for promoting effective conservation, sustainable use of natural resources, and mitigating anthropogenic climate change that we face today (e.g., Zachos et al., 2008). In reconstructing Earth history, geochronology and chronostratigraphy provide temporal and spatial context for interpreting geological, environmental and biotic events and help unravel causal relationships and processes that are at work (Bowring et al., 1998; Burgess et al., 2014; EARTHTIME initiative). For many years, efforts by early geologists focused on splicing together geological records from around the world, guided by means of fundamental principles of superpositional relationships and biostratigraphic correlation. These efforts later were augmented by incorporation of numerical radioisotopic dating and eventually culminated in development of the first geologic time scale (Holmes, 1937). Since then, the geologic time scale has been an integral part of the geological sciences and paved a way towards more integrated approaches in studies of Earth history (Gradstein et al., 2012). Over time, the time scale itself has evolved significantly, as facilitated by discoveries of different dating methods and technological innovations in our ability to measure various proxies for time more precisely and accurately. Today, the focus of timescale-building has shifted from correlating and organizing known rock units into a hierarchy of relative order, to numerical calibration of the time scale at high precision,

and the precision with which we can date specific events (or layers) has made remarkable improvements (Bowring et al., 2006).

Recent high-resolution radioisotopic dates have unveiled issues that were formerly masked by relatively large analytical uncertainties. These "growing pains" of geochronology include but are not limited to: accurate and precise determination of decay constants of radiogenic nuclides, true ages of $^{40}Ar/^{39}Ar$ monitor standards, and interlaboratory comparison and cross calibration between different chronometers (Min et al., 2000; Schmitz and Bowring, 2001; Jourdan and Renne, 2007; Kuiper et al., 2008; Renne et al., 2010, 2011). Considering that one's ability to adequately resolve causal relationships and determine rates and patterns of geological processes rests ultimately upon the precision and accuracy of geochronological data that are used, understanding uncertainties that stand in a way of obtaining high-precision ages has become as crucial as framing the geological questions themselves.

The overarching theme of this dissertation has to do with improving our ability to reconstruct Earth history in a better temporal framework. More specifically, the topics that I investigated include: how to achieve high precision geochronologic data, especially using $^{40}Ar/^{39}Ar$ sanidine and U-Pb zircon methods; how to integrate various geochronological data into a coherent timeline; and how to investigate underlying potential causal relationships between biological and environmental changes recorded in sedimentary strata using high-precision geochronological data. These questions are addressed within the context of the exemplar system provided by the early to middle Eocene Green River and Bridger Formations within the Greater Green River Basin (hereafter GGRB) in southwestern Wyoming (Figure 1.1). The basin has been known for

its rich geological and paleontological records since the 1800's (Hayden, 1869; Leidy, 1869; Matthew, 1909; Bradley, 1964; Roehler, 1992), and the basin deposits provide a unique window into a time during which significant climatic and biological changes have occurred (Zachos et al., 2001; Clyde et al., 2001; Woodburne et al., 2009a; Sexton, et al., 2011). The extensive fossiliferous deposits of the GGRB are inter-layered with volcaniclastic sediments that are suitable for magnetostratigraphic analyses as well as radioisotopic dating, making the basin an ideal setting for improving geochronologic calibrations for the early to middle Eocene (Machlus et al., 2004; Smith et al., 2008, 2010). In this dissertation, within the framework of new geochronologic and chronostratigraphic information from the GGRB, I study the Bridgerian/Uintan North American Land Mammal "Age" (NALMA) faunal transition, test different calibration models for the Geomagnetic Polarity Time Scale (GPTS, Chapter 2), assess potential correlation between the mammalian faunal evolution from the Bridger Formation and middle Eocene climate (Chapter 3), and explore the systematic biases in geochronology, especially in inter-laboratory and inter-chronometer biases of $^{40}Ar/^{39}Ar$ and U-Pb geochronology (Chapter 4).

Climatic and Faunal Background

The middle Eocene Bridger Formation was deposited during the period of the Early Eocene Climatic Optimum (EECO) and the climatic cooling subsequent to peak warming (Zachos et al., 2001; Murphey and Evanoff, 2007). The EECO represents a prolonged interval of a super-greenhouse condition characterized by the warmest temperature and highest atmospheric CO_2 concentration in the Cenozoic (Pearson and Palmer, 2000). Unlike the well known Paleocene-Eocene Thermal Maximum (PETM)

that occurred just prior to the EECO, the EECO was a peak of a longer-term warming that began ~80 Ma. However, recent studies have shown $\delta^{13}C$ evidence in marine sediments that indicates 13 distinct hyperthermals (short-term warming) in Chrons C21 and C22 (Sexton et al., 2011), demonstrating that within the longer interval of super greenhouse climate, there was much shorter-duration variability that had never before been recognized. In the Bighorn Basin, potential causal relationships between the hyperthermals and biota has been discussed (Clyde and Gingerich, 1998). It is one of the goals of this dissertation to decipher biotic changes in the Bridger Basin in the climatic context of the EECO via an improved chronology.

The NALMA biochronological system defines temporal association of rock units based on a particular assemblage of fossil mammals preserved within (Wood et al., 1941). The most recent versions of this biochronolgy divide the Cenozoic into about 20 generally recognized intervals of time of variable durations. Because of the relatively rapid pace of Cenozoic mammalian evolution, NALMAs have historically been used as the principle method of temporal correlation on regional and continental scales. Boundaries of the NALMA biochronology are delimited by significant turnover events, or reorganization of faunal composition of fossil mammals. The NALMAs relevant to this dissertation are, from oldest to youngest, the Wasatchian, Bridgerian and Uintan which together span most of the Eocene (Robinson et al., 2004).

The transition from the Wasatchian to the Bridgerian is characterized by a major faunal expansion, marked by an increase in in-situ origination (not many immigrants) and a low number of extinctions, in association with an increase in temperature and precipitation (Woodburne et al., 2009a; Gunnell et al., 2009). At this time, the number of

mammalian genera reached the post-Cretaceous/Paleogene boundary peak of 105. However, throughout the rest of the Bridgerian, mammalian generic diversity shows a steady decline until the Bridgerian/Uintan boundary, at which time the diversity picks up once again. The Bridgerian NALMA is in many ways a transitional period making a transition from the tropical and closed-habitat fauna which was dominant in the previous Wasatchian NALMA to the cool and open-habitat fauna that became established in the following Uintan NALMA. The Bridgerian NALMA is subdivided into four biochronological zones (Br1a, Br1b, Br2 and Br3, Gunnell et al. 2009). The earliest part of the Bridgerian (Br1a) has been described as the "Bridgerian expansion" by Woodburne et al. (2009b), for the overwhelming number of first appearances relative to that of last appearances. The increase in first appearances was not so much due to immigration, unlike at the time of the Clarkforkian/Wasatchian boundary that co-occurred with the PETM. The Br1a fauna is characterized by a non-skewed, and even distribution of taxa, implying a relative stability in the fauna (Woodburne et al., 2009a). However, starting in Br1b, the loss in faunal diversity and balance becomes increasingly prominent. In Br2, *Hyopsodus* species represent 61% of the entire mammalian fauna, indicating an imbalance in faunal composition and a significant reduction in taxonomic diversity. In Br3, the fauna begins to show signs of more extensive taxonomic turnover. The interval between Br1b and Br3 is called the "Bridgerian crash" for its significant increase in the number of last appearances despite a relatively constant level of first appaearance (Woodburne et al, 2009a). This deterioration eventually marks the Bridgerian/Uintan turnover event.

In the early part of the Bridgerian, the local climatic condition in the Rocky Mountain interior basins is reconstructed to have been tropical, as characterized by mean annual temperatures of 20 °C and mean annual precipitation of 76 cm/year (Wilf, 2000). However, by the end of the Bridgerian, leaf-margin analyses shows the reconstructed mean annual temperature declined to 15 °C accompanied by development of seasonality and arid condition. Woodburne et al. (2009b) argued for a direct coupling between the warm climate during the EECO and the faunal evolution during the Bridgerian, however, to test the supposed direct climate-biota coupling, comparison of both records must be made at a higher temporal resolution than has been available previously—a key objective of this dissertation.

Geological Setting

The Bridger Formation is well exposed in the Bridger Basin, which is one of the sub-basins of the GGRB, and it is physiographically outlined to the north by Blacks Fork River and to the south by the Uinta Mountains (Hayden, 1871). The formation is about 860 m thick and underlain by and in some places interfingers with the lacustrine Green River Formation while being overlain unconformably by the Oligocene Bishop Conglomerate (Murphey and Evanoff, 2007, Figure 1.2). The transition from the lacustrine Green River to the fluvial Bridger Formation is attributed to the change in the balance of sedimentary influx and accommodation space, caused by an increased volcanic activity in the sediment source (Challis/Absaroka volcanic field) that overfilled the paleolake Gosiute (Carroll et al., 2006). The Bridger Formation is composed mainly of green and gray mudstones and volcanic ash beds as well as limestone and sandstone. The limestone beds indicate short-term resurgences of a lake system.

The stratigraphy of the Bridger Formation is relatively straightforward (Figure 1.2). The first systematic geological work on the Bridger Formation was conducted by Matthew (1909), who erected a stratigraphic nomenclature for the unit. Matthew (1909) subdivided the Bridger Formation into five lithological units termed the Bridger A, B, C, D, and E (from the lowest to highest), with boundaries delimited by laterally persistent limestone beds. This general stratigraphic system held up well for nearly a century until Murphey and Evanoff (2007) undertook a detailed stratigraphic study across the basin that resulted in revision of Matthew's lithological system. Throughout this work, I follow the terminology of Murphey and Evanoff (2007), although Matthew's units are incorporated in several places because many older fossil collections include locality information tied only to that older stratigraphic system of Matthew (1909).

Geochronology of the Greater Green River Basin

The deposits in the GGRB are known to be one of the most complete terrestrial stratigraphic records from the early to middle Eocene. They are rich in fossil vertebrates and volcanic deposits that are amenable to both magnetostratigraphic and high-resolution geochronological analyses. Therefore, it is an ideal setting for developing an integrative chronology for the Eocene, and its outcome has important implications for assessing and refining calibration of the standard Geological Time Scale (see discussion below). Clyde et al. (1997, 2001) sampled the upper Green River and lowest Bridger Formations in two locations within the GGRB for magnetostratigraphy and correlated the lower Bridger Formation to Chron C22r and C22n. However, in their sections the magnetostratigraphy does not extend beyond the Bridger A, leaving most of the Bridger Formation (and the Bridgerian NALMA) temporally unconstrained. The only extensive numerical

radioisotopic calibration of the Bridger Formation is provided by Murphey and Evanoff (2007) and Smith et al. (2008, 2010) who performed $^{40}Ar/^{39}Ar$ dating on sanidines from three volcanic ash beds within the Bridger Formation. However, some of these ash beds have not been precisely correlated to the Bridger Formation reference section, and thus calibration of most of the Bridger Formation remains ambiguous. With development of the first magnetostratigraphy for the Bridger Formation above Bridger A, it becomes possible to calibrate the entire Bridger Formation in terms of GPTS and constrain the timing of the Bridgerian/Uintan boundary.

Geomagnetic Polarity Time Scale

By nature, calibration of Geologic Time Scales and GPTS is an iterative process in which new data are used to adjust earlier versions, and thus, it is a mosaic of the best available geochronological data at the time of publication. The GPTS published as part of the Geologic Time Scale is referred as a standard, but since it is merely a model, there are often other published versions that are based on a different set of data. The relatively continuous recording of geomagnetic field reversals by sedimentary rocks on land has allowed development of more refined GPTS, which has played an integral role in unifying a large number of data into standard Geologic Time Scales. The GPTS is founded on the sea-floor magnetic anomaly sequence, compiled mostly from the South Atlantic with details inserted from the Indian and Pacific Oceans with faster spreading rates (e.g., Cande and Kent, 1992, 1995). This original distance profile has been instrumental in modeling the ages of chrons in previous GPTS, especially prior to application of astrochronology. In the "Geologic Time Scale 2012", post-Oligocene part of the GPTS is entirely calibrated by astronomical solution and anchored to absolute time.

Other parts of the pre-Oligocene timescale have also been constrained by astronomical tuning (e.g., Kent and Olsen, 1999; Westerhold and Röhl, 2009), but they are "floating" scales at present because of the lack of resolution in orbital variables older than 42 Ma (Laskar et al., 2011). Therefore, in Geologic Time Scale 2012, calibration of the Paleogene GPTS relies on interpolation of sea-floor magnetic anomalies using a spline-fit between a set of tie-points for the interval between (chrons C13r–C20r) and estimates of astronomical cycle duration relative to the Cretaceous/Paleogene boundary age estimate of 66.0 Ma (chrons C21n–C29r, Ogg, 2012). To keep pace with the ever-improving precision of radioisotopic dating, as well as new climatic data that are being recovered at the time scale of precessional cycles, calibration of the GPTS needs to be constantly checked for consistency with recent geological data and revised to reflect the most up-to-date and highest precision geochronological data available (e.g., Machlus et al., 2004; Lourens et al., 2005; Tsukui and Clyde, 2012). Towards this goal, studies from terrestrial sequences, such as those in the GGRB, for which radioisotopic, biochronological and magnetostratigraphic data from the same sequences can be integrated, are important in testing various existing models and fine-tuning numerical calibration of the Geologic Time Scale. Finally, in this dissertation, the terminology of Aubry et al. (2009) is followed to unambiguously distinguish dates (Ma) from durations of geological events (myr).

SUMMARY OF DISSERTATION CHAPTERS

Summary of Chapter 2

The first of the three main content chapters serves as the backbone of this dissertation, and its principle objective is to present a magnetostratigraphy and a high precision U/Pb ID-TIMS single-grain zircon geochronology of the Bridger Formation. The Bridger Formation is a type area for the Bridgerian NALMA, and thus it is of importance to devise a reliable chronostratigraphic framework in which the rich and diverse fossils from the Bridger Formation can be placed. And yet, the Bridger Formation (or the Bridgerian NALMA) as a whole has never been characterized by a magnetostratigraphy, it has been the "missing link" in the Eocene magnetostratigraphy from the region. The magnetostratigraphy presented herein was sampled by J. Flynn and others from a transect through one of the most fossiliferous parts of the Bridger Basin. The sampled interval spans from the Bridger B to the base of Bridger E within which the mammalian fauna underwent significant changes, including a major faunal transition marking the Bridgerian/Uintan NALMA boundary. This faunal transition is associated with the radiation of selenodont artidactyls, diversification of rodents and rhinoceratoid perissodactyls, and decline of certain "archaic" mammalian groups (Robinson et al., 2004; Gunnell et al., 2009). The precise nature of this biotic transition, however, remains uncertain due to the lack of understanding in the timing of the transition as well as the paucity of boundary-bearing sections in North America (Flynn, 1986; Prothero and Emry, 1996). The transitional interval is known in several places in North America, but the Bridger Formation (Turtle Bluff Member) has the best preservation, and thus, it has been designated as the stratotype for the biochron Ui1a, (Gunnell et al., 2009; see also Flynn, 1986, McCarroll et al. 1996, and Walsh, 1996). The magnetostratigraphy from the Bridger Formation, is hence critical to improving our understanding not only of the

timing of this major transition, but also the broader stratigraphic-temporal correlation and regional patterns of important faunal turnover events throughout the climatically transitional period. In addition to the magnetostratigraphy, three ash beds were sampled by John Dyni for dating by U/Pb ID-TIMS geochronology. They are the Church Butte tuff, Henrys Fork tuff, and Sage Creek Mountain tuff from Bridger B, C and E, respectively, and have been tied to the magnetostratigraphy. By having been characterized by both magnetostratigraphy and radioisotopic dates, these three ashes present an opportunity to test proposed calibration models for the Eocene part of the GPTS.

Summary of Chapter 3

In this chapter, macroevolutionary patterns of the Bridgerian fossil mammals from the Bridger Formation are studied within the chronostratigraphic context presented in Chapter 2. As previously addressed, the Bridgerian NALMA corresponds to the interval of initial climatic cooling following the peak warmth during the EECO. Bergmann's rule makes prediction that in cooler climates (such is often found in high latitudes and potentially during cooling intervals), the body mass of endotherms, like mammals, become larger in order to effectively prevent heat loss. This assertion has been tested and observed among many different taxa (Ashton, 2002; Meiri and Dayan, 2003; Blackburn and Hawkins, 2004; Gardner et al., 2014), but the results vary from study to study. The objective of this chapter is to study the effect of the climatic cooling after the peak-EECO on the body size of three Bridgerian taxa, including *Notharctus* (Primates), *Hyopsodus* ("Condylarthra") and *Orohippus* (Perissodactyla), all of which are relatively common within the Bridgerian fauna, and characterized by different ecomorphs, such as diet,

habitat, and locomotion. If Bergmann's rule was the dominant external force controlling body size evolution, these mammalian taxa are predicted display a size increase in accord with the cooling climate. Patterns may differ depending on the distinct ecomorphological traits of the taxa, but any deviation from the prediction would suggest the importance of other factors, such as seasonality, precipitation, predation pressure, that are more difficult to constrain and thus not directly considered here. Furthermore, different patterns among these three taxa might also indicate differential reactions to the same abiotic force depending on their adaptive strategies, but in any case, would contradict the hypothesis of a simple relationship between body size changes and climatic shifts.

An important factor in assessing the role of climate on body size evolution is that species identification of the analyzed specimens is made independent of its inferred relative body size or the stratigraphic position from which it is known. Both of these types of data have been frequently used in the past to distinguish closely related species in the Bridger sequence and elsewhere. However, use of either of these sources of information would make the species assignments non-independent of the metric to assess response to climate (body size) or temporal distribution of a particular species (stratigraphic position), thus limiting or negating the value of the tests of climate-faunal interactions. Presently, five species of *Notharctus* are recognized, but its species diagnoses have relied mainly on relative size differences and stratigraphic levels of origin. For example, those that are relatively large and from the Upper Bridger Formation have been identified as *N. robustior*, and those that are from the Lower Bridger Formation have been referred to as *N. tenebrosus*. The practice of using the body size to diagnose mammalian species has been used and considered valid for years, especially

among sympatric species. However, for this study in which size is the variable of interest, size-based species diagnosis must be avoided in order to circumvent circular reasoning. To this end, a phylogenetic analysis was first performed among individual specimens of *Notharctus* to identify specimens to species based solely on dental morphological characters. Doing so ensures that the resultant observations of body size evolution through time can be interpreted at the species level without a prior bias on the size-temporal distribution of a given species. For *Hyopsodus*, dental morphology (especially the presence/absence of certain cingulum) was used to make species identification. The body sizes of *Notharctus, Hyopsodus* and *Orohippus* were inferred based on crown area of molar dentition using an equation by Gingerich et al. (1982), and the temporal changes in the body size of three taxa are analyzed at both species and generic levels.

Summary of Chapter 4

The last of the three content chapters addresses technical and procedural aspects of obtaining the highest precision $^{40}Ar/^{39}Ar$ geochronological data. In the last decade, the geochronological community has made significant progress towards better understanding of the sources and impact of systematic uncertainties. However, the issue of inter-laboratory biases has remained under-explored. The collaborative effort of EARTHTIME has made a preliminary, yet significant, effort to evaluate the degree of existing inter-laboratory biases. Hemming et al. (2012) has shown that there is up to ~0.5% variations in the apparent age of Fire Clay tonstein, underscoring that inter-laboratory biases are as significant as inter-chronometer biases in obtaining radioisotopic dates. In this chapter, I present $^{40}Ar/^{39}Ar$ data from two volcanic ash deposits, the Eocene Henrys Fork tuff from the Bridger Formation and the Upper Carboniferous Fire Clay tonstein from the Hyden

Formation, collected in Sidney Hemming's AGES laboratory at the Lamont-Doherty Earth Observatory of Columbia University. Both of these samples have previously been dated in other labs by U-Pb as well as $^{40}Ar/^{39}Ar$ geochronology methods. The new $^{40}Ar/^{39}Ar$ results from these beds show a single population without evidence of geological complexities, showing that they are ideal candidates for monitoring inter-laboratory biases for $^{40}Ar/^{39}Ar$ geochronology and biases between the $^{40}Ar/^{39}Ar$ sanidine and U-Pb zircon systems. I show detailed analytical and data reduction procedures that were employed in obtaining the age from these samples and discuss potential sources and magnitudes of inter-laboratory biases as well as outlook for the future.

Summary of Chapter 5

The final chapter of the dissertation ties together main conclusions from the three content chapters and discusses them in terms of how they may be broadly related with one another. I also emphasize the potential of the GGRB stratigraphic record in shedding light on some fundamental and age-old questions such as mode and tempo of evolution, which could not be answered fully in older times when only a few radioisotopic control points existed. Finally, I conclude by presenting potential subjects of future research projects that are going to rest upon the results of this dissertation.

REFERENCES CITED

Ashton, K.G., 2002, Patterns of within-species body size variation of birds: Strong evidence for Bergmann's rule: Global Ecology and Biogeography, v. 11, p. 505-523.

Aubry, M.-P., Van Couvering, J.A., Christie-Blick, N., Landing, E., Pratt, B.R., Owen, D.E., and Ferrusquía-Villafranca, I., 2009, Terminology of geological time: Establishment of a community standard: Stratigraphy, v. 6, p. 100-105.

Blackburn, T.M. and Hawkins, B.A., 2004, Bergmann's rule and the mammal fauna of northern North America: Ecography, v. 27, p. 715-724.

Bowring, S.A., Erwin, D.H., Jin, Y.G., Martin, M.W., Davidek, K., and Wang, W., 1998, U/Pb zircon geochronology and tempo of the end-Permian mass extinction: Science, v. 280, p. 1039-1045.

Bowring, S.A., Schoene, B., Crowley, J.L., Ramezani, J., and Condon, D.J., 2006, High-precision U-Pb zircon geochronology and the stratigraphic record: progress and promise, *in* Olszewski, T., ed., Geochronology: Emerging Opportunities: Paleontological Society Papers, v. 11, p. 23-43.

Bradley, W.H., 1964, Geology of Green River Formation and Associated Eocene Rocks in Southwestern Wyoming and Adjacent Parts of Colorado and Utah: U.S. Geological Survey Professional Paper 496-A, 86 p.

Burgess, S.D., Bowring, S., and Shen, S.-Z., 2014, High-precision timeline for Earth's most severe extinction: Proceedings of the National Academy of Sciences, v. 111, p. 3316-3321.

Cande, S.C., and Kent, D.V., 1992, A new geomagnetic polarity time scale for the Late Cretaceous and Cenozoic: Journal of Geophysical Research–Solid Earth, v. 97, p. 13,917–13,951.

Cande, S.C., and Kent, D.V., 1995, Revised calibration of the geomagnetic polarity timescale for the Late Cretaceous and Cenozoic: Journal of Geophysical Research–Solid Earth, v. 100, p. 6093–6095.

Carroll, A.R., Chetel, L.M., and Smith, M.E., 2006, Feast to famine: Sediment supply control on Laramide basin fill: Geology, v. 34, p. 197-200.

Clyde, W.C., and Gingerich, P.D., 1998, Mammalian community response to the latest Paleocene thermal maximum: An isotaphonomic study from the northern Bighorn basin, Wyoming: Geology, v. 26, p. 1011-1014.

Clyde, W.C., Zonneveld, J.-P., Stamatakos, J., Gunnell, G.F., and Bartels, W.S., 1997, Magnetostratigraphy across the Wasatchian/Bridgerian NALMA boundary (early to middle Eocene) in the western Green River Basin, Wyoming: The Journal of Geology, v. 105, no. 6, p. 657–670, doi:10.1086/515970.

Clyde, W.C., Sheldon, N.D., Koch, P.L., Gunnell, G.P., and Bartels, W.S., 2001, Linking the Wasatchian/Bridgerian boundary to the Cenozoic Global Climate Optimum: New magnetostratigraphic and isotopic results from South Pass, Wyoming: Palaeogeography Palaeoclimatology Palaeoecology, v. 167, no. 1-2, p. 175-199.

Flynn, J.J., 1986, Correlation and geochronology of middle Eocene strata from the western United States: Palaeogeography Palaeoclimatology Palaeoecology, v. 55, p. 335-406.

Gardner, J.L., Peters, A., Kearney, M.R., Joseph, L., and Heinsohn, R., 2011, Declining body size: a thied universal response to warming?: Trends in Ecology and Evolution, v. 26, p. 285-291.

Gingerich, P.D., Smith, B.H., and Rosenberg, K., 1982, Allometric scaling in the dentition of primates and prediction of body weight from tooth size in fossils: American Journal of Physical Anthropology, v. 58, p. 81-100.

Gradstein, F.M., Ogg, J.G., Schmitz, M.D., and Ogg, G.M., 2012, The Geologic Time Scale 2012: Oxford, U.K., Elsevier, 1176 p.

Gunnell, G.F., Murphey, P.C., Stucky, R.K., Townsend, K.E., Robinson, P, Zonneveld, J.P., and Bartels, W.S., 2009, Biostratigraphy and biochronology of the latest Wasatchian, Bridgerian, and Uintan North American Land-Mammal "Ages.", *in* Albright, L.B. III, ed., Papers on Geology, Vertebrate Paleontology, and Biostratigraphy in Honor of Michael O. Woodburne: Museum of Northern Arizona, Flagstaff, Arizona, Museum of Northern Arizona Bulletin, v. 65, p. 279-330.

Hayden, F.V., 1869, U.S. Geological Survey of the Territories, 3rd Annual Report, Chapter XII, Review of Leading Groups, etc.: Washington, D.C., p. 190-191.

Hayden, F.V., 1871, Preliminary report (4thAnnual) of the U.S. Geological Survey of Wyoming and contiguous territories: Washington, D.C., 511 p.

Hemming, S, Heizler, M.T., Jicha, B., Machlus, M., Rasbury, E.T., Renne, P.R., Singer, B.S., Swisher, C.C. and Turrin, B.D., 2012, Inter-laboratory evaluation of $^{40}Ar/^{39}Ar$ Data for sanidines from the Fire Clay tonstein: Mineralogical Magazine, v. 76, p. 1832.

Holmes, A., 1937, The Age of the Earth (new edition, revised and rewritten): Nelson, London, 263 pp.

Jourdan, F., and Renne, P.R., 2007, Age calibration of the Fish Canyon sanidine $^{40}Ar/^{39}Ar$ dating standard using primary K– Ar standards: Geochimica et Cosmochimica Acta, v. 71, p. 387–402.

Kent, D.V., and Olsen, P.E., 1999, Astronomically tuned geomagnetic polarity time scale for the Late Triassic: Journal of Geophysical Research, v. 104, p. 12831-12841.

Kuiper, K.F., Deino, A., Hilgen, F.J., Krijgsman, W., Renne, P.R., and Wijbrans, J.R., 2008, Synchronizing rock clocks of Earth history: Science, v. 320, no. 5875, p. 500-504.

Laskar, J., Fienga, A., Gastineau, M., and Manche, H., 2011, La2010: A new orbital solution for the long-term motion of the Earth: Astronomy and Astrophysics, v. 532, A89.

Leidy, J., 1869, Notice of Some Extinct Vertebrates from Wyoming and Dakota: Proceedings of the Academy of Natural Sciences of Philadelphia, v. 21, p. 63-67.

Lourens, L.J., Sluijs, A., Kroon, D., Zachos, J.C., Thomas, E., Röhl, U., Bowles, J., and Raffi, I., 2005, Astronomical pacing of late Palaeocene to early Eocene global warming events: Nature, v. 435, p. 1083-1087.

Machlus, M., Hemming, S.R., Olsen, P.E., and Christie-Blick, N., 2004, Eocene calibration of geomagnetic polarity time scale reevaluated: Evidence from the Green River Formation of Wyoming: Geology, v. 32, no. 2, p. 137-140.

Matthew, W.D., 1909, The carnivora and insectivora of the Bridger Basin, middle Eocene: American Museum of Natural History Memoirs, v. 9, p. 289-567.

McCarroll, S.M., Flynn, J.J., and Turnbull, W.D., 1996, Biostratigraphy and magnetostratigraphy of the Bridgerian-Uintan Washakie Formation, Washakie Basin, Wyoming, *in* Prothero, D.R., and Emry, R.J., eds., The Terrestrial Eocene-Oligocene transition in North America: Cambridge, UK, Cambridge University Press, p. 25-39.

Meiri, S., and Dayan, T., 2003, On the validity of Bergmann's rule: Journal of Biogeography, v. 30, p. 331-351.

Min, K., Mundil, R., Renne, P.R. and Ludwig, K.R., 2000, A test for systematic errors in $^{40}Ar/^{39}Ar$ geochronology through comparison with U–Pb analysis of a 1.1 Ga rhyolite: Geochimica et Cosmochimica Acta, v. 64, p. 73–98.

Murphey, P.C., and Evanoff, E., 2007, Stratigraphy, fossil distribution and depositional environments of the upper Bridger Formation (middle Eocene), southwestern Wyoming: Wyoming State Geological Survey Report of Investigation, scale 1:50,000, 1 sheet.

Ogg, J.G., 2012. Geomagnetic Polarity Time Scale, *in* Gradstein, F.M., Ogg, J.G., Schmitz, M.D., and Ogg, G.M, eds, The Geologic Time Scale 2012, Oxford, U.K., Elsevier, p. 85-114.

Pearson, P.N., and Palmer, M.R., 2000, Atmospheric carbon dioxide over the past 60 million years: Nature, v. 406, p. 695-699.

Prothero, D.R., and Emry, R.J., 1996, The Terrestrial Eocene-Oligocene transition in North America: Cambridge, UK, Cambridge University Press, 708 p.

Renne, P.R., Mundil, R., Balco, G., Min, K. and Ludwig, K.R., 2010, Joint determination of ^{40}K decay constants and $^{40}Ar^*/^{40}K$ for the Fish Canyon sanidine standard, and improved accuracy for $^{40}Ar/^{39}Ar$ geochronology: Geochimica et Cosmochimica Acta, v. 74, p. 5349–5367.

Renne, P.R., Balco, G., Ludwig, K.R., Mundil, R., and Min, K., 2011, Response to the comment by W.H. Schwartz et al. on "Joint determination of ^{40}K decay constants and $^{40}Ar^*/^{40}K$ for the Fish Canyon sanidine standard, and improved accuracy for $^{40}Ar/^{39}Ar$ geochronology" by P.R. Renne et al. (2010): Geochimica et Cosmochimica Acta, v. 75, p. 5097-5100.

Robinson, P., Gunnell, G.F., Walsh, S.L., Clyde, W.C., Storer, J.E., Stucky, R.K., Froehlich, D.J., Ferrusquia-Villafranca, I., and McKenna, M.C., 2004, Wasatchian through Duchesnean biochronology, *in* Woodburne, M.O., ed., Late Cretaceous and Cenozoic mammals of North America : Biostratigraphy and geochronology: New York, Columbia University Press, p. 106-155.

Roehler, H.W., 1992, Description and correlation of Eocene rocks in stratigraphic reference sections for the Green River and Washakie Basins, southwest Wyoming: U.S. Geological Survey Professional Paper 1506-D, 83 p.

Schmitz, M.D., and Bowring, S.A., 2001, U-Pb zircon and titanite systematics of the Fish Canyon Tuff: an assessment of high-precision U-Pb geochronology and its application to young volcanic rocks: Geochimica et Cosmochimica Acta, v. 65, p. 2571-2587.

Sexton, P.F., Norris, R.D., Wilson, P.A., Pälike, H., Westerhold, T., Röhl, U., Bolton, C.T., and Gibbs, S., 2011, Eocene global warming events driven by ventilation of oceanic dissolved organic carbon: Nature, v. 471, p. 349-352.

Smith, M.E., Carroll, A.R., and Singer, B.S., 2008, Synoptic reconstruction of a major ancient lake system: Eocene Green River Formation, western United States: Geological Society of America Bulletin, v. 120, no. 1-2, p. 54-84.

Smith, M.E., Chamberlain, K.R., Singer, B.S., and Carroll, A.R., 2010, Eocene clocks agree; coeval $^{40}Ar/^{39}Ar$, U-Pb, and astronomical ages from the Green River Formation: Geology, v. 38, p. 527-530.

Tsukui, K. and Clyde, W.C., 2012, Fine-tuning the calibration of the early to middle Eocene geomagnetic polarity time scale: Paleomagnetism of radioisotopically dated tuffs from Laramide foreland basins: Geological Society of America Bulletin, v. 124, no. 5-6, p. 870-885, doi:10.1130/B30545.1.

Walsh, S.L., 1996, Theoretical biochronology, the Bridgerian-Uintan boundary and the "Shoshonian Subage" of the Uintan, *in* Prothero, D.R., and Emry, R.J., eds., The Terrestrial Eocene-Oligocene transition in North America: Cambridge, UK, Cambridge University Press, p. 52-74.

Westerhold, T., and Röhl, U., 2009, High resolution cyclostratigraphy of the early Eocene - new insights into the origin of the Cenozoic cooling trend: Climate of the Past, v. 5, no. 3, p. 309-327.

Wilf, P., 2000, Late Paleocene–early Eocene climate changes in southwestern Wyoming: Paleobotanical analysis: Geological Society of America Bulletin, v. 112, p. 292–307.

Wood, H.E., Chaney, R.W., Clark, J., Colbert, E.H., Jepsen, G.L., Reeside, J.B., and Stock, C., 1941, Nomenclature and correlation of the North American continental Tertiary: Geological Society of America Bulletin, v. 52, p. 1-48.

Woodburne, M.O., Gunnell, G.F., and Stucky, R.K., 2009a, Land mammal faunas of North America rise and fall during the early Eocene: Denver Museum of Nature and Science Annals, no. 1, 78 p.

Woodburne, M.O., Gunnell, G.F., and Stucky, R.K., 2009b, Climate directly influences Eocene mammal faunal dynamics in North America: Proceedings of the National Academy of Sciences, v. 106, p. 13399-13403.

Zachos, J., Pagani, M., Sloan, L., Thomas, E., and Billups, K., 2001, Trends, rhythms, and aberrations in global climate 65 Ma to present: Science, v. 292, p. 686-693.

Zachos, J.C., Dickens, G.R., and Zeebe, R.E., 2008, An early Cenozoic perspective on greenhouse warming and carbon-cycle dynamics: Nature, v. 451, p. 279-283.

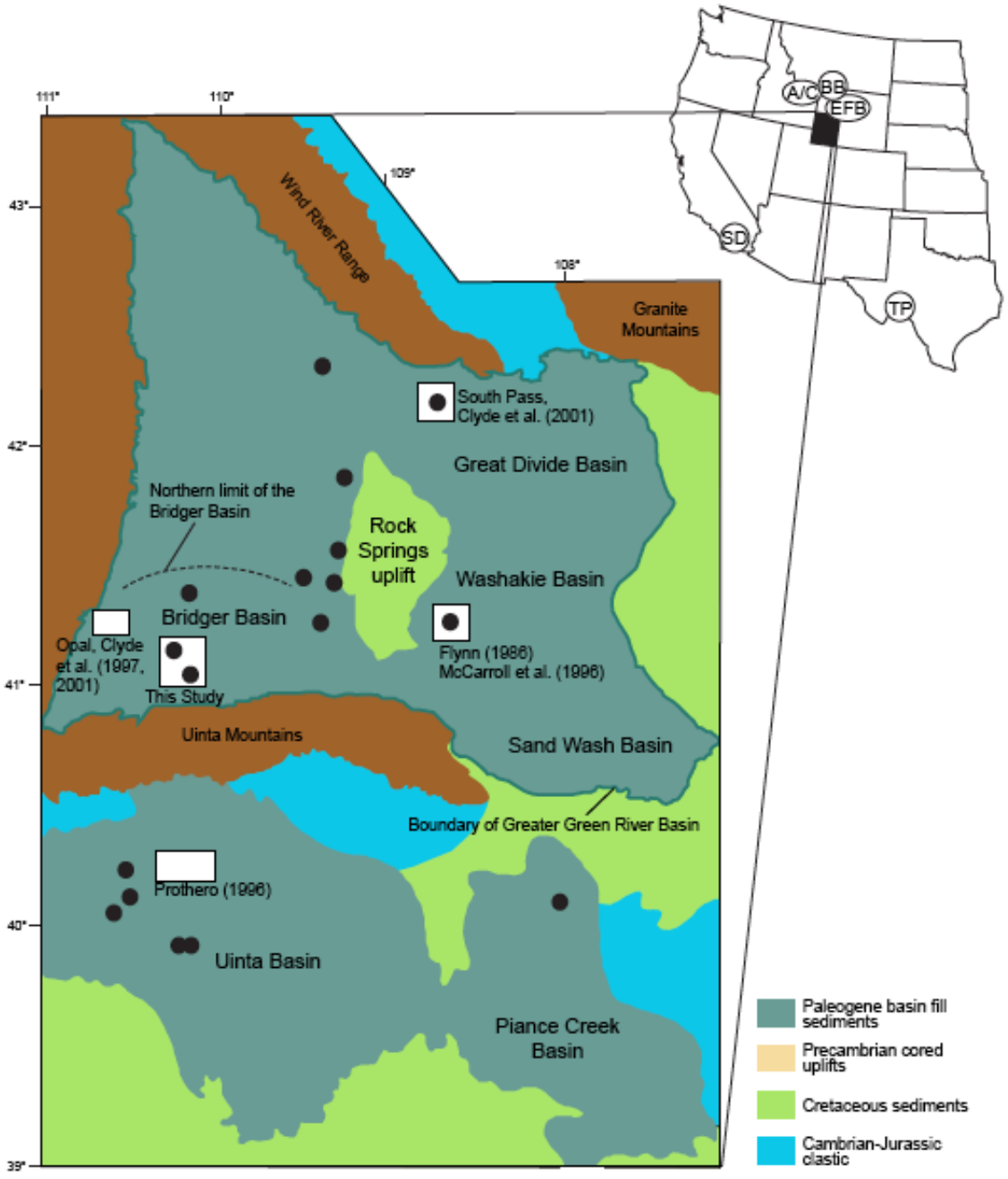

Figure 1.1. Schematic map of the Greater Green River Basin and the surrounding basins that are relevant for this study. White boxes indicate locations of magnetostratigraphy from the Early to Middle Eocene. Filled circles indicate locations of tuffs that have been dated either by $^{40}Ar/^{39}Ar$ or U/Pb dating (Murphey, 1999; Smith et al., 2008, 2010; Machlus et al., 2004, 2015). In the map of the western U.S., A/C - Absaroka/Challis

volcanic field, BB - Bighorn Basin, EFB - East Fork Basin, SD – San Diego, CA, and TP - Trans Pecos, TX.

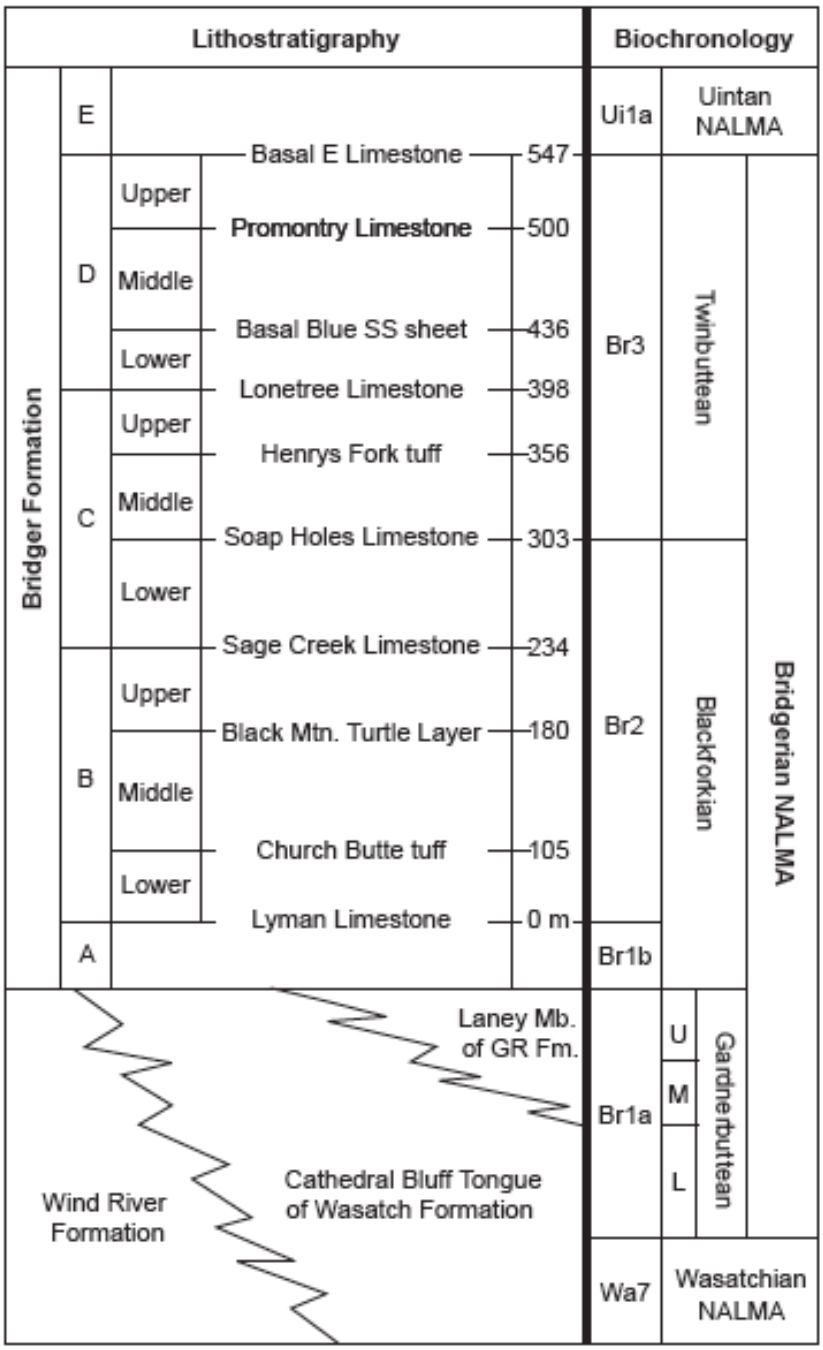

Figure 1.2. Lithostratigraphic nomenclature of the Bridger Formation and underlying unites as well as the biochronological nomenclature of the Bridgerian NALMA. GR Fm – Green River Formation.

Chapter 2

Magnetostratigraphy and U-Pb geochronology of the Middle Eocene Bridger Formation (Wyoming, USA): implications for the age and correlation of the Bridgerian/Uintan NALMA boundary and calibration of the Geomagnetic Polarity Time Scale

ABSTRACT

The age of the Bridgerian/Uintan boundary has been regarded as one of the biggest outstanding problems in North American Land Mammal "Age" (NALMA) biostratigraphy. Herein I present a magnetostratigraphy and U-Pb zircon geochronology of the Bridger Formation from the Bridger Basin in southwestern Wyoming. The ~560 meter composite section spans from the lower Bridger B to the Bridger E, including the Bridgerian/Uintan NALMA boundary in the uppermost part of the section. Paleomagnetic analysis of samples from 90 sites indicates two paleomagnetic reversals that are correlated to an interval spanning Chrons C22n, C21r, and C21n by comparison to the Geomagnetic Polarity Time Scale (GPTS). This correlation places the Bridgerian/Uintan boundary within Chron C21n, during the initial cooling phase following the peak of the Early Eocene Climatic Optimum. Based on the bio- and magnetostratigraphic correlation, I also provide correlation of other Bridgerian/Uintan boundary bearing sections to the GPTS, demonstrating that in the western North America, the Bridgerian/Uintan boundary occurs everywhere in Chron C21n. In addition, U-Pb zircon geochronological analyses were performed on the Church Butte tuff, Henrys Fork tuff, and Sage Creek Mountain tuff from the Bridger Formation. High-precision U-Pb dates and the paleomagnetic

polarity data from the tuffs from the Greater Green River Basin were used to assess prior age models for the Early-Middle Eocene part of the GPTS. The evaluation of the models indicates that the Option 3 age model of Westerhold et al. (2007, 2008) best reconciles the geological data from the Greater Green River Basin.

INTRODUCTION

The Greater Green River Basin (GGRB, including the Bridger Basin) in southwestern Wyoming, USA contains one of the most complete and fossiliferous sedimentary records from the Early to Middle Eocene, and thus, its chronostratigraphy bears unique significance for calibration of the Eocene part of the Geomagnetic Polarity Time Scale (GPTS) as well as North American Land Mammal "Ages" (NALMA) biochronology (e.g., Ogg et al., 2012; Wood et al., 1941; Woodburne et al., 1987). The basin has a long history of geological and paleontological investigations dating back to the late 1800s, which have since culminated in documentation of one of the richest fossil mammal collections, geochemical and geomorphic evolution of the basin, a suite of chronostratigraphic studies that include $^{40}Ar/^{39}Ar$ and U/Pb ages from volcanic ash beds, as well as magnetostratigraphy and cyclostratigraphy (e.g., Leidy, 1869; Matthew, 1909; Bradley, 1964; Roehler, 1992a, b; Surdam and Stanley, 1980; Smith et al., 2008, 2010; Murphey and Evanoff, 2007; Machlus et al., 2008, 2015; Mayer, 2008; Clyde et al., 1997, 2001).

The fossil mammals recovered from the basin preserve two key faunal transitions from the Eocene (Wasatchian/Bridgerian and Bridgerian/Uintan NALMA boundaries) that represent reorganizations of faunal composition (Robinson et al., 2004). Faunal

turnovers are an integral part of macroevolution and provide insights into the ways in which biotas and environments interact and affect each other. Episodes of mammalian turnover are used to subdivide the Cenozoic into smaller subsets of time, forming the basis for a mammalian biochronology known as Land Mammal "Ages" (for North America, North American Land Mammal "Age", NALMA). The concept was never codified in International Stratigraphic Codes, but as an informal biochronologic unit, it is both practical and useful for regional correlation of terrestrial deposits and thus remains in wide use today. The NALMA sequence has historically been calibrated in time via the GPTS because fossil bearing sediments are often amenable to magnetostratigraphy. The NALMAs that are documented in the GGRB are from the oldest, Wasatchian (Wa), Bridgerian (Br) and Uintan (Ui), and they generally span the time during and immediately following the Early Eocene Climatic Optimum (Zachos et al., 2001, 2008), which refers to an interval of the highest atmospheric CO_2 and temperature in the last ~80 myr (Pearson and Palmer, 2000). Previous magnetostratigraphic studies from the basin have demonstrated that the Wasatchian/Bridgerian NALMA boundary is coincident in timing with the peak of the Early Eocene Climatic Optimum, whereas the Bridgerian and Uintan NALMAs occur during the interval of subsequent cooling, which eventually leads to the Eocene/Oligocene climatic transition (Zachos et al., 1996). Woodburne et al. (2009) suggested that the observed faunal dynamics during the Paleogene were strongly climate driven, but to demonstrate the suggested causality, the biotic and abiotic (climatic) changes must be placed within a rigorous temporal framework (e.g., Bowring et al., 1998). Only with an improved chronology for the GGRB, can the relative timing of the biotic and climatic changes be made clear and help unravel the dynamics within the

terrestrial environment during and the transitional interval following the Early Eocene Climatic Optimum.

The Bridger Formation is well exposed in the Bridger Basin, a physiographic basin within the southwestern part of the GGRB (Figure 1.1). It has yielded a large number of mammalian fossils that have been the subject of many seminal works in vertebrate paleontology (e.g., Hayden, 1869; Cope, 1882; Matthew, 1909; Granger, 1914; Wood, 1934; Gazin, 1962, 1976; McGrew and Sullivan, 1970), and has also been selected as the type area for the Bridgerian NALMA (Gunnell et al., 2009). Both the Wasatchian/Bridgerian and Bridgerian/Uintan NALMA transitions have been identified in the Bridger Formation, but despite its importance in mammalian biostratigraphy, no magnetostratigraphic study has ever been published for the Bridger Formation, above the lowermost Bridger A (Clyde et al., 2001). Thus, the abundant fossil mammals from the Bridger Formation largely remain without a temporal control, including the precise timing of the Bridgerian/Uintan NALMA boundary.

In this study, a new magnetostratigraphy is presented based on 302 samples from 90 sites within a ~560 m composite section. It represents one of the most continuous terrestrial sections spanning this faunally and climatically variable period. The Bridger Basin magnetostratigraphy provides the missing magnetostratigraphic link between the correlative regional magnetostratigraphies of Clyde et al. (2001, Wa7-Br1b), Flynn (1986, late Br-early Ui) and Prothero (1996, late Br to late Ui), and it has the potential to permit direct correlation of biostratigraphic records from the western U.S. The magnetostratigraphic framework is pinned to absolute time by high-precision U-Pb CA/ID-TIMS dates on zircons from three volcanic ash beds from the Bridger Formation.

These three ash beds (Church Butte tuff, Henrys Fork tuff, and Sage Creek Mountain tuff) are the first in the Bridger Formation to be dated by the U-Pb zircon geochronology. The new magnetostratigraphy and U-Pb geochronology from the Bridger Formation, combined with the NALMA biochronology, form a basis for a robust and integrated chronostratigraphic framework for the Greater Green River Basin, and also provide a unique opportunity to test calibration of the early Paleogene section of the GPTS that remains controversial (Westerhold and Röhl, 2009; Westerhold et al., 2012; Machlus et al., 2004, 2015).

GEOLOGICAL SETTING

The Greater Green River Basin encompasses four sub-basins, including the Bridger Basin, Great Divide Basin, Washakie Basin, and Sand Wash Basin, all of which were once connected and underlain by a paleolake Gosiute that deposited the Green River Formation (Figure 1.1). The Bridger Basin is a physiographic basin and refers to the area south of the Blacks Fork and west of Rock Springs Uplift (Hayden, 1871; Murphey and Evaoff, 2007, Figure 1.1). The geology of the Bridger Formation was systematically studied first by Matthew (1909) who proposed a lithological subdivision that separates the unit into five lithological subdivisions (A, B, C, D and E from lowest to highest) by extensive "white layers" (limestones, Figure 1.2). Of the five lithological units, Bridger B, C and D were further subdivided into five finer units (B1-B5, C1-C5, and D1-D5). The Bridger A-E division of Matthew (1909) has remained in wide use to this day, however, the 1-5 subdivision of the Bridger B, C and D became superseded by a more rigorous stratigraphic system by Evanoff et al. (1998) and Murphey and Evanoff (2007) who

subdivided the Bridger B, C and D into lower, middle and upper units using persistent marker beds and ash fall tuffs (Figure 1.2). Wood (1934) also combined Bridger A and Bridger B into the Blacks Fork Member and Bridger C and Bridger D into the Twin Buttes Member, but this organization was based on faunal similarities within these units rather than lithological characteristics.

Most of the Bridger Formation was deposited in fluvial environments by meandering streams after the paleolake Gosiute became overfilled with an increased volcaniclastic influx from the Absaroka and Challis volcanic field to the northwest of the GGRB (Surdam and Stanley, 1980; Chetel et al., 2011, Figure 1.1). In the southern part of the Bridger Basin, near the depositional axis along the Uinta Mountains, the Bridger Formation interfingers with the Laney Member of the Green River Formation. The Bridger Formation is also found in the Great Divide Basin and Sand Wash Basin, while the Washakie Formation of the Washakie Basin and the Fowkes Formation of the Fossil Basin are considered, in part, equivalent to the Bridger Formation because of similar age and lithology. The Bridger Formation consists of a succession of mostly grey and green volcaniclastic mudstone and sheet and ribbon sandstone of flood plain origin. It also interfingers with grey or tan limestones, brown shale of lacustrine origin and grey to white ash fall tuffs (Roehler, 1992b). Smectite (altered volcanic glass) is common in the mudstone, which produces the characteristic “popcorn” surface in weathered outcrops. Also present are red mudstone, grey conglomerate, and brown carbonaceous shale of swamp origin. Evaporite deposits are especially abundant in the Bridger E, which suggests a warm and dry climate towards the end of the Bridger Formation (Murphey and Evanoff, 2007).

Bridger A is the lowest subdivision of the Bridger Formation and overlies the Wasatch Formation in the basin margin (Figure 1.2, McGrew and Sullivan, 1970; Gingerich, 1979; Gunnell, 1998; Zonneveld et al., 2000; Zonneveld et al., 2003). It is separated from the overlying Bridger B by the ostracodal Lyman Limestone or Marker Bed G of McGrew and Sullivan (1970). The Bridger B, C and D can be seen in the "classic" Bridger localities around the Sage Creek Mountain and Cedar Mountain in the southern Bridger Basin (Figure 2.1). The Bridger B is especially well exposed in the Crooked Canyon, Grizzly Buttes and Devil's Playground (Figure 2.1). The Sage Creek Limestone separates the Bridger B from Bridger C, which is well exposed in a large stretch in between the local topographic highs such as Sage Creek Mountain and Cedar Mountain. The Bridger D and Bridger E are marked at the base by the Lonetree Limestone and Basal E Limestone, respectively, and can be found on slopes of Twin Buttes, Black Mountain, Cedar Mountain, Sage Creek Mountain and Hickey Mountain, all of which are uncomformably capped by the Oligocene Bishop Conglomerate (Murphey and Evanoff, 2007).

MAMMALIAN BIOSTRATIGRAPHY

In the following, I adopt the biochronological nomenclature of Gunnell et al. (2009). The lowest Bridgerian biochronological zone, Br1a, (Gardnerbuttean subage, previously referred to as Br0 which is no longer recognized) occurs in the Cathedral Bluffs Member of the Wasatch Formation and Laney Shale Member of the Green River Formation in the GGRB (Figure 1.2). It is characterized by a very high alpha diversity and contains a transitional fauna with a large number of Wasatchian holdover taxa such

as *Shoshonius*, *Coryphodon*, and *Didymictis* (Gunnell et al., 2009). The Br1b (lower Blacksforkian subage, often confusingly referred to as Bridger A as in the lithostratigraphic unit) is the oldest subage of the Bridgerian NALMA that is preserved in the Bridger Formation. Important index taxa from the biochronological zone include *Anaptomorphus westi*, *Smilodectes mcgrewi*, and *Sciuravus eucristidens* (Gunnell et al., 2009). Br2 (upper Blacksforkian subage) roughly corresponds to the extent of Matthew's (1909) lithological unit Bridger B, but this biochron is also found in strata above the top of Bridger B (Sage Creek Limestone) into the lowest 70 m of the overlying Bridger C lithostratigraphic unit. There is a large number of range-through taxa in the Br2 fauna, including *Hyrachyus modestus*, *Omomys carteri*, *Paramys delicatior*, *P. delicates*, *Scenopagus curtidens*, *Sinopa minor*, and *Thinocyon velox* (Gunnell et al., 2009). Characteristic Br2 taxa include *Notharctus tenebrosus* and *N. pugnax*. Br3 corresponds to the rest of Bridger C and Bridger D. This interval is characterized by a sudden decrease in the number of first appearance datums (FAD) and an increase in the number of last appearance datums (LADs), marking the beginning of the faunal turnover that takes its fullest form at the Bridgerian/Uintan NALMA boundary. Br3 index taxa include *Hyrachyus princeps*, *Miacis sylvestris*, *Orohippus agilis*, *Palaeosyops robustus*, *Telmatherium validus*, and *Thisbemys perditus* (Gunnell et al., 2009).

Ui1a represents the key transitional period from the Bridgerian to Uintan NALMA, and its faunal evidence is best recorded in the Bridger E (Turtle Bluff Member) of the Bridger Formation and in the Devil's Graveyard Formation in Trans-Pecos, Texas (Figure 1.1, Walton, 1992; Murphey and Dunn, 2009). Gunnell et al. (2009) defined the stratigraphic position of the Bridgerian/Uintan NALMA boundary in the Bridger

Formation to be at the base of the Basal E Limestone (Figure 1.2). The transitional fauna has also been found in other localities including the Uinta Basin, East Fork Basin, and in San Diego area (Figure 1.1). Ui1b has not been formally defined due to the lack of a suitable stratotype, but it can be seen in the middle unit of the Adobe Town Member of the Washakie Formation and the Friars Formation in San Diego area (Flynn, 1986; Walsh, 1996).

PREVIOUS CHRONOSTRATIGRAPHY

Magnetostratigraphy

Currently available chronostratigraphic data from the GGRB mainly consists of magnetostratigraphies from two basin margin localities (Clyde et al., 1997, 2001) and from the Washakie Basin (Flynn, 1986) as well as a suite of $^{40}Ar/^{39}Ar$ ages and U-Pb ages (Smith et al., 2008, 2010; Machlus et al., 2015, Table 2.1, Figure 1.1). Clyde's et al. (2001) composite magnetostratigraphic section sampled the Wasatch Formation (Cathedral Bluffs Member), Green River Formation (Laney Member) and lowermost portion of the Bridger Formation (Bridger A), which were correlated to Chrons C24n.1n to C22n (Figure 2.2). The Washakie Formation section sampled by Flynn (1986) is thought to overlap in part with the Bridger Formation, but correlation of its magnetozones to the GPTS has remained elusive (McCarroll et al., 1996). To this day, the only magnetostratigraphy from the Bridger Formation above the Bridger A is an unpublished Master's thesis by Jerskey (1981). That study, however, is hampered by small sample size, and its data are not supported statistically and thus will not be discussed further. The lack of magnetostratigraphic data from the bulk of the Bridger Formation has been a

setback in the effort to establish a basin-wide chronostratigraphic framework for the GGRB to place the basin records in a greater geographic and temporal context. The new Bridger Formation magnetostratigraphy presented herein represents an important step towards improved understanding of the Bridgerian NALMA and correlation of the Early-Middle Eocene deposits not only within the GGRB but also beyond.

Radioisotopic Dating

Numerical constraints for the age of the GGRB deposits have been provided by both $^{40}Ar/^{39}Ar$ and U-Pb geochronology (Table 2.1). Smith et al. (2008, 2010) proposed an age model for the GGRB based on a suite of $^{40}Ar/^{39}Ar$ ages from 29 ash beds in the Green River and Bridger Formations using laser incremental heating experiments and/or laser fusion experiments on single- and multiple-crystal aliquots. In Smith et al. (2008), $^{40}Ar/^{39}Ar$ dates were calculated relative to the Taylor Creek rhyolite (28.34 ± 0.28 Ma; Renne et al., 1998), but the dates were recalculated to the astronomically calibrated age of 28.201 Ma for the Fish Canyon sanidine standard (FCs_{K08}, Kuiper et al., 2008) in Smith et al. (2010). The use of astronomically calibrated FCs_{K08} enables direct comparison of $^{40}Ar/^{39}Ar$ and U-Pb dates because the astronomical method reduces the estimated absolute uncertainty of $^{40}Ar/^{39}Ar$ geochronology from ~2.5% to less than 0.25%, reducing the apparent $^{40}Ar/^{39}Ar$ and U-Pb offset. More recently, Machlus et al. (2015) dated 7 ash beds from the Wilkins Peak Member of the Green River Formation using high precision ID-TIMS zircon geochronology (Table 2.1). The dataset was used to propose a new strategy for establishing an orbital calibration for the Green River Formation, and thus, their data are highly precise at the uncertainty on the order of a single processional cycle.

These radioisotopic data of Smith et al. (2008, 2010) and Machlus et al. (2015) constrain the basin deposits in absolute time, however, many of the radioisotopically dated ashes were sampled from the basin center and have not been directly correlated to the existing magnetostratigraphic sections, which were collected in the basin margin where fluvial sediments are exposed more extensively (Figure 1.1). In order to build an integrative and basin-wide network of chronostratigraphy, it is important to combine the magnetostratigraphic and radioisotopic datasets and correlate basin center to the basin margin. As the first step, Tsukui and Clyde (2012) determined the polarity of many of the ashes that had been previously dated by $^{40}Ar/^{39}Ar$ dating method by Smith et al. (2008). However, that study targeted individual tuff beds instead of a continuous magnetostratigraphic section, so it was not possible to reliably assign a specific chron to each ash bed. The U-Pb dates of the three ashes presented herein can be correlated directly into the Bridger Basin magnetostratigraphy, and thus bear implication on the GPTS calibration for the relevant chrons.

MAGNETOSTRATIGRAPHY

Paleomagnetic Sampling

Paleomagnetic samples were collected by teams led by J. Flynn from 90 stratigraphic levels in six stratigraphic sections near the town of Mountain View, Uinta County, Wyoming, in the southern Bridger Basin (Figure 2.1, Table 2.2). The stratigraphic sections were measured using Jacob's staff and correlated physically using laterally traceable marker beds to form a ~560 m long composite section. At least three individually oriented samples were collected from each site. Depending on the

availability of rock type amenable for paleomagnetic analysis and the quality of exposure in the outcrops, the spacing of sites varied, but on the average, was ~7 m. After weathered loose sediments were removed from the surface, samples were taken from one of the following lithology: very fine to fine sandstone (42 sites), blocky and massive siltstone (mudstone) (27 sites), tuffaceous fine grained sandstone and/or ash (13 sites), and calcareous claystone (7 sites). An inferred depositional environment for many of the sampled lithofacies is fluvial with an exception of the calcareous claystone, which is likely to have been deposited by the paleolake Gosiute during periods of its short-term resurgence. There were no measurable dips to the strata from which the samples were collected, precluding the need for tectonic correction on the measured paleomagnetic vectors.

The lowest section, Beer Bottles and Bikers (BBB), is from the lower Bridger B and was sampled in the Little Dry Creek drainage in the Crooked Canyon area (Figure 2.1). The Little Dry Creek (LDC) section begins about 12 m above the top of the BBB section within the upper portion of the lower B and extends into the lower portion of the middle Bridger B. It was collected in the Little Dry Creek drainage in the Crooked Canyon area. The Cottonwood Creek (CWC) section overlaps with the upper 5 m of the LDC section and spans the upper part of the middle Bridger B and all of the upper Bridger B, up to the Bridger B/C boundary, which is marked by the Sage Creek Limestone. This section was taken on the northeast side of the Cottonwood Creek Bench. The Sage Creek Mountain (SCM) section begins at the Butcherknife Limestone, ~30 m above the Sage Creek Limestone and extends up to ~13 m below the Bridger C/D boundary which is defined by the Lonetree Limestone. This section was measured on the

northwest side of the Sage Creek Mountain. The Hickey Mountain (HM) section spans from the Lonetree Limestone to the Upper Limestone, covering the lower and middle Bridger D. This section was measured on the east to southeast side of Hickey Mountain. Finally, the Upper Sage Creek (USC) section begins at the Lonetree Limestone and spans the entire Bridger D and the lowermost 28 m of the Bridger E, overlapping with the HM section. It was sampled on the north flank of the Sage Creek Mountain. The GPS coordinates of the sections are listed in Table 2.2.

Paleomagnetic Analysis

All paleomagnetic analyses were performed by C. Nunez and J. Flynn in the magnetically shielded Paleomagnetics Laboratory of the Field Museum of Natural History (samples from BBB, LDC, CWC, LDC and HM sections) and by K. Tsukui at the Lamont-Doherty Earth Observatory Paleomagnetics Laboratory (USC section only). Samples were first cut and ground into 2.5 cm cubes with a saw and hand-sanded before measurement to remove surface impurities. Bulk magnetic susceptibility was measured on a Molspin Minisep magnetic susceptibility system before demagnetization. The paleomagnetic samples were progressively demagnetized between room temperature (25 °C) and 700 °C using Schonstedt TSD-1 thermal demagnetizer and GSD-1 A.C. demagnetizer (at FMNH) and 2G DCSQUID rock magnetometer (at LDEO). After every demagnetization step, natural remanent magnetization (NRM) was measured on the Molspin Minispin spinner magnetometer (at FMNH) and a 2G Model 760 DC-SQUID rock magnetometer (at LDEO). Following every heating step, magnetic susceptibility measurements were made with a Bartington MS2B instrument. Initial pilot studies were

carried out on representative samples to determine the best protocol for the remaining samples (shown with asterisks in Table 2.3).

Characteristic remanent magnetization (ChRM) was determined for each sample by principle component analysis through demagnetization paths defined by higher-unblocking temperature steps trending toward the origin (Kirschvink, 1980). When defining the ChRM component, the origin was usually not included. However, there were cases in which there was strong overprint that was demagnetized at relatively high temperature, leaving the ChRM component to be defined only by two steps. If the ChRM component had clearly trended toward the origin, I then included the origin to define the ChRM component. The maximum angular deviation (MAD) of the ChRM was calculated for each sample, and at least three samples with MADs less than 20° were used to determine a statistically robust site mean direction. Samples with MADs >20° were rejected from further analyses. Sites that passed Watson's test for randomness at the 95% significance level at N = 3 with directional precision parameter (k) of >10 (<10) were classified as Class I (II) sites (Watson, 1956) and were used to define virtual geomagnetic poles (VGP). Sites that failed Watson's test or only had two samples with MAD less than 20° were identified as Class III sites, and they were used only to supplement the interpretation of magnetic polarity stratigraphy. The magnetic polarity of sites was inferred based upon the VPG of Class I and II sites, assuming that the ChRM ws primary in origin.

Paleomagnetic Results

Step-wise thermal demagnetization revealed either one or two NRM components in every sample. Many of the samples exhibited an overprint, which typically was

unblocked by 500 °C (Figure 2.3). After removal of the low-temperature component, the samples were progressively demagnetized up to 700 °C (Table 2.3). The sample and site statistics are summarized in Table 2.3 and Table 2.4, respectively.

The BBB section is the lowest of the composite section and 38.7 m thick including 6 sites. Lithology of samples from the section varies from very fine to fine sandstone (5 sites) to blocky and massive siltstone or mudstone (1 site). Samples from most of the sites show a pattern of stable demagnetization with the ChRM component isolated at temperatures between 500 °C and 700 °C. The only exception are the three samples from BBB-3 in which the NRM shows a stead increase from 300 °C to 700 °C, indicating that the low temperature steps (less than 300 °C) are likely to be ChRM. The lithology of these samples are "blue-green moderately sorted very fine to fine grained sandstone", but the collector (J. Flynn) noted an "obvious alteration rim found along fractures", and the observed increase in NRM after 300 °C may be due to the secondary alteration.

The LDC section from Bridger B is 80.5 m thick and includes 16 sites. Lithology of samples from the section varies from very fine to fine sandstone (2 sites), blocky and massive siltstone or mudstone (12 sites) to calcareous claystone (2 sites). Of the 16 sites, three sites were statistically unreliable because they did not satisfy the criteria of having at least 3 samples with MAD of less than 20°. Of the remaining 13 sites, four sites were of normal polarity, but only LDC-2 and LDC-3 were stratigraphically contiguous to be considered as a normal polarity chron. Both of these sites are characterized by lower-than-expected VGP latitude (15° and 22.5° respectively), and given its transient nature, they may indicate the case of cryptochron (Cande and Kent, 1992). Other sites of normal

polarity occurred sporadically throughout the section that is otherwise of reversed polarity, and some of they may be a result of insufficient demagnetization of a strong overprint.

The CWC section from lower Bridger C is 76 m thick and includes 12 sites. Lithology of samples taken from the section is either very fine to fine sandstones (9 sites) or blocky and massive siltstone or mudstone (3 sites). The lowest three sites of the section are relatively straightforward and are unambiguously of reversed polarity. However, the sites between CWC-4 and CWC-7 yielded statistically unreliable demagnetization. If the samples with MAD up to 30° were allowed in determination of site mean directions, CWC-4 would be of reversed polarity, CWC-5 would be indeterminate, CWC-6 would be of normal polarity, and CWC-7 would be of reversed polarity. The pattern of switching polarity continues up-section to CWC-8 though CWC-11, however, in any part of this interval, no two contiguous sites are characterized by the same polarity.

The SCM section from the upper part of the Bridger C is 122.2 m thick and includes 18 sites. Lithology of samples from the section is either very fine to fine sandstone (10 sites), blocky and massive siltstone or mudstone (3 sites), tuffaceous fine grained sandstone or ash (3 sites) or calcareous claystone (1site). For the most part, the section consists of sites that are unambiguously of reversed polarity. The exceptions are the three samples from SCM-6 that were characterized by normal polarity based on ChRM isolated between 25 °C and 625 °C. Based on the temperature at which the ChRM was isolated, it is unlikely that the NRM component is due to an overprint. This site is clearly an outlier within a section that is otherwise entirely of reversed polarity.

The HM section from Bridger D is 100.3 m thick and includes 14 sites. Lithology of samples from the section varies from very fine to fine sandstone (1 site), blocky and massive siltstone or mudstone (5 sites), tuffaceous fine grained sandstone or ash (7 sites) to calcareous claystone (1 site). Step-wise demagnetization was straightforward for most of the section except for HM-14, which exhibited complex demagnetization behavior that was beyond interpretation. The rest of the section was entirely of reversed polarity.

Magnetic mineralogy of the samples is difficult to infer based only on the available data. However, the majority of the samples had unblocking temperature of greater than 625 °C, indicative of hematite or maghemite as the main magnetic carrier. In addition, though to a lesser extent, it appears that there are minor contributions from titanohematite and titanomagnetite. For the samples used to infer site mean directions, and ultimately, the VGP latitude, the average MAD of the ChRM was 7.6°. Of the 69 sites that were included in calculation of the VGP latitude, 50 sites were characterized by reversed polarity, with ChRM showing S-SE declinations and moderate to steep negative inclinations (mean of declination in tectonic coordinates = 160.1°, mean of inclination in tectonic coordinates = −51.3°, $\alpha 95$ = 5.9°, Figure 2.4). The remaining sites showed normal polarity, with N-NW directions and moderate to steep positive inclinations (mean of declination in tectonic coordinates = 331.1°, mean of inclination in tectonic coordinates = 49.5°, $\alpha 95$ = 17.9°, Figure 2.4).

In order to recognize polarity reversals and magnetozones, at least two contiguous sites that are assigned to be either Class I or Class II must have the same polarity. Two magnetic reversals were identified based on 69 sites in the Bridger Basin composite section (Figure 2.5). Polarity zone A+ spans 0-60.9 m within lower Bridger B; polarity

zone B- spans 60.9-495.9 m within the rest of Bridger B, entire Bridger C and most of Bridger D, and polarity zone C+ spans 505.1-557.8 m within the uppermost part of Bridger D and Bridger E.

Correlation to the GPTS

In correlating the composite paleomagnetic stratigraphy to the GPTS, I rely on the known position of the Bridgerian/Uintan boundary with respect to the magnetostratigraphy. In the Bridger Basin, the lithostratigraphic position of the Bridgerian/Uintan NALMA boundary has been designated at the base of Bridger E at the Basal E Limestone (Gunnell et al., 2009, Figure 1.2), and the Bridger E beds are characterized by polarity zone C+ in this study. In San Diego area where the Bridgerian/Uintan boundary has been recognized (Flynn, 1986; Walsh et al., 1996), fossiliferous Paleogene marine and terrestrial facies of the La Jolla and Poway Groups interfinger, making it possible to directly calibrate the mammalian biostratigraphy with the GPTS via standard marine biochronologies (Figure 2.6; Flynn, 1986). Thus, the San Diego sections are instrumental in temporally calibrating the Bridgerian/Uintan boundary by the GPTS and it plays a pivotal role in facilitating correlation of other boundary-bearing sections to the GPTS.

In San Diego area, the Bridgerian/Uintan boundary (Earliest Uintan) was initially thought to occur in the upper part of the Friars Formation because of an overlapping temporal unit between the classic Bridgerian and Uintan NALMAs there (Figure 2.6, Flynn, 1986). This stratigraphic interval occurred within a reversed polarity interval correlated with Chron C20r, and thus, Flynn (1986) concluded that the Bridgerian/Uintan boundary occurred within a reversed polarity interval, most likely Chron C20r (Figure

2.6). However, more recent faunal sampling by Walsh (1996) revised the biostratigraphic position of the Bridgerian/Uintan boundary from the upper Friars Formation as was suggested by Flynn (1986) to extend into the lower part of the Friars Formation (Figure 2.6). Within MS-5 Genessee Avenue magnetostratigraphic section, a Los Angeles County Museum locality (LACM-314), which had yielded the lowest stratigraphic datum of the boundary-defining taxa, Amynodon and Leptoreodon, was located within a normal polarity interval in the lower part of the Friars Formation (Walsh et al., 1996, Figure 2.6). This normal polarity interval was considered to be the same as the one found in the underlying Ardath Shale, which had been assigned to Chron C21n based on correlation of its in-situ planktonic foraminifera and nannoplankton floras to the marine biostratigraphy (Berggren et al., 1985). The Ardath Shale contains a suite of marine floras that as a whole, suggests an upper/late Zone NP14 age. The upper NP14 is assigned to Chrons C21n and C21r in the Geologic Time Scale (Vandenberghe et al., 2012), and because the Ardath Shale was mostly of normal polarity in the type section (Flynn, 1986; Walsh et al., 1996), it was assigned to Chron C21n (Flynn, 1986; Walsh et al., 1996). Because of the stratigraphic proximity to the Ardath Shale, the normal polarity interval in the lower Friars Formation was interpreted by both Flynn (1986) and Walsh et al. (1996) to be also part of Chron C21n. Thus, in San Diego, the Bridgerian/Uintan boundary has been established to lie within Chron C21n, and via faunal (mammalian) correlation, the polarity interval C+ (which contains the Bridgerian/Uintan boundary) in the Bridger Basin magnetostratigraphy is pinned to Chron C21n.

As for the rest of the Bridger Basin magnetostratigraphic section, there is no evidence to suspect that there is a significant hiatus within the sampled interval, so each

magnetozone can be correlated to the GPTS sequentially from Chron C21n at the top, with the polarity interval B- to Chron C21r, and the polarity interval A+ at the base of the composite section to chron C22n. Combined with the magnetostratigraphy of the Bridger A by Clyde et al. (2001), the Bridger Formation as a whole spans from Chron C22r to C21n in the Greater Green River Basin. According to this chron assignment, sedimentation rate is inferred to be mostly uniform throughout the Bridgerian NALMA (Figure 2.7) if the magnetostratigraphy of Clyde et al. (2001) from the older parts of the GGRB and this study are spliced. Furthermore, the Wasatchian record from the Bighorn Basin (Clyde et al., 1994) can be added to show the inferred sedimentation rate for the entire Eocene (including the Wasatchian and Bridgerian NALMAs) in western Wyoming (Figure 2.7). Combining the records from the Bighorn Basin and GGRB, mammalian biostratigraphy can now be calibrated by the GPTS via magnetostratigraphy from the beginning of the Wasatchian to the Uintan, with the Clarkforkian/Wasatchian, Wasatchian/Bridgerian, and Bridgerian/Uintan NALMA boundaries assigned to Chrons C24r, C23r, and C21n, respectively.

U-PB GEOCHRONOLOGY

Materials

Church Butte Tuff (CBT)

The tuff is located at the boundary between the lower and middle Bridger B (Murphey and Evanoff, 2007, Figure 1.2). It is correlated to site LDC-8 (“persistent bright white marker bed”, JJF field notes) which occurs at ~81 m in the composite magnetostratigraphic section. The bed is composed of a ~0.7 m thick fine grained

pumiceous sand with abundant biotite and pink plagioclase and is olive green in color. It is well exposed near Church Butte in the Bridger Basin. Its $^{40}Ar/^{39}Ar$ date has been provided by Smith et al. (2008, 2010) to be 49.05 ± 0.16 Ma with MSWD of 1.19 (fully propagated error at 2σ and calibrated using FCs_{K08}), and based on discrete sampling, its paleomagnetic polarity has been determined to be of normal polarity based on 4 statistically significant samples (Tsukui and Clyde, 2012). The tuff provides the best estimate for the age of extremely rich Bridger B2 fossil vertebrates from localities in and around Crooked Canyon (Figure 2.1).

Henrys Fork Tuff (HFT)

The tuff marks the boundary between the middle and upper part of the Bridger C (Figure 1.2). It can be correlated to the composite magnetostratigraphic section near SCM-15 at the level of ~327 m. The tuff is widespread across the southern Bridger Basin and makes a useful marker bed. It is ~0.2 to 1 m in thickness and rich in biotite, which are often euhedral in shape, especially near the base of the bed. Its $^{40}Ar/^{39}Ar$ age was determined by Smith et al. (2008, 2010) to be 48.44 ± 0.15 Ma with MSWD of 1.04, and the paleomagnetic polarity was determined by Tsukui and Clyde (2012) to be reversed based on 4 statistically significant samples.

Sage Creek Mountain Tuff (SCM)

The tuff is located about halfway up within the Bridger E, at ~40 m above the top of the magnetostratigraphic section. Its position is critical, as it provides the best age estimate for the transitional Uintan (Ui1a-b) fauna at the Bridgerian/Uintan boundary. It is a ~2 m thick white pumiceous sandstone. Tsukui and Clyde (2012) showed that the tuff

is of normal polarity based on 4 statistically significant samples. Its $^{40}Ar/^{39}Ar$ age was determined by Smith et al. (2008, 2010) to be 47.45 ± 0.15 Ma with MSWD of 0.69.

Laboratory Procedures

Samples were processed to prepare mineral separates via standard rock crushing, sonication, magnetic and heavy-liquid separation. Specific morphological features that are often found in zircons of volcanogenic origin were sought at the time of picking. Under a binocular microscope, I preferentially selected zircons that were large, acicular, colorless, euhedral, crack-free and have doubly terminated prisms with melt inclusions along the crystallographic c-axis (Ramezani et al., 2011). The selected grains were treated with the chemical abrasion (CA) method of Mattinson (2005) before U and Pb separation as described in the following. The zircons were first annealed at 900 °C for 60 hours in order to prevent U vs. Pb elemental fractionation and procedural (as opposed to in situ) Pb loss, which results from the laboratory leaching procedure. This step can also suppress the $^{207}Pb^*$ vs. $^{206}Pb^*$ fractionation effect (Mattinson, 2005). The annealed zircons were then transferred to Teflon microcapsules and leached in HF acid at 180°C for 12 hours. The chemical leaching process is crucial for eliminating U rich metamict domains that are likely to have undergone open system behavior due to uranium radioactivity causing in-situ Pb loss. By only sampling zircon domains that are likely to have remained closed, it becomes possible to reduce the degree of discordance. The grains were subsequently subjected to multiple rinsing steps to remove zircon residue contained in the removed parts. The grains were rinsed by ultraclean (blank checked) H_2O and HCl acid, which were carefully pippetted out each time. HCl was added to the leached and cleaned zircons and were dried on a hot plate and soaked in sonicated bath for 30 minutes. After repeating

this procedure a few times, individual zircon fractions were put in a microcapsule and spiked with a mixed 205Pb-233U-235U tracer solution (ET535C) and dissolved in HF and HNO_3 at 220 °C for 48 hours. The dissolved fractions were then heated to complete dryness on a hot oven and turned first into fluoride salt and subsequently converted to chloride phase by mixing with HCl and heated at 180°C overnight, resulting in formation of uranium and lead chlorides. At this stage, the samples were put though anion exchange chemistry to remove the matrix. Pb and U were eluted simultaneously using a combination of 6N HCl and 0.1N HCl, respectively (Krogh 1982). The isolated Pb and U were stored in pre-cleaned beakers that had been fluxed with HCl and HF and finally mixed with phosphoric acid before evaporation on a hotplate. The eluted U and Pb coated by phosphoric acid were loaded together onto a single rhenium filament in silica-gel. The silica-gel lowers the ioniziation temperature of Pb while increasing the ionization efficiency to 3% and 5% for Pb and U, respectively. It also has additional advantage to stabilize the beam. Finally, the sample-loaded filaments were smoked to volatilize any impurities and placed onto a turret for mass spectrometry analysis.

All analyses were carried out on individual zircons and measured on a VG Sector-54 multi collector thermal-ionization mass spectrometer in the Bowring Lab at the Massachusetts Institute of Technology, using peak-hopping on a single Daly detector and static Faraday mode for Pb and UO_2, respectively. Raw data on isotopic ratios were filtered in Tripoli, and errors and weighted mean dates were calculated with U-Pb Redux software (Bowring et al., 2011; McLean et al., 2011). Due to the nature of this study, the U-Pb dates will be reported with the external error, which includes both tracer calibration and decay constant errors of Jaffey et al. (1971). Uncertainty on the tracer calibration is

0.015%. All dates in the following discussion are reported at 2σ unless otherwise noted. Details of age calculation and error propagation as well as various correction procedures are explained in McLean et al. (2011).

U-Pb Geochronology Results

Church Butte Tuff

Six single-grain CA-TIMS analyses show an overlapping and concordant cluster and give a weighted mean $^{206}Pb/^{238}U$ date of 48.899 ± 0.018/0.030/0.060 Ma with a MSWD of 1.39 after Th correction. However, as Figure 2-8.B shows, z1, z2 and z4 form a younger cluster, whereas z3, z5, and z6 form an older cluster. Considering that z5 and z6 have relatively large analytical errors and because CA treatment is likely to have reduced the chance of Pb loss, I consider the weighted mean and Th corrected age based on three younger analyses to be the best estimate for the eruption age of the Church Butte tuff.

Henrys Fork Tuff

Twelve out of 15 single-grain CA-TIMS analyses show an overlapping and concordant cluster and give a weighted mean $^{206}Pb/^{238}U$ date of 48.265 ± 0.015/0.028/0.059 Ma with a MSWD of 1.7 after Th correction. The remaining three analyses (z7, z17, and z21) are slightly older, likely due to the inclusion of detrital crystals mixed in by fluvial processes (Figure 2.9, Table 2.6), and thus the younger population is considered here to be the best estimate for the depositional age of the tuff.

Sage Creek Mountain Tuff

Four single-grain zircon analyses were made by Jahan Ramezani. All four analyses are concordant, but show a spread along the concordia. Due to the small sample

size, the population cannot be rigorously defined, and thus, I tentatively select the youngest single zircon analysis to be the best approximation for the eruption and depositional age. After Th correction, the $^{206}Pb/^{238}U$ date of the analysis is 47.192 ± 0.068/0.071/0.087 Ma (Figure 2.10, Table 2.7).

DISCUSSION

Implications of the Bridger Basin Magnetostratigraphy for the Other Bridgerian/Uintan Boundary-Bearing Sections

With the Bridger Formation now calibrated by the GPTS, it is now possible to suggest correlation of the magnetostratigraphies from other boundary-bearing sections (e.g., Washakie Basin, East Fork Basin; Flynn, 1986; McCarroll et al., 1996) to the GPTS based on faunal (mammalian) correlations. Correlation of these sections to the GPTS had previously been difficult because of the lack of datable horizons and/or a marker bed that would allow correlation to other records. In order to avoid circular reasoning, my proposed correlation is based solely on bio- and magnetostratigraphic evidence and does not consider any radioisotopic dates that may be available.

Washakie Basin

The bio- and magnetostratigraphy of the Washakie Basin have been studied by Flynn (1986) and McCarroll et al. (1996), but correlation of its magnetostratigraphy to the GPTS has remained ambiguous because of the sporadic distribution of fossil-bearing horizons, an unconformity of unknown duration at the "lower brown sandstone" and ~70 m of unsampled section due to extensive cover in the outcrop (Figure 2.6). In the Washakie Basin, Flynn (1986) sampled from the Laney Shale Member of the Green

River Formation up to the middle unit of the Adobe Town Member of the Washakie Formation, reporting ten polarity reversals within the 900-meter composite section (Figure 2.6). Flynn (1986) argued that the Earliest Uintan fauna occurred in a reversed polarity interval that was referred to as polarity interval B5- (Figure 2.6). Based on faunal correlation to the San Diego section that was available then, he assigned polarity interval B5- to Chron C20r, concluding that the Bridgerian/Uintan boundary occurred in Chron C20r in the Washakie Basin, as was thought for the San Diego sections at the time. He then assigned Chron C20n to the overlying normal polarity interval (C+) and Chron C19r to the reversed polarity interval near the top of the section (D-). Because of the presence of a few short normal polarity intervals, the lower part of the section below B5- was not correlated to the GPTS definitively, but instead, two options of correlation were proposed.

McCarroll et al. (1996) revisited the work of Flynn (1986) and argued that the oldest transitional fauna occurred in the lower portion of the middle part of the Adobe Town Member, within a normal polarity interval referred to as polarity interval C+ in Flynn (1986) or unsampled interval (Figure 2.6). Still lacking any independent means to correlate the section to the GPTS, McCarroll et al. (1996) proposed four possible correlations to the GPTS. Based on faunal correlation with the new Bridger Formation magnetostratigraphy, the polarity interval C+ from the Washakie Basin, which contains the Earliest Uintan fauna according to McCarroll et al. (1996), can now be assigned to Chron C21n. This interpretation is for the most part consistent with one of the four correlations (D) proposed by McCarroll et al. (1996). Furthermore, the new biostratigraphic assignment of the Bridgerian/Uintan boundary by McCarroll et al. (1996) is consistent with that known from San Diego and Bridger Basin in that the boundary lies

within a normal polarity interval. According to this correlation scheme and correlation D of McCarroll et al. (1996), a long reversed polarity interval (B-) that contains two short normal polarity intervals (B2+ and B4+) is correlative to Chron C21r, and the basal normal polarity interval is correlative to Chron C22n (Figure 2.11). This proposed correlation assumes that the two short normal polarity intervals within Chron C21r in the Washakie Basin magnetostratigraphy (B2+ and B4+) are short-lived excursions of unknown origin and do not represent true polarity reversals. The basal part of the Washakie section overlaps in time with the uppermost part of the magnetostratigraphy by Clyde et al. (2001), and the two are consistent in terms of the expected biostratigraphy and lithostratigraphy, providing further support for this proposed correlation (Figure 2.11). In this new correlation, Chron C21r, to which the early/late Bridgerian boundary is correlated in the Bridger Formation magnetostratigraphy, occurs in the Kinney Rim Member and the lowest part of the Adobe Town Member of the Washakie Formation in the Washakie Basin (Figure 2.11). This correlation is in agreement with Roehler (1973) and McCarroll et al. (1996) who stated that the early/late Bridgerian boundary is likely to occur in the Green River Formation or in the lowest part of the Kinney Rim Member and not much higher, due to the absence of any early Bridgerian fauna in the Washakie Formation.

East Fork Basin

The East Fork Basin in southeastern Absaroka Range, preserves one of the most continuous sections spanning the Bridgerian/Uintan boundary, but the correlation of its magnetostratigraphy to the GPTS has been contested. Flynn (1986) sampled for magnetostratigraphy in the Aycross Formation and overlying Tepee Trail Formation,

which were united into a composite section by overlapping the upper normal polarity chron (D+) from the Aycross Formation section and the lower normal polarity chron (D+) in the Tepee Trail Formation section (Figure 2.6). Within this magnetostratigraphic framework, Flynn (1986) identified the Earliest Uintan biochron to occur within the long reversed polarity interval (E-), and based on faunal correlation with the San Diego section as was known then, he correlated polarity interval E- to Chron C20r. However, as discussed earlier, more recent faunal collections by Walsh (1996) revised the stratigraphic position of the Earliest Uintan in San Diego to lie lower in that sequence, within the normal polarity chron that was assigned to Chron C21n. Furthermore, Sundell et al. (1984) pointed out that the upper normal interval in the Aycross Formation section (D+) and the only normal polarity interval in the East Fork Basin Tepee Trail Formation section (D+) by Flynn (1986) are not equivalent, and also that Flynn's (1986) magnetostratigraphic section did not sample part of stratigraphy, including the Blue Point Marker Bed, the Aycross/Tepee Trail Formation contact, and the lowermost Tepee Trail Formation (Figure 2.6). For these reasons, it is important to reevaluate Flynn's (1986) magnetostratigraphy in the East Fork Basin and its correlation to the GPTS. According to faunal evidence from other parts of the Absaroka Range (Eaton, 1985), the lowest stratigraphic occurrence of the transitional fauna (Forstercooperia, Epihippus, and Amynodon) lies in the lower part of the "Holy City beds" of the Tepee Trail Formation (Figure 2.6) at three localities (localities V-78004, V-78016/79022, and V-79021/79025). This stratigraphic interval generally corresponds to which that was not sampled by Flynn (1986). Stratigraphic positions of many of the most age-diagnostic earliest Uintan fossil localities have been tied into the magnetostratigraphic section of Sundell et al. (1984)

who identified that the lower part of the Tepee Trail Formation, including the "Holy City beds", is of normal polarity and correlative with Chron C21n (Figure 2.6). This chron assignment is in agreement with the conclusion reached based on magnetostratigraphy from the Bridger Basin as well as that from the Washakie Basin. Revised magnetostratigraphy for the East Fork Basin is provided in Figure 2.11.

In summary, the Bridger Formation magnetostratigraphy was correlated to the GPTS via faunal correlation to the San Diego section, with the Bridgerian/Uintan boundary assigned to Chron C21n. The agreement between San Diego and Bridger Basin represents an important step towards resolving the timing of the Bridgerian/Uintan boundary, which has been referred to as "one of the most problematic issues of Eocene biochronology" (Gunnell et al., 2009). In fact, it is now possible to correlate all the Bridgerian/Uintan boundary bearing sections in the western U.S. between San Diego, Bridger Basin, Washakie Basin, East Fork Basin, Uinta Basin and Trans Pecos, TX, and in all sections, the Bridgerian/Uintan boundary occurs in Chron C21n (Figure 2.11, 2.12).

Implications on Calibration of the GPTS

In Geologic Time Scale 2012, the GPTS for the Neogene and Oligocene is calibrated in absolute time by astronomical dating (Lourens et al., 2004; Pälike et al., 2006), resulting in a fairly stable and robust timescale (Vandenberghe et al., 2012). However, calibration of the early Paleogene portion of the GPTS has been much more challenging because radioisotopic data are only sporadically distributed across the time interval and can only be partially reconciled with the existing astronomical data. The difficulty stems from a few factors, including: (1) the "early to late Eocene cyclostratigraphic gap" in pelagic sediments due to shoaling of the calcite compensation

depth in response to the warming, which prevented deposition of cyclic carbonate sediments (Westerhold et al., 2012), (2) increasing uncertainties in the astronomical solution beyond 40 Ma, and (3) large uncertainties in prior radioisotopic dates that were used as tie points, and in the age of the $^{40}Ar/^{39}Ar$ standards such as the Fish Canyon sanidine. Most of these problems ultimately stem from the lack of a single precise orbital solution in time intervals older than 40 Ma due to increased uncertainty in key astronomical variables. This current circumstance precludes calibration of orbitally-tuned sections from the Paleogene without the use of radioisotopically dated ash beds whose positions are well known with respect to astronomical cycles. While there are several $^{40}Ar/^{39}Ar$ dated ash beds within Paleogene cyclostratigraphically defined sections (e.g. ash -17 and +19; Westerhold et al., 2009), the ~0.25% uncertainty in the accuracy of the $^{40}Ar/^{39}Ar$ method (including uncertainties of the decay constant and the age of the FCs) is too large to allow unambiguous identification of a single best tuning option (However, see Machlus et al., 2015). Because of these factors, calibration of the Paleogene GPTS remains controversial, and in Geologic Time Scale 2012, Vandenberghe et al. (2012) opted a hybrid solution of using both a radioisotopic age model (for the interval 53-37 Ma) and two separate astronomical age models (66-53 Ma and 37-23 Ma) for calibration of the entire Paleogene GPTS. It is important to note that when discussing numerical calibration, there is not one GPTS calibration that has been agreed upon by all researchers, but rather, there exist multiple calibration models that are based on different parameters and datasets. In the following, I will discuss the calibration models that have been proposed for the early Paleogene GPTS and then subject them to a test using the geological dataset from the GGRB (Table 2.8, Figure 2.13).

The first two models are for the interval between Chron C24r and C20n and based on $^{40}Ar/^{39}Ar$ dates from seven ash beds and magnetostratigraphy within the GGRB (Smith et al., 2008, 2010). The two models differ only by the age of FCs that was assumed in calculating the age of the ash beds. The $^{40}Ar/^{39}Ar$ ages are in agreement with the stratigraphic order of the ashes, demonstrating that the dataset is at least internally consistent, however, the models are handicapped by uncertainties in correlation of the ashes to the local magnetostratigraphy. Specifically, the Layered tuff, Sixth tuff, and Continental tuff were tied into the magnetostratigraphy of Clyde et al. (2001), with the Layered and Sixth tuffs correlated to the Chron C23n/C22r transition, and the Continental Peak tuff to Chron C22n. However, there is no direct evidence to support such a correlation, and in fact, Tsukui and Clyde (2012) showed that the Continental tuff is of reversed polarity. As can be seen in Figure 2.13, these models calibrate the early paleogene chrons characteristically younger by ~ 1 myr compared to all the other models evaluated in this study.

The remaining models are based on astronomical tuning of orbitally-paced geochemical proxy records in marine sediments (Westerhold and Röhl, 2009; Hilgen et al., 2010; Geological Time Scale 2012 [GTS2012]). Westerhold and Röhl (2009) presented estimates on chron durations from Chron C20 to C24 based on orbital tuning and cycle counting of Fe intensity data within marine sediments from ODP Leg 207 (Site 1258). For tuning the early Paleogene records, Westerhold and Röhl (2009) used the stable long eccentricity cycle (405-kyr) because its stability had been demonstrated beyond 40 Ma (Laskar et al., 2004). However, due to uncertainties in determining minima in the 405-kyr cycles within the Paleocene cyclostratigraphy (Westerhold et al., 2007),

direct correlation of the Chron C20-C24 interval to the orbital solution is not possible. For this reason, Westerhold and Röhl (2009) anchored the astronomical estimates of chron duration to the C24n/C24r reversal age, for which three alternative ages were proposed due to the inability to perform exact tuning on the Walvis Ridge cyclostratigraphic record (ODP Leg 208) to the orbital solution (La2004 and Va2003) using the 405-kyr cycle (Westerhold et al., 2007). These three proposed ages of the C24n/C24r reversal are offset by 405 kyr and are 53.53 Ma (Option 1), 53.93 Ma (Option 2), and 54.33 Ma (Option 3). For the following evaluation, I added the estimates of early Eocene chron durations by Westerhold and Röhl (2009) to the Option 1, 2 and 3 ages for the C24n/C24r polarity reversal. Furthermore, though indirectly, the age of the C24n/C24r polarity reversal bears on the age of the Paleocene Eocene Thermal Maximum (PETM) because the duration between the two events has previously been constrained to be 95 processional cycles (or 1995 kyr) by Westerhold et al. (2007). Similarly, if the Paleocene cyclostratigraphy from Leg 198 and 208 were added, Option 1, 2 and 3 models would imply the Cretaceous/Paleogene (K/Pg) age of 65.28 Ma, 65.68 Ma, and 66.08 Ma, respectively.

Hilgen et al. (2010) proposed an alternative astronomical model for the Paleocene in response to the noted discrepancy regarding the number of 405-kyr cycles in the Paleocene between sections in Zumaia and ODP Leg 198 (Shatsky Rise) and 208 (Walvis Ridge) (Hilgen et al., 2010; Kuiper et al., 2008; Westerhold and Röhl, 2009). By evaluating the Paleocene cyclostratigraphy from Zumaia as well as ODP Leg 198 and 208, Hilgen et al. (2010) argued that the entire Paleocene contains 25 405-kyr cycles rather than 24 as had been suggested by Westerhold et al. (2008). Using the $^{40}Ar/^{39}Ar$ age

(~66.0 Ma) of the ash beds near the K/Pg boundary as a starting point, Hilgen et al. (2010) re-tuned the Paleocene using the 405 kyr cycles, resulting in the age of ~56.0 Ma for the PETM and also in a much smoother seafloor spreading. This model is most similar to the Option 2 model (Figure 2.13).

Westerhold et al. (2015) presented astrochronology for the interval from 48 Ma to 41 Ma, closing the "Middle Eocene gap" to assemble a complete Eocene GPTS. The new data come from ODP Sites 702 (Leg 114) and 1263 (Leg 208), and astrochronology was constructed based on the 405-kyr cycles. In linking the new astrochronology of the Middle Eocene with the older records across the C21n/C21r boundary, the C21n/C21r age according to the option 2 model was used as the option 1 or 3 age for the boundary was inconsistent with the new Middle Eocene astrochronology.

Finally, in the GPTS2012 (Ogg, 2012), the age model for the Paleogene marine magnetic anomalies was derived by a combination of astronomical orbital tuning described above and radioisotopic age models using 6-order polynomial fit to bridge the Middle Eocene gap.

Assessment of Calibration Models

These eight competing calibration models described above and shown in Figure 2.13 were evaluated using the new U-Pb age data from the ash beds within the GGRB and the magnetostratigraphic data from the Bridger Formation. In addition to the U-Pb data from the three Bridger Formation ashes presented in this study, those in Machlus et al. (2015) are also used for a more comprehensive assessment of the calibration models. The U-Pb data in Machlus et al. (2015) were collected in the same laboratory using the same analytical procedures as those presented in this study. Both U-Pb datasets have a

precision at the 0.1% level or better, and thus, it permits a test of the calibration models at a much higher precision than was previously possible. Of all the tuffs from the GGRB for which high precision U-Pb ages are available, six of them have been associated with a particular chron, and paleomagnetic polarity has been determined for two other tuffs (Table 2.1). In this study, the goal is to identify a model that best meets all of the geological constraints imposed by the eight GGRB tuffs as dated by high precision U-Pb ages (including 2σ external error) and a specific chron with which the tuffs are associated in the magnetostratigraphy of the GGRB.

Figure 2.13 schematically shows the result of my assessment, and from this I conclude that Option 3 model is the one that best meets both U-Pb and magnetostratigraphic constraints for all of the GGRB tuffs except for the Grey tuff. All the other models are less ideal because according to their calibration, the U-Pb dates do no predict a correct chron for two or more tuffs. The Option 3 model estimates ages of 56.33 Ma and 66.08 Ma for the PETM and K/Pg boundary, respectively. The K/Pg boundary age is in agreement with the astronomical estimate of Kuiper et al. (2008) and also radioisotopic ages by Bowring et al. (2008, 66.1 Ma) and Renne et al. (2013, 66.043 ± 0.043 Ma) (Figure 2.14). On the other hand, the PETM age estimated by Option 3 (56.33 Ma) is older and is outside the error of the U-Pb age of 55.846 ± 0.118 Ma by Charles et al. (2011) (Figure 2.15). Thus, the Option 3 age model is consistent with most of the existing geochronological constraints for the age of the K/Pg boundary, but not for the U-Pb age for the PETM. The U-Pb age of the PETM by Charles et al. (2011) is closest to the estimate according to Option 2 model. Interestingly, however, if the assumption of 25 405-kyr cycles was employed for the duration of the Paleocene, the U-

Pb age of the PETM by Charles et al. (2011) would imply the age of ~66 Ma for the KTB, which is in agreement with the option 3 estimate. If the U-Pb date of Charles et al. (2011) is in fact correct, this observation hints at a possibility that the relative distance from Ash-17 to the PETM within Chron C24r is inaccurate. Ash -17 has been found well above the PETM in the middle part of Chron C24r at DSDP Site 550 and has been tied to ODP Site 1262 by cyclostratigraphy as well as dated by $^{40}Ar/^{39}Ar$ dating (Westerhold et al., 2009; Storey et al., 2007). Since the absolute age of the PETM is derived by interpolation relative to the position of Ash -17 within Chron C24r, the error in the relative distance between the ash and PETM could explain the 0.49 myr discrepancy between the astronomically derived Option 3 age and U-Pb age of the PETM. The relative position of the ash -17 is presently determined at C24r.57 based on magnetostratigraphy of DSDP 550 (Storey et al., 2007; Westerhold et al., 2009), and its cyclostratigraphic position has been shown to be correct based on bio- and cyclostratigraphic patterns. However, Westerhold et al. (2009) has suggested a lower number of cycles between the ash and PETM, and if true, it would shift the astronomical age estimate of the PETM younger in the direction of the U-Pb age by Charles et al. (2011). The fact that there is a relatively large difference between $^{40}Ar/^{39}Ar$ dating and astronomical tuning age of the ash -17 is also consistent with this hypothesis. In any case, it would be desirable to determine the stratigraphic position of the ash relative to the PETM in other sections.

Alternatively, Westerhold et al. (2009) has pointed out the possibility of an error in tuning of Zumaia. The section in Zumaia, Spain has been critical as it spans the K/Pg boundary, and it has been astronomically tuned while having been constrained by magnetostratigraphy as well. The K/Pg boundary is known to occur at a 405-kyr

eccentricity minimum. The successive minima around the time of the boundary are at 65.2 Ma, 65.6 Ma, 66.0 Ma, and 66.4 Ma, and the $^{40}Ar/^{39}Ar$ ages of the Z coal and IrZ coals from the boundary section in Hell Creek, MT suggest that 66.0 Ma is most likely (Kuiper et al., 2008). Taking this as a starting point, the Zumaia section was retuned to result in the astronomical age of 65.95 Ma for the K/Pg boundary (Kuiper et al., 2008). However, Westerhold et al. (2009) has noted that Kuiper's et al. (2008) tuning of Zumaia section contains 1 extra 405-kyr cycle than tuning of Westerhold et al. (2008) on records from Walvis Ridge or Shatsky Rise for the interval between the K/Pg boundary and Chron C28n (top). Adding the cycle would imply the age of the PETM to be 55.93 Ma, if the astronomical age of the boundary was to be held at 65.95 Ma, and the revised PETM age would be within error of the U-Pb age of Charles et al. (2011). The revised age of 55.93 Ma is inconsistent with the known relative duration between ash-17 and PETM, but this discrepancy has already been discussed earlier as a potential source of controversy regarding the age of the PETM.

Finally, the age of the FCs may also explain the difference between the option 3 age and U-Pb age of the PETM; if the Ash -17 was dated relative to the FCs age of 28.02 Ma (Renne et al., 1998) rather than 28.201 Ma, it would bring the age of the PETM closer to the estimate by Charles et al. (2011), but considering a growing number of studies that support the Kuiper's et al. (2008) calibration, this latter scenario is unlikely.

CONCLUSIONS

Two paleomagnetic reversals were recognized within the ~560 m composite magnetostratigraphic section from the middle Eocene Bridger Formation, which includes

the Bridgerian/Uintan boundary near the top. The correlation to the GPTS was facilitated by the faunal (mammalian) correlation of the Bridgerian/Uintan boundary with the San Diego section, in which the boundary had been tied with Chron C21n via marine biochronology (Flynn, 1986; Walsh et al., 1996). Combined with Clyde et al. (2001) who sampled the lowest part of the Bridger Formation, the formation spans from Chron C22r to C21n. Since the stratotype of the Bridgerian/Uintan boundary has been designated to be at the Basal E Limestone in the Bridger Formation, its magnetostratigraphy serves as a keystone in providing comprehensive inter-basinal correlation for the middle Eocene fossiliferous sections in the western U.S., including the Bridger Basin, Washakie Basin, Uinta Basin, East Fork Basin and Trans Pecos, TX and San Diego. In all of these locations, the Bridgerian/Uintan transition occurs in the normal polarity interval that is assigned to Chron C21n, and the faunal transition is shown to be synchronolous within the duration of Chron C21n.

The new magnetostratigraphy was tied to absolute time via three U-Pb ID-TIMS ages from the Church Butte tuff, Henrys Fork tuff and Sage Creek Mountain tuff, which were correlated to the magnetostratigraphic section. Combined with five other tuffs from the Greater Green River Basin, for which paleomagnetic polarity and U-Pb data were known, eight competing calibration models for the Early-Middle Eocene GPTS were evaluated. These tuffs have been dated at high precision of ~0.1%, and thus, it permits a test of the calibration models at a much higher precision than was previously possible. Comparison of the geological data from the eight tuffs with the GPTS calibration models reveals that the option 3 age model (Westerhold et al., 2007; Westerhold and Röhl, 2009) was most consistent with the geological constraints of the tuffs from the Greater Green

River Basin. The option 3 age model provides age estimates of 56.33 Ma and 66.08 Ma for the PETM and K/Pg boundary, respectively. The K/Pg boundary age is close to the radioisotopic ages of Bowring et al. (2008) and Renne et al. (2013), however, the PETM age is outside the estimated error of the U-Pb age by Charles et al. (2011). The observed discrepancy between the U-Pb date and astromomical estimate of the PETM suggests either that the Paleocene tuning is in error in Zumaia, or the relative distance between the ash-17 and PETM needs revising. However, the observed congruence between the radioisotopic data and astronomical estimate for the age of the K/Pg boundary represents an important step towards a more robust timescale for the early Paleogene.

REFERENCES CITED

Berggren, W.A., Kent, D.V., and Flynn, J.J., 1985, Paleogene geochronology and chronostratigraphy, *in* Snelling, N.J., ed., The Chronology of the Geological Record: Oxford, Memoir, Geological Society of London, v. 10, p. 141-195.

Bowring, S.A., Erwin, D.H., Jin, Y.G., Martin, M.W., Davidek, K., and Wang, W., 1998, U/Pb zircon geochronology and tempo of the end-Permian mass extinction: Science, v. 280, p. 1039-1045.

Bowring, S.A., Johnson, K.R., Clyde, W, Ramezani, J., Miller, I., and Peppe, D., 2008, A Paleocene timescale for the Rocky Mountains: status and potential: Geological Society of America Abstracts with Programs, v. 40, no. 6, p. 322.

Bowring, J.F., McLean, N.M., and Bowring, S.A., 2011, Engineering cyber infrastructure for U-Pb geochronology: Tripoli and U-Pb_Redux: Geochemistry, Geophysics, Geosystems, v. 12, no. 6, Q0AA19, doi:10.1029/2010GC003479.

Bradley, W.H., 1964, Geology of Green River Formation and associated Eocene rocks in southwestern Wyoming and adjacent parts of Colorado and Utah: U.S. Geological Survey Professional Paper 496-A, p. A1–A86.

Cande, S.C., and Kent, D.V., 1992, A new Geomagnetic Polarity Time Scale for the Late Cretaceous and Cenozoic: Journal of Geophysical Research-Solid Earth, v. 97, no. B10, p. 13917-13951.

Charles, A.J., Condon, D.J., Harding, I.C., Pälike, H., Marshall, J.E.A., Cui, Y., Kump, L., and Croudace, I.W., 2011, Constraints on the numerical age of the Paleocene-Eocene boundary: Geochemistry, Geophysics, Geosystems, v. 12, Q0AA17, doi:10.1029/2010GC003426.

Chetel, L.M., Janecke, S.U., Carroll, A.R., Beard, B.L., Johnson, C.M., and Singer, B.S., 2011, Paleogeographic reconstruction of the Eocene Idaho River, North American Cordillera: Geological Society of America Bulletin, v. 123, no. 1–2, p. 71–88, doi:10.1130/B30213.1.

Clyde, W.C., Stamatakos, J., and Gingerich, P.D. 1994, Chronology of the Wasatchian land-mammal age: magnetostratigraphic results from the McCullough Peaks section, northern Bighorn Basin, Wyoming: Journal of Geology, v. 102, p. 367-377.

Clyde, W.C., Zonneveld, J.-P., Stamatakos, J., Gunnell, G.F., and Bartels, W.S., 1997, Magnetostratigraphy across the Wasatchian/Bridgerian NALMA boundary (early to middle Eocene) in the western Green River Basin, Wyoming: Journal of Geology, v. 105, no. 6, p. 657-669.

Clyde, W.C., Sheldon, N.D., Koch, P.L., Gunnell, G.P., and Bartels, W.S., 2001, Linking the Wasatchian/Bridgerian boundary to the Cenozoic Global Climate Optimum: New magnetostratigraphic and isotopic results from South Pass, Wyoming: Palaeogeography Palaeoclimatology Palaeoecology, v. 167, no. 1-2, p. 175-199.

Cope, E.D., 1882, Synopsis of the Vertebrata of the Puerco Eocene epoch. Supplement on a new Meniscotherium from the Wasatch epoch: Proceedings of the American Philosophical Society, v. 20, p. 461-471.

Diehl, J.F., Beck, M.E., Beskediehl, S., Jacobson, D., and Hearn, B.C., 1983, Paleomagnetism of the Late Cretaceous Early Tertiary North-Central Montana Alkalic Province: Journal of Geophysical Research, v. 88, p. 593-609.

Eaton, J.G., 1985, Paleontology and correlation of the Eocene Tepee Trail and Wiggins Formations in the north fork of Owl Creek area, southeastern Absaroka Range, Hot Springs County, Wyoming: Journal of Vertebrate Paleontology, v. 5, p. 345–370.

Evanoff, E., Brand, L.R., and Murphey, P.C., 1998, The Bridger Formation (middle Eocene) of southwest Wyoming: widespread marker units and subdivisions of Bridger B through D: Dakoterra, v. 5, p. 115-122.

Flynn, J.J., 1986, Correlation and geochronology of middle Eocene strata from the western United States: Palaeogeography Palaeoclimatology Palaeoecology, v. 55, p. 335-406.

Gazin, C.L., 1962, A further study of lower Eocene mammalian faunas of southwestern Wyoming: Smithsonian Miscellaneous Collections, v. 144, no. 1, 98 p.

Gazin, C.L., 1976, Mammalian faunal zones of the Bridger middle Eocene: Smithsonian Contributions to Paleobiology, v. 26, p. 1-25.

Gingerich, P.D., 1979, Phylogeny of middle Eocene Adapidae (Mammalia, Primates) in North America: *Smilodectes* and *Notharctus:* Journal of Paleontology, v. 53, p. 153-163.

Granger, W., 1914, On the names of Lower Eocene faunal horizons of Wyoming and New Mexico: Bulletin of the American Museum of Natural History, v. 33, p. 201-207.

Gunnell, G.F., 1998, Mammalian fauna from the lower Bridger Formation (Bridger A, early middle Eocene) of the southern Green River Basin, Wyoming: Contributions from the Museum of Paleontology, University of Michigan, v. 30, p. 83-130.

Gunnell, G.F., Murphey, P.C., Stucky, R.K., Townsend, K.E., Robinson, P, Zonneveld, J.P., and Bartels, W.S., 2009, Biostratigraphy and biochronology of the latest Wasatchian, Bridgerian, and Uintan North American Land-Mammal "Ages.", *in* Albright, B., ed., Geology, Vertebrate Paleontology, and Biostratigraphy in Honor of Michael O. Woodburne: Museum of Northern Arizona Bulletin, v. 65, p. 279-330.

Hayden, F.V., 1869, U.S. Geological Survey of the Territories, 3rd Annual Report, Chapter XII, Review of Leading Groups, etc.: Washington, D.C., p. 190-191.

Hayden, F.V., 1871,Preliminary report (4thAnnual) of the U.S. Geological Survey of Wyoming and contiguous territories: Washington, D.C., 511 p.

Hilgen, F.J., Kuiper, K.F., and Lourens, L.J., 2010, Evaluation of the astronomical time scale for the Paleocene and earliest Eocene: Earth and Planetary Science Letters, v. 300, v. 139-151, doi:10.1016/j.epsl.2010.09.044.

Jaffey A. H., Flynn K. F., Glendenin L. E., Bentley W. C. and Essling A. M., 1971, Precision measurement of half-lives and specific of ^{235}U and ^{238}U: Physical Review Letters, v. C4, p. 1889–1906.

Jerskey, R.G., 1981, A paleomagnetic study of the Bridger Formation, southern Green River Basin, Wyoming [M.S. thesis]: Milwaukee, University of Wisconsin, 113 p.

Kirschvink, J.L., 1980, The least-squares line and plane and the analysis of paleomagnetic data: Geophysical Journal of the Royal Astronomical Society, v. 62, p. 699-718.

Krogh, T.E., 1982, Improved accuracy of U-Pb zircon ages by the creation of more concordant systems using an air abrasion technique: Geochimica et Cosmochimica Acta, v. 46, p. 637-649.

Kuiper, K.F., Deino, A., Hilgen, F.J., Krijgsman, W., Renne, P.R., and Wijbrans, J.R., 2008, Synchronizing rock clocks of Earth history: Science, v. 320, no. 5875, p. 500-504.

Laskar, J., Robutel, P., Joutel, F., Gastineau, M., Correia, A.C.M., and Levrard, B., 2004, A long-term numerical solution for the insolation quantities of the Earth: Astronomy & Astrophysics, v. 428, no. 1, p. 261-285.

Leidy, J., 1869, The extinct mammalian fauna of Dakota and Nebraska, including an account of some allied forms from other localities, together with a synopsis of the mammalian remains of North America: Journal of the Academy of Natural Sciences, v. 2, p. 1-472.

Lourens, L.J., Hilgen, F.J., Laskar, J., Shackleton, N.J., and Wilson, D., 2004, The Neogene Period, *in* Gradstein, F., Ogg, J., and Smith, A., eds., A Geological Timescale 2004: Cambridge, U.K., Cambridge University Press, p. 409-440.

Machlus, M., Hemming, S.R., Olsen, P.E., and Christie-Blick, N., 2004, Eocene calibration of geomagnetic polarity time scale reevaluated: Evidence from the Green River Formation of Wyoming: Geology, v. 32, no. 2, p. 137-140.

Matthew, W.D., 1909, The carnivora and insectivora of the Bridger Basin, middle Eocene: American Museum of Natural History Memoirs, v. 9, pt. 6, p. 289-567.

Machlus, M.L., Olsen, P.E., Christie-Blick, N., and Hemming, S.R., 2008, Spectral analysis of the lower Eocene Wilkins Peak Member, Green River Formation, Wyoming; support for Milankovitch cyclicity: Earth and Planetary Science Letters, v. 268, p. 64-75.

Machlus, M.L., Ramezani, J., Bowring, S.A., Hemming, S.R., Tsukui, K., and Clyde, W.C., 2015, A strategy for cross-calibrating U-Pb chronology and astrochronology of sedimentary sequences: an example from the Green River Formation, Wyoming, USA, Earth and Planetary Science Letters, v. 413, p. 70-78, doi:10.1016/j.epsl.2014.12.009.

Mattinson, J.M., 2005, Zircon U-Pb chemical abrasion ("CA-TIMS") method: Combined annealing and multi-step partial dissolution analysis for improved precision and accuracy of zircon ages: Chemical Geology, v. 220, p. 47–66, doi: 10.1016/j.chemgeo.2005.03.011.

Mayers, S.R., 2008, Resolving Milankovitchian controversies; the Triassic Latemar Limestone and the Eocene Green River Formation: Geology, v. 36, p. 319-322.

McCarroll, S.M., Flynn, J.J., and Turnbull, W.D., 1996, Biostratigraphy and magnetostratigraphy of the Bridgerian-Uintan Washakie Formation, Washakie Basin, Wyoming, *in* Prothero, D.R., and Emry, R.J., eds., The Terrestrial Eocene-Oligocene transition in North America: Cambridge, UK, Cambridge University Press, p. 25-39.

McGrew, P.O., and Sullivan, R., 1970, The stratigraphy and paleontology of Bridger A: Contributions to Geology, University of Wyoming, v. 9, p. 66-85.

McLean, N.M., Bowring, J.F., and Bowring, S.A., 2011, An algorithm for U-Pb isotope dilution data reduction and uncertainty propagation: Geochemistry Geophysics Geosystems, v. 12, Q0AA18, doi:10.1029/2010GC003478.

Murphey, P.C., and Dunn, R.H., 2009, *Hemiacodon engardae*, a new species of omomyid primate from the earliest Uintan Turtle Bluff Member of the Bridger Formation, southwestern Wyoming, USA: Journal of Human Evolution, v. 57, p. 123-130, doi:10.1016/j.jhevol.2009.05.006.

Murphey, P.C., and Evanoff, E., 2007, Stratigraphy, fossil distribution and depositional environments of the upper Bridger Formation (middle Eocene), southwestern Wyoming: Wyoming State Geological Survey Report of Investigation, scale 1:50,000, 1 sheet.

Ogg, J.G., 2012. Geomagnetic Polarity Time Scale, *in* Gradstein, F.M., Ogg, J.G., Schmitz, M.D., and Ogg, G.M, eds, The Geologic Time Scale 2012, Oxford, U.K., Elsevier, p. 85-114.

Pälike, H., Frazier, J., and Zachos, J.C., 2006, Extended orbitally forced palaeoclimatic records from the equatorial Atlantic Ceara Rise: Quaternary Science Reviews, v. 25, p. 3138-3149, doi:10.1016/j.quascirev.2006.02.011.

Pearson, P.N. and Palmer, M.R. 2000, Atmospheric carbon dioxide over the past 60 million years: Nature, v. 406, p. 695-699.

Prothero, D.R., 1996, Magnetic stratigraphy and biostratigraphy of the middle Eocene Uinta Formation, Uinta Basin, Utah, *in* Prothero, D.R., and Emry, R.J., eds., The Terrestrial Eocene-Oligocene transition in North America: Cambridge, UK, Cambridge University Press, p. 3-24.

Ramezani, J., Hoke, G.D., Fastovsky, D.E., Bowring, S.A., Therrien, F., Dworkin, S.I., Atchley, S.C., and Nordt, L.C., 2011, High-precision U-Pb zircon geochronology of the Late Triassic Chinle Formation, Petrified Forest National Park (Arizona, USA); temporal constraints on the early evolution of dinosaurs: Geological Society of America Bulletin, v. 123, p. 2142-2159.

Renne, P.R., Swisher, C.C., Deino, A.L., Karner, D.B., Owens, T.L., and DePaolo, D.J., 1998, Intercalibration of standards, absolute ages and uncertainties in $^{40}Ar/^{39}Ar$ dating: Chemical Geology, v. 145, p. 117-152, doi:10.1016/S0009-2541(97)00159-9.

Renne, P.R., Deino, A.L., Hilgen, F.J., Kuiper, K.F., Mark, D.F., Mitchell, W.S., Morgan, L.E., Mundil, R., and Smit, J., 2013, Time scales of critical events around the Cretaceous-Paleogene boundary: Science, v. 339, p. 684–687, doi:10.1126/science.1230492.

Robinson, P., Gunnell, G.F., Walsh, S.L., Clyde, W.C., Storer, J.E., Stucky, R.K., Froehlich, D.J., Ferrusquia-Villafranca, I., and McKenna, M.C., 2004, Wasatchian through Duchesnean biochronology, *in* Woodburne, M.O., ed., Late Cretaceous and Cenozoic mammals of North America: Biostratigraphy and geochronology, New York, Columbia University Press, p. 106-155.

Roehler, H.W., 1973, Stratigraphy of the Washakie formation in the Washakie Basin, Wyoming: U.S. Geological Survey Bulletin 1369, 40 p.

Roehler, H.W., 1992a, Correlation, composition, areal distribution, and thickness of Eocene stratigraphic units, greater Green River basin, Wyoming, Utah, and Colorado: U.S. Geological Survey Professional Paper 1506-E, 49 p.

Roehler, H.W., 1992b, Description and correlation of Eocene rocks in stratigraphic reference sections for the Green River and Washakie Basins, southwest Wyoming: U.S. Geological Survey Professional Paper 1506-D, 83 p.

Smith, M.E., Carroll, A.R., and Singer, B.S., 2008, Synoptic reconstruction of a major ancient lake system: Eocene Green River Formation, western United States: Geological Society of America Bulletin, v. 120, no. 1-2, p. 54-84.

Smith, M.E., Chamberlain, K.R., Singer, B.S., and Carroll, A.R., 2010, Eocene clocks agree; coeval $^{40}Ar/^{39}Ar$, U-Pb, and astronomical ages from the Green River Formation: Geology, v. 38, p. 527-530.

Steiger R. H., and Jäger E., 1977. Subcommission on geochronology – convention on use of decay constants in geochronology and cosmochronology. Earth and Planetary Science Letters, 36, 359-362.

Storey, M., Duncan, R.A., and Swisher, C.C., III, 2007, Paleocene-Eocene Thermal Maximum and the opening of the Northeast Atlantic: Science, v. 316, p. 587–589, doi:10.1126/science.1135274.

Sundell, K.A., Shive, P.N., and Eaton, J.G., 1984, Measured sections, magnetic polarity and biostratigraphy of the Eocene Wiggins, Tepee Trail and Aycross Formations within the southeastern Absaroka Range, Wyoming: Wyoming Geological Association Earth Science Bulletin, v. 17, p. 1–48.

Surdam, R.C., and Stanley, K.O., 1980, Effects on changes in drainage basin boundaries on sedimentation in Eocene Lakes Gosiute and Uinta of Wyoming, Utah, and Colorado: Geology, v. 8, p. 135-139.

Swisher, C.C., Dingus, L., and Butler, R.F., 1993, $^{40}Ar/^{39}Ar$ dating and magnetostratigraphic correlation of the terrestrial Cretaceous-Paleogene boundary and Puercan Mammal Age, Hell Creek-Tullock formations, eastern Montana: Canadian Journal of Earth Sciences, v. 30, p. 1981-1996, doi:10.1139/e93-174.

Tsukui, K. and Clyde, W.C., 2012, Fine-tuning the calibration of the early to middle Eocene geomagnetic polarity time scale: Paleomagnetism of radioisotopically dated tuffs from Laramide foreland basins: Geological Society of America Bulletin, v. 124, no. 5-6, p. 870-885, doi:10.1130/B30545.1.

Vandenberghe, N., Hilgen, F.J., and Speijer, R.P., 2012, The Paleogene period *in* Gradstein, F.M., Ogg, J.G., Schmitz, M.D., and Ogg, G.M, eds, The Geologic Time Scale 2012, Oxford, U.K., Elsevier, p. 855-921.

Walsh, S.L., 1996, Theoretical biochronology, the Bridgerian-Uintan boundary and the "Shoshonian Subage" of the Uintan, *in* Prothero, D.R., and Emry, R.J., eds., The Terrestrial Eocene-Oligocene transition in North America: Cambridge, UK, Cambridge University Press, p. 52-74.

Walsh, S.L., Prothero, D.R., and Lundquist, D.J., 1996, Stratigraphy and paleomagnetism of the middle Eocene Friars Formation and Poway Group, southwestern San Diego County, California, *in* Prothero, D.R., and Emry, R.J., eds., The Terrestrial Eocene-Oligocene transition in North America: Cambridge, UK, Cambridge University Press, p. 120–154.

Walton, A.H., 1992, Magnetostratigraphy of the lower and middle members of the Devil's Graveyard Formation (Middle Eocene), Trans-Pecos Texas, *in* Prothero, D.R., and Berggren, W.A., eds., Eocene-Oligocene climatic and biotic evolution: Princeton, New Jersey, Princeton University Press, p. 74–87.

Watson, G.S., 1956, A test for randomness of directions: Monthly Notices of the Royal Astronomical Society Geophysical Supplement, v. 7, p. 160-161.

Westerhold, T., Röhl, U., Laskar, J., Raffi, I., Bowles, J., Lourens, L.J., and Zachos, J.C., 2007, On the duration of magnetochrons C24r and C25n and the timing of early Eocene global warming events: Implications from the Ocean Drilling Program Leg 208 Walvis Ridge depth transect: Paleoceanography, v. 22, no. 1, PA2201.

Westerhold, T., and Röhl, U., 2009, High resolution cyclostratigraphy of the early Eocene - new insights into the origin of the Cenozoic cooling trend: Climate of the Past, v. 5, no. 3, p. 309-327.

Westerhold, T., Röhl, U., McCarren, H.K., and Zachos, J.C., 2009, Latest on the absolute age of the Paleocene–Eocene Thermal Maximum (PETM): New insights from exact stratigraphic position of key ash layers +19 and −17: Earth and Planetary Science Letters, v. 287 p. 412–419.

Westerhold, T., Röhl, U., and Laskar, J., 2012, Time scale controversy: accurate orbital calibration of the early Paleogene: Geochemistry Geophysics Geosystems, v. 13, Q06015, doi:10.1029/2012gc004096.

Westerhold, T., Röhl, U., Frederichs, T., Bohaty, S. M., and Zachos, J.C., 2015, Astronomical calibration of the geological timescale: closing the middle Eocene gap: Climate of the Past, v. 11, p. 1665–1699.

Wood, H.E., 1934, Revision of the Hyrachyidae: Bulletin of the American Museum of Natural History, v. 67, p. 181-295.

Wood, H.E., Chaney, R.W., Clark, J., Colbert, E.H., Jepsen, G.L., Reeside, J.B., and Stock, C., 1941, Nomenclature and correlation of the North American continental Tertiary: Geological Society of America Bulletin, v. 52, p. 1-48.

Woodburne, M.O., 1987, Cenozoic mammals of North America: Geochronology and biostratigraphy: Berkeley, University of California Press, 336 p.

Woodburne, M.O., Gunnell, G.F., and Stucky, R.K., 2009, Climate directly influences Eocene mammal faunal dynamics in North America: Proceedings of the National Academy of Sciences, v. 106, p. 13399-13403.

Zachos, J.C., Quinn, T.M., and Salamy, S., 1996, High-resolution (104years) deep-sea foraminiferal stable isotope records of the Eocene-Oligocene climate transition: Paleoceanography v. 11, p. 251-266.

Zachos, J., Pagani, M., Sloan, L., Thomas, E., and Billups, K., 2001, Trends, rhythms, and aberrations in global climate 65 Ma to present: Science, v. 292, no. 5517, p. 686-693.

Zachos, J.C., Dickens, G.R., and Zeebe, R.E., 2008, An early Cenozoic perspective on greenhouse warming and carbon-cycle dynamics: Nature, v. 451, p. 271-283, doi:10.1038/nature06588.

Zijderveld, J.D.A., 1967, A.C. demagnetization of rocks: analysis of results, *in* Collinson, D.W., Creer, K.M., Runcorn, S.K., eds., Methods of Palaeomagnetism: Amsterdam, Elsevier, p. 254-286.

Zonneveld, J.-P., Gunnell, G.F., and Bartels, W.S., 2000, Early Eocene fossil vertebrates from the southwestern Green River Basin, Lincoln and Uinta counties, Wyoming. Journal of Vertebrate Paleontology, v. 20, p. 369-386.

Zonneveld, J.-P., Bartels, W.S., and Clyde, W.C., 2003, Stratal architecture of an Early Eocene fluvial-lacustrine depositional system, Little Muddy Creek area, southwestern Green River Basin, Wyoming, *in* Raynolds, R.G., and Flores, R.M., eds., Cenozoic Systems of the Rocky Mountain Region: Denver, Colorado, Rocky Mountain Section, SEPM (Society for Sedimentary Geology) p. 253-287.

Table 2.1. Summary of available geochronology from the Greater Green River Basin.

Tuff	Formation*	Dating method	Mineral†	Method§	Weighted mean age (Ma)	2 sig external error (Ma)	Standard age# (Ma)	MSWD**	N	Decay constant††	References
Sage Creek Mt. pumice	B	$^{40}Ar/^{39}Ar$	S	SF, MI	47.450	0.15	FCs=28.201	0.69	45	NR	Smith et al. (2010)
Tabernacle Butte tuff	B	$^{40}Ar/^{39}Ar$	S	SF, MI	48.400	0.15	FCs=28.201	0.78	40	NR	Smith et al. (2010)
Henrys Fork tuff	B	$^{40}Ar/^{39}Ar$	S	SF, MF	48.440	0.15	FCs=28.201	1.04	71	NR	Smith et al. (2010)
		$^{206}Pb/^{238}U$	Z	Single grain, CA-TIMS	48.265	0.059	ET535 spike	1.70	12	Jaffey et al. (1971)	This work
Leavitt Creek tuff	B	$^{40}Ar/^{39}Ar$	S	SF	48.920	0.31	FCs=28.201	0.28	12	NR	Smith et al. (2010)
Church Butte tuff	B	$^{40}Ar/^{39}Ar$	S	SF, MI	49.050	0.16	FCs=28.201	1.30	42	NR	Smith et al. (2010)
		$^{206}Pb/^{238}U$	Z	Single grain, CA-TIMS	48.899	0.06	ET535 spike	1.39	6	Jaffey et al. (1971)	This work
Continental Peak tuff	B	$^{40}Ar/^{39}Ar$	S	MF	48.960	0.28	FCs=28.201	0.29	12	NR	Smith et al. (2010)
Analcite	GR	$^{206}Pb/^{238}U$	Z	Multigrain, MA or CA-TIMS	49.230	0.13	ET535 spike	6.70	7	Steiger and Jager (1977)	Smith et al. (2010)
Sixth tuff	GR	$^{40}Ar/^{39}Ar$	S	SF, MF	49.240	0.18	FCs=28.201	0.59	30	NR	Smith et al. (2010)
		$^{40}Ar/^{39}Ar$	B	SI, MI	49.920	0.17	FCs=28.201	1.00	119	NR	Smith et al. (2010)
		$^{206}Pb/^{238}U$	Z	Single grain, CA-TIMS	49.686	0.069	ET535 spike	0.59	6	Jaffey et al. (1971)	Machlus et al. (2015)
Layered tuff	GR	$^{40}Ar/^{39}Ar$	S	MF	50.110	0.16	FCs=28.201	0.42	64	NR	Smith et al. (2010)
		$^{40}Ar/^{39}Ar$	B	Single-step laser-fusion	49.120	0.96	FCs=28.02	0.60	7	NR	Machlus et al. (2004)
		$^{206}Pb/^{238}U$	Z	Single grain, CA-TIMS	49.919	0.074	ET535 spike	0.83	7	Jaffey et al. (1971)	Machlus et al. (2015)
Main tuff	GR	$^{40}Ar/^{39}Ar$	S	MF	50.270	0.16	FCs=28.201	0.51	23	NR	Smith et al. (2010)
		$^{40}Ar/^{39}Ar$	B	Single-step laser-fusion	50.370	1.04	FCs=28.02	1.70	11	NR	Machlus et al. (2004)
		$^{206}Pb/^{238}U$	Z	Single grain, CA-TIMS	50.108	0.067	ET535 spike	0.70	7	Jaffey et al. (1971)	Machlus et al. (2015)
Grey tuff	GR	$^{40}Ar/^{39}Ar$	S	MF	50.860	0.25	FCs=28.201	0.53	8	NR	Smith et al. (2010)
		$^{206}Pb/^{238}U$	Z	Single grain, CA-TIMS	50.856	0.060	ET535 spike	1.50	12	Jaffey et al. (1971)	Machlus et al. (2015)
Boar tuff	GR	$^{40}Ar/^{39}Ar$	S	MF	51.130	0.27	FCs=28.201	1.74	13	NR	Smith et al. (2010)
Firehole	GR	$^{206}Pb/^{238}U$	Z	Multigrain, MA or CA-TIMS	51.660	0.20	ET535 spike	11.20	6	Steiger and Jager (1977)	Smith et al. (2010)
		$^{206}Pb/^{238}U$	Z	Single grain, CA-TIMS	51.527	0.061	ET535 spike	1.90	13	Jaffey et al. (1971)	Machlus et al. (2015)
		$^{40}Ar/^{39}Ar$	S	MF	51.400	0.25	FCs=28.201	0.36	20	NR	Smith et al. (2010)
Rife tuff	GR	$^{40}Ar/^{39}Ar$	B	MF, SF	51.610	0.33	FCs=28.201	0.68	15	NR	Smith et al. (2010)
Scheggs tuff	GR	$^{40}Ar/^{39}Ar$	S	SF, MF	52.210	0.16	FCs=28.201	0.34	83	NR	Smith et al. (2010)
Second tuff	GR	$^{206}Pb/^{238}U$	Z	Single grain, CA-TIMS	51.279	0.064	ET535 spike	1.10	9	Jaffey et al. (1971)	Machlus et al. (2015)
1448 tuff	GR	$^{206}Pb/^{238}U$	Z	Single grain, CA-TIMS	51.581	0.081	ET535 spike	1.00	7	Jaffey et al. (1971)	Machlus et al. (2015)

*B - Bridger Formation, GR - Green River Formation.

†S - sanidine, B - biotite, Z - zircon.

§MI - multicrystal laser incremental heating experiments; SI - single crystal laser incremental heating experiments; MF - multicrystal laser fusion experiments; SF - single crystal laser fusion experiments; MA - mechanically abraded; CA - chemically abraded; TIMS - thermal ionization mass spectrometry.

#FCs - Fish Canyon sanidine; ET535 - EARTHTIME 205Pb/233U/235U tracer.

**MSWD - mean square weighted deviation.

††NR - Not reported.

Table 2.2. Site data for the magnetostratigraphic sections.

Site	Site latitude	Site longitude	Notes	No. of sites	Thickness (m)	Stratigraphy	Location
BBB	41°14'0"N	110°15'0"W		6	38.7	Upper Bridger B2 or at least the lower part of Bridger B3	In Little Dry Creek drainage
LDC	41°13'45"N 41°13'35"N	110°14'20"W 110°14'10"W	LDC1-3 LDC4-16	16	80.5	Within Bridger B3	In Little Dry Creek drainage, Crooked Canyon area
CWC	41°13'45"N	110°12'0"W		12	76.0	Upper Bridger B	In Crooked Canyon area, northeast side of Cottonwood Creek Bench
SCM	41°10'15"N	110°9'15"W		18	122.2	Bridger C-D	Northwest side of Sage Creek Mountain
HM	41°5'45"N 41°5'45"N	110°10'45"W 110°11'15"W	HM1-4 HM5-14	14	101.2	Bridger D	On the east flank of Hickey Mountain
USC	N/A	N/A		24	190.8	Bridger D-E	North flank of the Sage Creek Mountain

NOTE: See Figure 2.3 for the location of the sites.

Table 2.3. Paleomagnetic sample statistics.

Sample	ChRM component†		Declination§	Inclination§	MAD	N#	Inferred magnetic carrier**
	Lower temperature (°C)	Higher temperature (°C)	(°)	(°)	(°)		
BBB-1A1	400	700	313.5	68.7	15.1	4	H/MH
BBB-1B1	100	700	349.9	58.9	2.8	7	H/MH
BBB-1C1	400	700	347.7	51.2	6.3	4	H/MH
BBB-1C2*	25	600	313.1	56.1	6.3	10	M
BBB-2A1	100	700	335.2	48.2	1.9	7	H/MH
BBB-2B1	50	700	320.7	42.6	4.0	10	H/MH
BBB-2B2*	100	650	309.2	34.1	1.8	11	H/MH
BBB-2C1	100	600	337.0	50.3	1.0	6	M
BBB-3A	100	300	1.1	60.9	2.0	3	T/T
BBB-3B	100	300	10.7	60.9	3.1	3	T/T
BBB-3C	100	9200	0.9	56.2	8.5	3	T/T
BBB-4A1	100	500	336.4	68.1	2.6	5	T/T, M
BBB-4B1	100	500	359.1	73.4	2.5	5	T/T, M
BBB-4C1	25	600	16.6	56.3	1.0	10	M
BBB-4C2*	25	660	0.8	53.1	3.0	13	H/MH
BBB-5A1	100	700	347.1	73.4	3.7	7	H/MH
BBB-5B	100	400	18.0	58.3	3.1	4	T/T
BBB-5C1	100	500	341.7	66.7	3.5	5	T/T, M
BBB-6A1	250	700	175.0	52.0	7.4	6	H/MH
BBB-6A2*	450	650	44.4	-42.7	26.7	7	H/MH
BBB-6B	100	600	77.7	66.4	8.2	6	M
BBB-6C1	200	600	272.8	47.9	8.5	5	M
LDC-1A1	400	625	173.7	-67.3	15.9	5	H/MH
LDC-1B1	200	300	129.7	-23.5	13.7	3	T/T
LDC-1B2*	450	650	168.8	-57.3	14.5	7	H/MH
LDC-1C1	300	625	139.4	-49.1	11.1	6	H/MH
LDC-1D1	500	625	143.7	-41.6	6.3	4	H/MH
LDC-2A1	200	700	297.7	-71.8	13.5	7	H/MH
LDC-2A2*	625	660	296.4	-41.7	6.2	3	H/MH
LDC-2B1	400	550	310.5	-10.1	2.3	3	M
LDC-2C1	500	625	318.1	0.8	5.8	4	H/MH
LDC-3A1	300	625	298.2	-1.7	0.5	6	H/MH
LDC-3B1	25	625	303.2	5.1	1.3	9	H/MH
LDC-3C1	25	625	295.5	6.2	0.9	9	H/MH
LDC-4A1	500	700	170.5	-40.2	4.9	3	H/MH
LDC-4A4*	400	660	173.9	-52.6	19.8	9	H/MH
LDC-4B1	200	625	167.4	-55.8	5.8	7	H/MH
LDC-4C1	200	625	178.5	-48.4	5.0	7	H/MH
LDC-5A1	200	625	137.7	-40.9	10.4	7	H/MH
LDC-5B1	550	625	168.6	-67.9	16.2	3	H/MH
LDC-5C3	550	625	147.8	-67.1	0.8	3	H/MH
LDC-6A1	200	600	23.9	63.7	8.8	6	M
LDC-6B1	25	550	48.2	65.4	2.0	7	M
LDC-6C1	25	500	28.9	57.9	1.6	6	T/T, M
LDC-7A1	500	700	357.2	-51.8	22.9	3	H/MH

LDC-7A2*	450	660	349.1	-39.5	11.4	8	H/MH
LDC-7B1	400	625	156.2	-52.6	15.7	5	H/MH
LDC-7C1	400	625	107.3	-55.0	14.1	5	H/MH
LDC-7D1	600	9625	209.2	-71.4	4.5	3	H/MH
LDC-8A1	100	500	16.9	67.5	4.0	5	T/T, M
LDC-8B1	25	500	332.9	83.5	3.3	6	T/T, M
LDC-8C1	25	500	16.2	73.2	2.4	6	T/T, M
LDC-9A1	300	625	165.3	-53.5	3.2	6	H/MH
LDC-9B1	300	625	166.7	-50.7	8.4	6	H/MH
LDC-9C1	300	625	154.8	-47.5	8.6	6	H/MH
LDC-10A1	400	625	49.8	-9.7	24.7	5	H/MH
LDC-10B	400	600	107.6	-17.2	32.1	4	M, H/MH
LDC-10C1	300	9400	91.0	-71.0	1.8	3	T/T
LDC-10C2*	500	625	147.5	-48.2	28.0	5	H/MH
LDC-11A2*	530	600	40.3	6.3	40.9	3	M, H/MH
LDC-11B2	200	550	129.2	-29.3	16.2	5	M
LDC-11C1	400	550	144.8	-21.5	13.1	3	M
LDC-11D1	200	500	107.9	-23.5	8.1	4	M
LDC-12A1	50	700	186.8	-3.0	1.5	10	H/MH
LDC-12A2*	200	660	178.9	-3.7	0.9	11	H/MH
LDC-12B1	25	625	143.9	-18.7	1.9	9	H/MH
LDC-12C	25	625	120.6	-9.2	0.6	9	H/MH
LDC-13A1	300	600	173.4	-58.8	18.6	5	M, H/MH
LDC-13B1	300	625	152.2	-57.2	13.2	6	H/MH
LDC-13C1	300	625	149.3	-53.8	12.5	6	H/MH
LDC-14B1	400	9500	179.1	-15.9	8.7	3	T/T, M
LDC-14B2*	400	600	140.9	-26.3	22.3	6	M
LDC-14C1	300	500	190.7	-4.1	22.1	3	T/T, M
LDC-15A	300	625	10.8	-26.6	4.5	6	H/MH
LDC-15B	550	625	6.0	-10.3	1.1	3	H/MH
LDC-15C	550	625	7.9	-16.9	0.6	3	H/MH
LDC-16A	200	625	167.0	-45.0	3.6	7	H/MH
LDC-16B1	300	700	139.6	-56.4	9.5	5	H/MH
LDC-16B2*	500	660	171.4	-56.7	6.3	7	H/MH
LDC-16C1	300	625	164.8	-48.9	7.6	6	H/MH
CWC-1B1	200	625	181.2	-57.8	6.4	7	H/MH
CWC-1C1	250	700	150.8	-48.2	1.4	6	H/MH
CWC-1C2*	200	660	171.8	-52.5	3.1	11	H/MH
CWC-2A1	400	625	152.1	-56.7	11.4	5	H/MH
CWC-2B1	300	9500	161.8	-21.0	13.5	4	M
CWC-2B2	500	660	170.0	-58.7	11.8	7	H/MH
CWC-2C1	400	625	143.3	-43.0	12.5	5	H/MH
CWC-3A1	300	9500	159.8	-20.5	17.0	4	M
CWC-3A2*	500	660	185.0	-50.4	7.6	7	H/MH
CWC-3B1	300	625	168.2	-57.4	14.5	6	H/MH
CWC-3C1	400	625	184.0	-58.3	16.5	5	H/MH
CWC-4A2	500	625	109.2	-78.7	31.7	4	H/MH
CWC-4B1	400	9625	179.4	-60.2	16.7	6	H/MH
CWC-4C1	500	625	146.3	-43.3	14.2	4	H/MH
CWC-5A1	550	9625	1.6	30.0	31.3	4	H/MH
CWC-5B1	300	500	2.3	-41.4	12.6	3	M
CWC-5C1	500	9700	198.1	-28.8	18.5	4	H/MH

CWC-5C2*	530	650	351.8	50.0	17.6	5	H/MH
CWC-6A1	200	600	350.7	62.0	7.3	6	M, H/MH
CWC-6A3*	530	660	335.1	51.7	11.1	6	H/MH
CWC-6B1	500	625	9.7	54.3	39.1	4	H/MH
CWC-6C1	400	625	15.2	57.8	21.1	5	H/MH
CWC-7A	550	9600	201.4	-52.6	24.0	3	M, H/MH
CWC-7B	400	625	176.5	-50.9	31.9	5	H/MH
CWC-7C1	500	9600	193.1	-28.3	1.8	3	M, H/MH
CWC-7C2*	400	660	146.4	-46.0	18.2	9	H/MH
CWC-8A	25	400	28.6	73.1	2.6	5	T/T
CWC-8B1	25	500	349.7	76.8	3.2	6	M, T/T
CWC-8C1	25	500	39.4	82.7	4.2	6	M, T/T
CWC-9A	200	625	166.5	-56.0	5.8	7	H/MH
CWC-9B	200	625	211.3	-58.1	18.1	7	H/MH
CWC-9C	200	700	159.6	-35.0	19.7	7	H/MH
CWC-9D*	200	660	162.4	-50.3	5.4	11	H/MH
CWC-10A2	25	625	341.7	84.0	1.9	9	H/MH
CWC-10B2	25	625	333.2	55.7	3.6	9	H/MH
CWC-10C4	25	625	340.3	74.6	2.6	9	H/MH
CWC-11A1	400	700	153.9	-20.1	13.1	4	H/MH
CWC-11A2*	530	660	146.4	-11.1	0.9	6	H/MH
CWC-11B1	25	625	152.0	-5.9	1.7	9	H/MH
CWC-11C1	25	625	146.6	-4.6	1.4	9	H/MH
CWC-12A1	300	600	198.1	13.9	7.8	4	M, H/MH
CWC-12A2*	25	660	190.7	-11.3	1.7	13	H/MH
CWC-12B1	25	625	25.5	-10.2	0.9	9	H/MH
CWC-12C1	25	625	215.7	-13.9	0.6	9	H/MH
SCM-1A1	50	500	221.0	-30.8	20.7	8	M, T/T
SCM-1A2	25	450	118.2	-32.9	16.3	6	T/T, M
SCM-1B1	100	500	172.8	-64.0	11.7	5	M, T/T
SCM-1C3	25	500	112.8	-43.6	11.7	6	M, T/T
SCM-1D1	200	600	137.2	-56.7	18.3	6	M, H/MH
SCM-2A1	500	600	91.2	-56.9	27.6	3	M, H/MH
SCM-2B1	400	600	120.2	-28.3	7.7	4	M, H/MH
SCM-2C3	500	625	133.0	-53.0	11.4	4	H/MH
SCM-2D	400	625	104.7	-19.6	11.2	5	H/MH
SCM-3A1	500	625	122.2	-23.3	26.6	4	H/MH
SCM-3B	600	9625	34.6	-13.7	26.1	3	H/MH
SCM-3C1	250	500	121.1	-0.7	7.7	4	M
SCM-3C2*	500	650	120.6	-51.7	10.3	6	H/MH
SCM-4A1	25	600	8.4	71.5	1.2	8	M, H/MH
SCM-4B	300	625	128.7	-29.3	1.3	6	H/MH
SCM-4C1	200	625	108.5	-33.1	6.4	7	H/MH
SCM-5A1	150	600	145.6	-34.1	9.1	7	M, H/MH
SCM-5A2*	450	660	261.1	-83.9	12.9	8	H/MH
SCM-5B1	500	625	139.4	-75.8	7.3	4	H/MH
SCM-5C	500	625	104.8	-69.7	11.7	4	H/MH
SCM-6A1	25	625	315.8	17.2	1.4	9	H/MH

SCM-6B3	25	625	315.2	20.7	1.4	9	H/MH
SCM-6C1	25	625	312.2	17.9	1.7	9	H/MH
SCM-7A4*	25	660	175.6	1.1	0.9	13	H/MH
SCM-7B1	25	625	189.4	2.0	0.9	9	H/MH
SCM-7C3	25	625	175.7	-2.8	0.8	9	H/MH
SCMT-1-1	200	300	159.2	-17.9	17.6	3	T/T
SCMT-1-2*	600	650	116.2	-7.1	15.5	3	H/MH
SCM-8A1	250	700	163.5	-54.6	18.9	6	H/MH
SCM-8A2*	500	660	158.7	-57.8	8.0	7	H/MH
SCM-8B1	400	625	187.6	-55.6	7.8	5	H/MH
SCM-8C1	400	625	168.0	-60.4	9.2	5	H/MH
SCM-9A1	500	625	222.6	-57.1	29.1	4	H/MH
SCM-9B1	500	9600	312.2	-86.5	12.0	3	M, H/MH
SCM-9B3	600	9625	139.9	-56.6	13.0	3	H/MH
SCM-9C1	500	625	83.4	-54.0	15.4	4	H/MH
SCM-10A1	400	700	203.8	-65.2	4.6	4	H/MH
SCM-10A2*	400	660	172.8	-62.8	5.2	9	H/MH
SCM-10B1	300	625	190.4	-58.1	3.0	6	H/MH
SCM-10C1	200	625	167.8	-63.5	4.6	7	H/MH
SCM-11A1	250	700	162.1	-56.9	3.9	6	H/MH
SCM-11A2*	530	660	165.2	-60.9	2.5	6	H/MH
SCM-11B2	200	625	160.5	-59.9	5.4	7	H/MH
SCM-11C1	300	625	159.2	-62.0	4.7	6	H/MH
SCM-12A1	150	700	150.8	-49.1	4.0	8	H/MH
SCM-12A2*	530	650	174.3	-54.8	1.4	5	H/MH
SCM-12B	300	625	158.4	-47.8	9.5	6	H/MH
SCM-12C1	300	625	162.1	-51.4	3.2	6	H/MH
SCM-13A1	600	9700	133.1	-34.6	2.2	3	H/MH
SCM-13A2*	530	650	162.2	-37.8	6.2	5	H/MH
SCM-13B1	500	625	181.3	-25.7	8.0	4	H/MH
SCM-13C1	400	625	182.2	-46.4	11.1	5	H/MH
SCM-14A1	500	625	241.3	-23.4	3.4	4	H/MH
SCM-14B1	400	625	227.2	-19.5	7.8	5	H/MH
SCM-14C1	500	625	210.2	-48.5	2.7	4	H/MH
SCM-15A1	200	700	185.7	-55.0	15.5	7	H/MH
SCM-15A4*	25	600	132.1	-48.9	7.3	10	M, H/MH
SCM-15B1	25	500	163.0	-59.0	13.2	6	M
SCM-15C1	200	625	171.4	-58.4	11.8	7	H/MH
SCM-15D1	300	625	234.2	-59.5	11.4	6	H/MH
SCM-16A1	100	500	359.4	70.0	19.0	5	M, T/T
SCM-16B1	300	500	218.3	11.6	10.8	3	M, T/T
SCM-16B2*	450	600	172.7	-35.9	22.7	5	M, H/MH
SCM-16C2	200	500	45.3	17.0	29.6	4	M, T/T
SCM-17A2*	530	660	177.5	-45.2	7.4	6	H/MH
SCM-17B1	400	625	170.2	-62.3	3.4	5	H/MH
SCM-17C1	300	9400	150.4	-38.5	6.5	3	T/T
SCM-18A1	250	500	125.7	-17.7	10.7	4	M

SCM-18A2*	530	660	116.4	-44.3	18.2	6	H/MH
SCM-18B2		Unable to resolve ChRM because of strong overprint					
SCM-18C1	400	625	129.8	-31.3	5.5	5	H/MH
HM-1A	500	625	230.1	-72.0	1.6	4	H/MH
HM-1B1	25	625	193.2	-61.3	1.1	9	H/MH
HM-1C1	250	700	194.5	-48.9	1.6	6	H/MH
HM-1C2*	25	660	184.0	-51.9	1.7	13	H/MH
HM-1D1	25	625	194.2	-55.1	0.8	9	H/MH
HM-2A	400	625	160.7	-60.6	14.3	5	H/MH
HM-2B1	500	625	124.9	-35.0	30.7	4	H/MH
HM-2C1	400	625	143.0	-4.9	40.1	5	H/MH
HM-3A	200	625	105.6	-37.3	6.6	7	H/MH
HM-3B1	200	625	103.4	-38.0	14.2	7	H/MH
HM-3C1	150	700	75.9	-35.3	16.9	8	H/MH
HM-3C2*	560	660	97.2	-65.9	22.7	5	H/MH
HM-4A2	600	9625	183.4	-79.6	16.9	3	H/MH
HM-4B1	600	9700	112.9	-20.3	6.4	3	H/MH
HM-4B2*	600	660	104.4	-57.4	13.0	4	H/MH
HM-4C1	600	9625	169.9	-51.8	23.3	3	H/MH
HM-5A1	300	625	138.6	-60.8	19.7	6	H/MH
HM-5B2	300	625	149.5	-66.6	9.4	6	H/MH
HM-5C1	300	600	293.3	-66.5	10.6	5	H/MH
HM-5D1	150	700	167.0	-46.6	5.3	8	H/MH
HM-5D3*	300	650	165.7	-60.1	5.9	9	H/MH
HM-6A1	550	625	118.4	-20.8	17.8	3	H/MH
HM-6B	500	600	182.3	-63.7	9.9	3	H/MH
HM-6C	500	600	108.8	-83.6	12.4	3	H/MH
HM-7A2	550	9625	193.9	-57.4	25.9	4	H/MH
HM-7B2	550	625	169.5	-61.4	5.0	3	H/MH
HM-7C1	250	700	192.6	-33.5	15.0	6	H/MH
HM-7C2*	560	660	162.0	-60.2	14.7	5	H/MH
HM-8A2	200	600	156.5	-37.5	2.2	6	M, H/MH
HM-8B2	200	600	146.4	-39.7	4.6	6	M, H/MH
HM-8C1	200	625	158.7	-41.6	3.0	7	H/MH
HM-9A2	200	625	183.1	-57.1	7.3	7	H/MH
HM-9B1	200	600	172.5	-39.1	17.7	6	M, H/MH
HM-9C1	600	9700	165.2	-65.8	14.6	3	H/MH
HM-9C3*	300	660	207.3	-56.4	12.0	10	H/MH
HM-10A1	100	700	157.1	-46.5	4.2	9	H/MH
HM-10A2*	300	660	164.1	-54.0	5.8	10	H/MH
HM-10B1	200	600	164.7	-53.5	2.8	6	M, H/MH
HM-10C	200	625	168.1	-52.5	4.0	7	H/MH
HM-11A1	500	600	177.5	36.5	33.8	3	M, H/MH
HM-11B1	300	550	203.4	32.4	26.6	4	M
HM-11C2	200	500	349.1	64.1	14.9	4	M, T/T
HM-12A	550	625	170.5	-64.1	2.9	3	H/MH
HM-12B2	200	625	171.6	-50.7	5.6	7	H/MH
HM-12C1	200	625	165.3	-56.9	7.2	7	H/MH
HM-12D1	400	625	182.2	-60.9	13.6	5	H/MH
HM-13A1	25	300	151.6	-15.6	1.0	7	T/T
HM-13A2*	25	625	151.3	-16.3	2.0	11	H/MH
HM-13B	25	500	154.0	-19.7	2.0	6	M

HM-13C	25	600	153.2	-18.2	1.2	8	M, H/MH
HM-14B1	400	550	117.1	-69.9	18.8	3	M
HM-14C1	150	500	291.8	-39.1	13.9	6	M, T/T
HM-14C3*	25	500	307.2	-7.4	15.7	7	M, T/T
USC-1A*	300	600	146.9	-59.0	6.9	7	M, H/MH
USC-1B	200	450	107.7	-42.5	19.1	4	T/T, M
USC-1C	200	450	184.5	-45.5	15.5	4	T/T, M
USC-2A			Unable to interpret				N/A
USC-2B	450	9500	130.0	-11.2	15.4	3	M
USC-3A*	200	600	183.9	-62.9	3.4	8	M, H/MH
USC-3B	200	450	162.3	-65.2	4.8	4	M
USC-3C	200	400	238.1	-56.7	5.0	3	T/T, M
USC-4A	300	500	130.4	-36.5	17.0	4	M
USC-4B	300	500	124.7	-25.7	6.7	4	M
USC-5A*	400	600	197.6	-37.1	13.9	6	M, H/MH
USC-5C	300	9450	207.4	-61.0	8.5	4	T/T, M
USC-6A	200	400	194.4	-46.1	3.7	3	T/T, M
USC-6B1	200	500	173.3	-31.6	20.2	5	M
USC-7A*	100	600	155.3	-60.4	5.7	9	M, H/MH
USC-7B	200	450	147.0	-55.9	3.6	4	T/T, M
USC-8A	200	500	183.7	-53.5	9.0	5	M
USC-8B	400	500	185.2	-49.9	6.9	3	M
USC-9A*	200	600	187.5	-50.5	8.7	8	M, H/MH
USC-9B	200	400	121.5	-76.1	13.3	3	T/T, M
USC-9C1	300	450	192.4	-14.8	2.5	3	T/T, M
USC-10A	200	500	179.7	-29.8	7.7	5	M
USC-10B	200	500	168.6	-52.3	6.4	5	M
USC-11A*	200	600	157.9	-45.2	8.2	8	M, H/MH
USC-11B	300	450	192.3	-5.4	11.9	3	T/T, M
USC-11C	400	9450	40.2	12.2	15.0	3	T/T, M
USC-12A	100	450	203.0	-61.8	4.7	5	T/T, M
USC-12B	100	450	187.0	-42.9	9.8	5	T/T, M
USC-13A*	25	400	358.3	1.4	22.4	5	T/T, M
USC-13B	100	450	31.6	-12.4	11.8	5	T/T, M
USC-13C1	100	400	27.6	64.7	3.6	4	T/T, M
USC-14B1	100	300	277.7	44.6	14.3	3	T/T
USC-14B2	100	300	275.3	32.2	9.1	3	T/T
USC-15A*	100	600	176.8	-56.2	6.5	9	M, H/MH
USC-15B1	100	450	163.8	-58.7	3.9	5	T/T, M
USC-15C1	100	400	173.8	-62.0	3.8	4	T/T, M
USC-16A	200	400	342.7	18.4	6.7	3	T/T, M
USC-16B	100	400	0.9	66.0	21.0	4	T/T, M
USC-17A*	100	400	41.7	78.7	9.1	4	T/T, M
USC-17B	100	400	16.8	62.5	3.0	4	T/T, M
USC-17C	100	450	346.0	68.5	15.9	5	T/T, M
USC-18A	100	500	315.6	57.9	2.6	6	M
USC-18B	100	500	341.2	66.5	4.2	6	M
USC-19A*	100	300	76.2	53.4	15.7	3	T/T
USC-19B	100	300	340.7	62.0	11.7	3	T/T
USC-19C	300	9400	340.3	35.9	7.1	3	T/T, M
USC-20A1	300	450	101.6	55.7	28.7	3	T/T, M
USC-20B	100	400	163.7	4.9	21.8	4	T/T, M

USC-21A*	100	600	2.7	42.4	9.7	9	M, H/MH
USC-21B	100	450	11.3	34.9	8.8	5	T/T, M
USC-21C	100	450	0.2	26.5	5.3	5	T/T, M
USC-23A*	100	500	225.5	7.2	20.1	6	M
USC-23B	100	9200	67.7	65.7	12.2	3	T/T
USC-23D1	200	9300	18.6	1.0	20.6	3	T/T
USC-24A	100	500	267.1	7.5	2.7	6	M
USC-24B1	100	500	269.3	9.9	3.3	6	M

*Astrisk is shown next to samples that were run as a pilot sample.

[†]If the temperature was preceded by 9, the origin was included as one of the steps in defining the characteristic component.

[§]In geographic coordinates.

[#]Number of demagnetization steps included in defining the characteristic component.

**T/T - titanohematite or titanomagnetite, M - magnetite, H/MH - hematite or maghemite.

Table 2.4. Paleomagnetic site statistics.

Site	Level (m)	Declination* (°)	Inclination* (°)	N†	R§	*k*#	α_{95}**	Lat_{VGP}† (°)	$Long_{VGP}$†† (°)	Class§§
BBB-1	0.0	332.9	59.9	4	3.93	40.55	14.6	69.6	167.5	I
BBB-2	7.3	324.4	44.4	4	3.93	45.92	13.7	57.0	143.7	I
BBB-3	14.0	4.1	59.4	3	3.00	424.27	6.0	86.7	-3.4	I
BBB-4	21.0	0.4	63.4	4	3.93	44.97	13.9	86.3	-105.9	I
BBB-5	28.0	358.7	67.1	3	2.96	52.30	17.2	81.4	-115.9	I
BBB-6	38.7	204.3	77.5	3	2.51	4.05	71.6	18.9	-120.4	III
LDC-1	50.7	146.5	-49.0	5	4.75	15.98	19.7	-60.7	-32.2	I
LDC-2	58.6	308.2	-30.6	4	3.49	5.91	41.4	15.0	121.0	I
LDC-3	60.9	299.0	3.2	3	2.99	195.78	8.8	22.5	140.9	I
LDC-4	60.9	172.6	-49.3	4	3.98	120.48	8.4	-77.4	-79.5	I
LDC-5	67.3	147.8	-59.3	3	2.91	22.10	26.9	-65.7	-12.2	I
LDC-6	74.9	33.0	62.7	3	2.99	136.90	10.6	65.7	-38.1	I
LDC-7	82.4	116.7	-80.2	4	3.24	3.97	53.1	-47.2	44.4	I
LDC-8	83.9	10.7	75.2	3	2.97	73.46	14.5	68.1	-96.8	I
LDC-9	91.5	162.1	-50.7	3	2.99	247.10	7.9	-72.6	-48.9	I
LDC-10	99.5	91.0	-71.0	1	N/A	N/A	N/A	-33.4	27.0	IV
LDC-11	105.0	127.4	-25.6	3	2.91	21.85	27.0	-36.7	-35.7	I
LDC-12	108.0	158.1	-9.6	4	3.56	6.83	38.0	-48.7	-76.0	I
LDC-13	113.5	157.7	-57.0	3	2.98	114.71	11.6	-72.4	-24.9	I
LDC-14	118.1	179.1	-15.9	1	N/A	N/A	N/A	-56.9	-108.6	IV
LDC-15	123.2	8.2	-17.9	3	2.98	90.45	13.0	39.0	59.3	I
LDC-16	131.2	161.3	-52.4	4	3.95	63.20	11.6	-73.0	-43.2	I
CWC-1	126.2	166.8	-53.5	3	2.97	59.06	16.2	-77.3	-50.5	I
CWC-2	134.6	156.4	-45.4	4	3.84	18.32	22.1	-65.9	-49.3	I
CWC-3	142.2	172.4	-47.4	4	3.82	16.94	23.0	-75.9	-81.8	I
CWC-4	149.7	159.6	-52.9	2	1.95	19.34	60.3	-72.1	-39.3	III
CWC-5	157.6	328.8	-30.2	3	0.75	0.89	180	25.7	103.3	III
CWC-6	165.2	341.9	57.1	2	1.99	74.38	29.4	75.6	151.5	III
CWC-7	171.9	172.6	-39.5	2	1.88	8.11	104.4	-70.2	-89.7	III
CWC-8	178	17.2	78.3	3	2.98	127.19	11.0	17.2	-96.2	I
CWC-9	183.5	171.9	-51.6	4	3.86	20.75	20.7	-78.9	-71.8	I
CWC-10	191.3	336.2	71.5	3	2.94	31.35	22.4	68.5	-148.0	I
CWC-11	199.2	149.7	-10.4	4	3.97	104.32	9.0	-45.0	-64.9	I
CWC-12	202.2	199.3	-11.1	4	1.93	1.45	147.2	-50.4	-141.3	III
SCM-1	232	129.5	-51.3	4	3.80	15.31	24.3	-49.0	-16.4	I
SCM-2	234.1	117.4	-34.1	3	2.87	15.48	32.5	-32.6	-23.3	I

SCM-3	241.8	120.9	-29.4	2	1.85	6.63	123.3	-33.4	-28.5	III
SCM-4	249.7	108.1	-3.1	3	1.60	1.43	180.0	-14.6	-31.1	III
SCM-5	257.9	138.7	-69.5	4	3.70	9.93	30.7	-60.0	17.7	I
SCM-6	265.7	314.4	18.6	3	3.00	949.44	4.0	38.9	134.8	I
SCM-7	270.3	180.2	0.1	3	2.98	94.84	12.7	-48.8	-110.5	I
SCM-T	272.2	137.2	-13.4	2	1.86	7.12	115.8	-38.8	-50.2	III
SCM-8	273.3	169.6	-57.6	4	3.97	119.61	8.4	-81.5	-36.9	I
SCM-9	280.9	109.3	-70.3	3	2.81	10.31	40.5	-42.8	21.3	I
SCM-10	288.5	183.6	-63.1	4	3.97	102.94	9.1	-85.7	106.3	I
SCM-11	296.2	161.8	-59.9	4	4.00	1040.60	2.8	-76.3	-15.8	I
SCM-12	303.8	160.9	-51.1	4	3.98	142.68	7.7	-72.1	-45.6	I
SCM-13	311.4	164.7	-37.8	4	3.81	16.02	23.7	-66.2	-72.6	I
SCM-14	319.2	227.9	-31.0	3	2.88	16.18	31.7	-42.3	176.0	I
SCM-15	327.4	173.9	-60.6	5	4.75	16.30	19.5	-85.4	-13.0	I
SCM-16	328	235.1	56.9	2	1.36	1.57	180	3.4	-150.8	III
SCM-17	338.7	164.9	-49.3	3	2.93	26.71	24.3	-73.6	-57.4	I
SCM-18	354.2	124.4	-31.2	3	2.94	31.78	22.2	-36.7	-30.1	I
HM-1	367	195.7	-58.5	5	4.91	46.35	11.4	-77.9	163.6	I
HM-2	374.6	160.7	-60.6	1	N/A	N/A	N/A	-75.5	-11.9	IV
HM-3	381.9	94.9	-37.6	3	2.95	37.23	20.5	-17.2	-7.0	I
HM-4	388	116.2	-54.8	3	2.66	5.87	56.3	-40.7	-5.0	I
HM-5	395.7	165.6	-67.8	5	4.65	11.31	23.8	-76.1	28.9	I
HM-6	404.8	135.4	-60.0	3	2.59	4.91	63.0	-56.7	-5.4	III
HM-7	413.6	178.1	-52.6	3	2.89	18.66	29.4	-81.9	-98.8	I
HM-8	421.3	153.9	-39.7	3	2.99	221.70	8.3	-61.3	-52.4	I
HM-9	429.5	182.0	-55.6	4	3.90	29.01	17.3	-84.8	-128.3	I
HM-10	436.2	163.3	-51.7	4	3.99	317.60	5.2	-74.0	-48.1	I
HM-11	445.3	349.1	64.1	1	N/A	N/A	N/A	80.8	-165.6	IV
HM-12	452.1	172.2	-58.3	4	3.98	140.27	7.8	-83.7	-37.0	I
HM-13	459.7	152.5	-17.4	4	4.00	1309.10	2.5	-49.7	-65.4	I
HM-14	467.3	301.3	-50.3	3	2.21	2.52	104.30	-0.2	116.9	III
USC-1	367	145.6	-53.8	3	2.78	9.16	43.3	-62.2	-23.1	I
USC-2	375.8	130.0	-11.2	1	N/A	N/A	N/A	-33.1	-44.6	IV
USC-3	386.5	197.9	-65.5	3	2.90	19.11	29.0	-75.7	126.9	I
USC-4	394.1	127.4	-31.1	2	1.99	93.71	26.1	-38.9	-32.4	III
USC-5	402.7	201.3	-49.1	2	1.95	21.75	56.4	-69.5	-173.9	III
USC-6	410.3	182.7	-39.3	2	1.96	27.81	49.3	-70.9	-117.8	III
USC-7	419.1	150.9	-58.2	2	2.00	331.10	13.8	-67.7	-16.4	III
USC-8	427.7	184.5	-51.7	2	2.00	934.54	8.2	-80.5	-133.7	III
USC-9	435.9	182.9	-49.6	3	2.62	5.32	59.8	-79.0	-123.4	I
USC-10	447.8	175.1	-41.2	2	1.96	23.01	54.7	-72.0	-95.5	III
USC-	456	142.1	-28.0	3	1.26	1.15	180.0	-48.0	-47.6	III

11										
USC-12	467	193.3	-52.6	2	1.97	29.39	47.8	-76.8	-167.3	III
USC-13	474.9	30.4	26.1	2	1.56	2.29	180.0	51.9	17.0	III
USC-14	493.2	276.4	38.4	2	1.99	84.02	27.6	18.7	172.6	III
USC-15	495.9	171.5	-59.1	3	2.99	307.78	7.0	-83.4	-28.7	I
USC-16	505.1	348.1	42.5	2	1.82	5.54	152.30	70.7	104.4	III
USC-17	513.6	10.5	71.1	3	2.96	47.80	18.0	74.0	-88.2	I
USC-18	522.7	326.6	62.8	2	1.98	62.00	32.3	65.4	178.2	III
USC-19	531	6.4	59.2	3	2.65	5.66	57.6	85.0	-8.6	I
USC-21	545.3	4.6	34.7	3	2.97	76.25	14.2	67.6	58.4	I
USC-23	553.2	67.7	65.7	1	N/A	N/A	N/A	42.8	-52.4	IV
USC-24	557.8	268.2	8.7	2	2.00	1261.00	7.0	1.5	164.3	III

NOTE: USC-20 (from 536.8 m) and USC-22 (550.5 m) are removed from the table due to no data.

*In geographic coordinates.

[†]N indicates the number of samples with MAD less than 20°.

[§]R is resultant vector.

[#]k is precision parameter.

**α_{95} is a cone of 95% confidence about estimated mean direction.

[††]$Long_{VGP}$ and Lat_{VGP} refer to longitude and latitude, respectively, of site virtual geomagnetic pole (VGP) where positive is north and east.

[§§]See text for discussion on Class assignment. Those sites with only 1 statistically significant sample are labeled as Class IV.

Table 2.5. U-Pb isotopic data for Church Butte tuff.

Fraction	Composition			Isotopic Ratios								Dates (Ma)						Correlation Coefficients
	Pbc (pg)*	Pb*/ Pbc †	Th/ U§	206Pb/ 204Pb#	208Pb/ 206Pb**	206Pb/ 238U <Th> **††	±2σ %	207Pb/ 235U**	±2σ %	207Pb/ 206Pb <Th> **††	±2σ %	206Pb/ 238U <Th> ††	±2σ abs	207Pb/ 235U§§	±2σ abs	207Pb/ 206Pb <Th>††	±2σ abs	206Pb/238U <Th>-207Pb/235U
z1	0.4	18.0	0.68	1041.7	0.219	0.007607	(.11)	0.04930	(1.08)	0.04703	(1.05)	48.854	0.054	48.87	0.52	50	25	0.317
z2	0.4	20.8	0.84	1156.2	0.269	0.007609	(.10)	0.04932	(.97)	0.04703	(.94)	48.866	0.051	48.89	0.46	50	23	0.287
z3	0.6	12.2	0.50	744.6	0.159	0.007616	(.16)	0.04950	(1.72)	0.04716	(1.67)	48.907	0.078	49.06	0.82	56	40	0.374
z4	0.5	25.3	0.72	1442.2	0.231	0.007610	(.11)	0.04933	(.89)	0.04703	(.85)	48.872	0.051	48.89	0.43	50	20	0.444
z5	0.5	29.0	0.59	1707.6	0.187	0.007617	(.09)	0.04937	(.78)	0.04703	(.74)	48.915	0.044	48.93	0.37	50	18	0.445
z7	0.9	7.1	1.01	390.8	0.323	0.007616	(.26)	0.04972	(2.79)	0.04737	(2.73)	48.91	0.12	49.3	1.3	67	65	0.299

Note: This table was generated in U-Pb Redux program.

*Total mass of common Pb.

†Ratio of radiogenic Pb (including 208Pb) to common Pb.

§Th contents calculated from radiogenic 208Pb and the 207Pb/206Pb date of the sample, assuming concordance between U-Th and Pb systems.

#Measured ratio corrected for fractionation and spike contribution only.

**Measured ratios corrected for fractionation, tracer and blank.

††Corrected for initial Th/U disequilibrium using radiogenic 208Pb and Th/U[magma] = 2.80000.

§§Isotopic dates calculated using the decay constants λ238 = 1.55125E-10 and λ235 = 9.8485E-10 (Jaffey et al. 1971).

Table 2.6. U-Pb isotopic data for Henrys fork tuff.

Fraction	Composition			Isotopic Ratios								Dates (Ma)						Correlation Coefficients
	Pbc (pg)*	Pb*/ Pbc †	Th/ U§	206Pb/ 204Pb#	208Pb/ 206Pb**	206Pb/ 238U <Th> **††	±2σ %	207Pb/ 235U**	±2σ %	207Pb/ 206Pb <Th> **††	±2σ %	206Pb/ 238U <Th> ††	±2σ abs	207Pb/ 235U§§	±2σ abs	207Pb/ 206Pb <Th>††	±2σ abs	206Pb/238U <Th>-207Pb/235U
z1	0.4175	30.0524	0.7622	1706.4117	0.2440	0.0075	0.0744	0.0487	0.6353	0.0471	0.6177	48.2288	0.0358	48.2795	0.2995	50.7963	14.7677	0.2802
z2	0.2595	19.8290	0.6790	1155.8490	0.2173	0.0075	0.0914	0.0487	1.0103	0.0470	0.9887	48.3117	0.0440	48.3250	0.4768	48.9811	23.6256	0.2736
z3	0.3421	11.8200	0.9127	658.2812	0.2921	0.0075	0.1512	0.0488	1.6766	0.0471	1.6313	48.2438	0.0727	48.3315	0.7913	52.6854	38.9387	0.3388
z4	0.2906	29.7870	0.8226	1666.6989	0.2632	0.0075	0.0827	0.0487	0.8224	0.0470	0.7905	48.2352	0.0398	48.2752	0.3877	50.2645	18.8890	0.4217
z5	0.6010	34.9667	1.0962	1831.3273	0.3507	0.0075	0.0888	0.0488	0.7256	0.0471	0.6920	48.2835	0.0427	48.3598	0.3427	52.1442	16.5353	0.4224
z7	0.3441	32.0445	0.7628	1817.9946	0.2441	0.0075	0.0755	0.0488	0.6256	0.0471	0.6106	48.3392	0.0364	48.4210	0.2958	52.4699	14.5939	0.2456
z8	0.4960	13.7435	0.6511	812.3077	0.2084	0.0075	0.1123	0.0489	1.2860	0.0472	1.2522	48.2977	0.0540	48.4889	0.6089	57.9521	29.8638	0.3373
z10	0.5025	14.4202	0.8521	810.3970	0.2727	0.0075	0.1265	0.0491	1.3260	0.0474	1.2903	48.2622	0.0608	48.6554	0.6300	68.0705	30.7131	0.3236
z14	0.5100	7.7289	0.7450	454.2593	0.2384	0.0075	0.1933	0.0492	2.3415	0.0475	2.2872	48.2392	0.0929	48.7275	1.1140	72.8157	54.3852	0.3177
z15	0.5828	10.4557	0.7803	603.1075	0.2497	0.0075	0.1416	0.0486	1.7169	0.0469	1.6806	48.2281	0.0681	48.1730	0.8078	45.4344	40.1699	0.2931
z16	0.4788	33.8362	0.7270	1935.7589	0.2327	0.0075	0.0761	0.0488	0.5703	0.0471	0.5459	48.2839	0.0366	48.3593	0.2693	52.1000	13.0529	0.3680
z17	0.5033	9.6915	0.7871	559.1206	0.2519	0.0075	0.1409	0.0496	1.8334	0.0478	1.8154	48.3970	0.0679	49.1683	0.8800	86.9342	43.0539	0.1642
z18	0.8401	6.7118	0.8620	386.2441	0.2759	0.0075	0.1985	0.0487	2.6822	0.0470	2.6451	48.2193	0.0953	48.2623	1.2642	50.3973	63.1581	0.2220
z21	0.5293	14.1878	0.8106	805.6203	0.2594	0.0075	0.1143	0.0492	1.2618	0.0474	1.2348	48.4194	0.0551	48.8050	0.6012	67.7868	29.3963	0.2749
z22	0.8686	9.7380	0.7820	562.5007	0.2503	0.0075	0.1485	0.0493	1.8614	0.0475	1.8282	48.3182	0.0715	48.8465	0.8877	74.8519	43.4553	0.2597

Note: This table was generated in U-Pb Redux program.

*Total mass of common Pb.

†Ratio of radiogenic Pb (including 208Pb) to common Pb.

§Th contents calculated from radiogenic 208Pb and the 207Pb/206Pb date of the sample, assuming concordance between U-Th and Pb systems.

#Measured ratio corrected for fractionation and spike contribution only.

**Measured ratios corrected for fractionation, tracer and blank.

††Corrected for initial Th/U disequilibrium using radiogenic 208Pb and Th/U[magma] = 2.80000.

§§Isotopic dates calculated using the decay constants λ238 = 1.55125E-10 and λ235 = 9.8485E-10 (Jaffey et al. 1971).

Table 2.7. U-Pb isotopic data for Sage Creek Mountain tuff.

Fraction	Composition			Isotopic Ratios								Dates (Ma)						Correlation Coefficients
	Pbc (pg)*	Pb*/ Pbc †	Th/ U§	206Pb/ 204Pb#	208Pb/ 206Pb**	206Pb/ 238U <Th> **††	±2σ %	207Pb/ 235U**	±2σ %	207Pb/ 206Pb <Th> **††	±2σ %	206Pb/ 238U <Th> ††	±2σ abs	207Pb/ 235U§§	±2σ abs	207Pb/ 206Pb <Th>††	±2σ abs	206Pb/238U <Th>-207Pb/235U
z1	0.5599	14.3947	0.9754	779.6338	0.3121	0.0073	0.1436	0.0477	1.4287	0.0471	1.3890	47.1920	0.0675	47.2836	0.6601	51.9334	33.1627	0.3203
z2	0.2404	45.5622	1.2987	2257.0520	0.4155	0.0074	0.0862	0.0477	0.5930	0.0469	0.5696	47.3438	0.0407	47.2962	0.2741	44.8865	13.6349	0.3295
z3	0.4170	16.7953	0.5480	1006.9540	0.1754	0.0074	0.1202	0.0476	1.1488	0.0468	1.1132	47.3814	0.0568	47.2287	0.5301	39.4823	26.6441	0.3400
z4	0.4207	36.1261	0.7376	2043.3506	0.2361	0.0074	0.0812	0.0477	0.6599	0.0470	0.6440	47.2871	0.0382	47.3217	0.3051	49.0746	15.3994	0.2446

Note: This table was generated in U-Pb Redux program.

*Total mass of common Pb.

†Ratio of radiogenic Pb (including 208Pb) to common Pb.

§Th contents calculated from radiogenic 208Pb and the 207Pb/206Pb date of the sample, assuming concordance between U-Th and Pb systems.

#Measured ratio corrected for fractionation and spike contribution only.

**Measured ratios corrected for fractionation, tracer and blank.

††Corrected for initial Th/U disequilibrium using radiogenic 208Pb and Th/U[magma] = 2.80000.

§§Isotopic dates calculated using the decay constants λ238 = 1.55125E-10 and λ235 = 9.8485E-10 (Jaffey et al. 1971).

Table 2.8. Summary of published calibration of the GPTS.

Chron	Option 1	Option 2	Option 3	Hilgen et al. (2010)	GPTS2014	Westerhold et al. (2015)	Smith et al. (2008)	Smith et al. (2010)
C20r (o)	N/A	N/A	N/A	N/A	45.724	N/A	45.71	45.99
C21n (o)	47.396	47.791	48.191	47.837	47.349	47.723	46.52	46.8
C22n (y)	48.661	49.056	49.456	49.102	48.566	48.954	48.3	48.59
C22n (o)	49.299	49.694	50.094	49.74	49.344	49.593	49.07	49.37
C23n.1n (y)	50.768	51.163	51.563	51.209	50.628	51.051	49.71	50.01
C23n.1n (o)	50.992	51.387	51.787	51.433	50.835	51.273	49.88	50.18
C23n.2n (y)	51.064	51.459	51.859	51.505	50.961	51.344	50.04	50.34
C23n.2n (o)	51.443	51.838	52.238	51.884	51.833	51.721	50.5	50.8

Note: o - older age, y - younger age.

Table 2.9. Summary of suggested dates for key geological events.

	Ash-17	PETM	K/Pg Boundary	FCs	Matuyama-Brunhes Boundary
	(Ma)	(Ma)	(Ma)	(Ma)	(ka)
Astronomical Models					
Dinarès-Turell et al. (2003)			65.777		
Westerhold et al. (2007)					
Op1 (anchored to C24r/C24n = 53.53 Ma)		55.53	65.280 ± 0.010		
Op2 (anchored to C24r/C24n = 53.93 Ma)		55.93	65.680 ± 0.010		
Op3 (anchored to C24r/C24n = 54.33 Ma)		56.33	66.08 ± 0.010		
Kuiper et al. (2008)			65.957 ± 0.040	28.201	791
Westerhold et al. (2009)	55.12 ± 0.12 (FCs_{R98}) 55.48 ± 0.12 (FCs_{K08})	55.651-55.933 (FCs_{R98}) 56.011-56.293 (FCs_{K08})			
Hilgen et al. (2010)		56.0	66.00		
Westerhold et al. (2012)	54.85 ± 0.05	55.530±0.05	65.250 ± 0.06 65.08~65.26 (using FCs = 27.89 Ma)	27.89	
Westerhold et al. (2015)	55.280	55.930	66.022	28.10	
Radioisotopic Dates					
Swisher et al. (1993)			65.99±0.12 (IrZ coal, FCs_{K08})		
Storey et al. (2007)	55.473 ± 0.12 (FCs_{K08})				
Crowley et al. (2007)					767.1
Bowring et al. (2008)			66.1		
Channell et al. (2010)				27.93	773.2
Jaramillo et al. (2010)		56.3			
Charles et al. (2011)		55.846±0.118	implies ~66.0		
Renne et al. (2013)			66.043 ± 0.043 (FCs_{R10}) 65.836 ± 0.061 (FCs_{K08})		

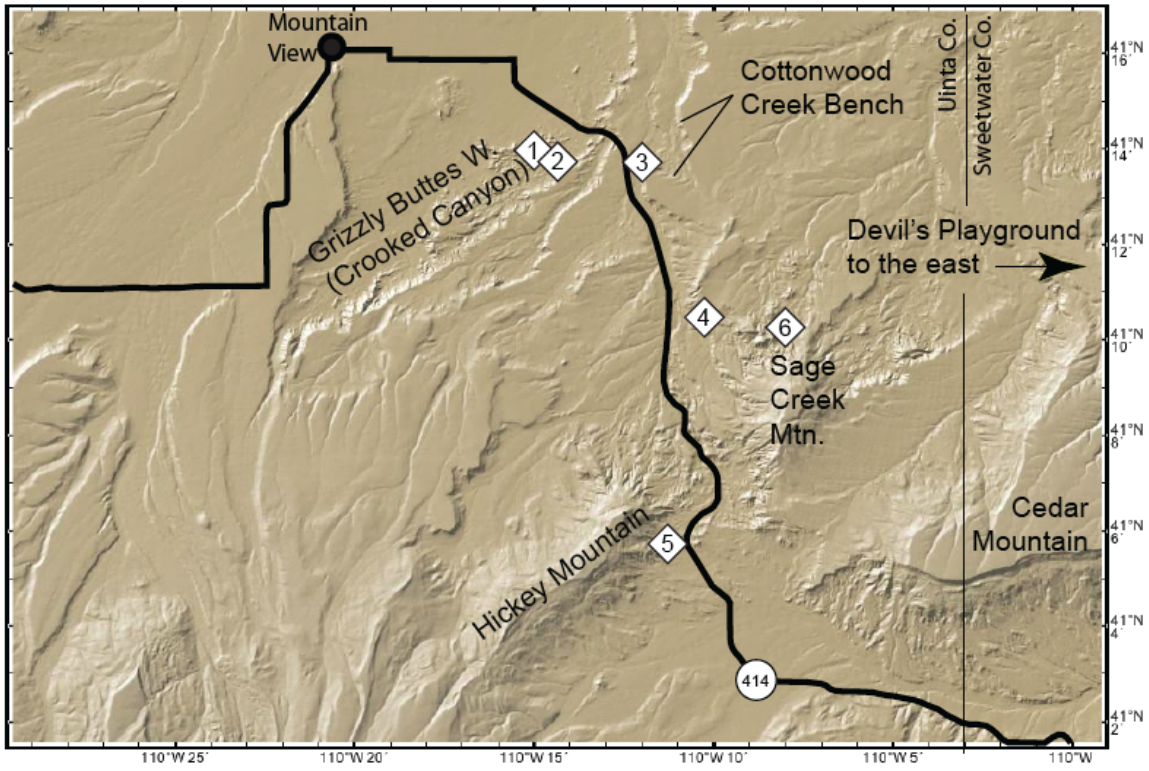

Figure 2.1. Map of the southern Bridger Basin. Diamonds show sites of paleomagnetic sections. 1 - BBB, 2 - LDC, 3 - CWC, 4 - SCM, 5 - HM, 6 - USC sections. Base map taken from GeoMapApp (Lamont-Doherty Earth Observatory).

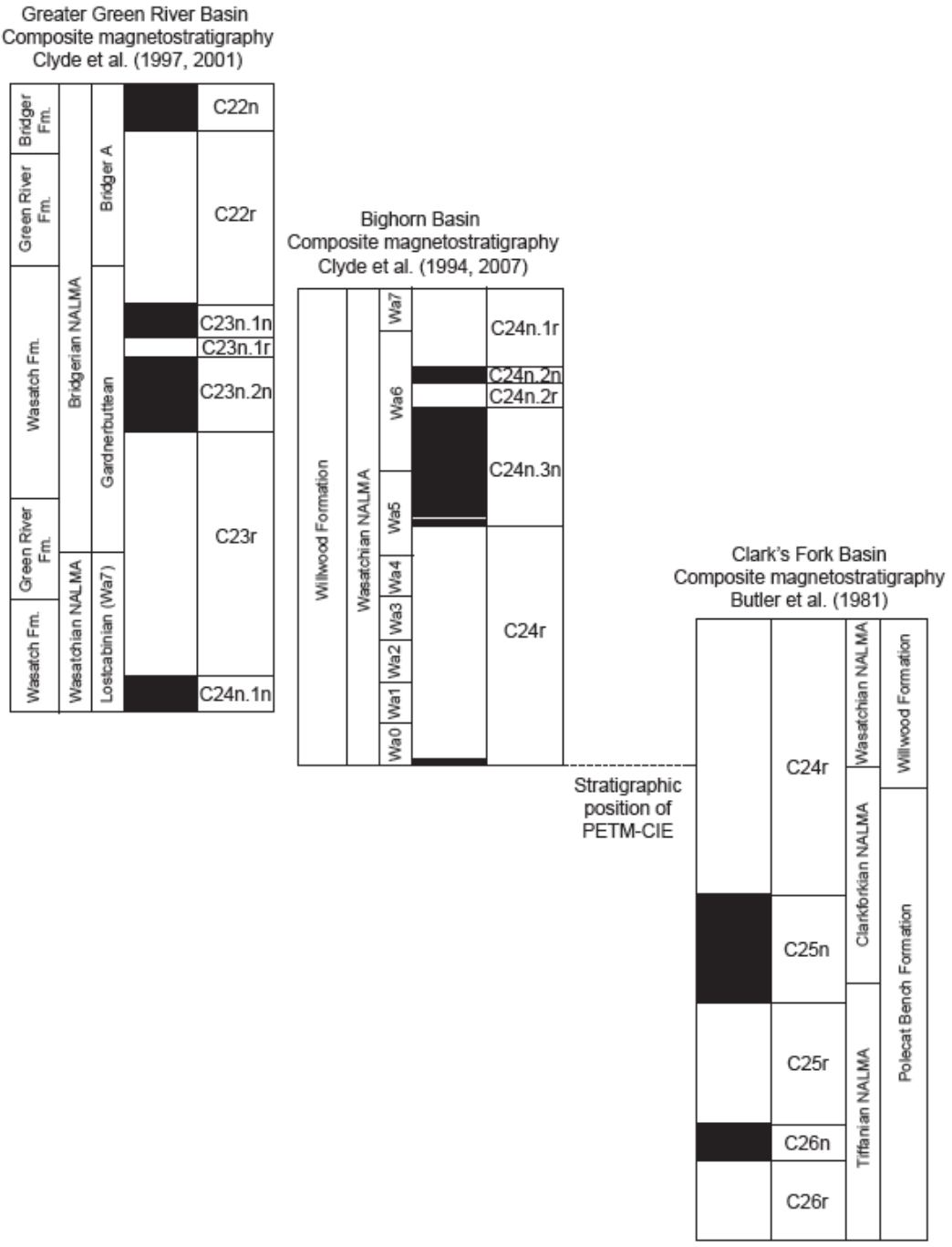

Figure 2.2. Currently available magnetostratigraphy for the early Paleogene from western Wyoming, including the Greater Green River Basin, Bighorn Basin and Clark's Fork Basin. Wa - Wasatchian NALMA.

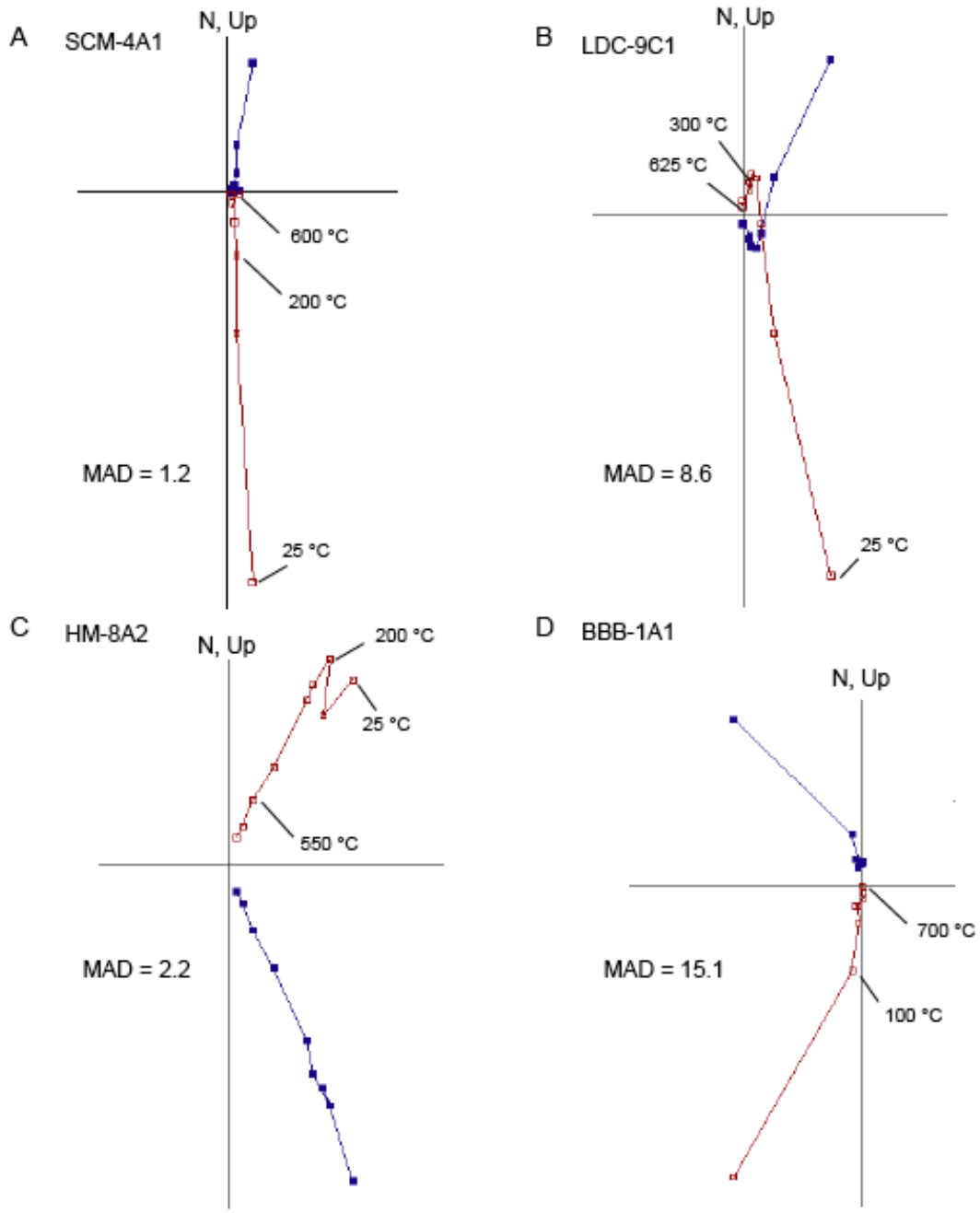

Figure 2.3. Vector end-point diagrams (Zijderveld, 1967) showing thermal demagnetization of natural remanent magnetization for four representative samples from the Bridger Formation. Open (filled) squares show vector end points in the vertical (horizontal) plane. Selected demagnetization temperature steps are given next to data points. (A) SCM-4A1: thermal demagnetization isolated the characteristic component between 25° and 600°. (B) LDC-9C1: present-day field component was removed between

25° and 200° and characteristic component was isolated between 300° and 625°. (C) HM-8A2: an overprint was removed at 25° and 100°, and the characteristic component was isolated between 200° and 600°. (D) BBB-1A1: an overprint was removed between 25° and 300°, and the characteristic component was isolated between 400° and 700°.

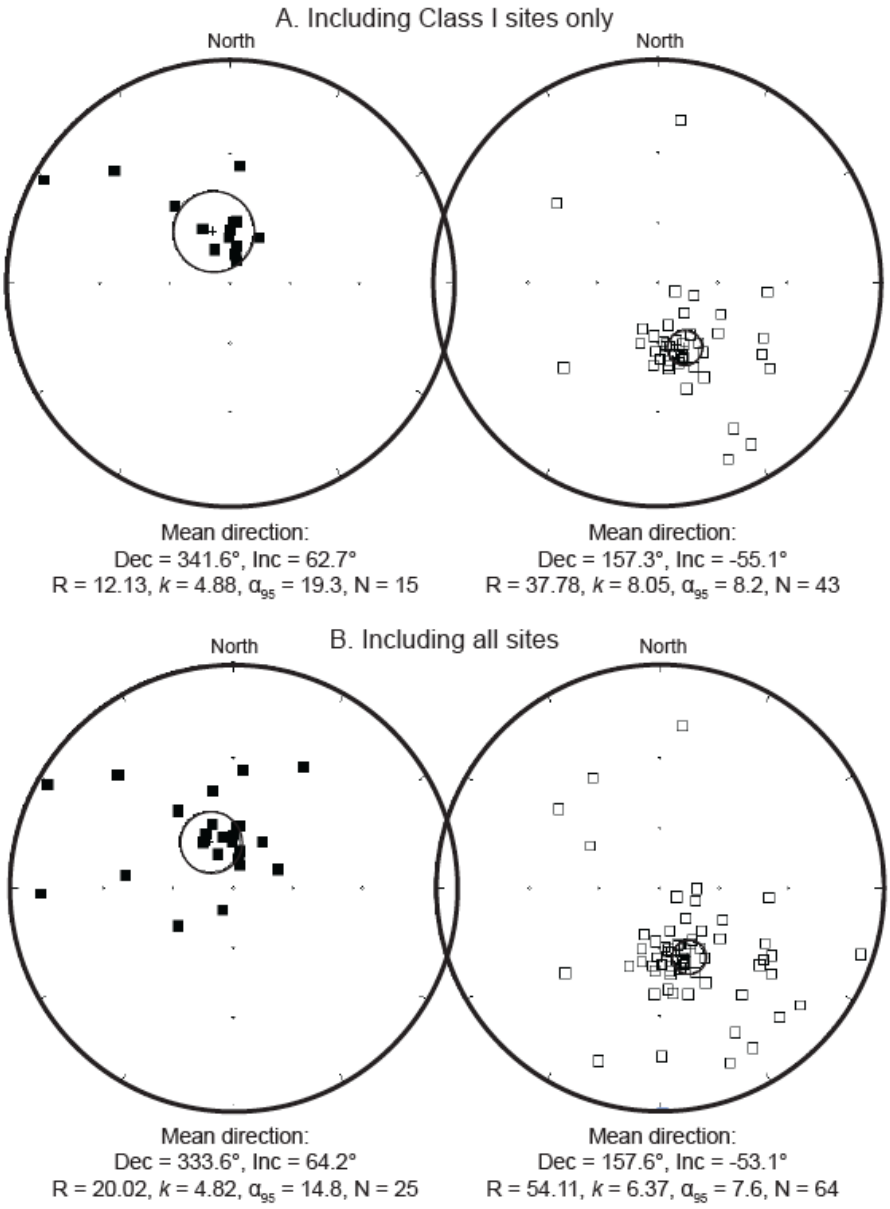

Figure 2.4. Equal-area projections of site directions for normal polarity sites (left column) and reversed polarity sites (right column) in tectonic coordinates for (A) Class I sites only and (B) all sites, including Class I, II, III and IV. Inner circles show a 95% cone of confidence around the estimated mean direction. Filled (open) symbols lie on the lower (upper) hemisphere of the projection. Fisher statistics are also shown where R is the resultant vector, k is the precision factor, α95 is the 95% confidence limit, and N is the number of sites.

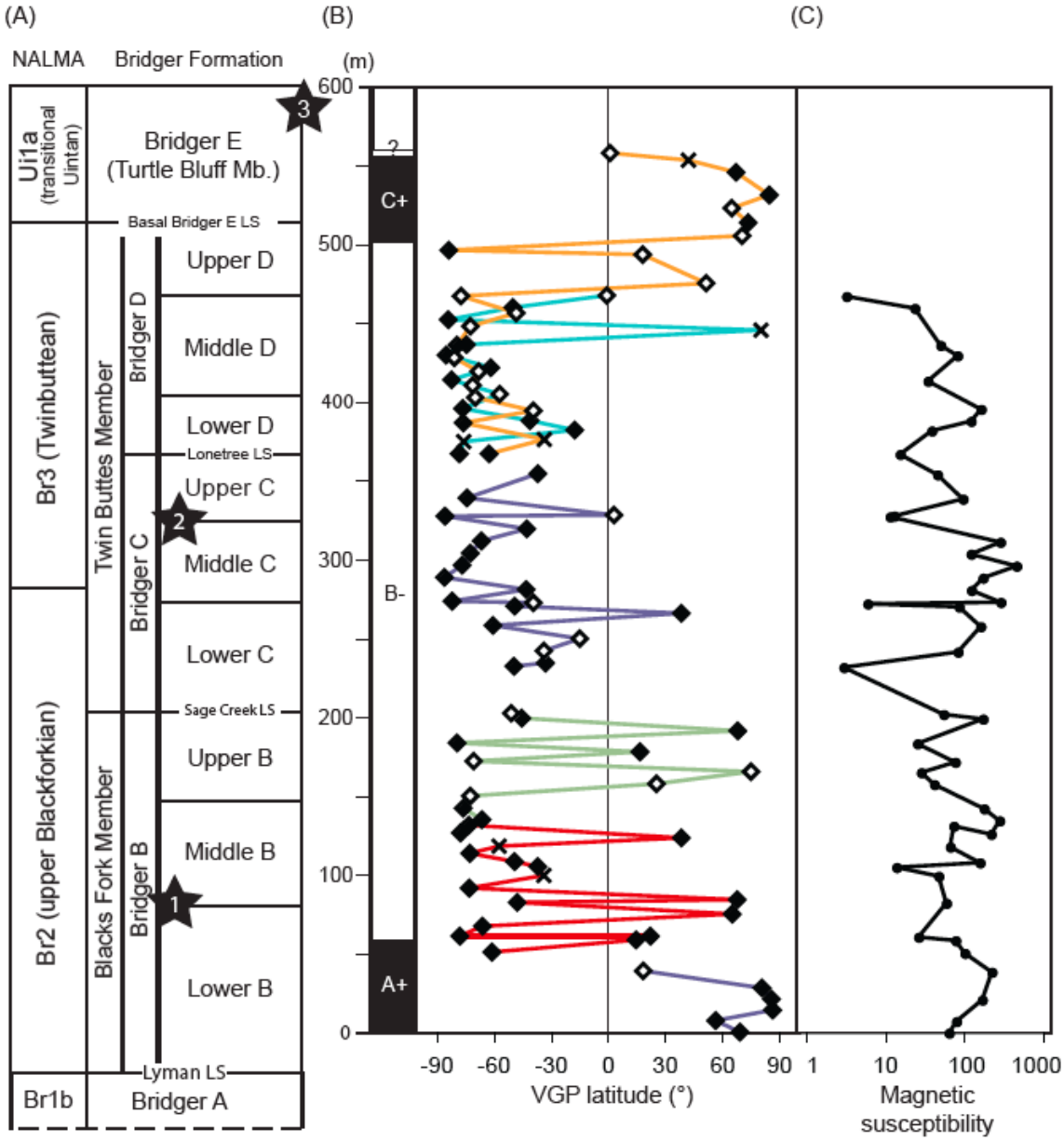

Figure 2.5. (A) Nomenclature of the Bridgerian NALMA and Bridger Formation. Stars indicate the stratigraphic position of (1) Church Butte tuff, (2) Henrys Fork tuff, and (3) Sage Creek Mountain tuff. (B) Estimated VGP (virtual geomagnetic pole) latitude for all the statistically significant sites. Filled diamonds show Class I sites that were used in defining site polarity. Open diamonds and crosses show Class III and Class IV sites, respectively, that were used only to supplement the interpretation of magnetic

stratigraphy. According to my analyses, there were no Class II sites. The sections are color-coded and from bottom to top: BBB, LDC, CWC, SCM, HM and USC. (C) Magnetic susceptibility from representative samples is shown in a log scale.

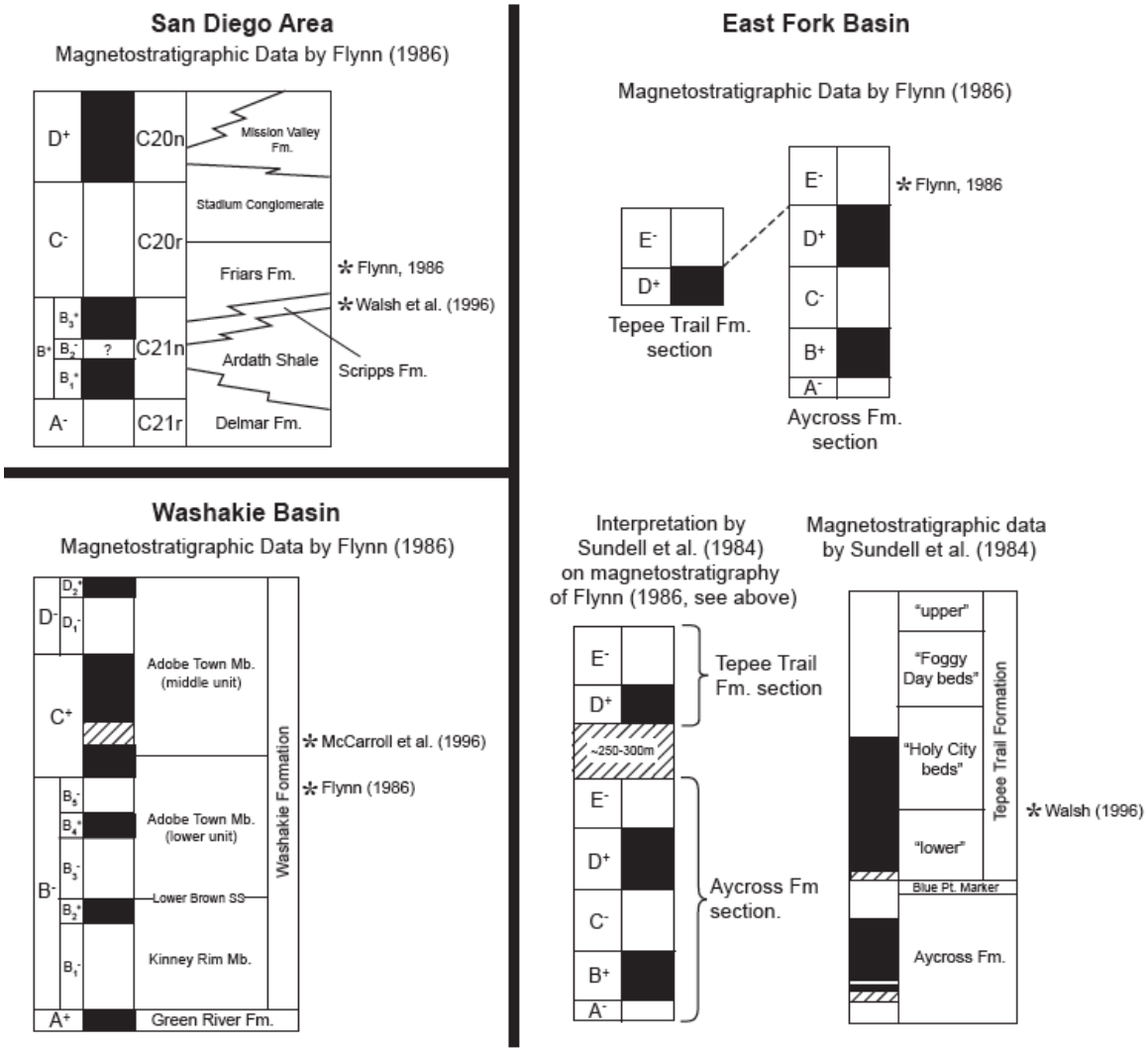

Figure 2.6. Bio-magnetostratigraphic data from San Diego area, Washakie Basin and East Fork Basin (see Figure 1.1 for the location of the basins). San Diego section has been correlated directly to the Geomagnetic Polarity Time Scale (GPTS) via marine biochronology, and thus the chrons are indicated in the section. On the other hand, the sections from the Washakie Basin and East Fork Basin are without independent constraints to permit correlation to the GPTS. Asterisk indicates the proposed stratigraphic position of the Bridgerian/Uintan boundary according to the study indicated. Diagonal lines indicate unsampled intervals. Sections are not drawn to scale.

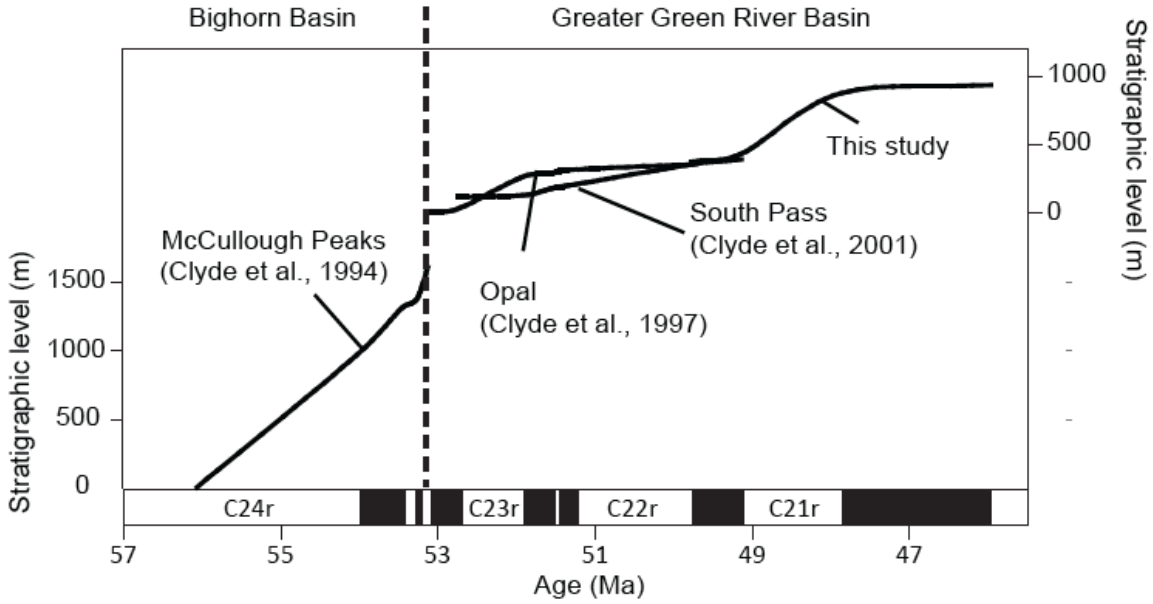

Figure 2.7. Inferred sedimentation rate for the composite stratigraphic interval spanning the Wasatchian through the earliest Uintan based on the magnetostratigraphic data from the Bighorn Basin and Greater Green River Basin. Note that with the exception of the base of the McCullough Peaks section, the sedimentation rate is overestimated for the lower and upper ends of each section because the top (base) of the section is artificially assumed to be equivalent in the age of the younger (older) age of the corresponding chron.The stratigraphic distance between the McCullough Peaks section and Opal section is unknown. See Figure 1.1 for the location of these sections.

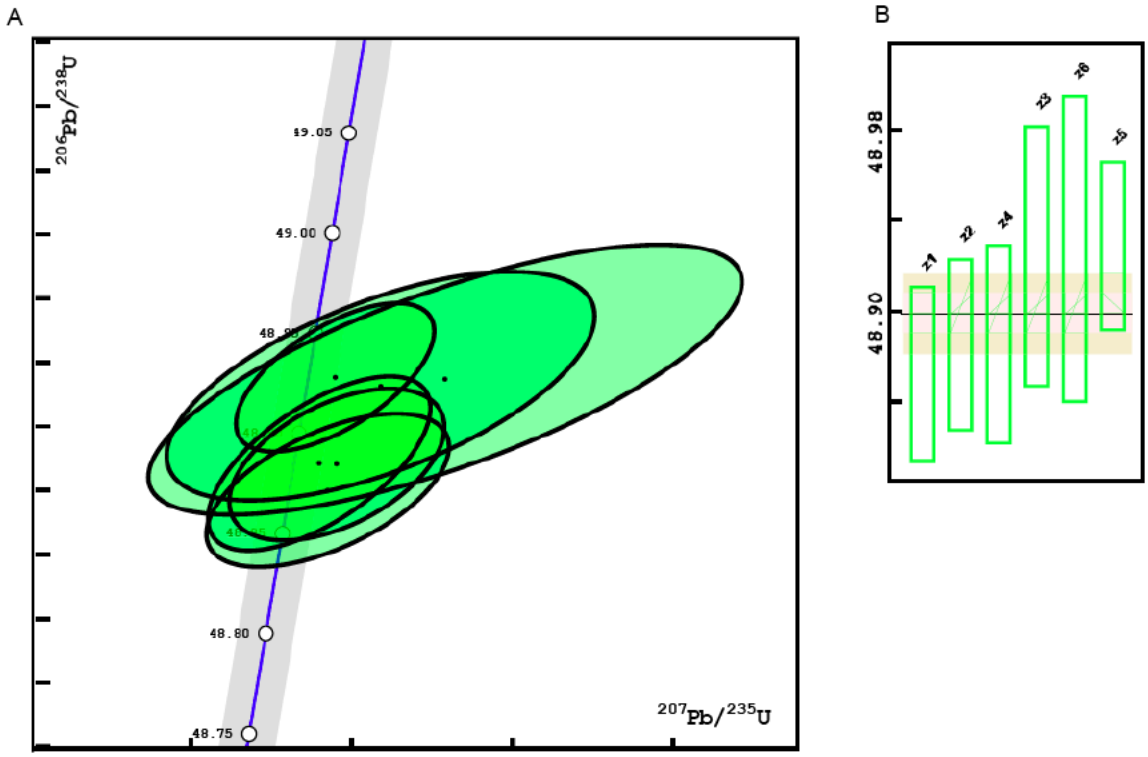

Figure 2.8. A. Concordia diagram of the Church Butte tuff. An ellipse represents a single grain U-Pb ID/CA-TIMS analysis with 2σ uncertainty. Ellipses in dark green are the single-grain analyses that were included in weighted mean age calculation. Diagonal line represents concordia with 2σ uncertainty envelope. B. Age distribution plots for the analyzed zircon samples from the Church Butte tuff. Bar heights represent 2σ analytical uncertainty of individual zircon analyses.

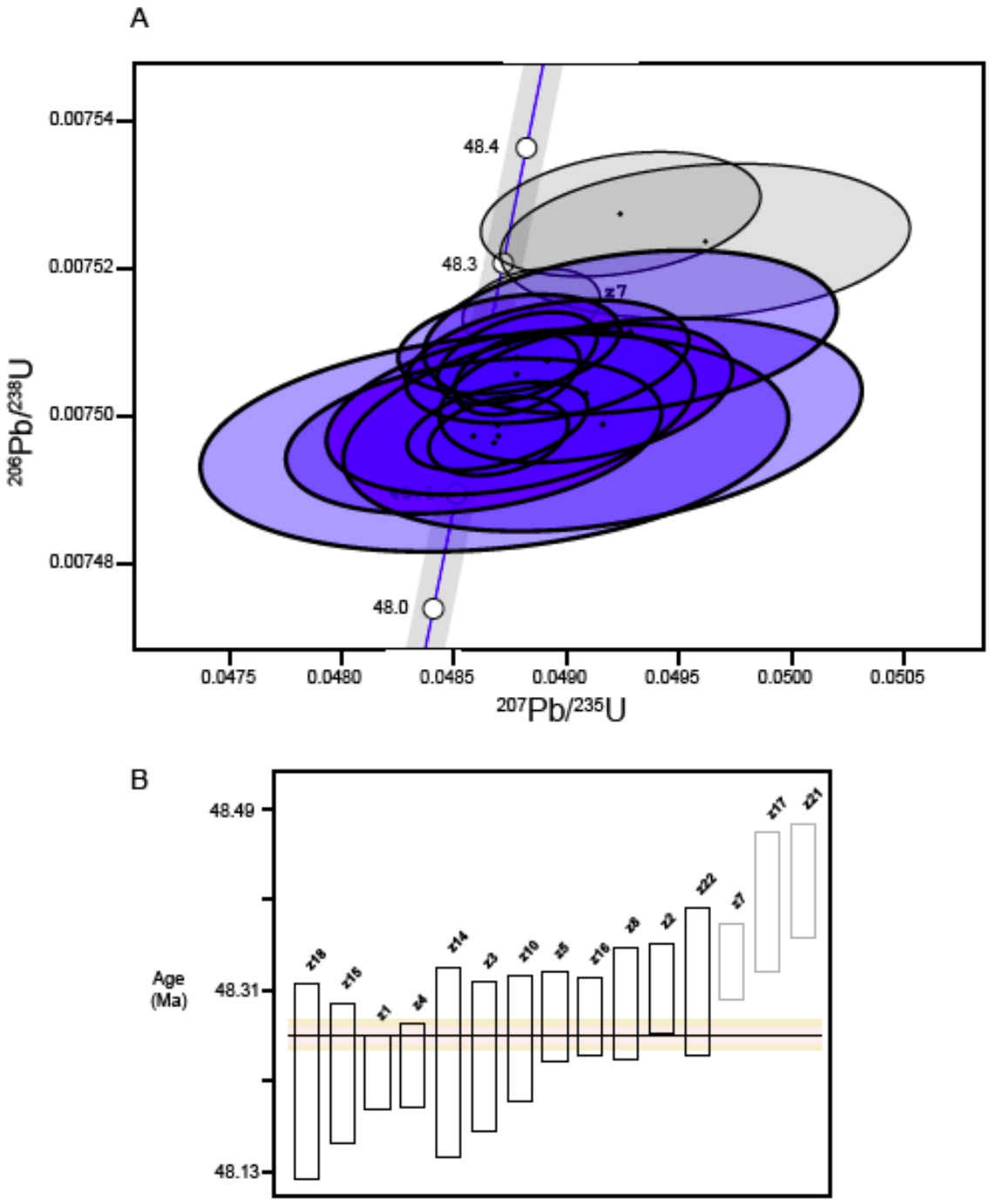

Figure 2.9. A. Concordia digram of the Henrys Fork tuff. An ellipse represents a single grain U-Pb ID/CA-TIMS analysis with 2σ uncertainty. Ellipses in blue are the single-grain analyses that were included in weighted mean age calculation. Diagonal line represents concordia with 2σ uncertainty envelope. B. Age distribution plots for analyzed

zircon samples from the Henrys Fork tuff. Bar heights represent 2σ analytical uncertainty of individual zircon analyses. The zircon analyses that were used in age calculation are shown in black.

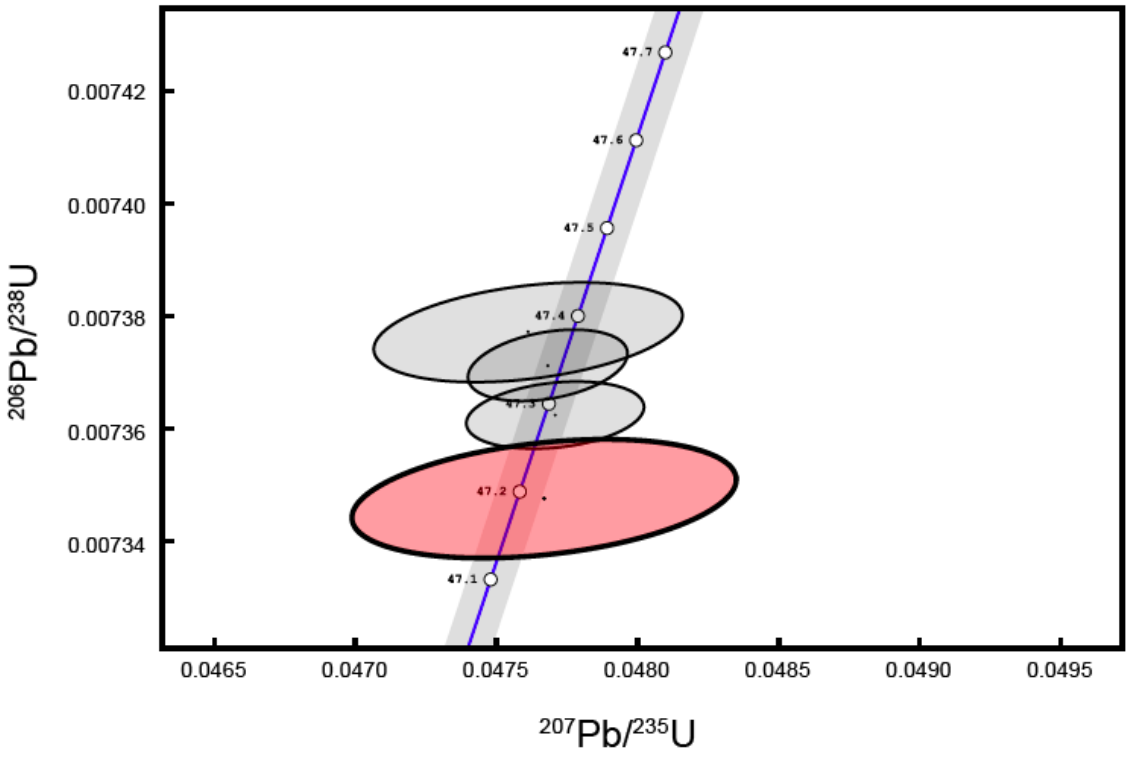

Figure 2.10. Concordia diagram of the Sage Creek Mountain tuff. An ellipse represents a single grain U-Pb ID/CA-TIMS analysis with 2 sigma uncertainty. Ellipse in red is the youngest analysis that is taken to be the best age approximation for the sample. Diagonal line represents concordia with 2 sigma uncertainty envelope.

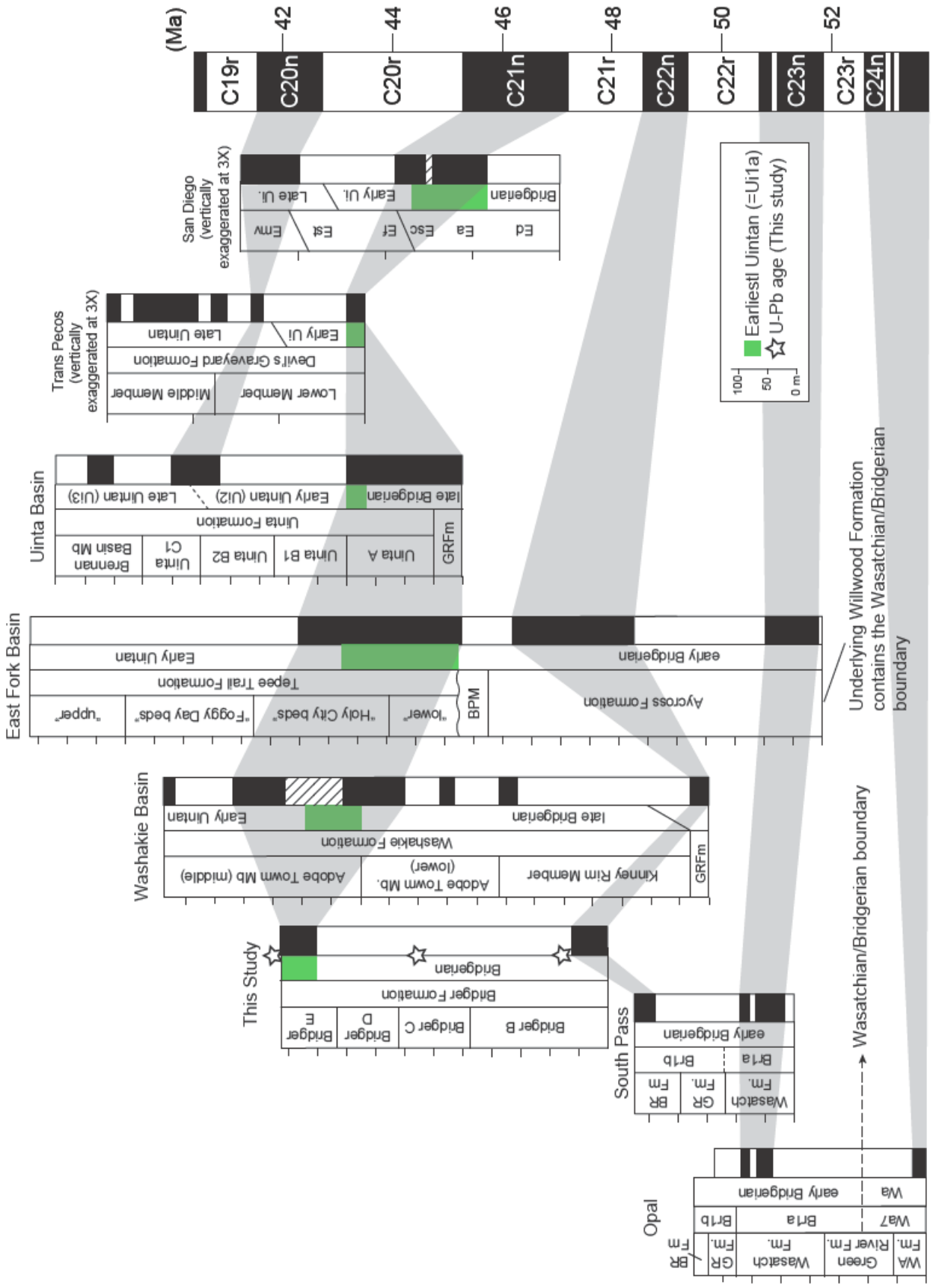
(Ma)
42
44
46
48
50
52
C19r
C20n
C20r
C21n
C21r
C22n
C22r
C23n
C23r
C24n
San Diego (vertically exaggerated at 3X)
Bridgerian
Early Ui.
Late Ui.
Ed
Ea
Esc
Ef
Est
Emv
Trans Pecos (vertically exaggerated at 3X)
Early Ui
Late Uintan
Devil's Graveyard Formation
Lower Member
Middle Member
Uinta Basin
late Bridgerian
Early Uintan (Ui2)
Late Uintan (Ui3)
Uinta Formation
GRFm
Uinta A
Uinta B1
Uinta B2
Uinta C1
Brennan Basin Mb
East Fork Basin
Early Uintan
early Bridgerian
Tepee Trail Formation
"upper"
"Foggy Day beds"
"Holy City beds"
"lower"
BPM
Aycross Formation
Underlying Willwood Formation contains the Wasatchian/Bridgerian boundary
Washakie Basin
Early Uintan
late Bridgerian
Washakie Formation
GRFm
Kinney Rim Member
Adobe Town Mb. (lower)
Adobe Town Mb (middle)
This Study
Bridgerian
Bridger Formation
Bridger B
Bridger C
Bridger D
Bridger E
South Pass
Wasatch Fm.
GR Fm
BR Fm
Br1a
Br1b
early Bridgerian
Wasatchian/Bridgerian boundary
Opal
WA Fm.
Green River Fm.
Wasatch Fm.
GR Fm.
BR Fm
Wa
early Bridgerian
Wa7
Br1a
Br1b
Earliestl Uintan (=Ui1a)
U-Pb age (This study)
100
50
0 m

Figure 2.11. Suggested inter-basinal correlation of the Bridgerian/Uintan boundary bearing sections in the western U.S. among each other and to the GPTS (see Figure 1.1 for the location and reference of the sections). The sections are scaled in terms of stratigraphic thickness. The earliest Uintan (Ui1a) interval is shown in green. Shaded area indicates an unsampled or ambigious interval. WA Fm = Wasatch Formation, BR Fm = Bridger Formation, BPM = Blue Point Marker, Ed = Delmar Formation, Ea = Ardath Shale, Esc = Scripps Formation, Ef = Friars Formation, Est = Stadium Conglomerate, Emv = Mission Valley Formation.

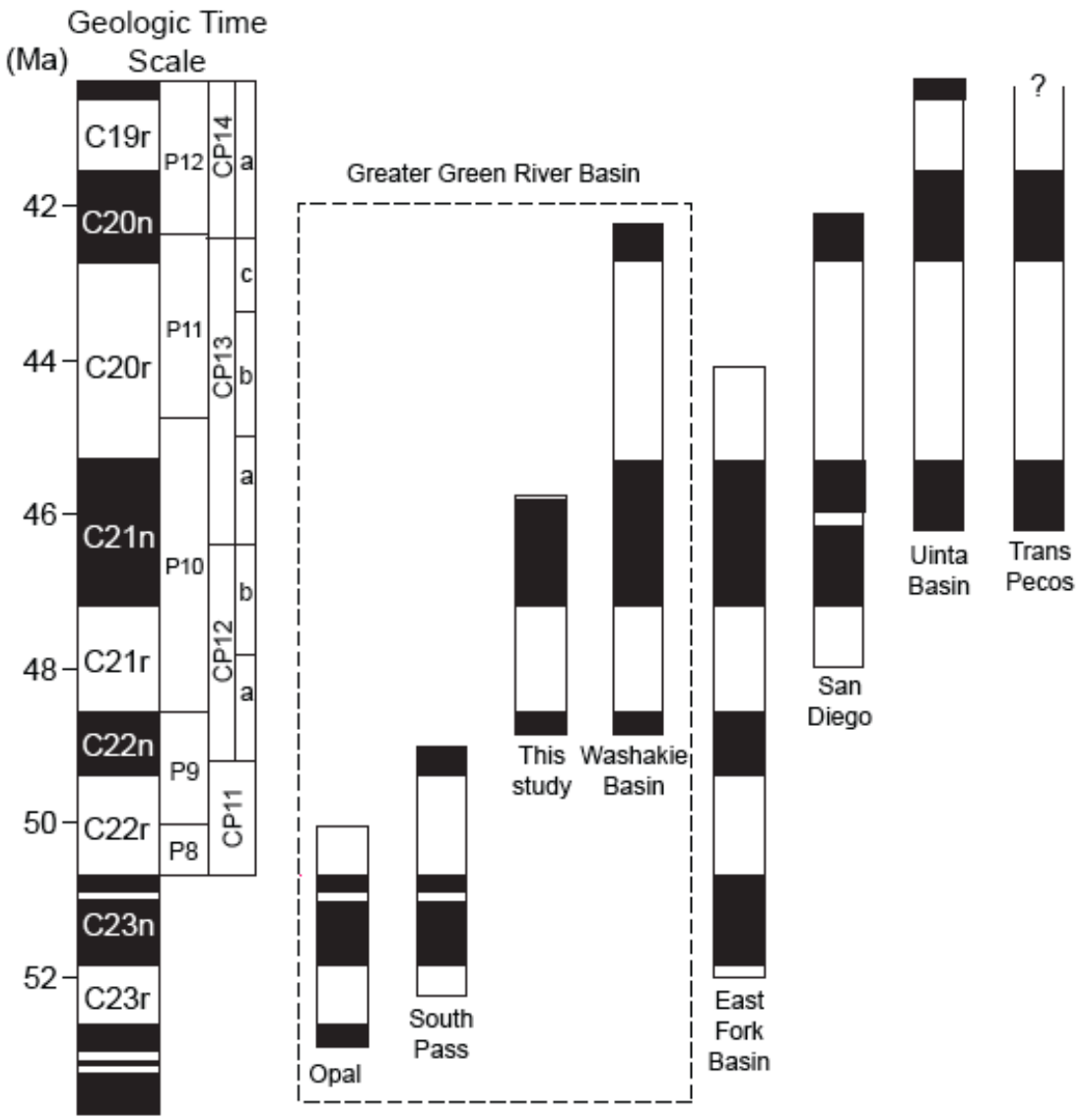

Figure 2.12. Correlation of the Bridgerian/Uintan boundary bearing sections in the western U.S. to the Geologic Time Scale (see Figure 1.1 for the location and references of the sections). The sections are scaled to time.

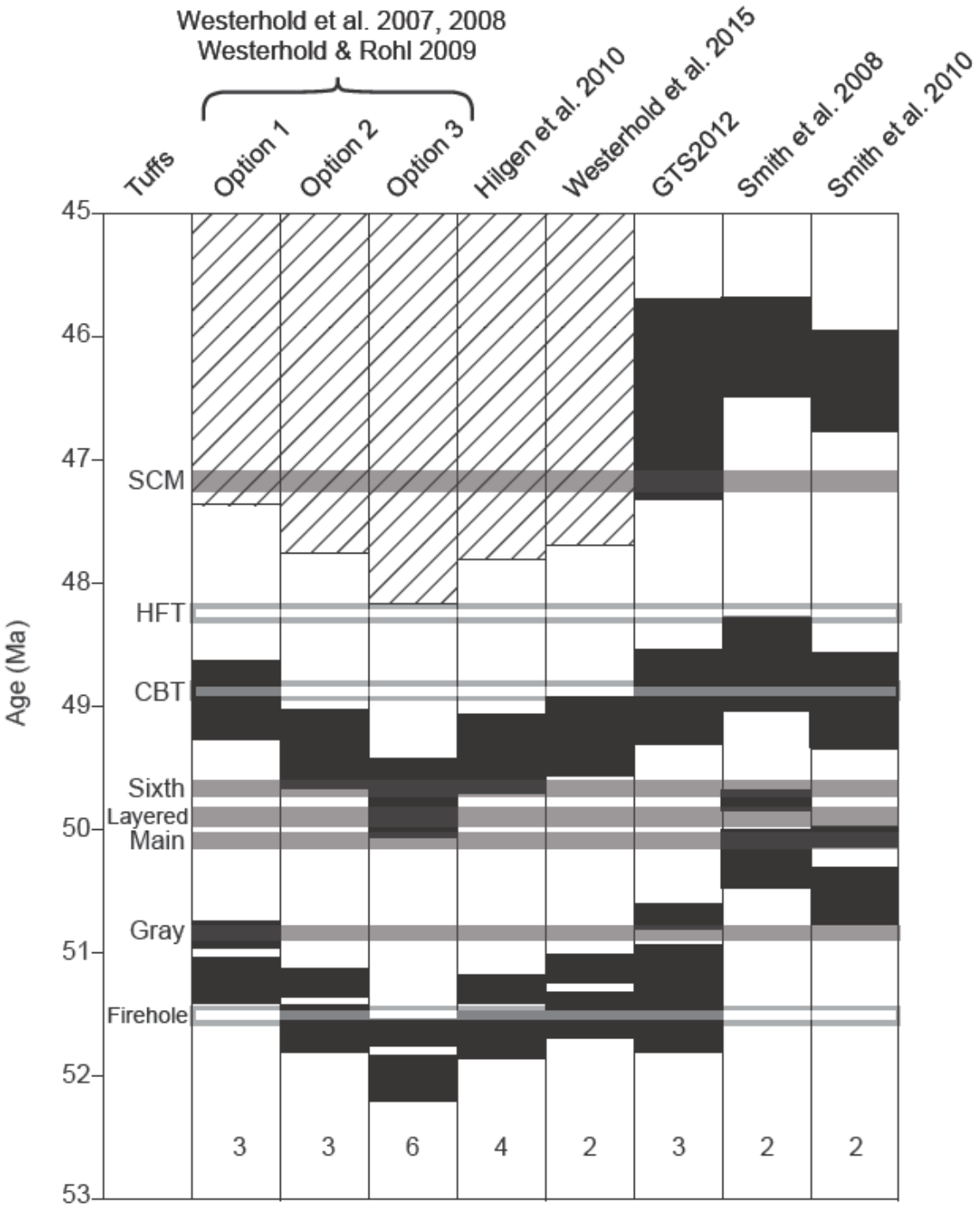

Figure 2.13. Eight calibration models for the early-middle Eocene GPTS that were evaluated in this study. Boxes extending across all the models represent the U-Pb age of ash beds that are, from youngest to oldest, Sage Creek Mountain tuff, Henrys Fork tuff, Church Butte tuff, Sixth tuff, Layered tuff, Main tuff, Grey tuff, and Firehole tuff. Of

these, white (grey) boxes indicate ash beds of reversed (normal) polarity, whereas the height of each box indicates the U-Pb age including 2 sigma external errors. The left five models do not provide calibration for the polarity reversals younger than Chron C21n(o). In each model, the oldest normal chron is Chron C23n.2n. The numbers at the bottom indicate the number of tuffs that show agreement between known and predicted chron of the tuffs in each age model.

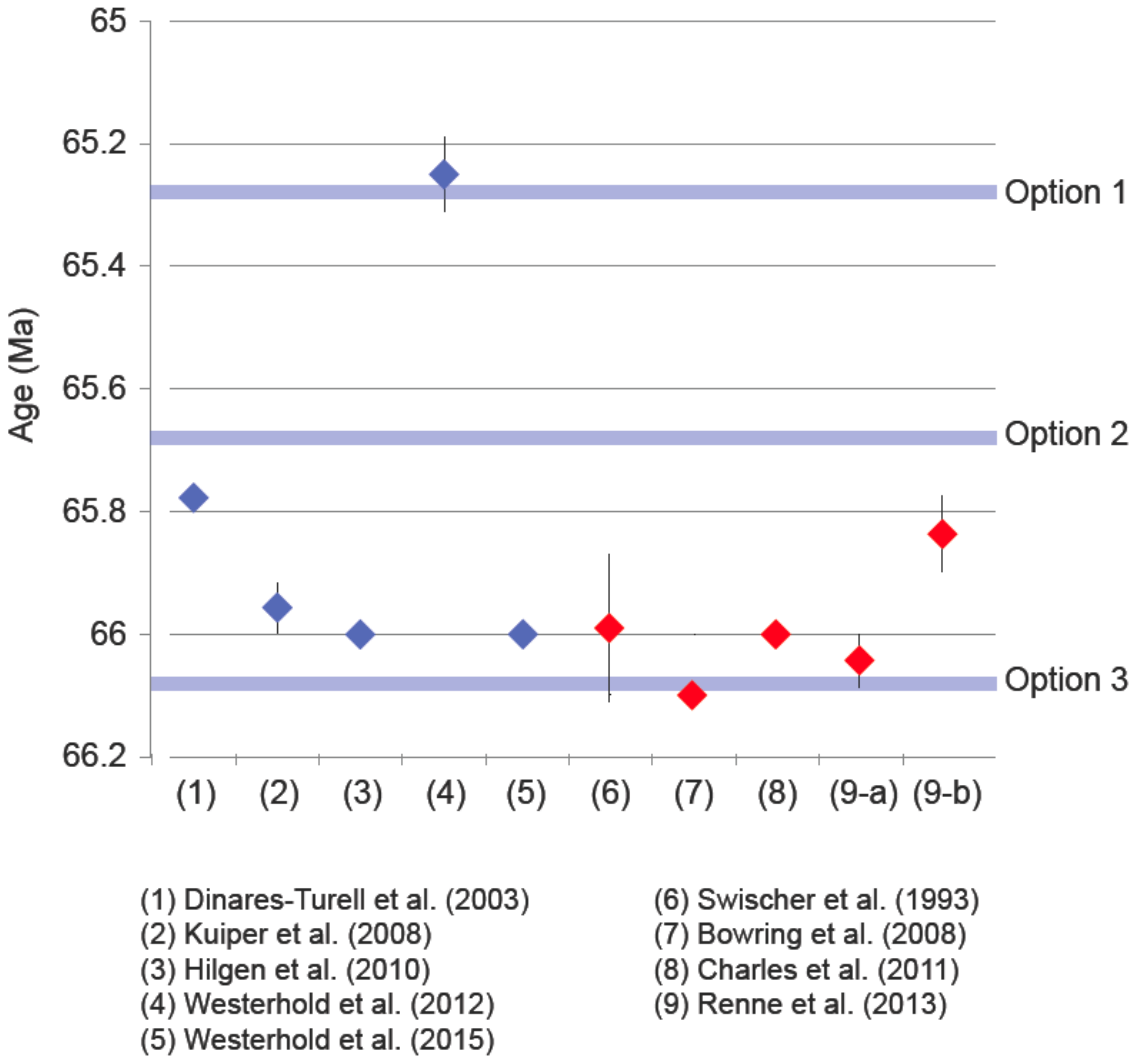

Figure 2.14. Proposed ages for the Cretaceous/Paleogene boundary. Thick horizontal lines indicate the Option 1, 2 and 3 ages of the K/Pg boundary by Westerhold et al. (2007, 2008), with 10 kyr error envelope. Blue diamonds indicate astronomical estimates, whereas red diamonds indicate the estimates based on radioisotopic dating. Error bars represent full external uncertainty. 9-a and 9-b are $^{40}Ar/^{39}Ar$ dates relative to Fish Canyon sadine calibration of Renne et al. (2010) and Kuiper et al. (2008), respectively.

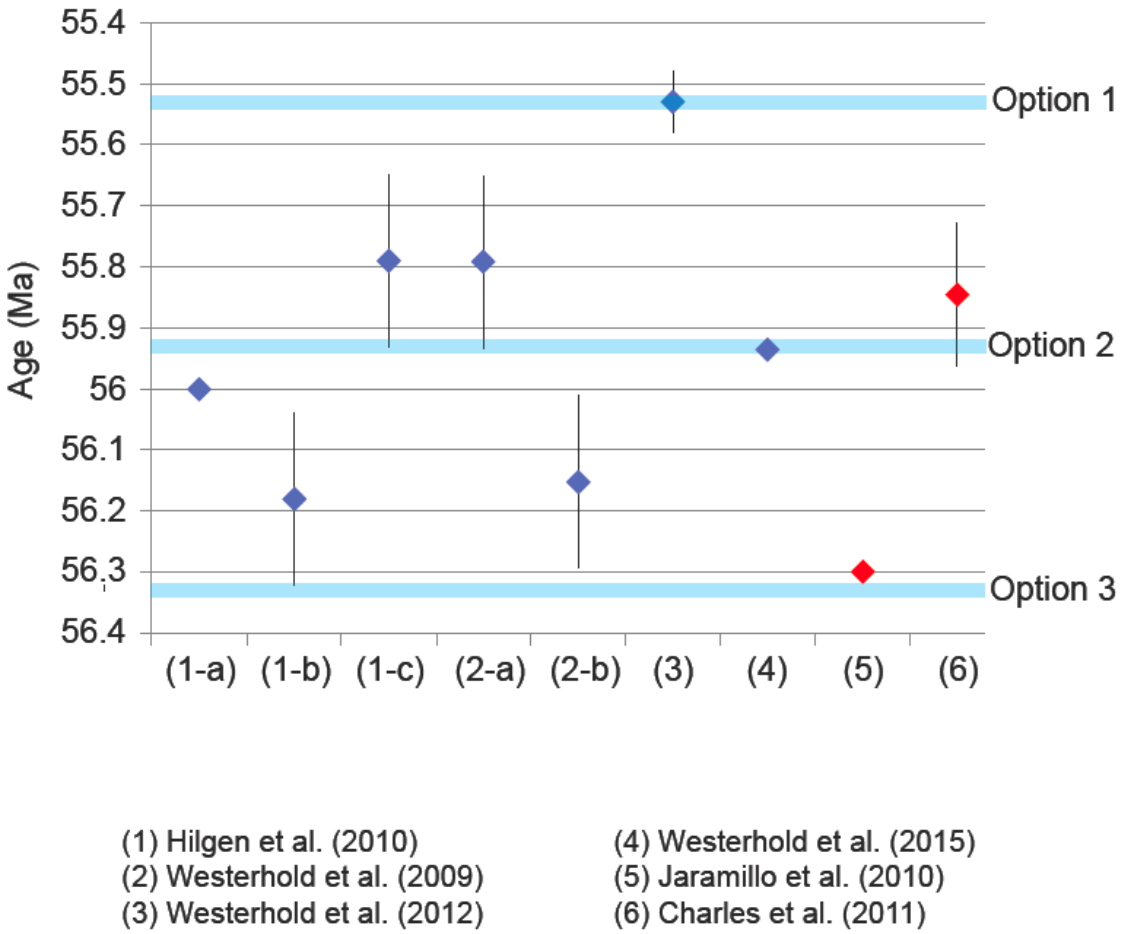

Figure 2.15. Proposed ages for the onset of the Paleocene Eocene Thermal Maximum (PETM). Thick horizontal lines indicate the Option 1, 2 and 3 ages of the PETM by Westerhold et al. (2007, 2008), with 10 kyr error envelope. Blue diamonds indicate astronomical estimates, whereas red diamonds indicate the estimates based on radioisotopic dating. Error bars represent full external uncertainty. 1-a estimate was derived by tuning the 405-kyr carbonate maximum to the 405-kyr minimum around 66.0 Ma and assuming 25 405-kyr cycles in the Paleocene. 1-b and 1-c estimates are based on the assumption that there are 672 kyrs between the PETM and ash-17 and using the $^{40}Ar/^{39}Ar$ age of ash-17 by Storey et al. (2007) as calculated relative to the Fish Canyon sanidine age of Kuiper et al. (2008) and Renne et al. (1998), respectively.

Chapter 3

New approaches to reconstructing and interpreting body size evolution of *Notharctus* (Primates: Adapidae), *Hyopsodus* ("Condylarthra": Hyopsodontidae) and *Orohippus* (Perissodactyla: Equidae) in the Middle Eocene Bridger Formation (Bridgerian NALMA) during the climatic deterioration after the Early Eocene Climatic Optimum

ABSTRACT

Most of the Bridgerian North American Land Mammal "Age" is from the initial cooling phase subsequent to the peak of the Early Eocene Climatic Optimum, and thus, if Bergmann's rule pertains, the Bridgerian mammals are expected to shown an increase in size. This hypothesis is tested among *Notharctus*, *Hyopsodus*, and *Orohippus*, using their molar dentition as a proxy for body size. These taxa represent three different ecomorphs, and I investigate if their patterns of body size change are consistent with the prediction according to Bergmann's rule, and how their ecological adaptation may have affected their response to the climate change. Prior to analyzing the body size evolution, specimens of *Notharctus* and *Hyopsodus* were identified to species based on morphological characters in their dentition. This practice differs from previous studies in which species identification relied on relative size of the individuals and stratigraphic levels of origin. Within the new framework of species identification, five species of *Notharctus* were recognized, among which, *N. pugnax*, *N. robustior* and *N.* sp. indet. exhibited statistically significant body size increase in the time span of interest. Based on

dental morphology, I recognized five species of *Hyopsodus*. Within the morphology-based species identification, body size analysis showed that *H. despiciens* and *H. lepidus* exhibited a statistically significant increase within the sampled interval. When analyzed at the generic level, a statistically significant increase was observed for both *Notharctus* and *Hyopsodus*. Morphology based species identification could not be fulfilled for *Orohippus*, but its analysis at the generic level showed a lack of statistically significant size increase. Thus, among the three taxa from the Bridgerian, Bergmann's rule is supported by three species of *Notharctus*, and two species of *Hyopsodus*, but not by *Orohippus*.

INTRODUCTION

Body size is a powerful indicator of the species' adaptive strategy to its environment, and its temporal change has been documented in both extant endotherms and ectotherms from terrestrial and aquatic environments (Damuth and MacFadden, 1990a; Gardner et al., 2011). While there is likely multiple causation behind any observed body size shifts, some of the changes have been attributed to climate change (Millien et al., 2006; Daufresne et al., 2009). One of the most notable cases of climate-induced body size change was observed at the time of Paleocene-Eocene Thermal Maximum during which short-term hyperthermals are thought to have caused dwarfism among Early Eocene *Hyracotherium* (Gingerich, 2006; Secord et al., 2012). This observed trend conforms to the empirical generalization suggested by Bergmann (1847) regarding the negative correlation between latitude and body size of endotherms. Although Bergmann (1847) referred to latitude and body size, the same negative

correlation can be expected between temperature and body size according to the thermoregulatory and geometric arguments about heat loss. Body size is an integral part of organisms' biology and one of the most observable traits among extinct and extant organisms (Schmidt-Nielsen, 1984). Thus, it has been studied a number of times to illustrate macroevolutionary trends (e.g., Ashton et al., 2000; Meiri and Dayan, 2003). While there is little doubt that ambient climatic conditions such as temperature have a first order impact on the biota, its exact mechanism as well as the magnitude and direction of the biotic response to it vary from case to case, and the subject of the body size evolution within the context of climate change remains a topic of interest in paleobiology (e.g., Ashton et al., 2000; Ashton, 2002; Meiri and Dayan, 2003; Blackburn and Hawkins, 2004; Orcutt and Hopkins, 2013).

The rich and diverse mammalian fauna from the Bridgerian North American Land Mammal "Ages" (NALMA, Wood et al., 1941) in the Bridger Basin of southwestern Wyoming presents an excellent opportunity for investigation on macroevolution (e.g., West, 1979; Gunnell, 1997, 1998, 2002; Gunnell and Bartels, 2001; Woodburne et al., 2009a). The fossil mammals of the Bridgerian NALMA appeared during the peak of the Early Eocene Climatic Optimum (EECO; Zachos et al., 2001; Clyde et al., 2001; Woodburne et al., 2009b), and in many ways, it represents the last of the tropical and closed-habitat mammalian fauna in North America, as the Earth climate entered the beginning phases of current icehouse conditions in the middle Eocene (Robinson et al., 2004). In this study, body size of three Bridgerian mammals, *Notharctus*, *Hyopsodus* and *Orohippus,* are analyzed over a ~2 million year interval within the framework of morphological character-based species identification. The resultant patterns of the body

size evolution will be compared with the global climate using the chronostratigraphy of the Bridger Formation presented in Chapter 2. If climate (temperature) were the most important factor in the observed changes in body size of these fossil mammals and Bergmann's rule pertains, then the three taxa would be expected to show body size increase in accord with the general cooling trend following the EECO. In order to ensure close comparison of the faunal and marine climatic data, only the specimens with stratigraphic control are included in this study. The biochronologic nomenclature of Gunnell et al. (2009) is followed.

In studies like this one, it is important that reliability of taxonomy be first established before inferring any macroevolutionary trends in the fossil record (Alroy, 2003). In the same vein, I also argue that investigation must be carried out at the species level because evolution acts on individuals rather than at higher taxonomic levels. Furthermore, if the study involves analysis of body size, the individual specimens must be identified based on morphological characters. Previous macroevolutionary studies on the Bridgerian fauna were performed within the framework of species identification that was based on the relative size and/or stratigraphic origin of the specimens. Such methods would be prone to circular reasoning so it is important to identify specimens without regard to size or stratigraphic origin of the specimens.

In this chapter, lower tooth positions are designated with a lower case letter (e.g., m1 for a lower first molar), and upper tooth positions are designated with an upper case letter (e.g., M1 for an upper first molar). Abbreviations: AMNH – American Museum of Natural History; UCM – University of Colorado (Boulder), W – maximum buccolingual

tooth width, L – maximum mesiodistal tooth length (all measurements are in millimeters).

METHODS

This study differentiates itself from previous studies of West (1979) and Gunnell (1998) in two ways. First, the improved chronostratigraphic framework for the Bridger Formation provides more refined temporal and spatial context in which to analyze the evolutionary data. The specimens included in this study are characterized by either locality information or stratigraphic position based on the stratigraphic nomenclature of Matthew (1909) (AMNH specimens), or meter levels relative to well-known marker beds (UCM specimens) of Murphey and Evanoff (2007). The stratigraphic system of Matthew (1909) divides the Bridger Formation into five units (A through E in the ascending order), and B, C and D are further subdivided into five numbered units (B1-B5, C1-C5, and D1-D5) (Figure 1.2). The lettered units are separated using basin-wide marker beds, but the numbered units in Bridger B, C and D are defined more arbitrarily. In proposing a more rigorous stratigraphic system for the Bridger Formation, Murphey and Evanoff (2007) maintained the lettered units of Matthew (1909) but subdivided B, C and D into lower, middle and upper units using well-defined marker beds (Figure 1.2). To consider all of the specimens in the common stratigraphic framework, the first task was to place all the specimens in a single stratigraphic context regardless the type of stratigraphic data of its origin. However, it is presently not possible to establish a detailed correlation between the two stratigraphic systems, so for the purpose of integrating the AMNH and UCM specimens and plotting them on the same stratigraphic scale, it was tentatively assumed

that Matthew's (1909) numbered units are of equal thickness within Bridger B, C and D. For the goals of this study, however, the accuracy of the correlation between the two stratigraphic systems is not critical, as statistical analyses of body size changes are performed using broader time bins (Bridger B, C and D), which are equivalent between the two systems.

The second way in which this study differs from the previous studies is that species determinations are made *independent* of both body size and stratigraphic position of the specimens, and also body size analyses are conducted at the intraspecific level. Due to their abundance, Bridgerian *Notharctus* and *Hyopsodus* had been used in previous macroevolutionary studies (Gingerich, 1979; West 1979; Gunnell, 1998; 2002), however, these studies make use of body size data of individual specimens to *recognize* species, and the analysis was conducted only at the interspecific level. However, if the goal of a study is to decipher body size change over time at the species level, then body size-based and stratigraphic occurrence-based species identifications should not be used, in order to avoid circular reasoning. In this study, character-based species diagnoses were first developed for both *Notharctus* and *Hyopsodus* independent of the *a priori* notion of the relative body size and stratigraphic occurrences, before investigating the body size evolution at the intraspecific level,

Species Identification

Notharctus

It is one of the most commonly preserved and intensively studied adapid primates in the Early to Middle Eocene of North America (Granger and Gregory, 1917, Robinson, 1957, Gazin, 1958, West, 1976; Hamrick and Alexander, 1996). There have been at least

five species reported in the literature, although their systematics have never been rigorously studied. Their ecomorph is reconstructed to be arboreal quadrupedal leapers with mostly frugivorous and folivorous diets (Beecher, 1983). They co-existed with primates of similar form, including omomyids such as *Smilodectes*. Compared to their omomyid counterparts, *Notharctus* was more abundant in number but the taxonomic (species) diversity was not as great as for *Smilodectes* (Gunnell, 2002). *Notharctus* went extinct by the end of the Bridgerian except for a few fossils known from the Uintan of Texas.

As it was difficult to diagnose species based only on discrete, non-overlapping dental features (i.e., there is within-species polymorphism among these closely related, often sympatric species), I used a phylogenetic analysis on all specimens to cluster OTUs (opearational taxonomic units, at the individual level) and diagnose species based on the results of the phylogenetic analysis. To this end, 102 specimens (64 m1, 71 m2, 37 M1, and 35 M2 specimens) from the AMNH and UCM collections were coded for 48 dental characters (Table 3.1), and the data were analyzed in the phylogenetic software "Mesquite" using heuristic searches for the minimum tree length and Wasatchian-aged *Pelycodus*, *Copelemur*, and *Cantius* as the outgroup (Gingerich and Simons, 1977). All characters were treated as unordered and of equal weight. The individual specimens were identified to be the species of the holotype with which they were clustered.

Hyopsodus

As a type of condylarthra and archaic ungulate, it is a common mammal in the Paleocene and Eocene fossil records of North America. Gingerich (1994) investigated the body size evolution of over 1000 specimens of 4 species of Clarkforkian and early

Wasatchian-aged *Hyopsodus* from the Clarks Fork Basin, WY within a detailed stratigraphic record. Gingerich's (1994) species identification, however, relied exclusively on differences in molar size. Using the occlusal area of M1 as a proxy for body size, Gingerich (1994) concluded that the *H. loomisi*-to-*H. latidens* lineage, as a whole and within individual species, showed a non-random pattern of stasis. Similarly, within the Bridgerian-aged *Hyopsodus*, West (1979) used a stratophenetic approach for phylogenetic reconstruction and demonstrated stasis within the time span of the Bridger Formation at the genus level. West (1979) included samples from the middle Bridger B to middle Bridger D, and based on the tooth size (length of m2) and stratigraphic occurrence, recognized three morphometrically-defined species of *Hyopsodus*. Based on the relative size of each group and its stratigraphic origin, he then made a taxonomic interpretation, suggesting at least two speciation events. Specifically, he assigns *H. paulis* and *H. minusculus* to the larger and smaller species, respectively, from the early Bridgerian. Similarly, from the upper Bridgerian, the two size groups were referred to as *H. despiciens* and *H. lepidus* for the larger one and smaller one, respectively. However, it is unclear what taxonomic group these size groups represent (although he assumes they represent species without giving valid explanation) and furthermore, it is circular to make species identification based on size and claim that there is stasis over some stratigraphic interval in the observed body size. His study was conducted at the interspecific level, and it is possible that size change of individual species are masked by analysis at a more inclusive taxonomic scale. For instance, if two species were present in his data set, with species A displaying a pattern of size increase while species B had an opposite pattern of size decrease by the same magnitude - if viewed at the generic level, the composite

dataset could appear constant and taken to indicate stasis rather than two opposite trends of body size change at the intraspecific level. I argue that because evolution acts on individuals rather than species as a whole, faunal analyses must be conducted at the species level in order to obtain biologically meaningful understanding on evolutionary patterns. In this study, I began by first finding morphological (dental) characters that can be used to identify each of the five species (*H. paulus, H. lepidus, H. marshi, H. despiciens,* and *H. minisculus*) recognized in the Bridgerian by Gazin (1968) *other than* size and stratigraphic occurrence.

Body Size Estimation

Based on studies of extant primates, Gingerich et al. (1982) established a general empirical relationship between the size of molars and body size in primates (with an exception of tarsiers). The relationship yields a coefficient of correlation (r^2) value of >0.95 according to the geometric scaling model. As a body size estimator, the dentition was primarily used because teeth tend to be preserved more frequently than other body parts and thus allow for a larger dataset. The dentition is not only more readily available, but also, species diagnosis is often based on dental characters (Gingerich, 1974), so it is the best material on which to estimate body size of an individual. This practice is further validated by the study of Sears et al. (2008) who used the extant and Miocene platyrrhines to show that dental variables outperform other cranial or postcranial variables in their ability to predict body mass.

Only the teeth of known position were used in this analysis. Measurements were taken at the maximum buccolingual tooth width and mesiodistal tooth length of upper and lower first and second molars (only for the *Notharctus* sample for m2/M2) using a digital

caliper. Three readings were recorded for width and length and the average and standard deviation were calculated. Since the allometric relationship of tooth size to body mass is exponential, an exponential equation that is log transformed is used in the following form: log Y = log b + a log X, where Y = tooth size, b = constant, a = allometric scaling coefficient, and X = body mass. For primates, I used values for a and b that were empirically determined by Gingerich et al. (1982). The values used for slope and intercept of each tooth position are 1.62 (1.37) and 2.72 (3.49) for M1 (M2), respectively. Similarly for the lower dentition, slope was 1.49 (1.31) and intercept was 3.55 (3.92) for m1 (m2), respectively. The data for *Notharctus* and *Hyopsodus* are provided in Table 3.2 and Table 3.3, respectively.

RESULTS

Phylogenetic Analysis of *Notharctus*

Five distinct groups of *Notharctus* are recognized in the phylogenetic analysis based on 48 dental morphological characters (Table 3.4). The preferred phylogenetic hypothesis is the majority-rule consensus tree that was chosen from 100 trees that were produced by the heuristic search in Mesquite (Figure 3.1). In this tree, all of the *Notharctus* specimens formed one monophyletic ingroup. The tree length was 164, and the consistency index and retention index were 0.341 and 0.698, respectively. Since this phylogenetic analysis was performed on individual specimens rather than at a higher taxonomic rank such as species, individual variations within populations are likely to not only exist but also to have played a role in the phylogenetic analysis.

The five distinct clusters branching at nodes 153, 41, 73, and 102 (labeled in Figure 3.1) included the holotype of *N. tenebrosus, N. robustior, N. robinsoni,* and *N. pugnax*, respectively, and the individual specimens that were found within those clades were referred to as the species of the holotype with which they were found. The most basal paraphyletic group was without any type material, so at present, it is referred to as *N.* sp. indeterminate (*N.* sp. indet.). There are 17 specimens of *N. tenebrosus*, 26 *N. pugnax*, 14 *N. robinsoni*, 12 *N. robustior*, and 18 *N.* sp. indet. According to the phylogenetic result, *N.* sp. indet. is basal to all the other species of *Notharctus*, followed by *N. tenebrosus, N. robustior,* leaving *N. robinsoni* and *N. pugnax*. It is not my goal here to infer a phylogenetic relationship among these species, but the phylogenetic position of *N. robinsoni* is interesting. Based on its temporal position and fused mandibular symphysis, it had been suggested by Gingerich (1979) to be ancestral to all the other species of *Notharctus*, however, in this tree, *N. robinsoni* is shown to be one of the most derived clades. The characters that characterize major branching nodes are summarized in Table 3.5. According to the phylogenetic analysis of the individual specimens, all five species of *Notharctus* were present in Bridger B, C and D strata. This is in contrast with the finding of previous studies in which each species was found to be present only in a single biozone (Gingerich, 1979; Gunnell, 1998).

Body Size Analysis of *Notharctus*

In the following, body size data are analyzed within the framework of the species identification described above. As shown in bivariate plots (Figure 3.2) of the length and width of m1 and m2 of all the *Notharctus* specimens, there are no significant size discontinuities between the species as recognized by the discrete dental characters,

suggesting that the species of *Notharctus* cannot be diagnosed on the size data alone. This result questions the validity of what is a common and generally accepted practice of diagnosing *Notharctus* species based on size differences. Furthermore, the result shown here conflicts with the previously known size relationship of *Notharctus*, in which *N. tenebrosus* was the smallest, followed by *N. robinsoni*, and *N. pugnax/N. robustior* in the ascending order (Gingerich, 1979).

In order to analyze the temporal size change, the Bridger Formation was divided into three major time bins, Bridger B, C, and D, which are the lithological units in which the fossils were found (Figure 1.2). According to the chronostratigraphic work presented in Chapter 2, these time bins together represent ~1.7 myr, but are likely not of equal duration. Bridger B and Bridger C are likely to have had sedimentation rate twice as fast as Bridger D, and thus, Bridger D represents greater time span than either Bridger B and Bridger C. Body size changes of each species of *Notharctus* over the duration of the Bridger Formation are shown in Figure 3.3. The data are log transformed to remove variability due to different absolute body sizes of the individuals. Student's t-test was conducted on the dataset to test for statistically significant changes in the body size between the time bins (Table 3.6). Statistically significant size increase was found for Bridger B/C and Bridger B/D among *N. pugnax. N. robustior* showed a statistically significant change toward larger size between Bridger B and C, and finally, *N.* sp. indet. showed a statistically significant increase for Bridger B/C and Bridger B/D. At the generic level, there is a statistically significant directional trend towards larger body size for Bridger B/C and Bridger B/D. For *N. robinsoni* and *N. tenebrosus*, body size changes

across stratigraphic intervals were not considered because most of the specimens are from Bridger B. The temporal body size evolution of all five species is shown in Figure 3.4.

When viewed in terms of the distribution of body size groups, there is a shift in the most common body size among *Notharctus* from Bridger B, C and to D (Figure 3.5). During the Bridger B interval, about half of the specimens were in the range of 2000-4000 g, and the largest body size present was lower than 8000 g. However in Bridger C, the most common body size range increases to 4000-6000 g, and the smallest body size range (2000-4000 g) that was most common in Bridger B becomes least common, and more than half of the Bridger C specimens are larger than 6000 g. Also noteworthy is that in Bridger C, every body mass group is represented. In Bridger D, the individuals with body size of 2000-4000 g no longer exist, and the most common size range moves up even more to 6000-8000 g. More than half of the Bridger D specimens are larger than 8000 g, while the body sizes less than 6000 g are almost absent in the Bridger D specimens.

Aside from body size, the species composition also changes over the course of the Bridger Formation (Figure 3.6). In Bridger B and C, the percentage represented by each species in each time bin is relatively even. However, in Bridger D, more than half of the genus is represented by just one species (*N. pugnax*), an increase achieved at the expense of the decrease in relative abundances of *N. tenebrosus, N. robustior,* and *N.* sp. indet. Furthermore, during Bridger D, *N. pugnax* not only dominates the *Notharctus* population, but also, it is the sole constituent of the largest body size bin (10000-12000 g). The observed abundance and dominance of the largest *N. pugnax* during Bridger D is an

indication that there was a selective pressure that favored large body size towards the end of the Bridgerian NALMA.

The range of the estimated body size found within each bio-zone is different for the Bridger B, C and D. While the spread could be influenced by the sampling density, coefficient of variation (CV) can be used to assess the dispersion across the bio-zones (Figure 3.7). The CV in overall *Notharctus* body size estimates varies from 0.13 in Lower D to 0.57 in Middle D. When viewed by species, The CV of body mass for each species is 0.31, 0.29, 0.52, 0.30 and 0.37 for *N. tenebrosus, N. pugnax, N. robustior, N. robinsoni*, and *N.* sp. indet., respectively, indicating that *N. robustior* has the largest spread in body size whereas *N. pugnax* has the least spread. The CV of *N. pugnax* and *N. tenebrosus* decreases over time from Bridger B to D, whereas that of *N. robustior* shows an increase over the same interval. In any case, some of the *Notharctus* species have CVs that are too high to typically be considered a single species, leaving a possibility that dental morphological characters alone may not be sufficient to differentiate all species. For the other species, due to their smaller sample sizes, it is either not possible to calculate a CV or the data are insufficient to recognize a trend.

Species identification of *Hyopsodus*

By comparison with the type material, every specimen of *Hyopsodus* from the Bridger Formation was identified based on a set of criteria related to the presence or absence of cingulae on lower molars (Table 3.7). *H. paulus* was recognized based on the absence of hypoconulid-entoconulid cingulum on m3. *H. minisculus* was characterized by the absence of anterior-buccal cingulum on m1 and m2, and also by the absence of hypoflexid on all lower molars. *H. lepidus* was diagnosed based on the absence of

anterior-buccal cingulum on m1. *H, despiens* was distinctive in having entoconid-lingual cingulum on m2 and m3. It was also characterized by the presence of cingulum between metaconid and entoconid on all lower molars. *H. marshi* could not be characterized by the presence or absence of cinguli, but was noted for its general robust appearance. Of the 71 specimens studied, more than half of them were identified to be *H. despiciens, H. lepidus,* and *H. minisculus*. *H. lepidus, H. minisculus,* and *H. paulis* are present throughout the Bridger B-D, but *H. despiciens* and *H. marshi* are restricted to only the Upper Bridger (C+D) and Bridger B, respectively. *H. despiciens* from the Upper Bridger shows the most complex tooth morphology, as characterized by a cingulum on the buccal side, a feature not found in any other *Hyopsodus* species from the Bridger Formation. In contrast, *H. minisculus*, which is the only species found in Bridger B1, was characterized by the least complex tooth morphology as seen by the lack of cingulae in areas where a cingulum was present in all other species.

Body Size Analysis of *Hyopdosus*

Bivariate plots of length against width show that no distinct size groups can be recognized in the populations of Bridgerian *Hyopsodus*, other than that there are six outliers that are smaller than those in the main cluster (Figure 3.8). The lack of distinct size groups argues against the traditional use of size of m1 as a reliable basis for diagnosing the species of *Hyopsodus*. The CVs for the occulusal area of m1 in the five recognized species varied between 0.12 and 0.19, and this is in general agreement with the within-sample variability of extinct and extant mammalian species (Gingerich, 1974; Table 3.8). *H. minisculus* and *H. marshi* show the largest spread in the size (CV = 0.19), whereas *H. despiciens* shows the minimum spread (CV = 0.12).

Since there is no close extant relative of *Hyopsodus* to be used as an analogue for developing an empirical relationship between the body size and tooth area, the body mass was not estimated for *Hyopsodus*, but instead, the occlusal area of m1 was used as a proxy for the body size. In terms of the evolution of m1 size, when compared between three time bins (Bridger B, C and D) at the species level, only *H. lepidus* and H. *despiciens* show a statistically significant directional change within the sampled interval (Figure 3.9, Table 3.9). When compared at the generic level between the three time bins, Student's t-test shows that a significant change has occured between Bridger B and Bridger D (Figure 3.10).

The early equid *Orohippus* was also included in this study, but morphology based species identifications were not possible at this time, so analysis of its body size change was carried out at the generic level only. Student's t-test results were 0.78, 0.50, and 0.08 for Bridger B/C, C/D and B/D, respectively, and reveal that there was no significant size change during the study interval.

DISCUSSION

During the time of deposition of the Bridger Formation, the pCO_2 was at one of the lowest in the Paleogene, corresponding to the interval just subsequent to a sudden and significant drop in pCO_2 by ~3000 p.p.m. (Pearson and Palmer, 2000). The pCO_2 remained at that level for about 3 myr and then displayed a quick recovery to a level almost as high as the peak-EECO level. During the same period, CO_2 radiative forcing (a measure of global warming) is also estimated to have shown a sharp decline in parallel with the pCO_2. The pCO_2 level recorded during the Bridgerian time interval is

comparable with the levels recorded for the Neogene, which was in an icehouse condition unlike middle Eocene. Thus, most of the Bridgerian fauna was present in a period of very low pCO_2. Although there are no data to show how much cooling actually occurred in the Bridger Basin, the stable isotopic record from the equatorial Atlantic shows that δO_{18} drops from ~ -0.5 to -0.1 per mill during the interval between 49-47 Ma (Turner et al., 2014).

The morphology-based species identification of *Notharctus* reveals different patterns of body size change than had previously been known. Three of the five (*N. pugnax, N. robustior*, and *N.* sp. indet.) species show a statistically significant increase in body size over the course of the Bridger B, C and D, and the observed trend is consistent with the preposition made by Bergmann (1847). However, there is likely multiple causation responsible for the body size shift towards larger size, and factors other than temperature are considered here. For example, body mass is known to correlate with diet, population density, home range size, behavioral adaptations, community structure and biogeography to name a few (Damuth and MacFadden, 1990b). Of these, it has been shown that the forested habitat became more open towards the Uintan NALMA (Townsend et al., 2000), and it is conceivable that in response to the changing habitat, there was selection towards larger bodied individuals to forage more energetically-efficiently within a forest canopy that was becoming scarcer. Another possible factor is the introduction of competition. The first appearance datum of omomyine and anaptomorphine primates took place in Br3. These omomyids were smaller in body size than their adapid counterparts, and because of the similar substrate and diets they share with *Notharctus* (Beecher, 1983), it is possible that their appearance led to resource

partitioning and ultimately selection for larger individuals among the population of *Notharctus.*

Previous stratophenetic analyses proposed that there was a new species of *Notharctus* appearing in every biozone. For example, Gingerich (1979) suggested based on the size information that *N. robinsoni* was present in the Bridger A, which gave rise to *N. pugnax* and *N. tenebrosus* in Bridger B and finally in Bridger D, *N. pugnax* gave rise to *N. robustior*. My analysis is at odds with the previous phylogenetic hypothesis in that, it suggests that all the Bridgerian species of *Notharctus* already were present in Bridger B and remained until Bridger D. Thus, it appears that several species lived sympatrically and evolved side by side through time, rather than species getting replaced by (or evolved into) another species over time. The scenario presented previously by Gingerich (1979) suggests that cladogenetic differentiation was at work, whereas my result is more indicative of the anagenetic evolutionary model. The available data shows that in some stratigraphic intervals, there was no significant body size change, and thus it may seem to represent evolutionary stasis. However, there is also ample evidence that indicates significant body size change, so according to the data presented herein, the species of *Notharctus* in general show a combination of both stasis and directional change at the scale of biozones within the ~2 myr interval. Finally, the patterns of body size change are independent of specific localities, thus they are not result of migration through time in response to the changing climate.

Hyopsodus, on the other hand, displays different evolutionary patterns in terms of body size shift. According to the character-based species identification, the five recognized species of Bridgerian *Hyopsodus* generally are characterized by a lack of

significant body size change in the ~2 million years. This result is in agreement with that of West (1979), who showed a similar pattern at the generic level. The convergence of results from these two studies demonstrates that the pattern of stasis is a robust characteristic among the Bridgerian *Hyopsodus* populations. In view of the middle Eocene climate, the observed pattern of *Hyopsodus* body size evolution indicates that unlike *Notharctus*, the climate cooling either did not affect *Hyopsodus* as much or was buffered by some mechanisms. As Orcutt and Hopkins (2013) demonstrated among the Oligo-Miocene mammals in the northwestern U.S., the body size of *Hyopsodus* instead may have been controlled by a combination of environmental and ecological factors other than temperature. During Br2, the overall mammalian species diversity was on a dramatic decline in the Bridger Basin (Woodburne et al., 2009b), but *Hyopsodus* represented 61% of the entire fauna in species abundance. This clearly indicates that environmental conditions were in favor of *Hyopsodus.* The cool, arid, and seasonal condition are likely to have affected the length of growing season, and caused reduction in fruit production (Janis, 2007). Furthermore as is evidenced by the addition of taxa such as *Amynodon* and *Tetheopsis* in Br3, forested area was becoming scarcer. In face of these significant ecological changes, many of the mammalian taxa deteriorated, but *Hyopsodus* thrived, perhaps because they were equipped with advanced brain structure associated with the use of terrestrial echolocation (Orliac et al., 2012). *Hyopsodus* have been reconstructed to be herbivorous living in burrows and to a lesser extent trees as well (Matthews, 1928; Gazin, 1968; Williamson and Lucas, 1992). Their ability to move around, rest and forage both on the ground and in the trees might have also given them further advantage in adapting to the loss of densely canopied forested area than did other taxa. Also, living in

a subterranean habitat, the cooling climate may not have affected them as much as other taxa living above ground. At any rate, it is reasonably certain that *Hyopsodus* exploited new ecological opportunities that opened up as the result of the increased extinction in other taxa. In this study, *Hyopsodus* mostly did not show the body size increase at the intraspecific level, contrary to Bergmann's rule, but considering that there was an unusually skewed distribution of *Hyopsodus*, its body size evolution may be an exception to the rule. Finally, that the arboreal mammal (*Notharctus*) showed most significant size increase is interesting, and it may indicate that the loss or fragmentation of the forested habitat may be an important causal factor for the observed body size shit during the Bridgerian NALMA.

CONCLUSIONS

Evolution of size change in the dentitions of the Bridgerian-aged *Notharctus*, *Hyopsodus* and *Orohippus* was investigated to test the hypothesis regarding the interrelationship between climate (temperature) and body size. According to Bergmann's rule, the Bridgerian faunal elements, which were present during the period of global cooling following the peak of the EECO, are expected to have increased in size. Using character-based species identification, the analyses show that *Notharctus* at the generic level shows a statistically significant trend towards larger body size between Bridger B/C and Bridger B/D. When viewed at the intraspecific level, the overall body size increase is recognized for *N. pugnax, N. robustior and N.* sp. indet., but not for *N. tenebrosus*. In contrary, of the five species of *Hyopsodus,* as were diagnosed based on character based species identifications, only *H. despiciens* and *H. lepidus* show a statistically significant

trend of directional body size change within species. At the generic level, a statistically significant body size increase was recognized between Bridger B/D. In constrast, *Orohippus* shows a lack of significant size increase at the generic level. While this study was handicapped by the uneven distribution of specimens across the temporal interval of interest, by using morphological characters to diagnose species, it yielded a new perspective on body size evolution of the mammalian taxa that is not biased by *a priori* notion about the relative size of species. As a result, it illustrates a complex nature of the effect of climate change even within a single species. To better understand the causal relationship between the climate change and biotic response among the Bridgerian mammals, future research should be geared towards obtaining similar data from more taxa characterized by different ecomorphs, and more importantly, more local or regional (as opposed to global) climatic data from the Rocky Mountain intermontane basins.

REFERENCES CITED

Ashton, K.G., Tracy, M.C., and de Queiroz, A., 2000, Is Bergmann's rule valid for mammals?: The American Naturalist, v. 156, p. 390-415.

Ashton, K.G., 2002, Patterns of within-species body size variation of birds: Strong evidence for Bergmann's rule: Global Ecology and Biogeography, v. 11, p. 505-523.

Alroy, J., 2003, Taxonomic inflation and body mass distributions in North American fossil mammals: Journal of Mammalogy, v. 84, p. 431-443.

Beecher, R.M., 1983, Evolution of the mandibular symphysis in Notharctinae (Adapidae, Primates): International Journal of Primatology, v. 4, p. 99-112.

Bergmann, C., 1847, Uber die verhältnisse der wärmeoökonomie der thiere zu ihrer grösse: Go¨ttinger Studien, v. 3, p. 595-708.

Blackburn, T.M. and Hawkins, B.A., 2004, Bergmann's rule and the mammal fauna of northern North America: Ecography, v. 27, p. 715-724.

Clyde, W.C., Sheldon, N.D., Koch, P.L., Gunnell, G.P., and Bartels, W.S., 2001, Linking the Wasatchian/Bridgerian boundary to the Cenozoic Global Climate Optimum: New magnetostratigraphic and isotopic results from South Pass, Wyoming: Palaeogeography Palaeoclimatology Palaeoecology, v. 167, no. 1-2, p. 175-199.

Daufresnea, M., Lengfellnera, K., and Sommera, U., 2009, Global warming benefits the small in aquatic ecosystems: PNAS, v. 106, p. 12788-12793.

Damuth, J. and MacFadden, B.J., 1990a, Body size in mammalian paleobiology: Cambridge, Cambridge University Press, 397 p.

Damuth, J. and MacFadden, B.J., 1990b, Introduction: body size and its estimation, *in* Damuth, J., and MacFadden, B.J., eds., Body size in mammalian paleobiology: Cambridge, Cambridge University Press, p. 1-10.

Gardner, J.L., Peters, A., Kearney, M.R., Joseph, L., and Heinsohn, R., 2011, Declining body size: a thied universal response to warming?: Trends in Ecology and Evolution, v. 26, p. 285-291.

Gazin, C.L., 1958, A review of the middle and upper Eocene primates of North America: Smithsonian Miscellaneous Collections, v. 136, p. 1-112.

Gazin, C.L., 1968, A new primate from the Torrejon Middle Paleocene of the San Juan Basin, New Mexico: Proceedings of The Biological Society of Washington, v. 81, p. 629-634.

Gingerich, P.D., 1974, Size variability of the teeth in living mammals and the diagnosis of closely related sympatric fossil species: Journal of Paleontology, v. 48, p. 895-903.

Gingerich, P.D., and Simons, E.L., 1977, Systematics, phylogeny, and evolution of early Eocene Adapidae (Mammalia, primates) in North America: Contributions from the Museum of Paleontology, v. 24, p. 245-279.

Gingerich, P.D., 1979, Phylogeny of middle Eocene Adapidae (Mammalia, Primates) in North America: *Smilodectes* and *Notharctus*: Journal of Paleontology, v. 53, p. 153-163.

Gingerich, P.D., 1994, New species of *Apheliscus*, *Haplomylus*, and *Hyopsodus* (Mammalia, Condylarthra) from the late Paleocene of southern Montana and early Eocene of northwestern Wyoming: Contributions from the Museum of Paleontology, University of Michigan, v. 29, p. 119-134.

Gingerich, P.D., Smith, B.H., and Rosenberg, K., 1982, Allometric scaling in the dentition of primates and prediction of body weight from tooth size in fossils: American Journal of Physical Anthropology, v. 58, p. 81-100.

Gingerich, P.D., 2006, Environment and evolution through the Paleocene-Eocene thermal maximum: Trends in Ecology and Evolution, v. 21, p. 246-253.

Granger, W., and Gregory, W.K., 1917, A revision of the Eocene primates of the genus *Notharctus*: American Museum of Natural History Bulletin, v. 37, p. 841-859.

Gunnell, G.F., 1997, Wasatchian-Bridgerian (Eocene) paleoecology of the western interior of North America: Changing paleoenvironments and taxonomic composition of omomyid (Tarsiiformes) primates: Journal of Human Evolution, v. 32, p. 105–132.

Gunnell, G.F., 1998, Mammalian fauna from the lower Bridger Formation (Bridger A, early middle Eocene) of the southern Green River Basin, Wyoming: Contributions from the Museum of Paleontology, University of Michigan, v. 30, p. 83-130.

Gunnell, G.F., and Bartels, W.S., 2001, Basin margins, biodiversity, evolutionary innovation, and the origin of new taxa, *in* Gunnell, G.F., ed., Eocene Biodiversity: Unusual Occurrences and Rarely Sampled Habitats: New York, New York, Kluwer Academic/Plenum Publishers, p. 404-432.

Gunnell, G.F., 2002, Notharctine primates (Adapiformes) from the early to middle Eocene (Wasatchian-Bridgerian) of Wyoming: transitional species and the origins of *Notharctus* and *Smilodectes*: Journal of Human Evolution, v. 43, p. 353-380.

Gunnell, G.F., Murphey, P.C., Stucky, R.K., Townsend, K.E., Robinson, P, Zonneveld, J.P., and Bartels, W.S., 2009, Biostratigraphy and biochronology of the latest Wasatchian, Bridgerian, and Uintan North American Land-Mammal "Ages.", *in* Albright, L.B. III, ed., Papers on Geology, Vertebrate Paleontology, and Biostratigraphy in Honor of Michael O. Woodburne: Museum of Northern Arizona, Flagstaff, Arizona, Museum of Northern Arizona Bulletin, v. 65, p. 279-330.

Hamrick, M.W., and Alexander, J.P., 1996, The hand skeleton of *Notharctus tenebrosus* (Primates, Notharctidae) and its significance for the origin of the primate hand: American Museum Novitates, no. 3182, p. 1-20.

Janis, C., 2007, Artiodactyl paleoecology and evolutionary trends, *in* Prothero, D.R., and Foss, S.E., eds., The evolution of artiodactyls: The Johns Hopkins University Press, Baltimore, p. 292-315.

Matthew, W.D., 1909, The carnivora and insectivora of the Bridger Basin, middle Eocene: American Museum of Natural History Memoirs, v. 9, p. 289-567.

Matthew, W.D., 1928, The evolution of mammals in the Eocene: Proceedings of the Zoological Society of London, v. 1927, p. 947-985.

Meiri, S., and Dayan, T., 2003, On the validity of Bergmann's rule: Journal of Biogeography, v. 30, p. 331-351.

Millien, V., Lyons, S.K., Olson, L., Smith, F.A., Wilson, A.B., and Yom-Tov, Y., 2006, Ecotypic variation in the context of global climate change: revisiting the rules: Ecology Letters, v. 9, p. 853-869.

Murphey, P.C., and Evanoff, E., 2007, Stratigraphy, fossil distribution and depositional environments of the upper Bridger Formation (middle Eocene), southwestern Wyoming: Wyoming State Geological Survey Report of Investigation, scale 1:50,000, 1 sheet.

Orcutt, J.D., and Hopkins, S.S.B., 2013, Olico-Miocene climate change and mammal body-size evolution in the northwest United States: a test of Bergmann's Rule: Paleobiology, v. 39, p. 648-661, DOI: 10.1666/13006.

Orliac, M.J., Argot, C., and Gilissen, E., 2012, Digital cranial endocast of *Hyopsodus* (Mammalia, "Condylarthra"): A case of Paleogene terrestrial echolocation?: Plos One, v. 7, p. e30000.

Pearson, P.N., and Palmer, M.R., 2000, Atmospheric carbon dioxide over the past 60 million years: Nature, v. 406, p. 695-699.

Robinson, P., 1957, The species of *Notharctus* from the middle Eocene: Postilla, v. 28, p. 1-27.

Robinson, P., Gunnell, G.F., Walsh, S.L., Clyde, W.C., Storer, J.E., Stucky, R.K., Froehlich, D.J., Ferrusquia-Villafranca, I., and McKenna, M.C., 2004, Wasatchian through Duchesnean biochronology, *in* Woodburne, M.O., ed., Late Cretaceous and Cenozoic mammals of North America : Biostratigraphy and geochronology: New York, Columbia University Press, p. 106-155.

Schmidt-Nielsen, K., 1984, Scaling: why is animal size so important?: Cambridge, Cambridge University Press, 241 p.

Sears, K.E., Finarelli, J.A., Flynn, J.J., and Wyss, A.R., 2008, Estimating body mass in New World "monkeys" (Platyrrhini, Primates), with a consideration of the Miocene platyrrhine, *Chilecebus carrascoensis*: American Museum Novitates, no. 3617, p. 1-29.

Secord, R., Gingerich, P.D., Smith, M.E., Clyde, W.C., Wilf, P. and Singer, B.S., 2006, Geochronology and mammalian biostratigraphy of middle and upper Paleocene continental strata, Bighorn Basin, Wyoming: American Journal of Science, v. 306, p. 211-245.

Townsend, K.E.B., Rasmussen, D.T., Murphey, P.C., Evanoff, E., 2010, Middle Eocene habitat shifts in the North American Western interior: a case study: Palaeogeography, Palaeclimatology, Palaeoecology, v. 297, p. 144-158.

Turner, S.K., Sexton, P.F., Charles, C.D., and Norris, R.D., 2014, Persistence of carbon release events through the peak of early Eocene global warmth: Nature Geoscience, v. 7, p. 748-751.

West, R.M., 1976, Paleontology and geology of the Bridger Formation, southern Green River Basin, southwestern Wyoming. Part 1. History of field work and geological setting: Milwaukee Public Museum Contributions in Biology and geology, v. 7, p. 1-12.

West, R.M., 1979, Paleontology and geology of the Bridger Formation, southern Green River Basin, southwestern Wyoming. Part 3. Notes on *Hyopsodus*: Milwaukee Public Museum Contributions in Biology and geology, v. 25, p. 1-52.

Williamson, T.E., and Lucas, S.G., 1992, Fossil mammals and the early Eocene age of the San Jose Formation: New Mexico Geological Society Guidebook, v. 43, p. 311-316.

Wood, H.E., Chaney, R.W., Clark, J., Colbert, E.H., Jepsen, G.L., Reeside, J.B., and Stock, C., 1941, Nomenclature and correlation of the North American continental Tertiary: Geological Society of America Bulletin, v. 52, p. 1-48.

Woodburne, M.O., Gunnell, G.F., and Stucky, R.K., 2009a, Climate directly influences Eocene mammal faunal dynamics in North America: Proceedings of the National Academy of Sciences, v. 106, p. 13399-13403.

Woodburne, M.O., Gunnell, G.F., and Stucky, R.K., 2009b, Land mammal faunas of North America rise and fall during the early Eocene: Denver Museum of Nature and Science Annals, no. 1, 78 p.

Zachos, J., Pagani, M., Sloan, L., Thomas, E., and Billups, K., 2001, Trends, rhythms, and aberrations in global climate 65 Ma to present: Science, v. 292, p. 686-693.

Table 3.1. *Notharctus* character state list.

(1) p4 external cingula – strong (0); partial (1); absent (2)
(2) p4 metaconid – large (0); weak/absent (1)
(3) p4 paraconid – large (0); weak/absent (1)
(4) m1 entoconid notch – present (0); absent (1)
(5) m1 accessory cusp on paracristid – present (0); absent (1)
(6) m1 external cingulum – crenulate (0); not crenulate (1)
(7) m1 external cingulum – complete around talonid (0); partial (1); absent (2)
(8) m1 cristid obliqua – prominent (0); weak (1)
(9) m1 cristid oblique – continuous with metaconid (0); not continuous with metaconid (1)
(10) m2 entoconid notch – present (0); absent (1)
(11) m2 paraconid – cuspate (0); crescent (1); weak/absent (2)
(12) m2 cristid obliqua – prominent (0); weak (1)
(13) m2 external cingulum – crenulate (0); not crenulate (1)
(14) m2 external cingulum – complete around talonid (0); partial (1); absent (2)
(15) P3 shape – equilateral triangle (0); not equilateral triangle (1)
(16) P4 external cusp – divided (0); not divided (1)
(17) M1 internal border – no constriction (0); constricted
(18) M1 shape in outline – quadrate (0); not quadrate (1); square/round (2)
(19) M1 mesostype – large/cuspate (0); large/crescentic (1); small (2); absent (3)
(20) M1 paraconule – distinct to the side (0); distinct to the center (1); absent/weak (2)
(21) M1 metaconule – distinct (0); weak (1); absent (2)
(22) M1 external cingula – crenulate (0); not crenulate (1); not distinct (2)
(23) M1 metastyle – distinct (0); weak/absent (1)
(24) M1 parastyle – distinct (0); weak/absent (1)
(25) M1 internal cingulum – missing in center (0); continuous (1)
(26) M1 hypocone – present at equal height (0); present but not as tall (1); small (2); absent (3)
(27) M2 internal border – no constriction (0); constricted (1)
(28) M2 internal cingulum – heavy (0); weak (1)
(29) M2 shape in outline – quadrate (0); not quadrate (1)
(30) M2 mesostyle – large/cuspate (0); large/crescentic (1); small (2); absent (3)
(31) M2 metaconule – distinct (0); weak (1)
(32) M2 paraconule – distinct to the side (0); distinct to the center (1); absent/weak (2)
(33) M2 external cingula – crenulate (0); not crenulate (1); not distinct (2)
(34) M2 metastyle – distinct (0); weak/absent (1)
(35) M2 parastyle – distinct (0); weak/absent (1)
(36) M2 internal cingulum – missing in center (0); continuous (1)

(37) M2 hypocone – present at equal height (0); present but not as tall (1); small (2); absent (3)
(38) symphysis – unfused (0); fused (1)
(39) p4 protoconid – high (0); low (1); absent (2)
(40) m1 ento-metaconid shape – valley (0); wall (1)
(41) m2 ento-metaconid shape – valley (0); wall (1)
(42) m1 relative position of para-metaconid – triangular (0); proximal (1)
(43) m2 relative position of para-metaconid – triangular (0); proximal (1); no paraconid (2)
(44) m3 paraconid – cuspate (0); crescent (1); absent/weak (2)
(45) m3 shape – short (0); long (1)
(46) m3 extra cusp in entoconid region – present (0); absent (1)
(47) M1 internal lobe – vertical (0); sloped (1)
(48) M2 internal lobe – vertical (0); sloped (1)

Table 3.2. Measurement data of *Notharctus* specimens from AMNH and UCM collections.

Specimen ID	Locality	Stratigraphic Level	Lower M1			Lower M2			Upper M1			Upper M2			Average Body Weight (g)
			Avg W	Avg L	Body Wt (g)	Avg W	Avg L	Body Wt (g)	Avg W	Avg L	Body Wt (g)	Avg W	Avg L	Body Wt (g)	
N. tenebrosus															
AMNH11480	Grizzly Butte W		6.45	5.25	6623	7.00	5.65	6233							6428
AMNH13022	Grizzly Butte E	B2	6.23	4.72	2392	6.35	5.09	4785							3588
AMNH134401	Grizzly Butte E	B2	5.22	3.88	981	5.65	4.08	3073	5.40	6.40	4718	5.56	6.77	4724	3374
AMNH11456	LDC	B	5.80	4.54	1831	5.68	4.61	3631							2731
AMNH13026	Mid Cottonwood Creek	B3	6.41	5.13	3217										3217
AMNH5009	Black's Fork	N/A	5.94	4.32	1694	5.93	4.60	3831							2762
AMNH11990	Henrys Fork, BFPO	C2				6.12	5.33	4843							4843
AMNH13023	Mouth of Summer's Dry Creek	C1				5.77	4.94	4058							4058
AMNH11996	Mouth of Summer's Dry Creek	C	6.54	4.96	3075										3075
UCM69304	Loc. 94190	Lonetree Limestone 10.6 m above base of sheet sand beds	7.11	5.41	4837	7.57	5.75	7067							5952
UCM69991	Loc. 95014		6.79	5.02	3480	6.77	5.64	5952							4716
N. pugnax															
AMNH12575	Grizzly Butte E	B2	5.44	5.01	4792	6.04	5.22	4632	6.05	8.32	8676				6033

AMNH13029	Grizzly Butte E	B2	5.29	3.97	3250	5.60	4.16	3116							3183
AMNH14567	Grizzly Butte	B3							5.90	7.31	6755	6.04	8.04	6697	6726
AMNH11452	Church Buttes	N/A	6.16	4.65	5161										5161
AMNH18988	Mid Cottonwood Creek	B3	5.55	4.21	3810				5.25	7.09	5321	5.40	7.67	5386	4839
AMNH12576	5 miles E of Millersville	B4				6.36	4.99	4672							4672
AMNH11461	Millersville	B	6.09	4.59	4977	6.40	4.96	4673							4825
AMNH12010	Henrys Fork, Lonetree	C5							6.62	8.27	9941	6.51	8.74	8321	9131
AMNH11993	Twin Buttes	C5	6.63	5.41	7215	6.50	5.93	6026							6621
AMNH11991	Henrys Fork Hill	N/A							7.03	8.48	11412	7.13	9.58	10688	11050
AMNH11987	Henrys Fork Hill	D4							6.85	8.38	10734	6.99	9.41	10149	10442
AMNH140034	Henrys Fork	N/A										6.66	8.93	8841	8841
AMNH12565	Henrys Fork Hill	D4							6.69	7.90	9389	6.60	8.80	8559	8974
AMNH11995	Henrys Fork Hill	C5				6.94	5.55	6021							6021
AMNH11986	Henrys Fork Hill	C5							6.59	8.44	10199	6.75	8.93	9005	9602
AMNH12564	Henrys Fork Hill	D4	6.28	4.73	5448				6.64	7.63	8768	6.61	8.63	8350	7522
AMNH11982	Henrys Fork, BFPO	C4	6.36	5.39	6745	6.40	5.86	5814	6.78	8.27	10333	7.02	8.97	9561	8113
UCM68955	Loc. 94134	Upper White Limestone							6.67	8.37	10261				10261

UCM69989	Loc. 94135	Upper White Limestone	6.55	5.43	7125	7.08	5.41	5977								6551
UCM91368	Loc. 99021	Lonetree Limestone	6.67	5.41	7280	7.42	5.97	7231								7256
UCM69988	Loc. 95020	2.85 m above base of Lonetree Limestone	7.10	5.63	8480											8480
UCM21463	Loc. 99021	Lonetree Limestone							6.63	8.30	10024					10024
UCM69996	Loc. 94051	Hickey Reservoir Limestone							6.57	8.39	10052	6.72	9.39	9588		9820
UCM68955	Loc. 94134	Upper White Limestone							6.87	8.35	10722					10722
N. robustior																
AMNH18989	Grizzly Butte E	B2	5.03	4.12	3186	5.62	4.26	3229								3208
AMNH11469	Grizzly Butte W	N/A	5.55	4.22	3823	6.00	4.39	3660								3742
AMNH13130	Lower Cottonwood Creek	B3	5.75	4.68	4702	6.18	4.96	4464								4583
AMNH11460	LDC	N/A				6.33	5.26	4975								4975
AMNH12008	Henrys Fork, BFPO	C2				6.56	5.48	5500								5500
AMNH11451	Henrys Fork, Lonetree	N/A	6.58	5.14	6611	6.05	5.51	4982								5796
AMNH11985	Henrys Fork Hill	C5							6.76	8.41	10567	6.87	9.46	9984		10275
AMNH11992	Henrys Fork Hill	D4	6.34	5.04	6074	6.46	5.49	5404				6.63	8.65	8411		6630
AMNH11997	Henrys Fork Hill	C5	6.81	5.32	7324	7.09	5.66	6353								6838
UCM54242	Loc. 94199	Lonetree Limestone							7.57	9.21	14707					14707

N. robinsoni															
AMNH13027	Grizzly Butte E	B2							5.81	7.08	6256				6256
AMNH12002	Grizzly Butte E	B1	5.27	4.00	3268	5.43	4.34	3163							3216
AMNH11464	Grizzly Butte W	N/A				6.13	5.20	4699							4699
AMNH11481	Grizzly Butte W	N/A	5.34	3.58	2825										2825
AMNH18985	Grizzly Butte E	B2	5.32	3.97	3278	5.55	4.42	3334							3306
AMNH14568	Grizzly Butte	B3	5.66	4.35	4119	5.83	4.58	3726							3922
AMNH18990	Grizzly Butte E	B2-3	5.11	4.11	3250	5.42	4.41	3222	5.46	6.07	4409	5.51	6.93	4818	3925
AMNH12578	6 miles S of Granger	B1	5.05	3.84	2886	5.66	4.09	3090	5.29	5.85	3945	5.30	6.94	4577	3625
AMNH11463	Lower Cottonwood Creek	N/A	6.51	5.30	6810										6810
AMNH12001	Cottonwood Creek	B4				6.10	4.52	3886							3886
AMNH12000	Dry Creek	C2	6.09	4.83	5369	6.63	5.11	5089							5229
UCM72421	Loc. 96303	Upper White Limestone	6.31	5.15	6228										6228
***N.* sp. indet.**															
AMNH11466	Grizzly Butte	N/A	5.07	3.72	2769	5.26	3.96	2691							2730
AMNH12586	Grizzly Butte W	B2				5.92	4.50	3714							3714
AMNH11472	Grizzly Butte W	N/A				5.95	4.35	3577							3577
AMNH129384	Cosmic Hill	B2	5.02	3.70	2707										2707
AMNH11467	Grizzly Butte E	N/A	5.16	3.88	3027	5.54	3.97	2890							2958
AMNH11453	LDC	B	5.55	4.51	4221										4221

AMNH11449	Lower Cottonwood Creek	N/A							5.87	7.47	6938	6.21	8.25	7207	7073
AMNH11454	Millersville	N/A	5.96	4.24	4282										4282
AMNH18987	Mid Cottonwood Creek	B4				6.60	5.14	5098	6.11	7.72	7809	6.35	8.62	7891	6933
AMNH13031	LDC	B2	4.80	4.14	2993	5.22	4.35	3013							3003
AMNH12588	Sage Creek Spring	C	5.92	4.93	5307	6.23	5.24	4848							5077
AMNH12009	Henrys Fork	C3	5.74	4.76	4810	6.09	4.83	4229							4520
AMNH12006	Henrys Fork Hill	D4				7.16	5.82	6675							6675
UCM72418	Loc. 96303	Upper White Limestone	6.53	5.30	6841	7.05	5.53	6117							6479
UCM69983	Loc. 95017	Hickey Reservoir Limestone	6.71	5.94	8443	7.57	6.34	8031							8237
UCM94501	Loc. 2000054	15.1 m above base of Henrys Fork Limestone	6.46	5.14	6432	6.99	5.42	5892							6162

NOTE: Values for slope used are 1.49, 1.31, 1.62, and 1.37, while values for intercept used for m1, m2, M1 and M2 are 3.55, 3.92, 2.72, and 3.49, respectively (Gingerich, 1982).

Table 3.3. Measurement data of *Hyopsodus* m1 specimens from AMNH collections.

Specimen ID	Species	Strat level	Length (mm)	Width (mm)	LN (L*W)	Strat level (m)	Strat error (m)
19214g	*H. despiciens*	B2	3.76	3.08	2.45	84	21
13067	*H. despiciens*	B3	3.59	2.88	2.34	142.5	37.5
11921	*H. despiciens*	C1	3.67	2.91	2.37	268.5	34.5
12483	*H. despiciens*	C2	4.39	3.77	2.81	329.5	26.5
11933	*H. despiciens*	C2	4.18	3.22	2.60	329.5	26.5
11952	*H. despiciens*	C4	3.38	2.94	2.30	329.5	26.5
11917	*H. despiciens*	C5	4.1	3.38	2.63	377	21
11903	*H. despiciens*	C5	4.08	3.17	2.56	377	21
11906	*H. despiciens*	C5	3.97	3.19	2.54	377	21
12481	*H. despiciens*	C5	4.11	3.47	2.66	377	21
19221	*H. despiciens*	C5	3.78	3.11	2.46	377	21
11892	*H. despiciens*	D2	4.31	3.34	2.67	417	19
11957	*H. despiciens*	D2	4.17	3.46	2.67	417	19
11938	*H. despiciens*	D2	4.13	3.3	2.61	417	19
11940	*H. despiciens*	D3	4.1	3.18	2.57	468	32
12473	*H. despiciens*	D3	3.89	3.27	2.54	468	32
11883	*H. despiciens*	D4	3.74	3.02	2.42	523.5	23.5
11890	*H. despiciens*	D4	3.79	3.21	2.50	523.5	23.5
11970	*H. despiciens*	D4	4.02	3.45	2.63	523.5	23.5
12486	*H. despiciens*	D4	4.1	3.21	2.58	523.5	23.5
11969	*H. despiciens*	D4	3.87	3.21	2.52	523.5	23.5
11888a	*H. despiciens*	D4	3.72	3.05	2.43	523.5	23.5
11888b	*H. despiciens*	D4	3.91	3.07	2.49	523.5	23.5
11877 (Holo)	*H. despiciens*	D5	4.36	3.37	2.69	523.5	23.5
11934	*H. despiciens*	D5	4.16	3.53	2.69	523.5	23.5
11932	*H. despiciens*	D5	3.83	3.15	2.49	523.5	23.5
10994	*H. lepidus*	B2	3.47	3.09	2.37	121.5	58.5
11344	*H. lepidus*	B2	3.84	3.23	2.52	121.5	58.5
10981	*H. lepidus*	B2	3.58	3.04	2.39	121.5	58.5
11394	*H. lepidus*	B2	4.01	3.38	2.61	121.5	58.5
11373	*H. lepidus*	B2	3.99	3.22	2.55	121.5	58.5
19214f	*H. lepidus*	B2	3.51	2.91	2.32	121.5	58.5
19214b	*H. lepidus*	B2	3.69	3.2	2.47	121.5	58.5
13058	*H. lepidus*	B3	3.69	3.23	2.48	121.5	58.5
13067	*H. lepidus*	B3	3.59	2.88	2.34	121.5	58.5
12480	*H. lepidus*	B3	3.68	3.21	2.47	121.5	58.5
13062	*H. lepidus*	B5	3.55	3.03	2.38	207	27
13066	*H. lepidus*	B5	3.28	2.73	2.19	207	27

11908	*H. lepidus*	C2	4	3.44	2.62	329.5	26.5
11901	*H. lepidus*	C3	3.97	3.3	2.57	329.5	26.5
11900 (holo)	*H. lepidus*	C4	3.66	2.9	2.36	329.5	26.5
93385	*H. lepidus*	C4	3.23	2.59	2.12	329.5	26.5
11959 (star)	*H. lepidus*	C4	3.37	2.1	1.96	329.5	26.5
12485	*H. lepidus*	C5	3.62	2.88	2.34	377	21
11918	*H. lepidus*	C5	4	3.33	2.59	377	21
11892	*H. lepidus*	D2	4.31	3.34	2.67	417	19
11957	*H. lepidus*	D2	4.17	3.46	2.67	417	19
12473	*H. lepidus*	D3	3.89	3.27	2.54	468	32
11970	*H. lepidus*	D4	4.02	3.45	2.63	523.5	23.5
11888	*H. lepidus*	D4	3.72	3.05	2.43	523.5	23.5
12479	*H. lepidus*	D4	3.65	3.21	2.46	523.5	23.5
11397	*H. marshi*	B2	3.66	3.17	2.45	121.5	58.5
11879 (ref)	*H. marshi*	C2	4.42	3.71	2.80	329.5	26.5
11881 (ref)	*H. marshi*	C2	4.31	3.78	2.79	329.5	26.5
12494	*H. minisculus*	B1	2.98	2.49	2.00	31.5	31.5
12497	*H. minisculus*	B1	2.9	2.18	1.84	31.5	31.5
11348	*H. minisculus*	B2	4.02	3.26	2.57	121.5	58.5
11415 (star)	*H. minisculus*	B2	3.81	3.07	2.46	121.5	58.5
19219	*H. minisculus*	B2	3.17	2.78	2.18	121.5	58.5
19214d	*H. minisculus*	B2	3.54	3.05	2.38	121.5	58.5
19214a	*H. minisculus*	B2	3.49	3.14	2.39	121.5	58.5
19214h	*H. minisculus*	B2	3.79	3.09	2.46	121.5	58.5
11952	*H. minisculus*	C4	3.38	2.94	2.30	329.5	26.5
11917	*H. minisculus*	C5	4.1	3.38	2.63	377	21
11906	*H. minisculus*	C5	3.97	3.19	2.54	377	21
11940	*H. minisculus*	D3	4.1	3.18	2.57	468	32
11891	*H. minisculus*	D	3.67	2.9	2.36	523.5	23.5
12486	*H. minisculus*	D4	4.1	3.21	2.58	523.5	23.5
11948	*H. minisculus*	D4	3.88	3.24	2.53	523.5	23.5
11932	*H. minisculus*	D5	3.83	3.15	2.49	523.5	23.5
11393 (star)	*H. paulis*	B2	3.87	3.13	2.49	121.5	58.5
10972	*H. paulis*	B2	3.9	3.08	2.49	121.5	58.5
10983	*H. paulis*	B2	3.69	2.98	2.40	121.5	58.5
10984	*H. paulis*	B2	3.74	2.98	2.41	121.5	58.5
10995	*H. paulis*	B2	3.57	2.96	2.36	121.5	58.5
10969 (star)	*H. paulis*	B2	3.94	4.55	2.89	121.5	58.5
19208	*H. paulis*	B2	3.78	3.28	2.52	121.5	58.5
93345	*H. paulis*	B2	3.71	3.15	2.46	121.5	58.5
5003 (holo)	*H. paulis*	B2-4	3.65	2.79	2.32	121.5	58.5
13057	*H. paulis*	B3	3.55	2.88	2.32	121.5	58.5
11921	*H. paulis*	C1	3.67	2.91	2.37	268.5	34.5

11933	*H. paulis*	C2	4.18	3.22	2.60	329.5	26.5
11919	*H. paulis*	C2	3.75	3.1	2.45	329.5	26.5
11899	*H. paulis*	C2	3.64	3.05	2.41	329.5	26.5
11903	*H. paulis*	C5	4.08	3.17	2.56	377	21
11938	*H. paulis*	D2	4.13	3.3	2.61	417	19
11889	*H. paulis*	D4	4.29	3.6	2.74	523.5	23.5

Table 3.4. Character matrix of *Notharctus* specimens.

	11997B	11990L	11986U	13134L	11451L	12000L	93605Lwr	13027U	11991U	12575L	11481L	11466B*os	13022L	13029L	18985L	11469L	134401B	18990B	14568L	11449U	11456L	13130L	18987B	11453L	11452B	13031L	11461L**P	11460L	12568U	12008L
1	1	?	?	?	2	0	?	?	?	2	0	1	?	?	0	0	1	0	0	?	?	0	?	1	?	1	0/1	?	?	?
2	0	?	?	?	0	0	?	?	?	0	0	0	?	?	0	0	0	0	0	?	?	0	?	0	?	0	0	?	?	?
3	0	?	?	?	0	1	?	?	?	0	0	1	?	?	1	?	0	0	0	?	?	0	?	1	?	1	1	?	?	?
4	0	0	?	0	?	0	0	?	?	?	0	?	?	0	?	0	?	?	?	?	?	0	?	?	?	0	0	?	?	?
5	0	?	?	0	1	?	1	?	?	1	?	1	0/1	0	1	1	1	1	1	?	1	1	?	1	1	1	0	?	?	?
6	1	1	?	1	1	1	0	?	?	1	1	1	1	1	1	1	1	1	1	?	1	1	?	1	1	1	1	?	?	?
7	1	1	?	1	1	1	1	?	?	1	1	1	1	1	1	1	1	?	1	?	1	1	?	1	0	1	1	?	?	?
8	0	?	?	0	0	?	0	?	?	0	0	0	0	0	0	0	0	0	0	?	0	0	?	0	0	0	0	?	?	?
9	0	?	?	0	1	?	0	?	?	0	1	0	1	1	0	1	?	0	0	?	1	1	?	1	1	0	1	?	?	?
10	0	0	?	0	0	0	0	?	?	?	0	0	0	0	0	0	?	0	0	?	0	0	0	?	0	0	?	0	?	0
11	0	2	?	0	0	0	0	?	?	1/2	?	2	2	2	2	2	2	0	2	?	2	2	2	2	2	2	2	2	?	0
12	0	0	?	0	0	0	0	?	?	0	0	0	0	0	0	0	0	0	0	?	0	0	0	?	0	0	0	0	?	0
13	1	1	?	1	1	1	0	?	?	1	1	1	1	1	1	1	1	1	1	?	1	1	1	?	1	1	1	1	?	1
14	1	0	?	1	1	1	1	?	?	1	1	1	1	1	1	1	0	1	0	?	1	1	1	?	1	1	0	1	?	1
15	?	?	0	?	?	?	?	?	?	?	?	0	?	?	?	?	0	?	?	1	?	?	?	?	0	?	?	?	?	?
16	?	?	0	?	?	?	?	1	0	?	?	1	?	?	?	?	0/1	?	?	1	?	?	?	?	0	?	?	?	1	?
17	?	?	1	?	?	?	?	1	1	?	?	0	?	?	?	?	0	1	?	0	?	?	1	?	?	?	?	?	0	?
18	?	?	1	?	?	?	?	1	1	?	?	2	?	?	?	?	0	2	?	1	?	?	1	?	?	?	?	?	2	?
19	?	?	1	?	?	?	?	0	0	?	?	0	?	?	?	?	0	0	?	?	?	?	0	?	?	?	?	?	0	?
20	0	?	2	?	?	?	?	0	0	?	?	0	?	?	?	?	?	0	?	0	?	?	0	?	?	?	?	?	0	?
21	0	?	0	?	?	?	?	0	0	?	?	1	?	?	?	?	?	0	?	0	?	?	0	?	?	?	?	?	0	?
22	?	?	0	?	?	?	?	1	0	?	?	0	?	?	?	?	0	1	?	2	?	?	2	?	?	?	?	?	0	?
23	?	?	0	?	?	?	?	0	0	?	?	0	?	?	?	?	0	0	?	1	?	?	0	?	?	?	?	?	0	?
24	?	?	0	?	?	?	?	0	0	?	?	0	?	?	?	?	0	0	?	1	?	?	0	?	?	?	?	?	0	?
25	?	?	1	?	?	?	?	0	1	?	?	0	?	?	?	?	0	0	?	0	?	?	0	?	?	?	?	?	0	?
26	?	?	1	?	?	?	?	1	1	?	?	1	?	?	?	?	?	1	?	1	?	?	1	?	?	?	?	?	1	?
27	1	?	1	?	?	?	?	?	0	?	?	0	?	?	?	?	0	0/1	?	0	?	?	0	?	?	?	?	?	0	?
28	1	?	0	?	?	?	?	?	0	?	?	1	?	?	?	?	1	0	?	1	?	?	1	?	?	?	?	?	1	?
29	1	?	0	?	?	?	?	?	0	?	?	1	?	?	?	?	0	1	?	1	?	?	1	?	?	?	?	?	1	?
30	0	?	0	?	?	?	?	?	0	?	?	0	?	?	?	?	0	0	?	0	?	?	0	?	?	?	?	?	0	?
31	0	?	0	?	?	?	?	?	0	?	?	0	?	?	?	?	0	0	?	0	?	?	1	?	?	?	?	?	0	?
32	0	?	2	?	?	?	?	?	2	?	?	0	?	?	?	?	0	2	?	0	?	?	0	?	?	?	?	?	2	?
33	0	?	0	?	?	?	?	?	2	?	?	0	?	?	?	?	0	1	?	2	?	?	2	?	?	?	?	?	0	?
34	0	?	0	?	?	?	?	?	0	?	?	0	?	?	?	?	0	0	?	0	?	?	0	?	?	?	?	?	0	?
35	?	?	0	?	?	?	?	?	0	?	?	0	?	?	?	?	0	0	?	0	?	?	0	?	?	?	?	?	0	?
36	0	?	1	?	?	?	?	?	1	?	?	0	?	?	?	?	0	1	?	0	?	?	0	?	?	?	?	?	0	?
37	1	?	1	?	?	?	?	?	1	?	?	1	?	?	?	?	0/1	1	?	1	?	?	1	?	?	?	?	?	1	?
38	?	?	?	?	?	?	?	?	?	?	?	?	?	?	?	?	1	1	1	?	?	?	?	?	?	?	?	?	?	?
39	0	?	?	?	0	0	?	?	?	0	0	0	?	?	0	?	0	0	0	?	?	0	?	?	?	?	0	?	?	?
40	0	?	?	0	0	0	0	?	?	0	0	0	0	0	0	0	0	0	0	?	0	0	?	0	?	?	0	?	?	?
41	0	0	?	0	0	0	0	?	?	?	0	0	0	0	0	0	0	0	0	?	0	0	?	0	0	?	0	0	?	0
42	0	?	?	0	0	0	0	?	?	0	0	0	0	0	0	0	0	0	0	?	0	0	?	0	0	?	0	?	?	?
43	1	2	?	1	1	0	1	?	?	?	?	0	0	0	0	0	0	0	0	?	0	0	2	0	0	?	0	1	?	1
44	2	2	?	0	2	?	?	?	?	2	2	2	2	2	2	2	2	2	2	?	2	2	?	2	2	?	?	2	?	0
45	1	1	?	1	1	?	?	?	?	1	0	0	1	1	1	0/1	?	0	0	?	1	1	?	1	1	?	?	1	?	1
46	0	0	?	1	?	?	?	?	?	?	1	0	?	0	?	0	?	0	0	?	?	0	?	?	0	?	?	0	?	0
47	?	?	0	?	?	?	?	0	0	?	?	1	?	?	?	?	0	0	?	1	?	?	1	?	?	?	?	?	0	?
48	0	?	0	?	?	?	?	?	0	?	?	1	?	?	?	?	0	0	?	1	?	?	1	?	?	?	?	?	0	?

11993L	11984B	13133L	12588U	12576L	12564B	13023L	11985U	11982B*rr	11987U	12003L	14567U	12006L	12565U	129381L	OG16849B	C69989L	C91368L	C21463U	C54242U	C72421L	C68955U	C69996U	C72418L	C69991L	C69983L	C94501L	C69988L	C69304L	1727B*tb	18986B
?	?	1	?	?	1/2	?	?	?	1	?	?	?	?	?	0	2	?	?	?	?	?	?	?	?	1	1	1	1	1	0	2
?	?	0	?	?	0	?	?	?	0	?	?	?	0	?	0	0	?	?	?	?	?	?	?	?	0	0	0	0	0	0	0
?	?	0	?	?	0	?	?	?	1	?	?	?	1	?	0	1	?	?	?	?	?	?	?	?	?	1	1	0	0	0	0
0	0	0	?	0	0	?	?	0	0	?	?	?	?	?	0	1	0	?	?	?	0	?	?	0	?	0	0	0	0	?	?
1	1	1	?	0	0	?	?	1	?	?	?	?	0	?	1	1	0	1	?	?	1	?	?	1	1	1	1	0	0	?	?
1	1	1	?	1	1	?	?	1	1	?	?	?	1	?	1	1	1	1	?	?	1	?	?	1	1	1	1	1	1	1	?
0	1	1	?	1	1	?	?	1	0	?	?	?	?	?	0	0	1	0	?	?	0	?	?	1	?	1	0	1	1	?	?
0	0	0	?	0	0	?	?	0	0	?	?	?	0	?	0	1	0	0	?	?	0	?	?	0	0	0	0	0	0	?	?
1	1	1	?	1	1	?	?	1	1	?	?	?	1	?	0	1	1	1	?	?	1	?	?	0	1	1	0	1	1	?	?
0	?	0	?	0	?	0	?	?	0	?	0	?	0	?	0	1	0	0	?	?	0	?	?	0	?	0	0	?	0	0	?
2	?	2	?	2	?	2	?	?	2	?	2	?	2	?	2	2	2	2	?	?	0	?	?	2	2	2	0	?	0	?	?
0	?	0	?	0	?	0	?	?	0	?	0	?	0	?	0	1	0	0	?	?	0	?	?	0	?	0	0	?	0	?	?
1	?	1	?	1	?	1	?	?	1	?	1	?	1	?	1	1	1	1	?	?	?	?	?	1	1	1	1	?	1	1	?
0	?	0	?	1	?	1	?	?	0	?	1	?	1	?	0	1	1	0	?	?	?	?	?	1	0	1	0	?	0	0	?
?	?	?	0	?	0	?	0	?	1	?	?	?	?	?	?	?	?	?	?	0	?	0	?	?	?	?	?	?	?	?	?
?	1	?	1	?	0	?	?	?	0	0	?	0/1	?	?	?	1	?	?	0	0	?	0	?	?	?	?	?	?	?	?	?
?	?	?	1	?	1	?	1	?	1	1	?	1	?	1	?	0	?	?	1	1	?	1	1	?	?	?	?	?	?	1	?
?	?	?	0	?	1	?	1	?	1	1	?	1	?	1	?	1	?	?	1	1	?	1	1	?	?	?	?	?	?	1	?
?	0	?	0	?	?	?	0	?	0	0	?	0	?	0	?	3	?	?	0	0	?	0	0	?	?	?	?	?	?	?	1
?	0	?	2	?	0	?	0	?	0	0	?	0	?	2	?	0	?	?	0	0	?	0	0	?	?	?	?	?	?	?	?
?	0	?	1	?	0	?	0	?	0	0	?	0	?	0	?	0	?	?	0	0	?	0	0	?	?	?	?	?	?	1	?
?	?	?	2	?	?	?	0	?	1	0	?	1	?	0	?	?	?	?	1	0	?	0	0	?	?	?	?	?	?	?	1
?	0	?	0	?	?	?	0	?	0	0	?	0	?	0	?	1	?	?	0	0	?	0	0	?	?	?	?	?	?	?	0
?	?	?	0	?	0	?	0	?	1	0	?	0	?	?	?	?	?	?	0	0	?	0	0	?	?	?	?	?	?	?	1
?	?	?	0	?	1	?	0	?	0	1	?	0	?	1	?	0	?	?	1	0	?	1	1	?	?	?	?	?	?	0	?
?	1	?	1	?	1	?	1	?	1	1	?	1	?	1	?	2	?	?	1	1	?	1	1	?	?	?	?	?	?	1	?
?	1	?	0	?	1	?	1	?	1	1	?	1	?	1	?	0	?	?	?	?	?	?	1	?	?	?	?	?	?	1	?
?	0	?	1	?	0	?	1	?	0	0	?	0	?	0	?	1	?	?	?	?	?	?	0	?	?	?	?	?	?	1	?
?	1	?	1	?	0	?	1	?	1	1	?	1	?	0	?	1	?	?	?	?	?	?	0	?	?	?	?	?	?	1	1
?	?	?	0	?	0	?	0	?	0	0	?	0	?	0	?	3	?	?	?	?	?	?	0	?	?	?	?	?	?	0	0
?	0	?	1	?	0	?	0	?	0	0	?	0	?	1	?	1	?	?	?	?	?	?	0	?	?	?	?	?	?	0	1
?	2	?	2	?	2	?	0	?	2	2	?	2	?	2	?	2	?	?	?	?	?	?	2	?	?	?	?	?	?	?	?
?	?	?	2	?	0	?	0	?	2	0	?	1	?	0	?	1	?	?	?	?	?	?	0	?	?	?	?	?	?	2	0
?	?	?	0	?	0	?	0	?	0	0	?	0	?	0	?	1	?	?	?	?	?	?	0	?	?	?	?	?	?	0	0
?	0	?	0	?	0	?	0	?	0	0	?	0	?	0	?	1	?	?	?	?	?	?	0	?	?	?	?	?	?	0	1
?	1	?	0	?	1	?	0	?	1	1	?	1	?	1	?	0	?	?	?	?	?	?	1	?	?	?	?	?	?	0	?
?	1	?	1	?	1	?	1	?	1	1	?	1	?	1	?	2	?	?	?	?	?	?	1	?	?	?	?	?	?	1	?
?	?	?	1	?	?	?	?	?	?	?	?	?	?	?	1	?	?	?	?	?	?	?	?	?	?	?	?	?	?	1	?
?	?	0	?	?	0	?	?	?	0	?	?	?	0	?	0	0	?	?	?	?	?	?	?	?	0	0	0	0	0	0	0
0	0	0	?	0	0	?	?	0	0	?	?	?	0	?	0	0	0	0	?	?	0	?	?	0	?	0	0	0	0	?	?
0	?	0	?	0	?	0	?	?	0	?	0	?	0	?	0	0	0	0	?	?	0	?	?	0	0	0	0	?	0	?	?
0	0	0	?	0	0	?	?	0	?	?	?	?	0	?	0	0	0	0	?	?	0	?	?	?	0	0	0	0	0	0	?
0	?	0	?	0	?	2	?	?	0	?	2	?	0	?	0	2	0	0	?	?	0	?	?	0	0	0	0	?	0	0	?
2	2	2	?	?	?	2	?	2	2	?	2	?	?	?	2	2	?	?	?	?	2	?	?	?	2	2	0	2	2	?	?
1	?	1	?	?	?	1	?	1	1	?	1	?	?	?	0	0	?	?	?	?	?	?	?	?	1	1	0	1	1	?	?
1	?	?	?	?	?	0	?	1	0	?	0	?	?	?	0	1	?	?	?	?	0	?	?	?	0	0	0	0	0	?	?
?	?	?	0/1	?	0	?	0	?	0	0	?	0	?	0	?	1	?	?	0	1	?	0	0	?	?	?	?	?	?	1	?
?	0	?	0/1	?	0	?	0	?	0	0	?	0	?	0	?	1	?	?	?	?	?	?	0	?	?	?	?	?	?	1	?

12578B*tb	11983B	12010B	OG15624L*Pj	OG16850L	OG16849B	OG14655U	OG55514L	OG55511L*Ca	OG16089U**Pr	OG16153L	OG94304L	OG94417L	OG15681U	OG16092U	11992B	12579L	11480L*tb	122094L	12586L	11467L	12002L	12569U	12583L	11464L	129384L	11472L	18989L	18988U	13026L	12001L	11454L
0	1	0	2	1	2	?	2	2	?	1	?	1	?	?	1	0	1	?	1	?	0	?	1	?	2	?	0	?	1	0	1
0	0	0	0	0	0	?	1	0	?	0	?	0	?	?	0	0	0	?	0	?	0	?	0	?	0	?	0	?	0	0	0
1	0	0	2	1	1	?	1	1	?	1	?	1	?	?	0	0	0	?	1	?	0	?	1	?	0	?	0	?	0	0	1
0	?	?	?	1	1	?	0	0	?	1	1	1	?	?	0	0	?	0	0	?	?	?	?	?	0	0	0	?	0	?	0
1	1	?	0	1	1	?	0	1	?	1	1	1	?	?	0	0	1	1	?	1	1	?	?	?	0	?	0	?	1	?	1
1	1	?	1	1	1	?	1	1	?	1	1	1	?	?	1	1	?	1	?	1	1	?	?	?	1	1	1	?	1	?	1
1	?	?	2	0	0	?	1	1	?	1	1	1	?	?	1	1	?	0/1	?	1	1	?	?	?	1	1	1	?	1	?	1
0	0	?	0	1	0	?	0/1	1	?	0	0	0	?	?	0	1	0	0	?	0	0	?	?	?	0	?	0	?	0	?	0
1	1	?	0	0	0	?	1	0	?	0	0	0	?	?	1	1	1	1	?	1	?	?	?	?	1	?	0	?	1	?	1
0	?	?	0	1	1	?	?	0	?	1	1	1	?	?	?	?	?	?	0	0	?	?	0	0	0	0	0	?	0	0	?
2	2	?	0	0	0	?	?	0	?	0	?	0	?	?	0	?	?	?	0	2	?	?	?	0	?	2	2	?	?	0	?
0	0	?	1	1	1	?	?	0	?	1	1	1	?	?	0	?	?	?	0	0	0	?	0	0	0	0	0	?	?	0	?
1	1	?	1	1	1	?	?	1	?	1	1	1	?	?	1	?	?	?	1	1	1	?	1	1	1	1	1	?	?	1	?
1	?	?	0	0	1	?	?	1	?	1	0	1	?	?	1	?	?	?	1	1	1	?	1	1	1	1	0	?	?	1	?
?	?	?	?	?	?	0	?	?	?	?	?	?	1	?	?	?	?	?	?	?	?	?	?	?	?	?	?	1	?	?	?
1	0	?	?	?	1	1	?	?	1	?	?	?	1	1	?	?	?	?	?	?	?	1	?	?	?	?	?	1	?	?	?
0	?	1	?	?	0	0	?	?	0	?	?	?	1	0	?	?	?	?	?	?	?	1	?	?	?	?	?	1	?	?	?
2	1	1	?	?	1	1	?	?	1	?	?	?	1	1	?	?	?	?	?	?	?	2	?	?	?	?	?	1	?	?	?
0	0	0	?	?	?	1	?	?	3	?	?	?	3	3	?	?	?	?	?	?	?	0	?	?	?	?	?	?	?	?	?
0	0	0	?	?	0	0	?	?	0	?	?	?	0	0	0	?	?	?	?	?	?	0	?	?	?	?	?	?	?	?	?
0	?	0	?	?	0	0	?	?	0	?	?	?	0	0	0	?	?	?	?	?	?	1	?	?	?	?	?	?	?	?	?
1	0	?	?	?	?	0	?	?	1	?	?	?	0/1	0/1	?	?	?	?	?	?	?	1	?	?	?	?	?	0	?	?	?
0	0	0	?	?	1	1	?	?	1	?	?	?	1	1	?	?	?	?	?	?	?	0	?	?	?	?	?	?	?	?	?
?	0	?	?	?	?	1	?	?	1	?	?	?	1	1	?	?	?	?	?	?	?	0	?	?	?	?	?	0	?	?	?
1	?	1	?	?	0	0	?	?	0	?	?	?	0	0	?	?	?	?	?	?	?	1	?	?	?	?	?	1	?	?	?
1	?	1	?	?	1	1	?	?	3	?	?	?	2	2	?	?	?	?	?	?	?	1	?	?	?	?	?	1	?	?	?
0	0	1	?	?	0	0	?	?	0	?	?	?	0	0	1	?	?	?	?	?	?	?	?	?	?	?	?	1	?	?	?
0	0	0	?	?	1	1	?	?	0	?	?	?	0	0	1	?	?	?	?	?	?	?	?	?	?	?	?	0	?	?	?
1	1	1	?	?	1	1	?	?	1	?	?	?	1	1	1	?	?	?	?	?	?	1	?	?	?	?	?	0	?	?	?
0	0	0	?	?	2	1	?	?	3	?	?	?	3	3	0	?	?	?	?	?	?	0	?	?	?	?	?	0	?	?	?
1	0	0	?	?	1	0	?	?	0	?	?	?	0	0	0	?	?	?	?	?	?	1	?	?	?	?	?	?	?	?	?
2	?	0	?	?	0	0	?	?	0	?	?	?	0	0	0	?	?	?	?	?	?	2	?	?	?	?	?	?	?	?	?
1	1	0	?	?	1	0	?	?	1	?	?	?	1	0/1	0	?	?	?	?	?	?	1	?	?	?	?	?	0	?	?	?
0	0	0	?	?	1	1	?	?	1	?	?	?	1	1	0	?	?	?	?	?	?	0	?	?	?	?	?	?	?	?	?
0	0	0	?	?	1	1	?	?	1	?	?	?	1	1	?	?	?	?	?	?	?	1	?	?	?	?	?	?	?	?	?
1	?	1	?	?	0	0	?	?	1	?	?	?	1	1	0	?	?	?	?	?	?	?	?	?	?	?	?	1	?	?	?
1	?	1	?	?	3	1	?	?	3	?	?	?	2	2	1	?	?	?	?	?	?	1	?	?	?	?	?	1	?	?	?
?	?	?	?	?	?	?	?	?	?	?	?	?	?	?	?	1	1	?	1	?	?	?	?	?	?	?	?	?	?	1	?
0	0	0	0	0	0	?	0	0	?	0	?	0	?	?	0	0	0	?	0	?	0	?	0	?	0	?	0	?	0	0	0
0	?	?	0	0	0	?	0	0	?	0	0	0	?	?	0	0	?	0	?	0	0	?	?	?	0	0	0	?	0	?	0
0	?	?	0	0	0	?	?	0	?	0	0	0	?	?	0	?	?	?	0	0	0	?	0	0	0	0	0	?	?	0	?
0	0	?	0	0	0	?	0	0	?	0	0	0	?	?	0	0	0	0	?	0	0	?	?	?	0	?	0	?	0	?	0
0	0	?	1	1	1	?	?	0	?	0	?	0	?	?	0	?	?	?	0	0	?	?	?	0	?	2	0	?	?	0	?
2	?	?	2	0	0	?	0	0	?	0	2	?	?	?	0	?	?	?	?	2	?	?	2	?	?	?	?	?	2	2	2
1	?	?	0	0	0	?	0	?	?	1	0	?	?	?	1	?	0	?	0	0	?	?	0	?	?	?	?	?	1	1	1
0	?	?	?	?	?	?	?	?	?	1	1	?	?	?	0	?	?	?	0	0	?	?	?	?	1	?	?	?	0	?	0
0	0	0	?	?	1	1	?	?	1	?	?	?	1	1	?	?	?	?	?	?	?	1	?	?	?	?	?	0	?	?	?
0	0	0	?	?	1	1	?	?	1	?	?	?	1	1	1	?	?	?	?	?	?	?	?	?	?	?	?	0	?	?	?

4975L	11463L	5009L**Tr	12588L	12009L	11996L	11995L	140034U	12007L	11999L	YP11782L**rr	US3750L**rr	UW3007L**rn
1	0	1	?	0	1	2	?	?	?	0	?	0
?	0	0	?	1	0	0	?	?	?	0	?	0
0	0	0	?	1	0	?	?	?	?	0	?	0
?	?	?	?	0	0	0	?	?	?	0	?	0
1	?	1	1	1	1	1	?	?	?	0	?	1
1	1	1	?	1	1	1	?	?	?	1	?	1
1	0	1	?	1	1	0	?	?	?	0	?	0
0	0	0	0	0	0	0	?	?	?	0	?	0
?	?	?	1	1	1	1	?	?	?	0	?	1
?	?	0	?	0	?	?	?	0	0	0	0	0
2	?	2	0/2	2	?	?	?	?	0	0	0	0
0	?	0	0	0	?	?	?	0	0	0	0	0
1	?	1	1	1	?	?	?	1	1	1	1	1
1	?	1	1	1	?	?	?	1	0	0	0	1
?	?	?	?	?	?	?	?	?	?	?	?	?
?	?	?	?	?	?	?	?	?	?	?	?	?
?	?	?	?	?	?	?	?	?	?	?	?	?
?	?	?	?	?	?	?	?	?	?	?	?	?
?	?	?	?	?	?	?	?	?	?	?	?	?
?	?	?	?	?	?	?	?	?	?	?	?	?
?	?	?	?	?	?	?	?	?	?	?	?	?
?	?	?	?	?	?	?	?	?	?	?	?	?
?	?	?	?	?	?	?	?	?	?	?	?	?
?	?	?	?	?	?	?	?	?	?	?	?	?
?	?	?	?	?	?	?	?	?	?	?	?	?
?	?	?	?	?	?	?	?	?	?	?	?	?
?	?	?	?	?	?	?	?	?	?	?	?	?
?	?	?	?	?	?	?	1	?	?	?	?	?
?	?	?	?	?	?	?	0	?	?	?	?	?
?	?	?	?	?	?	?	0	?	?	?	?	?
?	?	?	?	?	?	?	0	?	?	?	?	?
?	?	?	?	?	?	?	0	?	?	?	?	?
?	?	?	?	?	?	?	0	?	?	?	?	?
?	?	?	?	?	?	?	2	?	?	?	?	?
?	?	?	?	?	?	?	0	?	?	?	?	?
?	?	?	?	?	?	?	0	?	?	?	?	?
?	?	?	?	?	?	?	1	?	?	?	?	?
?	?	?	?	?	?	?	1	?	?	?	?	?
?	1	1	?	?	?	?	?	?	?	?	?	?
0	0	0	?	0	0	0	?	?	?	0	?	0
?	0	0	?	0	0	0	?	?	?	0	?	1
0	?	0	?	0	?	?	?	0	0	0	0	1
0	?	0	0	0	0	0	?	?	?	0	?	0
0	?	0	0	0	?	?	?	?	0	0	0	0
2	?	2	2	?	2	?	?	2	2	0	?	2
0	?	?	0	0	1	?	?	1	1	1	?	0
0	?	0	?	0	0/1	?	?	0	?	0	?	1
?	?	?	?	?	?	?	?	?	?	?	?	?
?	?	?	?	?	?	?	0	?	?	?	?	?

Table 3.5. List of *Notharctus* synapomorphies.

Node	Character	State
3 (all *Notharctus*)	10	0
	12	0
	19	0
	23	0
	26	1
	30	0
	34	0
	35	0
	37	1
	46	0
39 (*N. tenebrosus, N. robustior, N. robinsoni, N. pugnax*)	3	0
	45	1
	47	0
	48	0
153 (*N. tenebrosus*)	17	0
40 (*N. robustior, N. robinsoni, N. pugnax*)	17	1
41 (*N. robustior*)	16	0
	27	1
70 (*N. robinsoni, N. pugnax*)	28	0
	32	2
	36	1
73 (*N. robinsoni*)	1	0
	16	1
	18	2
	22	1
	33	1
102 (*N. pugnax*)	16	0
	27	1

NOTE: See Figure 3.1 for the position of the nodes.

Table 3.6. Results of Student's t-test on *Notharctus* body size.

	N. tenebrosus	*N. pugnax*	*N. robustior*	*N. robinsoni*	*N.* sp. Indet	*Notharctus (at genus level)*
Bridger B/C	0.189	0.0003	0.03	N/A	0.139	2.15E-06
	(X)	(✓)	(✓)		(X)	(✓)
Bridger C/D	N/A	0.166	N/A	N/A	0.032	0.09014
		(X)			(✓)	(X)
Bridger B/D	N/A	0.00002	N/A	N/A	0.006	1.56433E-11
		(✓)			(✓)	(✓)

NOTE: P-values less than 0.05 indicate that there is a significant difference in the mean values of the body mass of the two biozones

Table 3.7. Dental characters of *Hyopsodus* specimens.

Character	AMNH10972	AMNH11879	AMNH10994	AMNH10984	AMNH11394	AMNH11373	AMNH11348	AMNH10995	AMNH11397	AMNH11415	AMNH19219	AMNH12494	AMNH11934	AMNH11883	AMNH12483	AMNH11890	AMNH11892	AMNH11957
m1																		
1	1	?	?	1	0	1	0	1	1	0	0	0	1	1	1	?	0	0
2	1	1	1	1	1	0	0	1	1	0	0	0	1	1	0	1	1	1
3	1	1	1	1	1	1	1	1	?	1	1	0	1	1	1	1	1	1
4	1	1	?	1	1	1	1	1	1	1	1	?	1	1	0	?	1	1
5	0	0	0	0	0	0	0	0	0	0	0	0	1	1	0	0	0	0
6	0	0	0	0	0	0	0	0	0	0	0	0	0	0	0	0	0	0
m2																		
1	1	1	1	1	1	1	0	1	1	0	1	0	1	1	1	?	1	1
2	1	0	1	1	1	1	0	1	1	0	0	0	1	1	1	1	1	1
3	1	1	1	1	1	1	1	1	1	1	1	1	1	1	1	1	1	1
4	1	1	1	1	1	1	1	1	1	1	1	?	1	1	1	?	1	1
5	0	0	0	0	0	0	0	0	0	0	0	0	1	1	0	?	?	0
6	0	0	0	0	0	0	0	0	0	0	0	0	0	0	0	0	0	0
m3																		
1	1	1	1	1	1	1	0	1	1	0	1	0	1	1	1	?	1	1
2	1	0	1	0/1	1	1	0	1	0	0	1	0	1	1	1	1	1	1
3	1	1	1	1	1	1	1	1	1	1	1	0/1	1	?	1	1	1	1
4	1	1	1	0	1	1	0	0	1	1	1	?	1	1	1	?	1	1
5	0	0	0	0	0	0	0	0	0	0	0	0	1	1	0	0	0	0
6	0	0	0	0	0	0	0	0	0	0	0	0	0	?	0	0	0	0

AMNH11938	AMNH11940	AMNH11970	AMNH11932	AMNH12486	AMNH11933	AMNH11921	AMNH11952	AMNH11917	AMNH11903	AMNH11906	AMNH19214d	AMNH19214a	AMNH19214f	AMNH19214h	AMNH19214b	AMNH12481	AMNH11969	AMNH11888	AMNH12479
1	0	0	?	1	1	1	0	1	1	0	1	0	1	1	1	1	0	1	1
1	0/1	1	0	0	1	1	1	0	1	0	0	0	1	0	1	1	1	1	1
1	1	1	1	1	1	1	1	1	1	1	1	1	1	1	1	1	1	1	1
1	?	1	1	1	1	1	?	1	1	1	?	1	1	1	1	1	1	1	1
0	0	0	0	0	0	0	0	0	0	0	0	0	0	0	0	0	0	0	0
0	0	?	0	0	0	0	0	0	0	0	0	0	0	0	0	1	1	0	0
1	0	1	1	1	1	1	0	1	1	0	1	0	1	1	1	1	1	1	1
1	0	1	0	0	1	1	?	0	1	0	0	1	1	0	1	1	1	1	1
1	1	1	1	1	1	1	?	1	1	1	1	1	1	?	1	1	1	1	?
1	1	1	1	1	1	1	1	1	1	1	1	1	1	1	1	1	1	1	1
0	0	0	0	0	0	0	0	0	0	0	0	0	0	0	0	1	0	0	0
0	0	0	0	0	0	0	0	0	0	0	0	0	0	0	0	1	1	0	0
N/A	0	1	N/A	1	1	N/A	0	N/A	1	N/A	1	0	1	?	1	1	1	1	1
N/A	0	1	N/A	0	1	N/A	0	N/A	?	N/A	0	1	1	0	1	1	1	1	1
N/A	0/1	1	N/A	?	1	N/A	1/2	N/A	1	N/A	?	1	1	1	1	1	1	1	1
N/A	1	1	N/A	1	1	N/A	0	N/A	1	N/A	1	1	1	1	1	1	1	1	1
N/A	0	0	N/A	0	0	N/A	0	N/A	0	N/A	0	0	0	0	0	1	0	0	0
N/A	0	0	N/A	0	0	N/A	0	N/A	0	N/A	0	0	0	0	0	0	0	0	0

AMNH12485	AMNH12473	AMNH93385	AMNH11901	AMNH11918	AMNH11908	AMNH19208	AMNH19221	AMNH13058	AMNH13067	AMNH12480	AMNH13062	AMNH13057	AMNH13066	AMNH10969	AMNH11344	AMNH10983	AMNH10981	AMNH10982	AMNH19217
1	1	1	0	0	1	1	1	1	0	0	1	1	0	1	0	1	0	1	0
1	1	1	1	1	1	1	1	1	0	1	1	1	1	1	1	1	1	1	0
1	1	1	1	1	1	1	1	1	1	1	1	1	1	?	1	1	1	1	1
1	1	1	1	1	1	1	?	1	1	1	1	1	1	1	1	1	0	1	1
0	0	0	0	0	0	0	0	0	0	0	0	0	0	0	0	0	0	0	0
0	0	0	0	0	0	0	1	0	0	0	0	0	0	0	0	0	0	0	0
1	1	1	1	1	1	1	1	1	1	1	1	1	1	1	1	1	1	1	1
1	1	1	1	1	1	1	1	1	1	1	1	1	1	1	1	1	1	1	1
1	1	1	1	1	1	1	1	1	1	1	1	1	1	1	1	1	1	1	1
1	1	1	1	1	1	1	1	1	1	1	1	1	1	1	1	1	1	1	1
0	0	0	0	0	0	0	?	0	0	0	0	0	0	0	0	0	0	0	0
0	0	0	0	0	0	0	?	0	0	0	0	0	0	0	0	0	0	0	0
1	N/A	N/A	N/A	1	N/A	1	1	N/A	1	N/A	1	N/A	1	1	1	1	1	1	1
1	N/A	N/A	N/A	1	N/A	1	1	N/A	0	N/A	1	N/A	1	1	1	1	1	0/1	1
1	N/A	N/A	N/A	1	N/A	1	1	N/A	1	N/A	0	N/A	1	1	1	1	1	1	1
1	N/A	N/A	N/A	1	N/A	1	1	N/A	?	N/A	1	N/A	1	1	1	0	1	1	1
0	N/A	N/A	N/A	0	N/A	0	0	N/A	0	N/A	0	N/A	0	0	0	0	0	0	0
0	N/A	N/A	N/A	0	N/A	0	?	N/A	0	N/A	0	N/A	0	0	0	0	?	0	0

AMNH93345	AMNH11948	AMNH11889	AMNH11891	AMNH11393	AMNH11899	AMNH11919	AMNH11959
1	1	1	0	1	1	1	1
1	0	1	0	1	1	1	1
1	1	1	?	1	1	1	1
1	1	1	1	1	1	1	1
0	0	0	0	0	0	0	0
0	0	0	0	0	0	?	0
1	1	N/A	1	1	1	1	1
1	0	N/A	0	1	1	1	1
1	1	N/A	1	1	1	1	1
1	1	N/A	1	1	1	1	1
0	0	N/A	0	0	0	0	0
0	0	N/A	0	0	0	0	1
1	N/A	1	1	1	1	1	1
1	N/A	?	0	1	1	1	1
1	N/A	1	1	1	1	1	1
1	N/A	?	1	1	0	1	1
0	N/A	0	0	0	0	0	0
0	N/A	0	0	0	?	0	0

NOTE: Characters refer to the presence (1) or absence (0) of cingulum in the following locations of m1-3: character 1-anterior-buccal corner; character 2-hypoflexid; character 3-post-hypoconid; character 4-hypo-entoconid; character 5-entoconid; character 6-basin between entoconid and metaconid.

Table 3.8. C.V. (coefficient of variance) of tooth size in *Hyopsodus* species.

	H. despiciens	*H. lepidus*	*H. marshi*	*H. minisculus*	*H. paulis*	At genus level
Bridger B	0.08	0.11	N/A	0.23	0.19	0.18
Bridger C	0.15	0.24	0.01	0.17	0.10	0.20
Bridger D	0.09	0.10	N/A	0.08	0.09	0.11
Bridger B-D	0.12	0.16	0.19	0.19	0.16	0.18

Table 3.9. Results of Student's t-test on *Hyopsodus* tooth size.

	H. despiciens	*H. lepidus*	*H. marshi*	*H. paulis*	*H. minisculus*	At genus level
Bridger B/C	0.216	0.512	N/A	0.882	0.242	0.171
Bridger C/D	0.704	0.101	N/A	0.059	0.843	0.149
Bridger B/D	**0.022**	**0.021**	N/A	0.118	0.092	**0.002**

NOTE: Assuming two-tailed distribution where p value < 0.05 is significant (shown in bold).

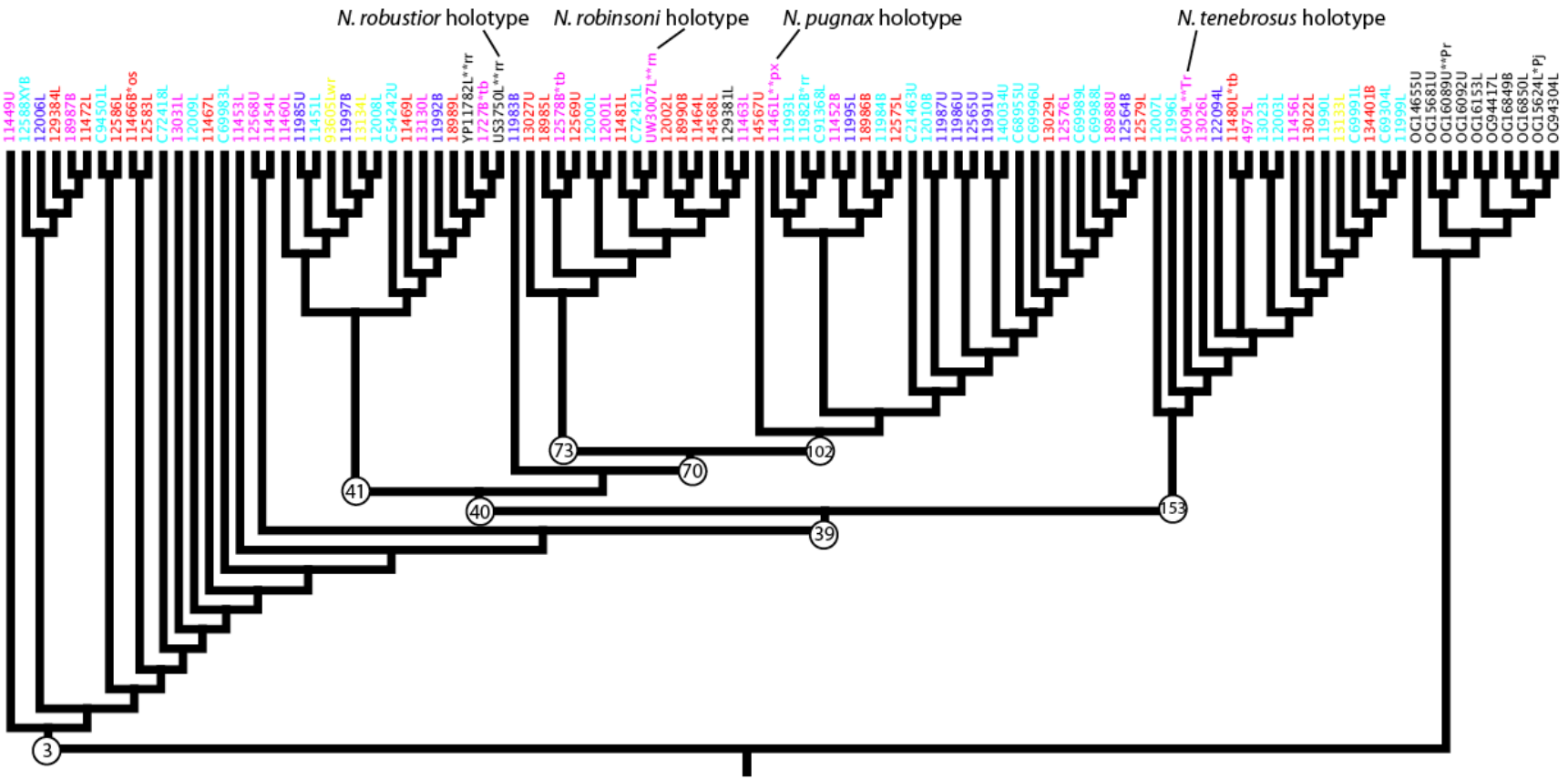
N. robustior holotype
N. robinsoni holotype
N. pugnax holotype
N. tenebrosus holotype
11449U
12588XYB
12006L
129384L
18987B
11472L
C94501L
12586L
114668*os
12583L
C72418L
13031L
12009L
11467L
C69983L
11453L
12568U
11454L
11460L
11985U
11451L
93605Lwr
11997B
13134L
12008L
C54242U
11469L
13130L
11992B
18989L
YP11782L**rr
17278*tb
US3750L**rr
11983B
13027U
18985L
12578B*tb
12569U
12000L
12001L
11481L
C72421L
UW30072L**rn
12002L
18990B
11464L
14568L
129381L
11463L
14567U
11461L**px
11993L
11982B*rr
C91368L
11452B
11995L
18986B
11984B
12575L
C21463U
12010B
11987U
11986U
12565U
11991U
140034U
C68955U
C69996U
13029L
12576L
C69959L
C69988L
18988U
12564B
12579L
12007L
11996L
5009L**Tr
13026L
122094L
11480L*tb
4975L
13023L
12003L
11456L
13022L
11990L
13133L
C69991L
134401B
C69304L
11999L
OG14655U
OG15681U
OG16089U**Pr
OG16092U
OG16153L
OG94417L
OG16849B
OG16850L
OG15624L*Pj
OG94304L
3
41
40
39
73
70
102
153

Figure 3.1. Majority consensus tree showing phylogenetic relationship of *Notharctus* specimens. Major nodes are indicated. Specimen numbers that begin with a C are those from the UCM collection. Everything else is from AMNH collections. Outgroups are marked with OG in the specimen name. Specimen numbers in red/pink are from the Lower Bridger, where red ones are from Grizzly Butte localities, and pink ones are from other Lower Bridger localities. Specimen numbers in light/dark blue are from the Upper Bridger, where dark blue ones are from Henrys Fork Hill localicities, and light blue ones are from other Upper Bridger localities. Holotype of *N. robinsoni* is from Gingerich (1979), and that of *N. robustior* is from Granger. Synapomorphies for the nodes shown in the figure can be found in Table 3.5.

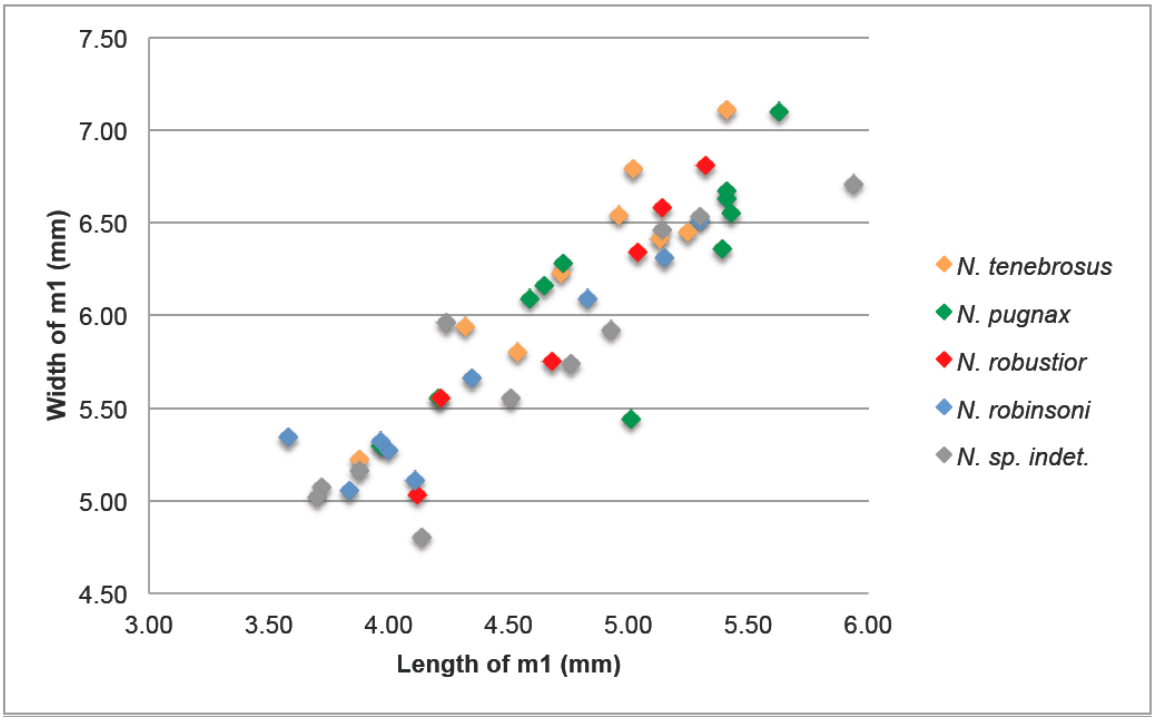

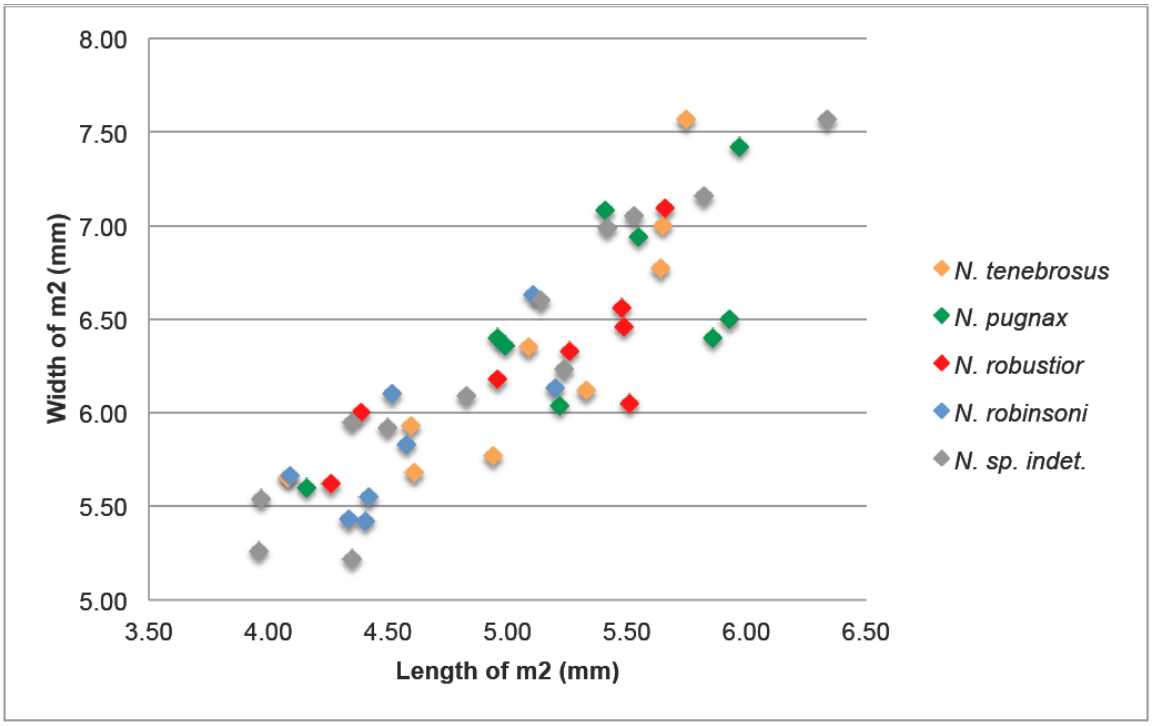

Figure 3.2. Bivariate plots showing a distribution of the length and width of m1 (top) and m2 (bottom) in *Notharctus* specimens.

Figure 3.3.A. *N. tenebrousus*

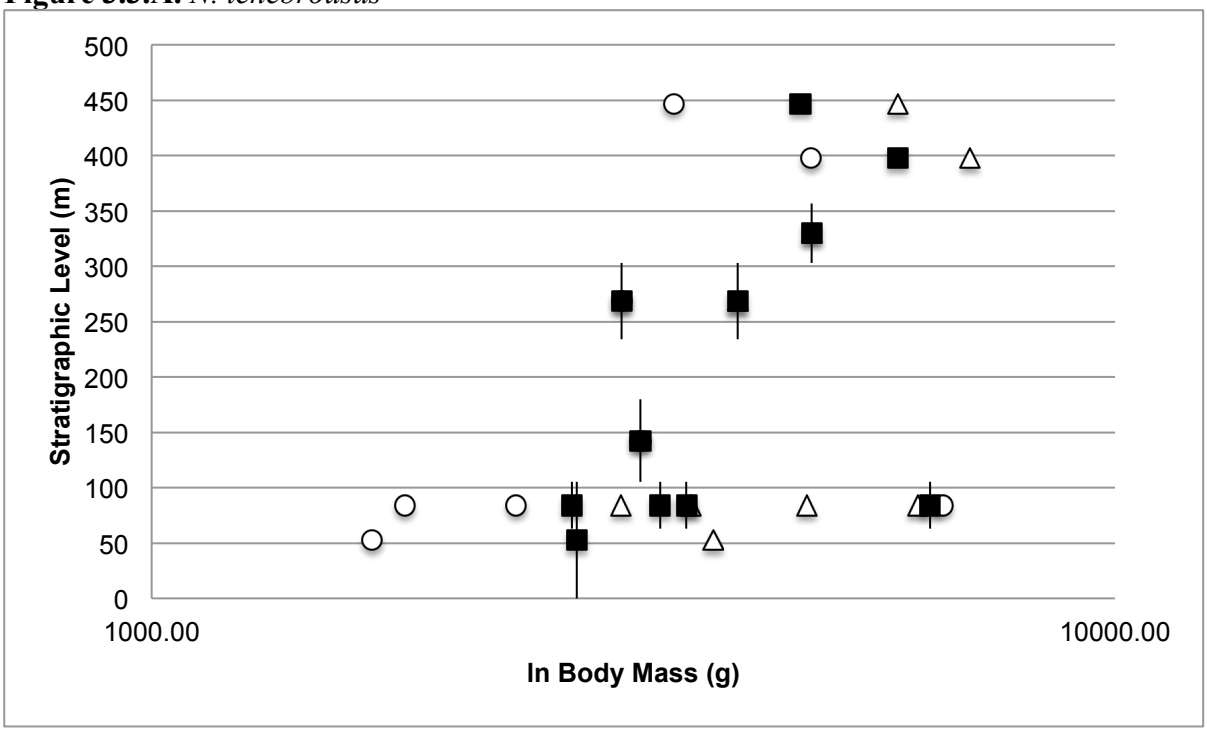

Figure 3.3.B. *N. pugnax*

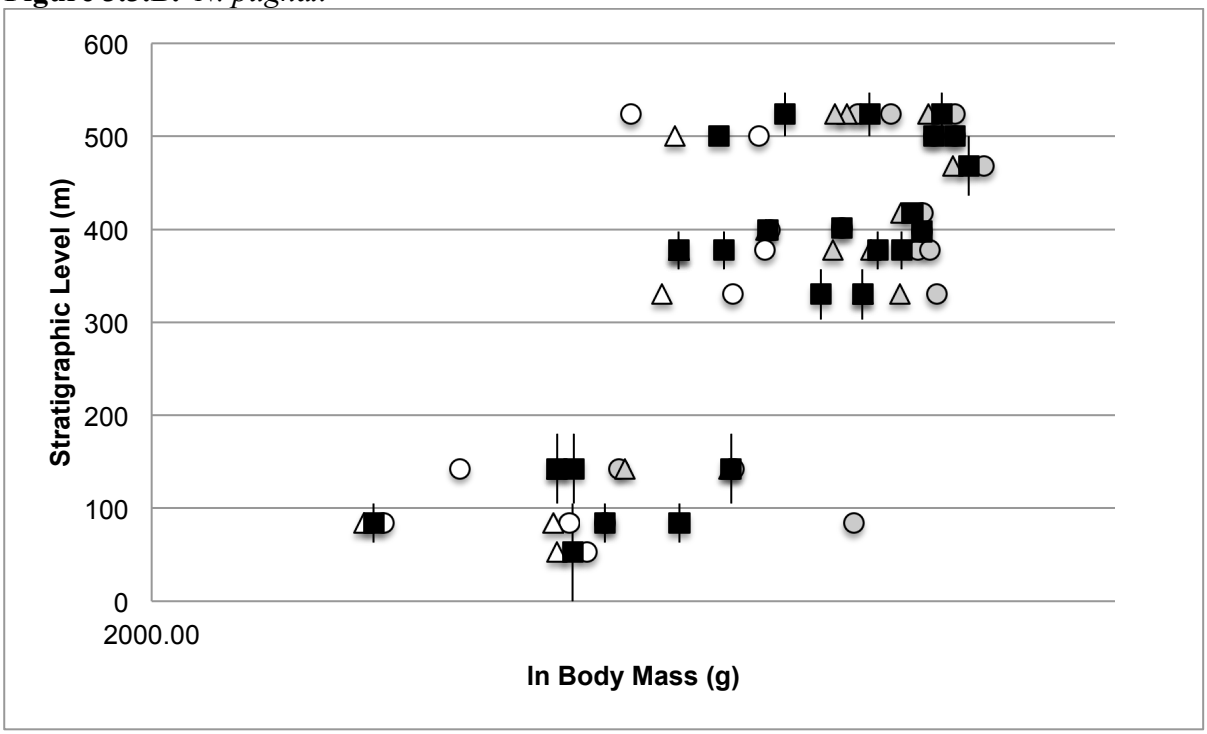

Figure 3.3.C. *N. robinsoni*

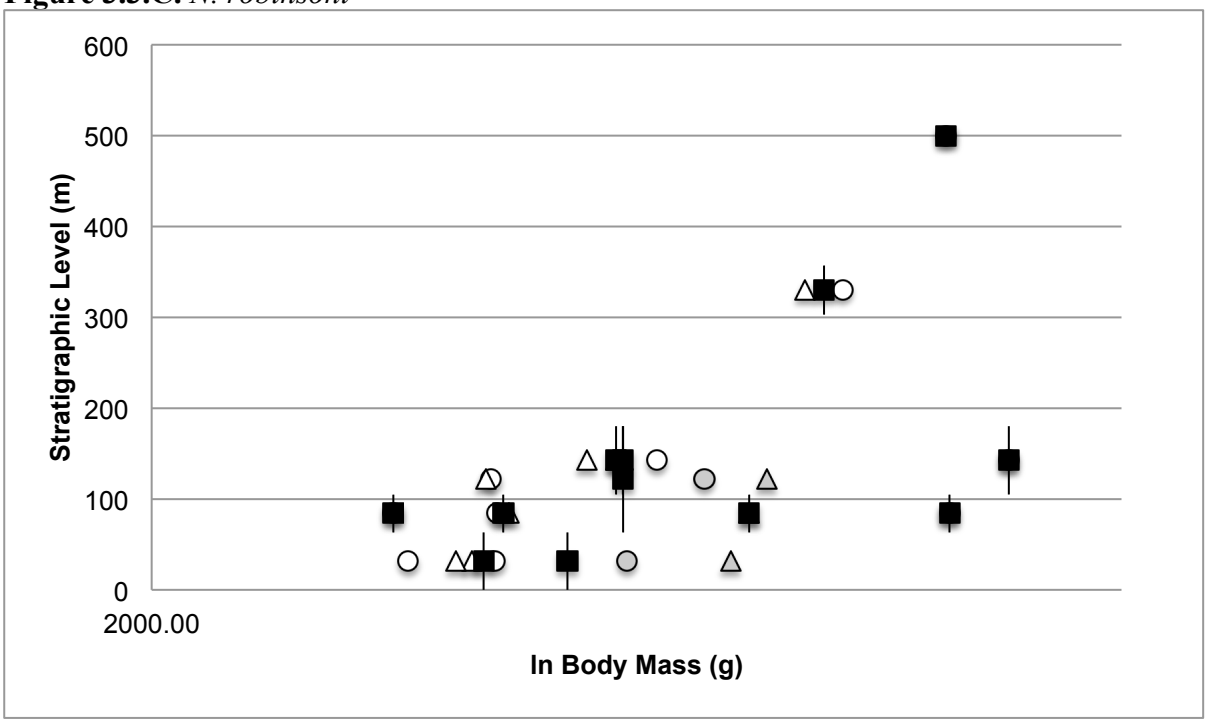

Figure 3.3.D. *N.* sp. indet.

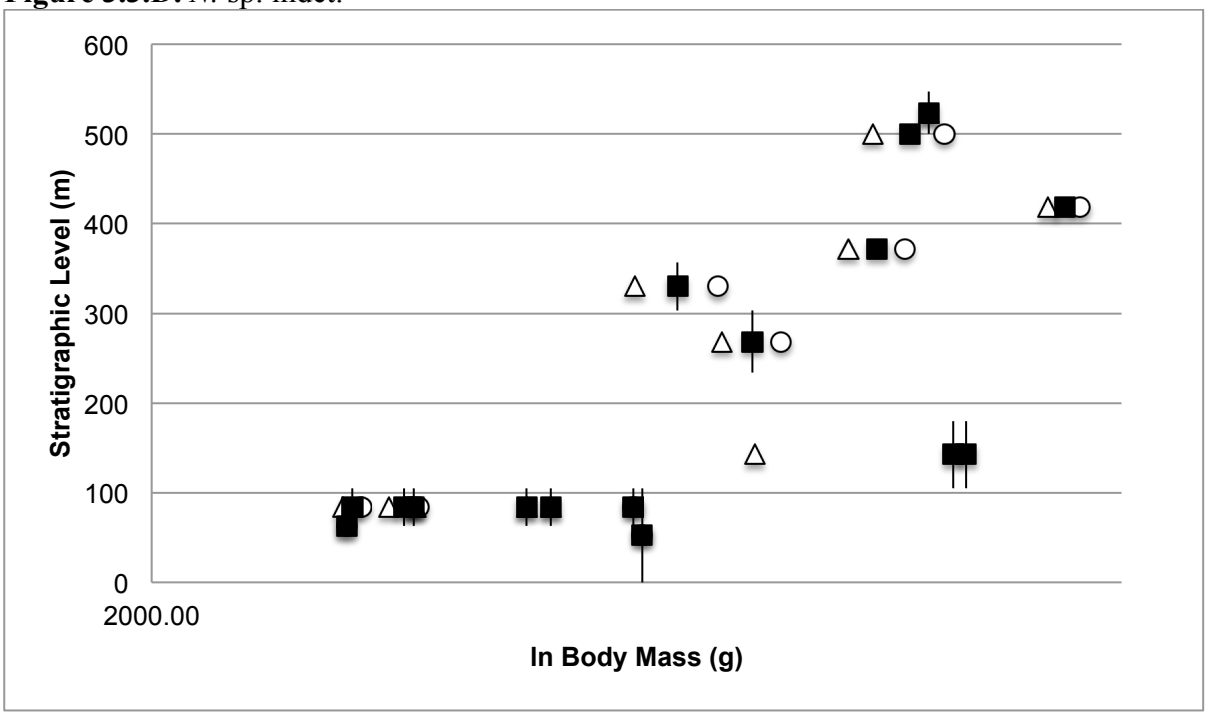

Figure 3.3.E. *N. robustior*

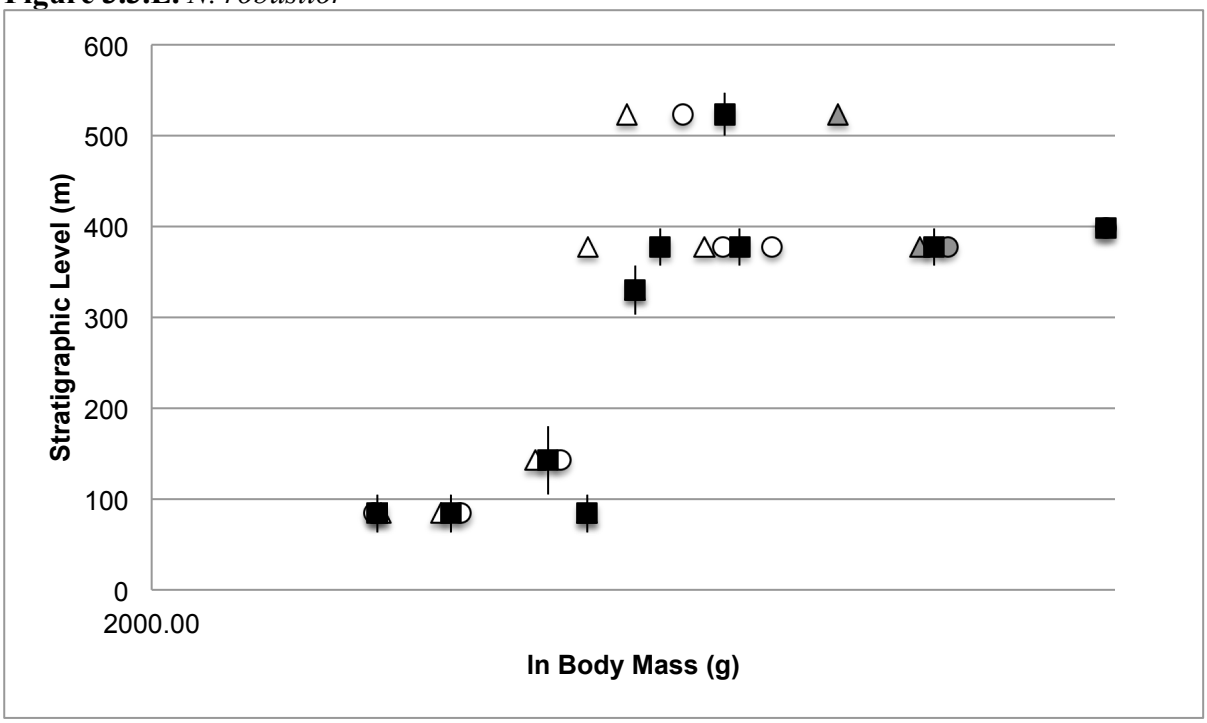

Figure 3.3. Body size evolution of (A) *Notharctus tenebrosus*, (B) *N. pugnax*, (C) *N. robinsoni*, (D) *N.* sp. indet, and (E) *N. robustior*. Open circle–m1, open triangle–m2, grey circle–M1, grey triangle–M2, and square–average. Stratigraphic errors are included for the average estimates where available.

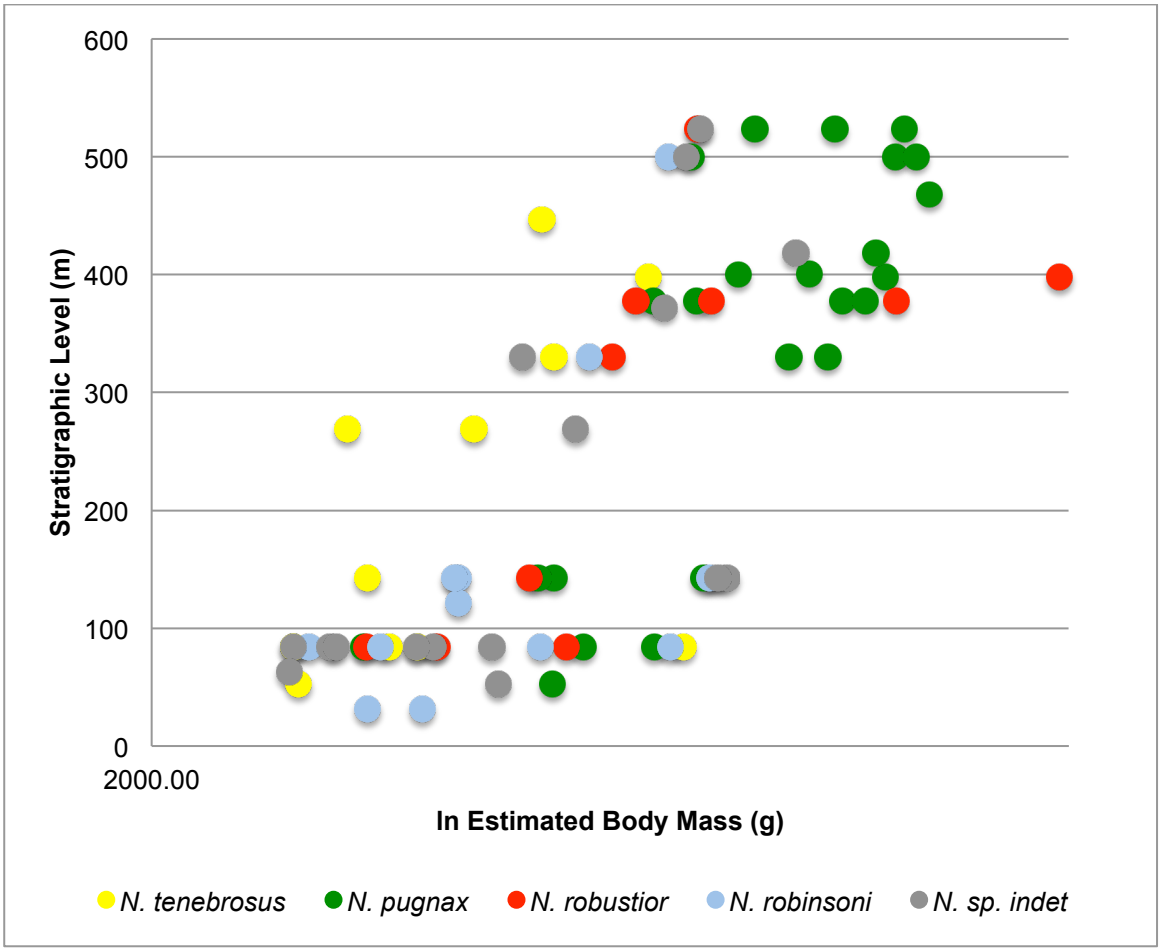

Figure 3.4. Body size change for all the species of *Notharctus* over Bridger B, C, and D. The data plotted in the figure is an average of body mass estimates based on all available dentition.

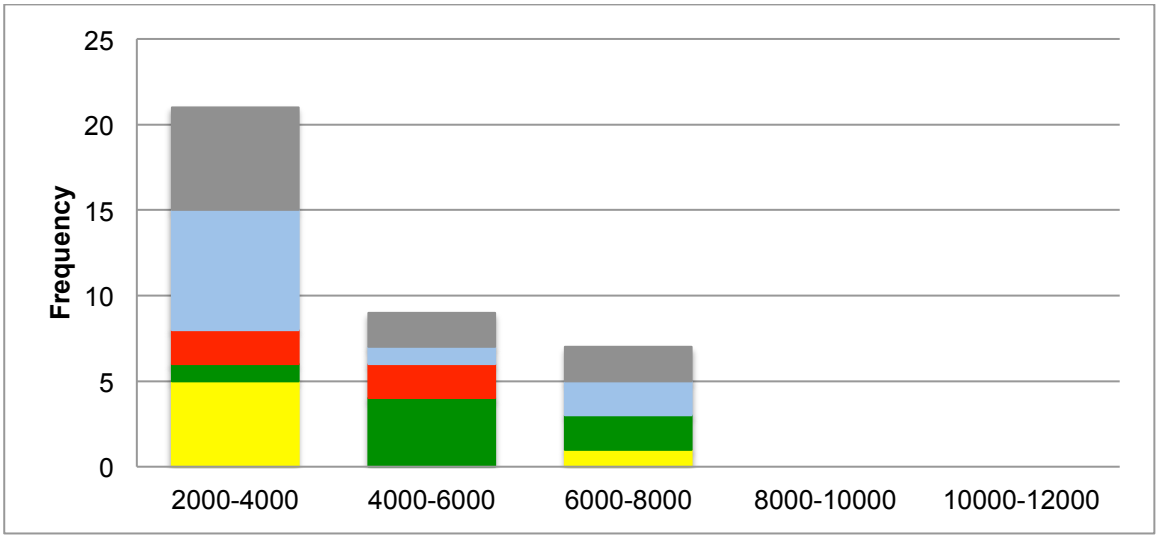
25
20
15
10
5
0
Frequency
2000-4000
4000-6000
6000-8000
8000-10000
10000-12000

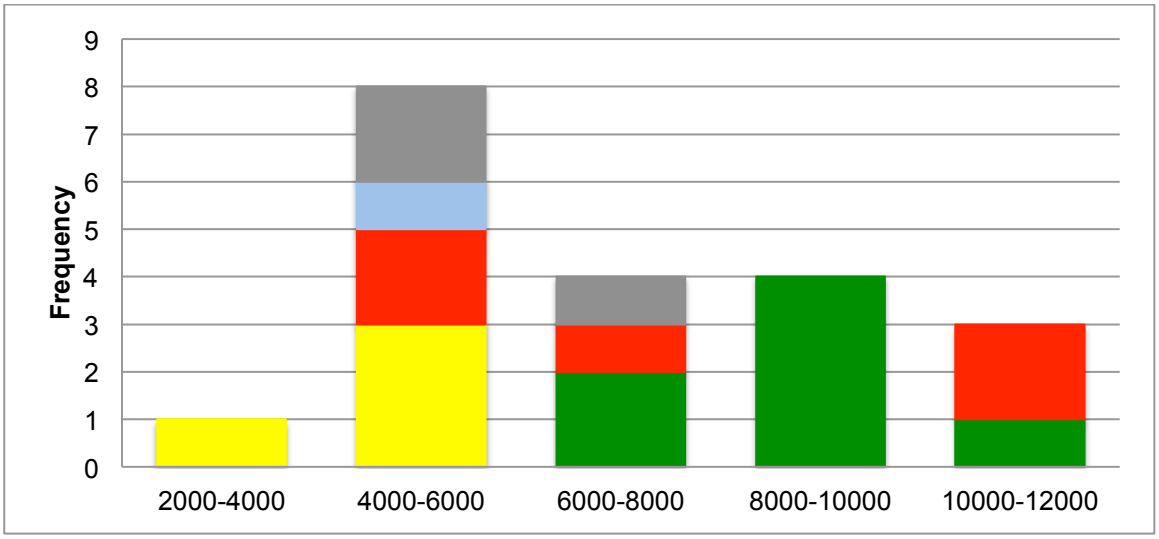
9
8
7
6
5
4
3
2
1
0
Frequency
2000-4000
4000-6000
6000-8000
8000-10000
10000-12000

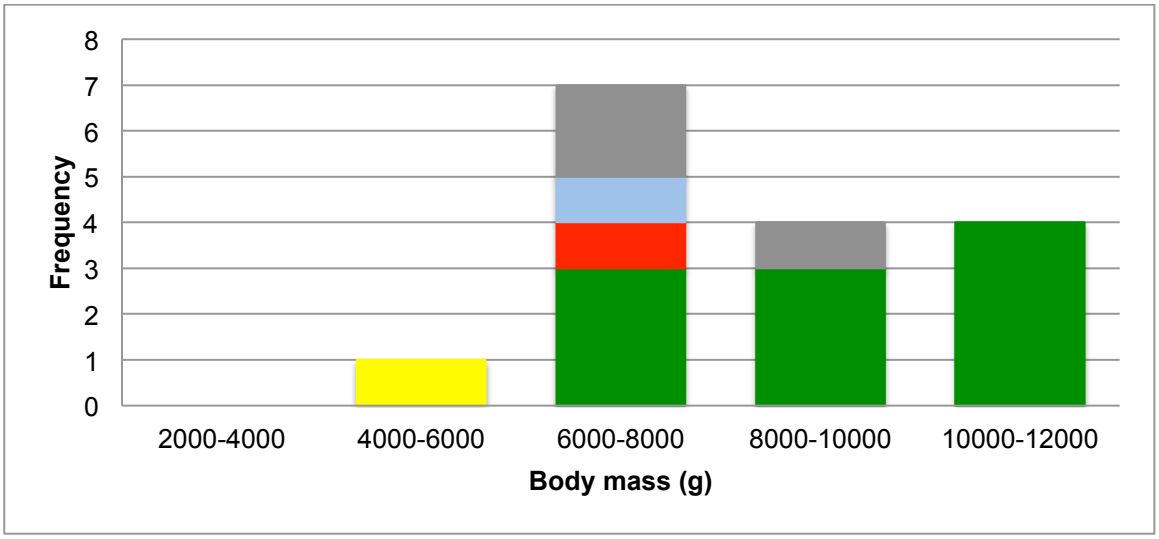
8
7
6
5
4
3
2
1
0
Frequency
2000-4000
4000-6000
6000-8000
8000-10000
10000-12000
Body mass (g)

Figure 3.5. Histograms showing the number of each *Notharctus* species in each body size group for Bridger B (top), C (middle) and D (bottom). Yellow–*N. tenebrosus*, green–*N. pugnax*, red–*N. robustior*, blue–*N. robinsoni*, gray–*N.* sp. indet.

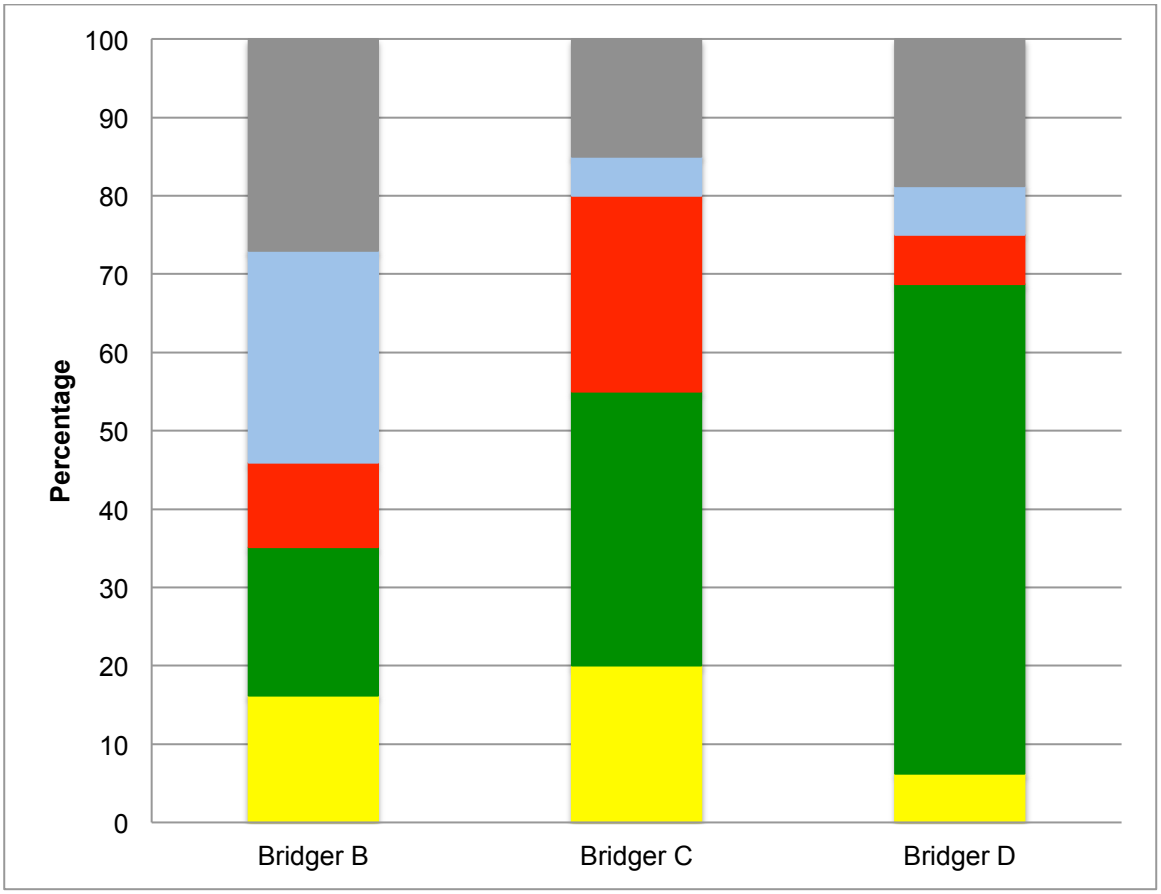

Figure 3.6. Histogram showing the percentage of each *Notharctus* species found in each biozone. Yellow–*N. tenebrosus*, green–*N. pugnax*, red–*N. robustior*, blue–*N. robinsoni*, and gray–*N.* sp.indet.

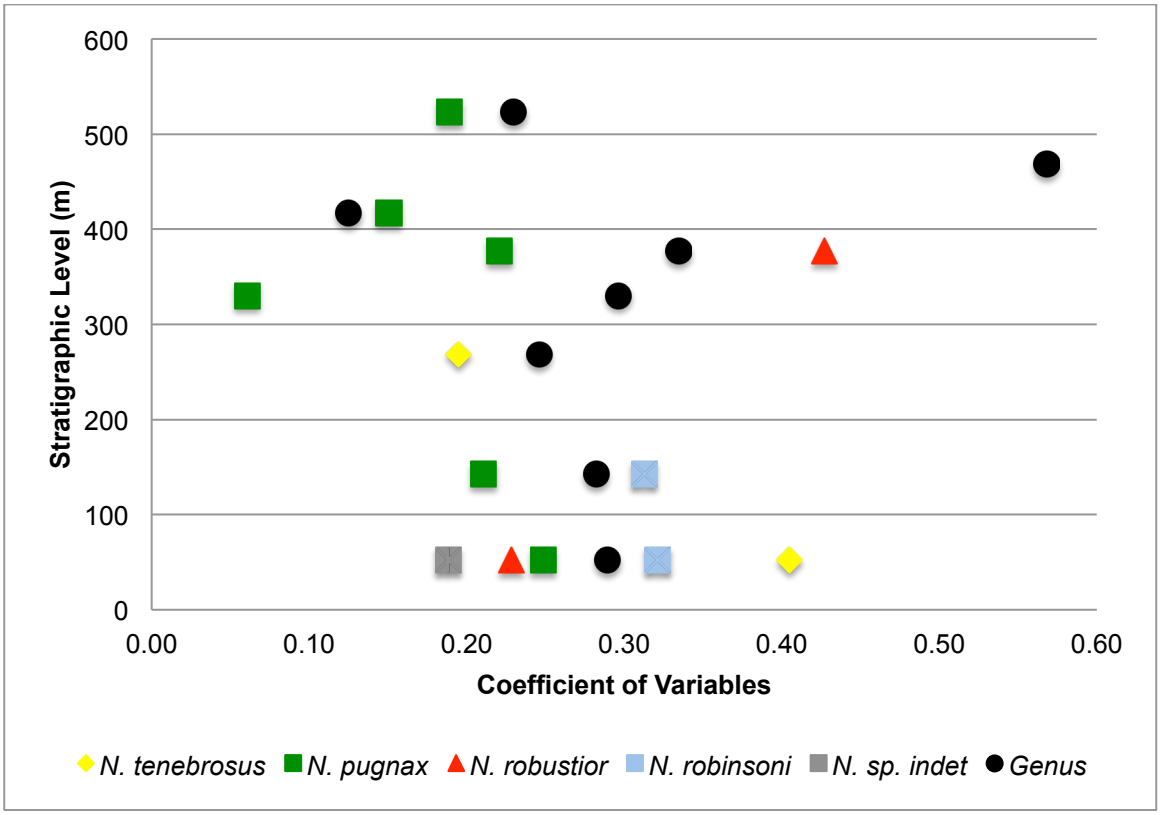

Figure 3.7. Coefficient of variables for the recognized species and genus of *Notharctus*.

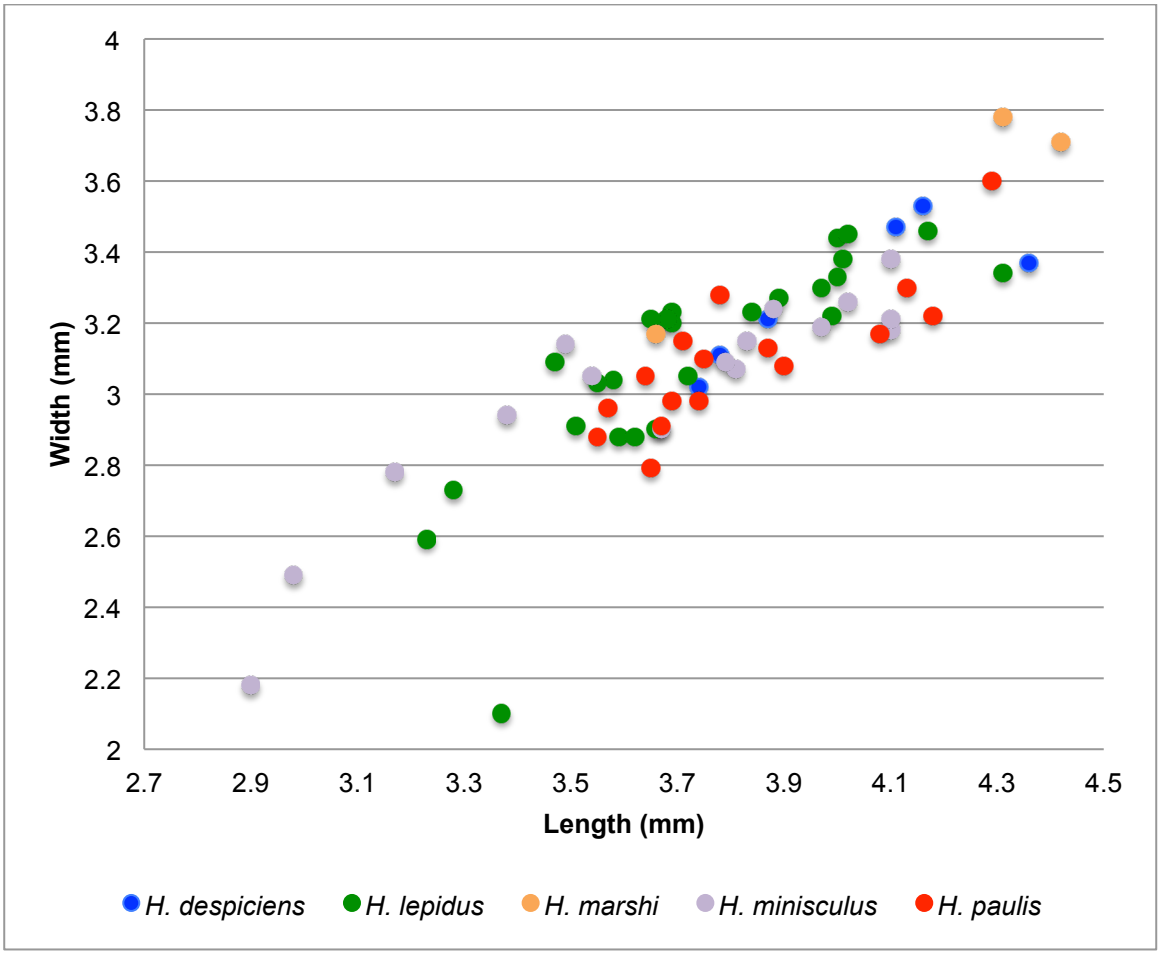

Figure 3.8. Bivariate plot showing the length and width of m1 of *Hyopsodus* specimens from AMNH collections. Species classification is based on dental morphology (see text).

Figure 3.9.A. *H. despiciens*

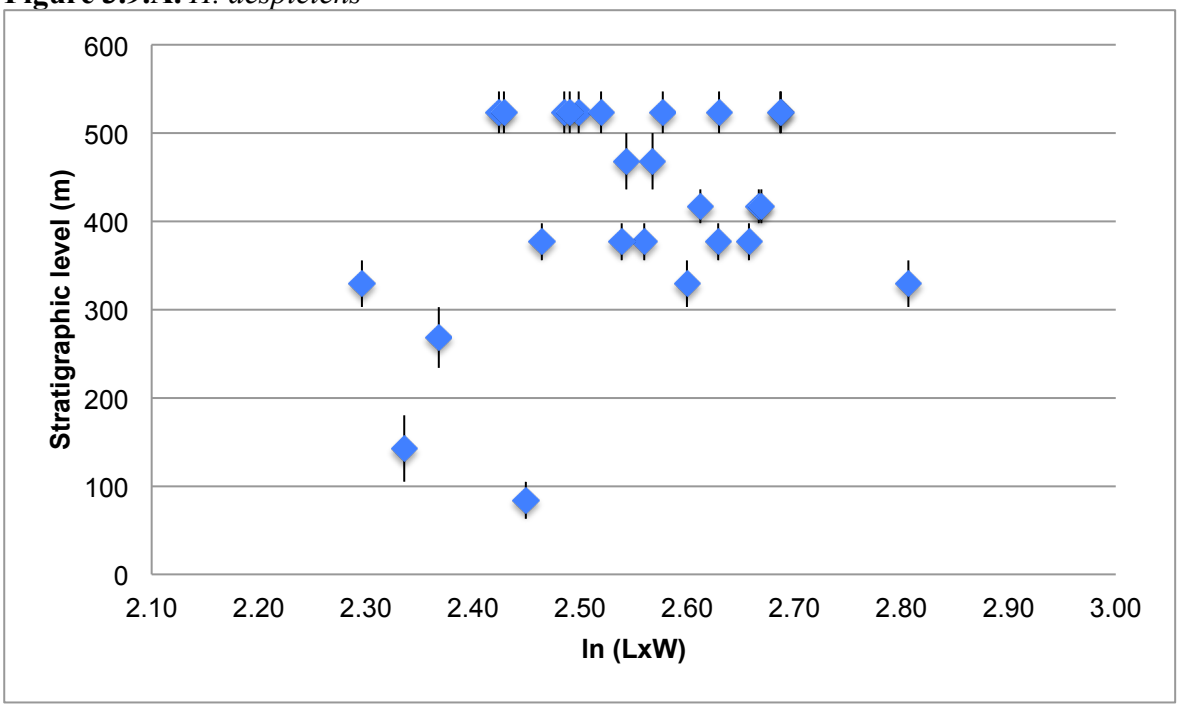

Figure 3.9.B. *H. lepidus*

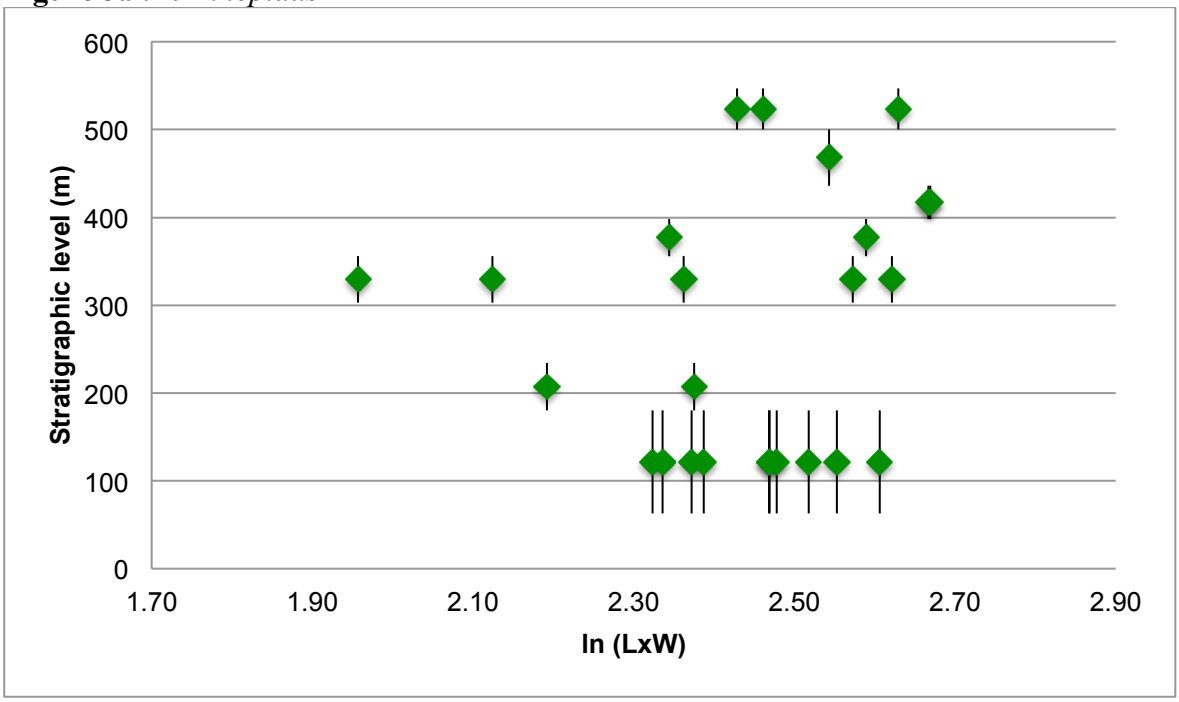

Figure 3.9.C. *H. marshi*

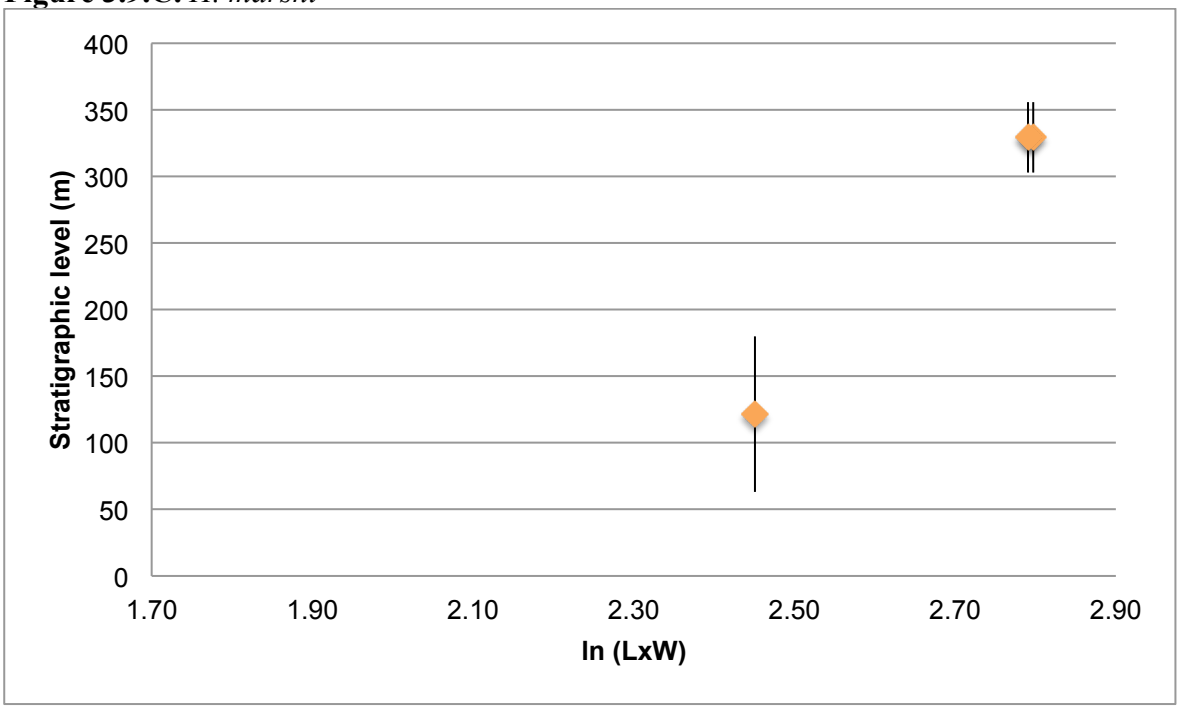

Figure 3.9.D. *H. paulis*

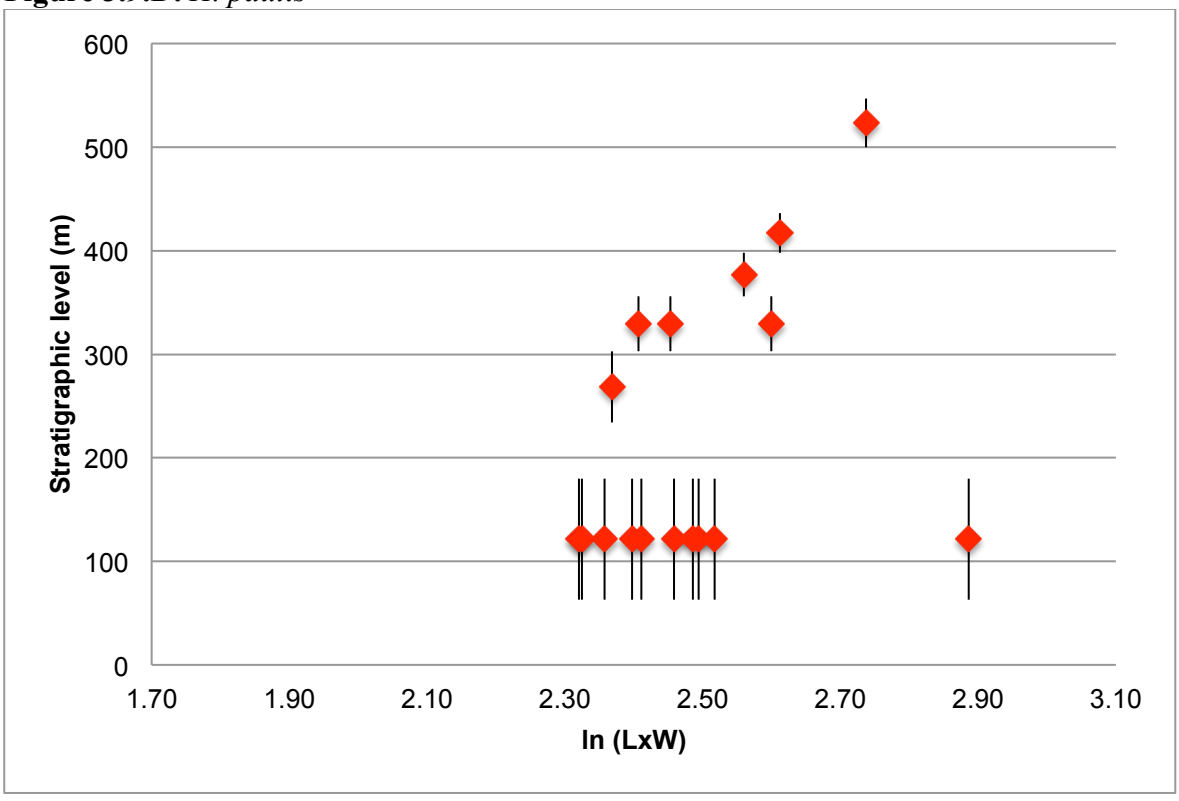

Figure 3.9.E. *H. minisculus*

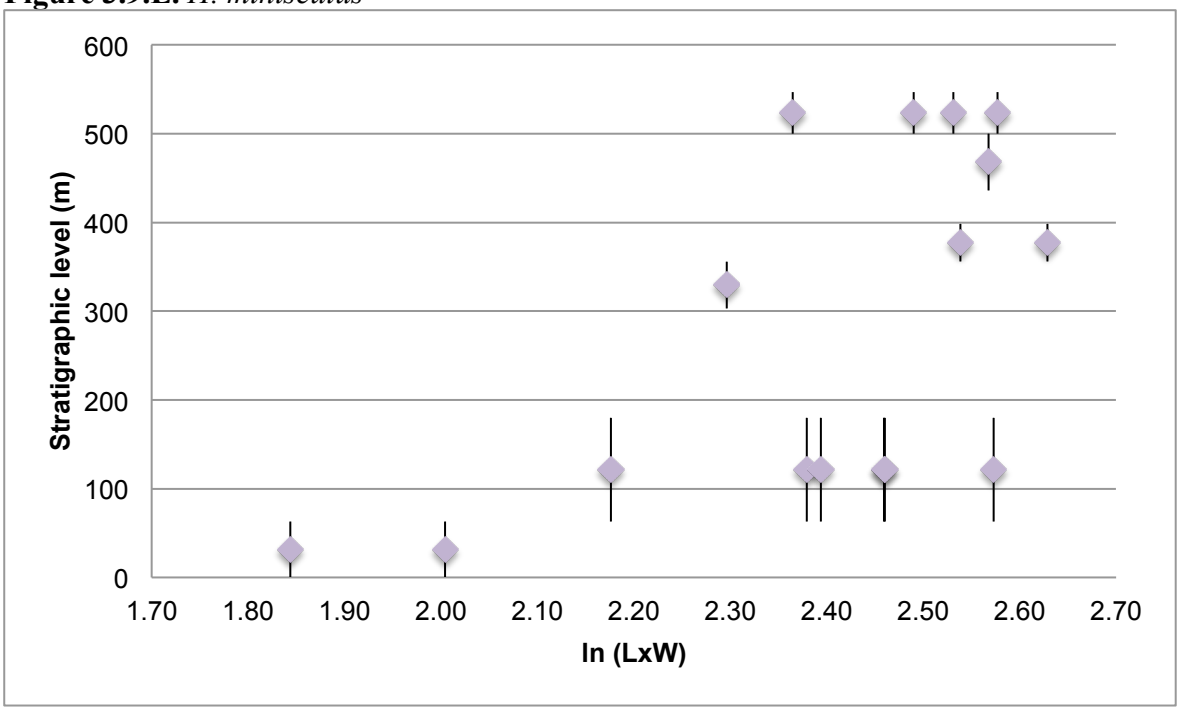

Figure 3.9. Occulusal area of m1 for (A) *Hyopsodus despiciens*, (B) *H. lepidus*, (C) *H. marshi*, (D) *H. paulus*, and (E) *H. minisculus* from the from Bridger B through Bridger D. Specimens were referenced to stratigraphic nomenclature of Murphey and Evanoff (2007), and stratigraphic errors are included where available.

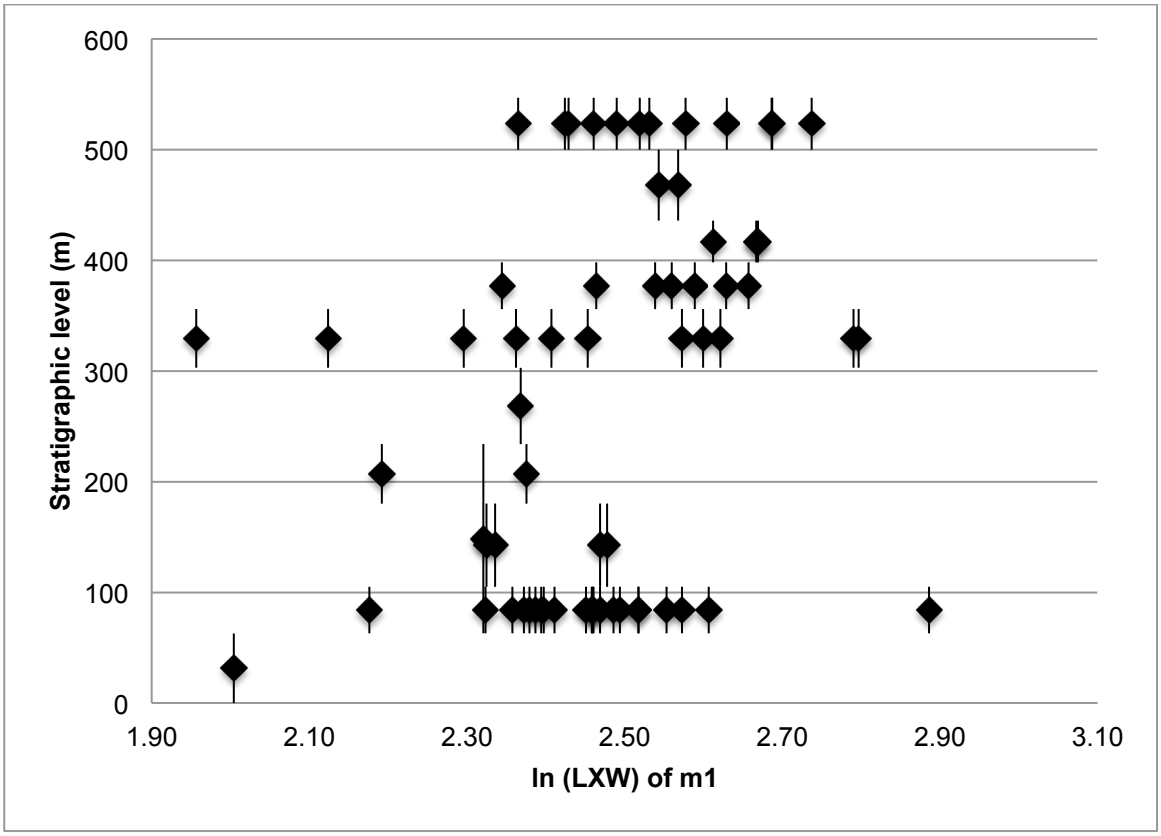

Figure 3.10. Stratigraphic change in the size of m1 in *Hyopsodus* shown at the generic level.

Chapter 4

$^{40}Ar/^{39}Ar$ sanidine geochronology of the Henrys Fork tuff (Middle Eocene) and Fire Clay tonstein (Upper Carboniferous) – critical observations from one laboratory on inter-laboratory calibration and biases

ABSTRACT

$^{40}Ar/^{39}Ar$ dates were obtained from sanidines from the middle Eocene Henrys Fork tuff and Upper Carboniferous Fire Clay tonstein, with the goal of making highly precise measurements of these two samples, keyed to the Fish Canyon monitor standard. Analytically, both samples were well characterized, as had been shown previously. The irradiation disk was arranged such that there would have been control from the Fish Canyon surrounding each of the unknown pits. However, due to several complications in the lab during the course of the experiment, only the analyses from one run disk (Disk 677) were of the quality needed for the goals of the study. As a result, the Fish Canyon sanidine standards that were irradiated near the center of the irradiation disk had to be discarded, and thus, the neutron fluence could not be mapped out precisely across the entire disk. The $^{40}Ar/^{39}Ar$ age relative to Fish Canyon sanidines is 47.828 ± 0.205 Ma and 311.937 ± 1.282 Ma for the Henrys Fork tuff and Fire Clay tonstein, respectively (1σ, including error on the age of the monitor). Because the ages were both offset about the same amount, we explored the option of using the U-Pb ID-TIMS ages of the Henrys Fork tuff and Fire Clay tonstein to test the agreement in the chronometers. The Henrys Fork tuff was dated at 48.260 ± 0.107 Ma (1σ, including error on the age of the monitor)

using the Fire Clay sanidines and assuming its age is the U-Pb zircon age. The Fire Clay tonstein was dated at 314.593 ± 0.699 Ma (1σ, including error on the age of the monitor), using the Henrys Fork sanidines and assuming its age is the U/Pb zircon age. Although the complications encountered render these data unpublishable, they show great promise as the ages of each sanidine sample, tied to the other ash using the other ash's U-Pb age, give results that are in close agreement between the two chronometers on the same sample (e.g., 314.593 ± 0.699 Ma vs. 314.554 ± 0.040 Ma for sanidine and zircon respectively from the Fire Clay tonstein, and 48.260 ± 0.107 Ma vs. 48.265 ± 0.015 Ma for sanidine and zircon respectively from the Henrys Fork tuff). With more careful experimental design and execution, these two ashes could be the much needed monitor standards for the Eocene and Late Paleozoic.

INTRODUCTION

High-resolution integration of diverse geochronological data into one coherent timeline is the ultimate objective of the Geologic Time Scale (Gradstein et al., 2004, 2012). This task, however, is an ongoing effort, as over time the level of attainable precision improves with application of new methodologies as well as technological innovations and analytical developments. Today, one of the most pressing issues in geochronology and timescale-building is cross-calibration of the two most widely used radioisotopic chronometers, the $^{40}Ar/^{39}Ar$ and U-Pb systems. Until recently, $^{40}Ar/^{39}Ar$ and U-Pb dating methods were used to date different periods of the Earth history, with $^{40}Ar/^{39}Ar$ and U-Pb geochronology being the main method of dating the Cenozoic and pre-Cenozoic, respectively. However, as Crowley et al. (2007) and Rivera et al. (2013)

have demonstrated, high precision U-Pb geochronology by ID/CA-TIMS (isotope dilution/chemical abrasion-thermal ionization mass spectrometry) is now applied to zircons that are younger than 2 million years old at a precision of 0.2%, thus extending application of U-Pb zircon geochronology to the youngest part of the timescale and necessitating cross calibration between the two chronometers. Furthermore, improvements in analytical techniques and sensitivities of mass spectrometers have enabled analytical precision in radioisotopic dating to approach the 0.1% level. At such high levels of analytical precision, systematic uncertainties considerably outweigh analytical uncertainties and are now the most critical limiting factor in the accuracy of radioisotopic dating (Min et al., 2000). As it stands today, the absolute accuracy of $^{40}Ar/^{39}Ar$ geochronology is limited to ~2.5% due to systematic uncertainties in the total decay constant of ^{40}K (Min et al., 2000; Renne et al., 2010, 2011) as well as the absolute age of monitor standards such as Fish Canyon sanidines (FCs).

Additional constraint in achieving accurate geochronological data is the inter-laboratory biases among $^{40}Ar/^{39}Ar$ laboratories, which currently limits the accuracy of the $^{40}Ar/^{39}Ar$ method at the 0.5% level for older samples (e.g., Hemming et al., 2013), and at the 1-2% level for younger samples such as Alder Creek (Heizler, 2013; however, see Turrin et al., 2014). As a widely used monitor standard, the FCs well-illustrate the magnitude of existing inter-laboratory biases, as they have been analyzed in many labs with different lab set-ups and data reduction methods. The existing dispersion in estimated ages for the FCs between labs amounts to more than 2% (Schmitz and Bowring, 2001; Daze et al., 2003). In order to reduce inter-laboratory biases, it is necessary to better understand known analytical limitations such as accurate and precise

determination of ^{36}Ar that is used to correct for atmospheric argon contamination and mass spectrometer mass fractionation bias (e.g., Turrin et al., 2010). These systematic and analytical challenges compromise the accuracy of $^{40}Ar/^{39}Ar$ geochronology and hamper its ability to be compared with data obtained by other methods such as high precision U-Pb dating and astronomical tuning.

Over the last decade, the geochronology community has made significant progress in our goals to understand and alleviate the systematic uncertainties in $^{40}Ar/^{39}Ar$ geochronology, but some significant disagreements remain that need to be addressed (e.g., Renne et al., 1994; Baksi et al., 1996; Hilgen et al., 1997; Kwon et al., 2002; Renne et al., 1998; Lanphere and Dalrymple, 2000; Spell and McDougall, 2003; Jourdan and Renne, 2007; Kuiper et al., 2008; Renne et al., 2010, 2011; Rivera et al., 2011). While some studies are comprehensive in nature, their approaches and foci can be broadly classified into one of the following four areas:

1. those that mainly use samples with paired $^{40}Ar/^{39}Ar$ and U-Pb data to address issues regarding the effects of decay constants (e.g., Villeneuve et al., 2000; Min et al., 2000; Schoene et al., 2006; Renne et al., 2010),

2. those that use astrochronology or historical events to calibrate the age of the FCs independent of radioactivity and decay constant uncertainties (e.g., Hilgen et al., 1997, Renne and Min, 1998, , Kuiper et al., 2008, Rivera et al., 2011),

3. those that re-evaluate intercalibration between and/or among primary and secondary $^{40}Ar/^{39}Ar$ standards (Baksi et al., 1996; Spell and McDougall, 2003; Jourdan and Renne, 2007), and finally

4. those that focus on more technical and analytical aspects (Turrin et al., 2010; Cox et al., 2010; Hemming et al., 2013).

However, despite the on-going efforts, the community goal of 0.1% accuracy is yet to be achieved, and it remains important to continue the community-wide effort to assess the concordance between the $^{40}Ar/^{39}Ar$ and U-Pb chronometers from the same samples spanning a large range of ages.

Herein, I present results of single-grain $^{40}Ar/^{39}Ar$ (sanidines) geochronology from two volcanic deposits, the middle Eocene Henrys Fork tuff from the Bridger Formation in the Bridger Basin and the Fire Clay tonstein from the middle Pennsylvanian Hyden Formation in the Appalachian Basin. The aim of this paper is to set the stage for evaluating inter-laboratory and inter-method biases using these two ash beds as exemplars, with the intention of shedding light on the state of our ability to achieve the highest possible accuracy for a $^{40}Ar/^{39}Ar$ sanidine date, at least in one laboratory.

MATERIALS

Henrys Fork Tuff

The Greater Green River Basin in southwestern Wyoming preserves one of the world's most continuous and fossiliferous stratigraphic sequences of early to middle Eocene lacustrine and fluvial strata. The basin deposits contain a number of volcanic ash beds of varying thicknesses (Smith et al., 2003, 2006, 2008, 2010; Machlus et al., 2004, 2015), biostratigraphically useful vertebrate fossils (Matthew, 1909; Gazin, 1976; Gunnell et al., 2009), and cyclic strata linked to orbital cycles (Bradley, 1929; Fischer and Roberts, 1991; Pietras et al., 2003; Meyers, 2008; Machlus et al., 2008; Smith et al.,

2010), making it an ideal setting in which to construct a multi-method chronology for the early to middle Eocene. The volcanic ash beds are thought to have originated from the Challis-Absaroka volcanic field (Surdam and Stanley, 1980), and have previously been dated by $^{40}Ar/^{39}Ar$ and U-Pb dating methods (Murphey et al., 1998; Machlus et al., 2004, 2015; Smith et al., 2008, 2010). Prior radioisotopic studies have demonstrated that many of the tuffs contain abundant phenocrysts amenable for high precision geochronology (especially sanidines and zircons), and in addition, paleomagnetic polarity of many of the tuffs has been determined to test the calibration of the Geomagnetic Polarity Time Scale (Tsukui and Clyde, 2012; this dissertation, Chapter 2). As a result, the basin has produced a large geochronological dataset based on different methods and provides a unique opportunity to conduct cross-calibration studies.

Table 2.1 summarizes the $^{40}Ar/^{39}Ar$ and U-Pb data collected to this date from the ash beds within the Greater Green River Basin. Smith et al. (2003, 2006, 2008) presented $^{40}Ar/^{39}Ar$ data on 17 tuffs from the basin, which form the basis for their basin-wide chronology. Most of their data were collected using a combination of multi- and single-crystal laser incremental heating experiments and/or multi- and single-crystal laser fusion experiments from sanidines, with a few exceptions in which biotites were used instead. Originally, those $^{40}Ar/^{39}Ar$ dates were calculated relative to the Taylor Creek sanidine using a calibration of 28.34 ± 0.28 Ma (relative to the GA-1550 biotite primary standard: 98.79 ± 0.96 Ma; Renne et al., 1998), but Smith et al. (2010) recalculated the dates using the Kuiper et al. (2008) calibration of the FCs (FCs_{K08}), thereby making them directly comparable to U-Pb dates and astrochronological data. Machlus et al. (2004) dated the Main and Layered tuffs using a single-step laser-fusion method on biotites. Those data

are in agreement with the results of Smith et al. (2003), but Machlus et al. (2004) emphasized the importance of single grain analyses, so as to avoid artificial underestimation of error and possible inclusion of xenocrystals of different ages that may not be apparent in the multi-grain analyses.

More recently, Smith et al. (2010) conducted multi-grain ID-TIMS U-Pb zircon analyses on the Firehole and Analcite tuffs, which had previously been dated by $^{40}Ar/^{39}Ar$ geochronology by Smith et al. (2008). The zircon grains were treated with either mechanical abrasion or chemical abrasion, and spiked with $^{208}Pb/^{235}U$ or $^{235}U/^{233}U/^{205}Pb$ (ET535) tracer solution. Eight grains from the Analcite tuff yielded a weighted mean age of 49.23 ± 0.13 (2σ, external error) based on 7 out of 8 grains with MSWD of 6.7. The weighted mean age for the Firehole tuff was 51.66 ± 0.20 (2σ, external error) based on 6 out of 9 grains with MSWD of 11.2. Smith et al. (2010) argued that the U-Pb and FCs_{K08}-calibrated $^{40}Ar/^{39}Ar$ data of the tuffs are in agreement, and thus at the age of ~50 Ma, the two chronometers are concordant when FCs_{K08} is applied.

Machlus et al. (2015) applied single-grain U-Pb ID/CA-TIMS geochronology to seven additional tuffs from the Green River Formation and increased the number of the tuffs from the Greater Green River Basin with paired $^{40}Ar/^{39}Ar$ and U-Pb dates. The weighted mean $^{206}Pb/^{238}U$ dates were based on 6 to 13 single grain analyses, and the summary of the results may be found in Table 2.1. These single-grain U-Pb dates have a precision of ±11 to ±52 kyr, which is less than the period of the astronomical cycle being tested, rendering them useful to test astronomical tuning models for the Paleogene.

Fire Clay Tonstein

The Fire Clay tonstein is an Upper Carboniferous kaolinized volcanic ash deposit from the Hyden Formation. It co-occurs with coal beds and found in a great distance across the Appalachian Basin (Kunk and Rice, 1994; Lyons et al., 2006; Machlus et al., 2006a, 2006b, Hemming et al., 2012). The deposit contains sanidines and zircons as well as monazite. These are all thought to have crystalized during explosive volcanism, and thus the deposit is well suited for intercalibration studies. Kunk and Rice (1994) performed $^{40}Ar/^{39}Ar$ stepwise heating experiments on seven ~100 mg samples of sanidine from the Fire Clay tonstein and reported the mean plateau age of 310.9 ± 1.6 Ma (2σ, using 27.79 ± 0.07 Ma for FCT-3 sanidine and 519.4 ± 2.4 Ma for MMhb-1) that is interpreted to represent an eruption age. Lyon et al. (2006) reported a $^{206}Pb/^{238}U$ single-crystal zircon age of 314.6 ± 0.9 (2σ). However, four out of five zircons showed evidence of inheritance, so the U-Pb age estimate is based only on a single concordant analysis. The saindines of the Fire Clay tonstein have been shown to be homogeneous at the single grain level (total range of 1%) and has been used to assess the pattern and magnitude of inter-laboratory variations among several $^{40}Ar/^{39}Ar$ laboratories (Machlus et al., 2006a, 2006b; Hemming et al., 2012; see Discussion).

LABORATORY PROCEDURES

Bulk samples were crushed with a jaw crusher, sonicated with de-ionized water to remove fine grained sediments, and sieved to concentrate grains that were between 150 μm and 250 μm. The remaining fraction was further separated by Frantz magnetic separator and LST heavy liquids to concentrate the non-magnetic grains that were the density of between 2.62 g/cc and 2.64 g/cc. The minerals were hand picked under a

binocular microscope to isolate grains that had physical properties of sanidines. The chemical compositions of the hand picked grains were confirmed using the Secondary Electron Microscope (SEM) at the American Museum of Natural History. However, the screening using the SEM was not accurate, and as a result, some plagioclase was mixed in with sanidines. For many of the ash beds from the Greater Green River Basin, contamination of sanidines with plagioclase posed a significant problem. SEM analyses were not carried out on the Fire Clay tonstein, as sanidines were relatively abundant in the sample.

The samples considered to be sanidine based on the SEM analyses were then transferred into a 2.5 cm diameter 37-pit aluminum disk for irradiation. In loading the grains, special care was taken not to stack the grains within each well so as to prevent differential dosage of neutron flux in the vertical plane. The samples were loaded in a controlled geometry, such that each sample pit was surrounded by standard pits on four sides for precise determination of J-value, except for the pits on the periphery of the disk which were surrounded by only three standard pits because of the disk edge (Figure 4.1). However, despite the original intent, precise data could not be obtained to constrain the horizontal variation in the J-value due to unforeseen analytical challenges (see following). For characterization of the neutron fluence influx, the FCs were assumed to have an age of 28.201 ± 0.046 Ma as determined by Kuiper et al. (2008), and the decay constants of Min et al. (2000) were applied. Each irradiation disk was vertically stacked along with four other disks and irradiated with fast neutrons for 8 hours at the USGS TRIGA reactor in Denver, CO. All the samples and standards were irradiated in a single batch (LDEO designation: USGS 39C). Interfering isotopes produced by nucleogenic

reactions during irradiation were corrected using the following production ratios: $(39/37)_{Ca}$ = 7.11e-4; $(38/37)_{Ca}$ = 3.29e-5; $(36/37)_{Ca}$ = 2.81e-4; $(38/39)_{K}$ = 1.314e-3; $(40/39)_{K}$ = 1.003e-3; and $(37/39)_{K}$ = 3.32e-4 (Dalrymple et al., 1981)

Once returned from the reactor, the irradiated grains were loaded into a 5 cm diameter, 109-spot stainless steel disk for single-grain total fusion analyses at Lamont-Doherty Earth Observatory (LDEO). The disk had already been thoroughly cleaned with 10% diluted nitric acid before loading. After baking out the extraction line for 4 hours, a set of blanks were run until the blank level had lowered to at least 2.28e-16 moles for ^{40}Ar. In each single-grain analysis, samples were fused with a CO_2 LASER at 7 watts for 60 seconds during which the disk was jogged to ensure thorough coupling of the LASER with the grain. The released gases were admitted into an automated extraction system for a two-stage clean-up for 180 and 120 seconds, during which the gases were exposed to Zr-Fe-V metal alloy getters set at 2 amps to strip off reactive gases such as H_2, CO, CO_2, and N_2, leaving only the inert gases. The remaining noble gases were admitted into a VG5400 mass spectrometer system equipped with a modified Neir ion source, and isotopic measurements were collected by peak hopping in static mode using an analogue multiplier. All analyses were conducted as single-crystal total fusions, and samples, monitor standards, air aliquots and blanks were analyzed using the protocol detailed below. The sensitivity of the mass spectrometer at this time was 8.621E-14 ± 3.63E-16 mol/nA based on glauconite runs on January 8, 2014.

All runs were made with 10 sequential hops in the analogue multiplier in the order of ^{40}Ar, ^{39}Ar, ^{38}Ar, ^{37}Ar, and ^{36}Ar with an integration time of 0.2 seconds for all of the isotopes. We measured 10 counts for ^{40}Ar, 15 counts for ^{39}Ar, 5 counts for ^{38}Ar, 5 counts

for ^{37}Ar, and 40 counts for ^{36}Ar. The multiplier baseline was measured at mass 35.5 after the measurement of ^{36}Ar in the first, fifth, ninth and tenth cycles. No trends were found in the baseline measurements, and the corrections were made based on the average of the measurements. Shots of atmospheric argon were routinely measured to monitor the stability of the mass spectrometer during the analytical period. Blank and air runs were interspersed within the run script such that a sequence of blank-air-blank runs was measured every three unknowns (which include samples and monitor standards). All the measurements reported here were performed over the course of an eight-day period.

RESULTS

Data Reduction

The irradiated grains were analyzed in LDEO-Disks 673 and 677. However, only those from Disk 677 are reported here because the running condition of the mass spectrometer during the analysis of Disk 673 was less than ideal and did not meet the goal of obtaining a high precision $^{40}Ar/^{39}Ar$ dataset. Specifically, air runs made during the analysis of Disk 673 were found to be unstable, and $^{40}Ar/^{36}Ar$ ratios showed higher-than-usual values with a large dispersion. As many as five out of ten cycles had to be deleted in the evolution of ^{40}Ar, and the accuracy in determination of mass discrimination was compromised. The proximal cause of the observed dispersion in $^{40}Ar/^{36}Ar$ is thought to be the asymmetrical peaks and machine's inability to locate the true center. The problem with obtaining a symmetric peak shape was probably caused by low humidity (< 20 %) in the lab at the time of analysis due to a broken humidifier. As a result of this mechanical trouble, all of the analyses run on Disk 673 were regarded as not of high enough precision

to be included in this study. This decision, however, has substantial consequences. Specifically, the FCs from 12 irradiation pits that were analyzed in Disk 673 had to be discarded, and as a consequence, analyses of the two ashes had to be based on a smaller number of FCs than had been intended, and also the initial goal of characterizing the J-value of sample pits by the FCs in the four surrounding pits could not be fulfilled.

Blanks and Air Pipets

The argon isotopic data from the laser single-crystal total fusion analyses were processed with the automated data collection software Mass Spec (developed by Al Deino, Berkeley Geochronology Center). For blanks and air aliquots, isotopic evolution of ^{40}Ar and ^{39}Ar was fitted with either auto-linear or parabolic regression depending on the Goodness of Fit (GOF) measure (Figure 4.2). In most cases, the GOF was better than 0.95 for ^{40}Ar and ^{39}Ar, and no outlier cycles were detected throughout the eight-day analytical period. For ^{38}Ar, ^{37}Ar ^{36}Ar, and multiplier baseline, a linear regression was used to extrapolate the isotopic value at time zero.

Blanks during the eight-day running period varied between ~7.76e-16 moles to ~4.31e-16 moles for ^{40}Ar and ~6.98e-18 moles to ~4.31e-18 moles for ^{36}Ar. Time series of blank measurements were fitted with a cubic regression for ^{40}Ar and ^{36}Ar, with a parabolic regression for ^{39}Ar, and with a linear regression for ^{38}Ar, ^{37}Ar, and the multiplier baseline (Figure 4.3). The interpolated blank contribution was subtracted from the air and unknown runs. The sample-to-background ratio was on average 121.8 and 1.5 for ^{40}Ar and ^{36}Ar, respectively for the Henrys Fork tuff; 310.0 and 1.2 for ^{40}Ar and ^{36}Ar, respectively for the Fire Clay tonstein; and 32.4 and 1.2 for ^{40}Ar and ^{36}Ar, respectively for the FCs.

The mass discrimination was determined based on analysis of the 0.1 cc of on-line air pipets, which had 3.6e-14 moles of ^{40}Ar. The evolution of ^{40}Ar of the air runs was fitted with a cubic regression, and ^{38}Ar and ^{36}Ar were fitted with a linear regression (Figure 4.4). $^{40}Ar/^{36}Ar$ ratios from the 26 air runs were fitted with an arithmetic mean, and the mass discrimination value was calculated to be 1.017 per atomic mass unit relative to the $^{40}Ar/^{36}Ar$ ratio of 298.5 (Lee et al., 2006) with a standard deviation of 0.0027 (Figure 4.5). Measured $^{40}Ar/^{36}Ar$ ratios from the air runs are shown in Figure 4.6.

Isotopic evolutions of the unknowns (which includes the Henrys Fork tuff, Fire Clay tonstein, and FCs) were evaluated carefully, and in most cases, the evolution of ^{40}Ar and ^{39}Ar were fitted with a parabolic regression, and ^{38}Ar, ^{37}Ar and ^{36}Ar with a linear regression (Figure 4.7). In the case of the Henrys Fork tuff, the average GOF measure was >0.99 for ^{40}Ar and ^{39}Ar, >0.7 for ^{38}Ar, 0.2 for ^{37}Ar, and 0.5 for ^{36}Ar. For the Fire Clay tonstein, it was on average 1.00 for ^{40}Ar, 0.995 for ^{39}Ar, 0.430 for ^{38}Ar, 0.194 for ^{37}Ar, and 0.93 for ^{36}Ar. In all cases, isotopic measurements from all 10 cycles were included.

Monitor Standards

The neutron fluence was monitored by the co-irradiated FCs, for which the astronomical calibration age of 28.201 Ma was used (Kuiper et al., 2008). At least three grains from seven aliquots of FCs were analyzed from the irradiation disk "USGS 39C" (Figure 4.1). However, it must be noted that despite the original intent to tightly estimate the J-value of the sample pits by surrounding them with four pits of the FCs, unfortunately, the FCs that were run in the well-characterized Disk 677 happened to be from the pits on the periphery (shaded pits in Figure 4.1). The FCs from the pits close to

the center of the irradiation disk were run in Disk 673 when the running condition was less than ideal, so the initial objective of having an evenly distributed J-value from the disk was compromised. Of those from Disk 677, the FCs analyses that did not meet the following criteria were excluded: those with: Ca/K < 1 (0 of 41); radiogenic ^{40}Ar (^{40}Ar*) < 97% and > 100% (5 of 41); and runs that were outside of 2 standard deviations (2 of 41). After the exclusion filter was applied, 34 of 41 possible analyses of FCs from the seven irradiation pits (Run ID Numbers 20212, 20228, 20233, 20234, 20238, 20239, and 20240, Figure 4.1) were used to calculate the J-value for the disk. The J-value for each monitor pit was characterized by three to seven analyses, as shown in Table 4.1. The MSWD of the J-value for each monitor pit varied between 0.22 and 0.89, with the exception of aliquot 20238, for which MSWD was 4.73. Taking all 34 analyses that passed the exclusion criteria, the disk-wide weighted mean J-value was determined to be 1.8024e-3 ± 1.3133e-6 with a MSWD of 1.51 (Figure 4.8), and this J-value was applied to all of the samples to calculate the age. The J-value was determined also for three quadrants (upper left, lower left, and lower right) of the irradiation disk, but none of them was more precisely determined than the J-value averaged over the entire disk (Table 4.2). For there was no extreme radial gradient in the J-value across the disk, no spatial correction was applied.

Samples

For the ash samples, less-rigorous outlier detection criteria were used than those for the monitor standards, resulting in exclusion of those with Ca/K ratios > 1 and ^{40}Ar*<92%. For the analyses of the Henrys Fork tuff, the signal intensity and ^{40}Ar*/^{39}Ar were correlated at the R^2 value of 0.2, indicating the absence of a pressure effect that

could have led to increasing the variance (Figure 4.9). The isotopic data for all the runs are presented in Table 4.3 (Henrys Fork tuff), Table 4.4 (Fire Clay tonstein), and Table 4.5 (FCs). In the following, the errors are reported at three levels including: error on unknown population; error on measurement of the monitor; and error on the age of the monitor. For comparison of U-Pb constrained $^{40}Ar/^{39}Ar$ age estimate and U-Pb zircon age, the error including all three parameters was used. It should be noted that the analytical error of the U/Pb zircon dates is very small relative to the errors reported here, and since the zircon samples were measured in the same lab using the same tracer, only the analytical error is needed to make the comparison.

Henrys Fork Tuff. A total of 33 sanidines were irradiated in three irradiation positions (Figure 4.1). Thirty single-grain total fusion analyses passed the outlier detection criteria described above and were included in the weighted-mean age calculation. Of the thirty analyses, nine are from irradiation position 7, 11 analyses are from irradiation position 20, and 10 analyses are from irradiation position 28. The 30 analyses form a single population (Figure 4.10) without any signs of outliers, although there is a slight skewness towards the younger age. When the populations from the three different irradiation positions are compared, they overlap within 2 standard deviations (Figure 4.11). Applying the J-value based on the entire irradiation disk (weighted mean J = 1.8024e-3 ± 1.3133e-6; n=34) to all the 30 analyses yields a weighted mean age of 47.828 ± 0.09/0.205/0.205 Ma (1σ) with a MSWD of 1.8.

Fire Clay Tonstein. All the grains from the Fire Clay tonstein were irradiated in a single irradiation position (20235, Figure 4.1). All but one analysis (20235-04A) passed the outlier detection criteria, and the remaining five single-grain total fusion analyses

form a single population (Figure 4.12). The excluded analysis (20235-04A) is more than 2 standard deviations younger than the mean age. Applying the J-value for the entire irradiation disk, the weighted mean age of the Fire Clay tonstein is 311.937 ± 0.4/1.282/1.282 Ma (1σ) with a MSWD of 0.4.

DISCUSSION

Henrys Fork Tuff

The $^{40}Ar/^{39}Ar$ data of the Henrys Fork tuff show a relatively simple population characterized by a MSWD of 1.8 and an analytical error of 0.18% (1σ), and all analyses from the three aliquots overlap within 2σ. However, as discussed previously, any horizontal gradient in the neutron fluence that may have existed could not be characterized as well as had been intended, and thus, the accuracy of the age reported here is handicapped by the inaccurate J-value. Alternatively, the $^{40}Ar/^{39}Ar$ age of the Henrys Fork tuff could be calculated using the assumption that the highly precise U-Pb age of the co-irradiated Fire Clay tonstein is correct. The Fire Clay tonstein was co-irradiated in the same irradiation disk and is located more proximal to the samples of the Henrys Fork tuff (Figure 4.1). The U-Pb zircon age of the Fire Clay tonstein is 314.554 ± 0.020 Ma (1σ, analytical error, MSWD = 1.2) by ID/CA-TIMS based on 26 single grain analyses (Erin Shea, personal communication). Using the U-Pb age of the Fire Clay tonstein as the monitor, the $^{40}Ar/^{39}Ar$ age of the Henrys Fork tuff was determined to be 48.260 ± 0.09/0.107/0.107 Ma (1σ). The difference between the U-Pb age and the U-Pb constrained $^{40}Ar/^{39}Ar$ age of the Henrys Fork tuff is 0.005 myr at a 0.01% difference (Figure 4.13, Table 4.6). Thus, these results demonstrate that at ~48 Ma, the two

chronometers are equivalent if the $^{40}Ar/^{39}Ar$ age is calibrated with the U-Pb age of the Fire Clay tonstein. In addition, the U-Pb based $^{40}Ar/^{39}Ar$ age is statistically indistinguishable from the FCs_{K08}-calibrated $^{40}Ar/^{39}Ar$ age of the same ash by Smith et al. (2008, 2010) who reported 48.440 ± 0.08/0.13/0.15 Ma (at 2σ, analytical/analytical and intercalibration uncertainty/fully propagated uncertainty) for the Henrys Fork tuff. The difference between the FCs-based $^{40}Ar/^{39}Ar$ age (this study) and U-Pb based $^{40}Ar/^{39}Ar$ age is ~0.6%, and although the origin of the difference is unclear, most likely and parsimonious explanation is the inaccurate determination of the J-value due to the inability to detect any horizontal gradients. In addition, it could also be due to the rather large difference in signal between the Fish Canyon and Henrys Fork sanidines.

The outcome that the U-Pb and $^{40}Ar/^{39}Ar$ chronometers are in agreement is consistent with that of Smith et al. (2010) who claimed equivalency between their U-Pb and $^{40}Ar/^{39}Ar$ ages at ~50 Ma for Firehole and Analcite tuffs from the Green River Formation (Table 2.1). Their $^{206}Pb/^{238}U$ ages, however, are characterized by excess scatter, as indicated by large MSWDs (6,7 and 11.2 for Analcite and Firehole tuffs, respectively), and more data are needed to rigorously prove the equivalency between the two chronometers at that age. At the moment of this writing, U-Pb and $^{40}Ar/^{39}Ar$ paired datasets are available from ca. ~20 samples from a wide range of ages. However, in all cases, one or both of the U-Pb and $^{40}Ar/^{39}Ar$ systems are complicated and do not meet the criteria recommended by Renne et al. (2010). Furthermore, most of them are from pre-Cenozoic deposits because effects of magma residence time of zircons and decay constants are known to diminish in older rocks. However, there is merit in conducting cross-calibration studies in Cenozoic pyroclastic rocks, because a reliable

astrochronology has been established for the last ~60 myr, and it can provide independent constraints that are free of uncertainties due to radioactive decay processes. More work is needed to attain this goal, but the Eocene-aged Henrys Fork tuff would be a viable sample to pursue this question further.

Fire Clay Tonstein

Despite a small number of analyses, single grain $^{40}Ar/^{39}Ar$ analyses of the Fire Clay tonstein showed a well-behaved population characterized by a MSWD of 0.4 and an analytical error of 0.13%. The accuracy of the age, however, is compromised by the aforementioned problem related to characterization of the J-value, but these analytical results provide additional support for the validity of the Fire Clay tonstein as a viable candidate as a $^{40}Ar/^{39}Ar$ monitor standard for the late Paleozoic (Machlus et al., 2006a, 2006b; Hemming et al., 2012). In order to provide a better age estimate for the Fire Clay tonstein, an $^{40}Ar/^{39}Ar$ age was calculated relative to the U-Pb age of the co-irradiated Henrys Fork tuff (this dissertation, Chapter 2). Using the U-Pb age of 48.265 ± 0.008 Ma (1σ, analytical uncertainty), the $^{40}Ar/^{39}Ar$ age of the Fire Clay is 314.593 ± 0.400/0.699/0.700 Ma, which is statistically indistinguishable from its U-Pb age.

A few years ago, a preliminary study was conducted to compare the $^{40}Ar/^{39}Ar$ dates of the Fire Clay tonstein among five labs (University of Wisconsin at Madison, Berkeley Geochronology Center, New Mexico Technology of Institute, Rutgers University, and LDEO). Although the analytical uncertainty was on the order of 0.012 – 0.045% (1σ), that study revealed that there was ~0.5% range in the apparent age. Furthermore, within the range of dispersion, the LDEO age was at the oldest at 315.53 ± 0.04 (2σ, analytical error, using the FCs_{K08} and the decay constants of Min et al., 2000),

but the FCs-based $^{40}Ar/^{39}Ar$ age of the Fire Clay reported here is at the youngest end, increasing the dispersion to ~0.9%. Machlus et al. have carried out preliminary work (currently in preparation for a paper) during the analytical sessions in 2005 and 2006 and showed the comparison of the Fish Canyon, Taylor Creek and GA1550 monitor standards were in good agreement. The study presented here has the dual problems that the Fish Canyon is not as well resolved as desirable, and additionally only six crystals of the Fire Clay were used, while in the Machlus study hundreds of measurements were made involving at least three different irradiation disks.

Lessons Learned and Future Studies

In this study, the experiment was designed with an emphasis on obtaining the highest possible precision $^{40}Ar/^{39}Ar$ data. To the end, the samples were loaded into an irradiation disk such that each sample pit was surrounded in four directions by monitor pits in order to well characterize the neutron fluence across the irradiation disk. However, unforeseen troubles interfered with the research goal, and as a result, all the reliable analyses of the FCs were obtained from those irradiated only in the outer pits. Some of the discrepancies between these $^{40}Ar/^{39}Ar$ results and those obtained in earlier studies are attributed to the inaccuracy in the J-value due to an unidentified flux gradient and other analytical artifact yielding a difference of ~ 0.6%. These results serve to show not only the importance in determining an accurate J-value, but also the realities and difficulties of obtaining highly reliable $^{40}Ar/^{39}Ar$ dates. Keeping in mind that these accidents can and do happen, I argue that it is important to plan an experiment that minimizes the chances of compromised results in the event of unforeseen less-than-ideal analytical conditions. For example, the problem of having all monitor standards come from the perimeter of the

irradiation disk can be avoided by treating a sample pit and three surrounding monitor pits as a single unit when loading the grains into the run disk. This way, one can ensure that at least some of the samples and the monitors that are most relevant to those samples are always analyzed under similar conditions. The failure to average out the neutron fluence is a leading candidate in my assessment of the reasons for not having been able to match the previous estimates for Henrys Fork and Fire Clay sanidines in this study. Another lesson to be learned in this experiment is the abundance of argon. The sample-to-background ratio for ^{40}Ar was significantly larger for the Henrys Fork and Fire Clay samples than for FCs. For the Henrys Fork tuff and Fire Clay tonstein, the ratios were 121.8 and 310.0, respectively, but for the FCs, it was only 32.4. In order to minimize biases that might result from such differences, for high precision $^{40}Ar/^{39}Ar$ dating, it is ideal to keep the dynamic range of the measured isotopes at a minimum. In the next phase of this experiment, it is crucial to analyze the FCs from a larger fraction, to match the sample to background ratio of the samples.

Furthermore, the sensitivities and linearity characteristics of detectors are also likely to vary within a lab over time and also between labs. In order to minimize such effects on the quality of the isotopic data, one possible solution is to devise additional $^{40}Ar/^{39}Ar$ monitor standards to minimize the sample and standard age differences to help reduce inter-laboratory biases. The need for more standards is important also in view of minimizing the effect of uncertainties in the decay constants on the $^{40}Ar/^{39}Ar$ ages. As pointed out by Hemming et al. (2011), the effect of uncertainties in the decay constants can be reduced if the ages of the unknown and monitor standard are close to one another. Towards the community goal of inter-laboratory biases of less than 0.1%, I argue that the

development of additional standards from a wide range of ages is critical and from analytical standpoints, the Fire Clay tonstein and Henrys Fork tuff are both viable candidates as a monitor standard for the Paleozoic and Paleogene, respectively.

As part of the EARTHTIME initiative, an organized and collaborative inter-calibration experiment is now underway to evaluate the inter-laboratory biases among $^{40}Ar/^{39}Ar$ labs. One of the difficulties with the problem of inter-laboratory biases in $^{40}Ar/^{39}Ar$ geochronology is that there are many free variables, and it is difficult to identify causes of the discordances. In order to find the most effective way to reduce inter-laboratory biases, the Argon Pipette Intercalibration System (APIS) experiment was designed by Turrin and others. By design, this experiment eliminates the problem of sample heterogeneity and creates a condition in which the potential sources of inter-laboratory inconsistencies are reduced to only a few factors, including gas purification, data reduction, and isotopic measurement. All the participating labs measure the same gas with the same isotopic composition at different gas volumes. So far, the experiment has been conducted at Rutgers, LDEO and New Mexico Tech, and in a preliminary report, Turrin et al. (2014) showed that the reported ages for the Alder Creek sanidines ranged by ~2% between 1.173 and 1.200 Ma (relative to FCs age of 28.02 Ma) during the initial experiments led by Heizler in which solid samples of Fish Canyon and Alder Creek sanidines were distributed. However, in the initial APIS experiments, two of the labs that were the most discrepant during the Heizler experiment found agreement at the 0.1% level (Turrin et al., 2014). The researchers involved in the experiment are not of one mind regarding the reason for the previous lack of agreement or the reason for the better agreement now. Certainly all of the participating labs have made a significant effort since

the experiments in 2007 to improve their analytical strategies. Turrin is convinced that the most important factor is holding the partial pressure of ^{40}Ar near constant in the mass spectrometer for standard and unknowns. He considers that it is possible to reduce the dispersion in beam intensity and pressure-dependent mass discrimination, and ultimately achieve the EARTHTIME goal of 0.1% precision. It is clear that this goal will be greatly facilitated by the distribution of standard gases, much like the distribution of a single tracer solution and synthetic zircon solutions greatly improved the agreement among U-Pb labs.

CONCLUSIONS

$^{40}Ar/^{39}Ar$ measurements were obtained from sanidines of the Middle Eocene Henrys Fork tuff and Upper Carboniferous Fire Clay tonstein. Relative to the co-irradiated FCs, I could not obtain highly accurate $^{40}Ar/^{39}Ar$ dates because of an inaccurate J-value, but using the U-Pb age of the other co-irradiated sample, I report precise $^{40}Ar/^{39}Ar$ ages that are indistinguishable from their corresponding U-Pb ages at 1σ. The differences between the ages determined using the two isotopic systems are in both cases less than 0.1% (that is less than the analytical uncertainty for the $^{40}Ar/^{39}Ar$ results), and thus, these results show promise that for the last ~300 myr, the $^{40}Ar/^{39}Ar$ and U-Pb systems are equivalent at the community goal of 0.1% at 1σ.

On the other hand, the ~0.6% bias from using the FCs is sobering, and I would like to emphasize the importance of having precise data on determining the neutron fluence. One way to circumvent this bias problem is to use a neutron fluence monitor that is close in age (and composition) to the sample that is being dated. The Henrys Fork tuff

and Fire Clay tonstein are both viable candidates for the Eocene and late Paleozoic, respectively, as their internal precision indicates a lack of complexity in the data, and homogeneity on a single grain scale has been demonstrated (Machlus et al., 2006a, 2006b). The relative contribution of the uncertainty in the decay constant can also be minimized by using a fluence monitor whose age is similar to the unknown. Finally, several sources of biases within my measurements that could provide hints about inter-laboratory biases were identified in this experiment. In the meantime, the on-going APIS experiment promises a better understanding of inter-laboratory biases. Although in some ways my experiment did not meet the original goals, the detailed presentation of my analytical procedures to promote transparency in the reporting, analysis and interpretation of data and the data treatment underlying the final reported ages is an important step toward my personal goal of achieving reliable results at the 0.1% level.

REFERENCES CITED

Baksi, A.K., Archibald, D.A., and Farrar, E., 1996, Intercalibration of $^{40}Ar/^{39}Ar$ dating standards: Chemical Geology, v. 129, p. 307–324.

Bradley, W.H., 1929, The varves and climate of the Green River epoch: U.S. Geological Survey Professional Paper, v. 158, p. 87–110.

Cox, S.E., Hemming, S.R., Turrin, B.D., Swisher, C.C., 2010, Nonlinearity of argon isotope measurements for samples of different sizes: Abstract V31A-2301 presented at 2010 Fall Meeting, AGU, San Francisco, Calif., 13-17 Dec.

Crowley, J.L., Schoene, B., and Bowring, S.A., 2007, U–Pb dating of zircon in the Bishop Tuff at the millennial scale: Geology, v. 35, p. 1123–1126.

Dalrymple, G.B., Alexander, E.C., Lanphere, M.A. and Kraker, G.P., 1981, Irradiation of samples for $^{40}Ar/^{39}Ar$ dating using the geological survey TRIGA reactor: USGS Professional Papers, v. 1176, 29 p.

Daźe A., Lee, J.K.W., and Villeneuve, M., 2003, An intercalibration study of the Fish Canyon sanidine and biotite $^{40}Ar/^{39}Ar$ standards and some comments on the age of the Fish Canyon Tuff: Chemical Geology, v. 199, p. 111–127.

Fischer, A.G., Roberts, L.T., 1991, Cyclicity in the Green River Formation (lacustrine Eocene) of Wyoming: Journal of Sedimentary Petrology, v. 61, p. 1146–1154.

Gazin, C.L., 1976, Mammalian faunal zones of the Bridger middle Eocene: Smithsonian Contributions to Paleobiology, v. 26, 25 p.

Gradstein, F.M., Ogg, J.G., and Smith, A.G., 2004, A Geologic Time Scale 2004: Cambridge, U.K., Cambridge University press, 610 p.

Gradstein, F.M., Ogg, J.G., Schmitz, M.D., and Ogg, G.M., 2012, The Geologic Time Scale 2012: Oxford, U.K., Elsevier, 1176 p.

Gunnell, G.F., Murphey, P.C., Stucky, R.K., Townsend, K.E., Robinson, P, Zonneveld, J.P., and Bartels, W.S., 2009, Biostratigraphy and biochronology of the latest Wasatchian, Bridgerian, and Uintan North American Land-Mammal "Ages.", *in* Albright, L.B. III, ed., Papers on Geology, Vertebrate Paleontology, and Biostratigraphy in Honor of Michael O. Woodburne: Museum of Northern Arizona, Flagstaff, Arizona, Museum of Northern Arizona Bulletin, v. 65, p. 279-330.

Heizler, M.T., 2013, Noise is now signal: Capturing the relevant from the distraction: Mineralogical Magazine, v. 77, p. 1281.

Hemming, S.R., Tsukui, K., Mesko, G.T., Ali, G., Cai, Y., Adler, A., Campbell, S., Crapster-Pregont, E., Doherty, C., Gombiner, J., Russell, J., Templeton, J., Tremblay, M. and Vankeuren, M., 2011, Intercalibration of Ar-Ar standards and samples at Lamont-Doherty Earth Observatory: Mineralogical Magazine**,** v. 75 p. 1006.

Hemming, S, Heizler, M.T., Jicha, B., Machlus, M., Rasbury, E.T., Renne, P.R., Singer, B.S., Swisher, C.C. and Turrin, B.D., 2012, Inter-laboratory evaluation of $^{40}Ar/^{39}Ar$ Data for sanidines from the Fire Clay tonstein: Mineralogical Magazine, v. 76, p. 1832.

Hemming, S.R., Turrin, B., and Swisher, C., III, 2013, Progress on inter-laboratory calibration of argon isotope measurements: Geological Society of America Abstracts with Programs*,* v. 45, p. 289.

Hilgen, F.J., Krijgsman, W., and Wijbrans, J.R., 1997, Direct comparison of astronomical and $^{40}Ar/^{39}Ar$ ages of ash beds: Potential implications for the age of mineral dating standards: Geophysical Research Letters, v. 24, p. 2043-2046.

Jourdan, F., and Renne, P.R., 2007, Age calibration of the Fish Canyon sanidine $^{40}Ar/^{39}Ar$ dating standard using primary K–Ar standards: Geochimica et Cosmochimica Acta, v. 71, p. 387–402.

Kuiper, K.F., Deino, A., Hilgen, F.J., Krijgsman, W., Renne, P.R., and Wijbrans, J.R., 2008, Synchronizing rock clocks of Earth history: Science, v. 320, p. 500-504.

Kunk, M.J., and Rice, C.L., 1994, High-precision $^{40}Ar/^{39}Ar$ age spectrum dating of sanidine from the Middle Pennsylvanian Fire Clay tonstein of the Appalachian basin: Geological Society of America Special Paper, v. 294, p. 105-113.

Kwon, J., Min, K., Bickel, P.J., and Renne, P.R., 2002, Statistical methods for jointly estimating the decay constant of ^{40}K and the age of a dating standard: Mathematical Geology, v. 34, p. 457-474.

Lanphere, M.A., and Dalrymple, G.B., 2000, First-principles calibration of ^{38}Ar tracers; implications for the ages of $^{40}Ar/^{39}Ar$ fluence monitors: U.S. Geological Survey Professional Paper, v. 1621, 10 p.

Lee, J.-Y., Marti, K., Severinghaus, J.P., Kawamura, K., Yoo, H.-S., Lee, J.B., and Kim, J.S., 2006, A redetermination of the isotopic abundances of atmospheric Ar: Geochimica et Cosmochimica Acta, v. 70, p. 4507–4512.

Lyons, P.C., Krogh, T.E., Kwok, Y.Y., Davis, D.W., Outerbridge, W.F., and Evans, H.T. Jr., 2006, Radiometric ages of the Fire Clay tonstein [Pennsylvanian (Upper Carboniferous), Westphalian, Duckmantian]: A comparison of U-Pb zircon single-crystal ages and $^{40}Ar/^{39}Ar$ sanidine single-crystal plateau ages: International Journal of Coal Geology, v. 67, p. 259-266.

Machlus, M., Hemming, S.R., Olsen, P.E., and Christie-Blick, N., 2004, Eocene calibration of geomagnetic polarity time scale reevaluated: Evidence from the Green River Formation of Wyoming: Geology, v. 32, p. 137-140.

Machlus, M., Crowley, J., Bowring, S.A., Hemming S.R., Rasbury, T., Swisher, C., III, and Turrin, B.D., 2006a, A Possible Standard for Both U/Pb and $^{40}Ar/^{39}Ar$ Dating: The Carboniferous Fire Clay Tonstein: Geological Society of America Abstracts with Programs, v. 38, p.116

Machlus, M., Bowring, S., Hemming, S., Rasbury, T., Swisher, C. and Turrin, B., 2006b, Testing the Carboniferous Fire Clay Tonstein as a Sanidine $^{40}Ar/^{39}Ar$ Standard: Geochimica et Cosmochimica Acta, v. 70, p. A380.

Machlus, M.L., Olsen, P.E., Christie-Blick, N., and Hemming, S.R., 2008, Spectral analysis of the lower Eocene Wilkins Peak Member, Green River Formation, Wyoming; support for Milankovitch cyclicity: Earth and Planetary Science Letters, v. 268, p. 64-75.

Machlus, M.L., Ramezani, J., Bowring, S.A., Hemming, S.R., Tsukui, K., and Clyde, W.C., 2015, A strategy for cross-calibrating U-Pb chronology and astrochronology of sedimentary sequences: an example from the Green River Formation, Wyoming, USA: Earth Planetary Science Letters, v. 413, p. 70-78.

Matthew, W.D., 1909, The carnivora and insectivora of the Bridger Basin, middle Eocene: American Museum of Natural History Memoirs, v. 9, p. 289-567.

Meyers, S.R., 2008, Resolving Milankovitchian Controversies: The Triassic Latemar Limestone and Eocene Green River Formation: Geology, v. 36, p. 319-322.

Min, K., Mundil, R., Renne, P.R. and Ludwig, K.R., 2000, A test for systematic errors in $^{40}Ar/^{39}Ar$ geochronology through comparison with U–Pb analysis of a 1.1 Ga rhyolite: Geochimica et Cosmochimica Acta, v. 64, p. 73–98.

Murphey, P.C., Lester, A., Bohr, B., Robinson, P., Evanoff, E., and Larson, E., 1999, $^{40}Ar/^{39}Ar$ dating of volcanic ash deposits in the Bridger Formation (middle Eocene), southwestern Wyoming: Geological Society of America Abstracts with Programs, v. 31, p. A233.

Pietras, J.T., Carroll, A.R., Singer, B.S., and Smith, M.E., 2003, 10 k.y. depositional cyclicity in the early Eocene: stratigraphic and $^{40}Ar/^{39}Ar$ evidence from the lacustrine Green River Formation: Geology, v. 31, p. 593–596.

Renne, P.R., Deino, A.L., Walter, R.C., Turrin, B.D., Swisher, C.C., Becker, T.A., Curtis, G.H., Sharp, W.D., and Jaouni, A.-R., 1994, Intercalibration of astronomical and radioisotopic time: Geology, v. 22, p. 783–786.

Renne, P.R., Swisher, C.C., Deino, A.L., Karner, D.B., Owens, T.L., and DePaolo, D.J., 1998, Intercalibration of standards, absolute ages and uncertainties in $^{40}Ar/^{39}Ar$ dating: Chemical Geology, v. 145, p. 117-152.

Renne, P.R., and Min, K., 1998, $^{40}Ar/^{39}Ar$ dating of the 79 AD eruption of Vesuvius: An ab initio basis for improved accuracy in $^{40}Ar/^{39}Ar$ geochronology: Mineralogical Magagine, v. 62A, p. 1255–1256.

Renne, P.R., Mundil, R., Balco, G., Min, K. and Ludwig, K.R., 2010, Joint determination of ^{40}K decay constants and $^{40}Ar^*/^{40}K$ for the Fish Canyon sanidine standard, and improved accuracy for $^{40}Ar/^{39}Ar$ geochronology: Geochimica et Cosmochimica Acta, v. 74, p. 5349–5367.

Renne, P.R., Balco, G., Ludwig, K.R., Mundil, R., and Min, K., 2011, Response to the comment by W.H. Schwartz et al. on "Joint determination of ^{40}K decay constants and $^{40}Ar^*/^{40}K$ for the Fish Canyon sanidine standard, and improved accuracy for $^{40}Ar/^{39}Ar$ geochronology" by P.R. Renne et al. (2010): Geochimica et Cosmochimica Acta, v. 75, p. 5097-5100.

Rivera, T.A., Storey, M., Zeeden, C., Hilgen, F.J., and Kuiper, K., 2011, A refined astronomically calibrated $^{40}Ar/^{39}Ar$ age for Fish Canyon sanidine: Earth and Planetary Science Letters, v. 311, p. 420-426.

Rivera, T.A., Storey, M., Schmitz, M.D., and Crowley, J.L., 2013, Age intercalibration of $^{40}Ar/^{39}Ar$ sanidine and chemically distinct U-Pb zircon populations from the Alder Creek Rhyolite Quaternary geochronology standard: Chemical Geology, v. 345, p. 87-98.

Schmitz, M.D. and Bowring, S.A., 2001, U–Pb zircon and titanite systematics of the Fish Canyon Tuff: an assessment of highprecision U–Pb geochronology and its application to young volcanic rocks: Geochimica et Cosmochimica Acta, v. 65, p. 2571–2578.

Schoene, B., Crowley, J.L., Condon, D.J., Schmitz, M.D. and Bowring, S.A., 2006, Reassessing the uranium decay constants for geochronology using ID-TIMS U/Pb data: Geochimica et Cosmochimica Acta, v. 70, p. 426–445.

Smith, M.E., Singer, B., and Carroll, A., 2003, $^{40}Ar/^{39}Ar$ geochronology of the Eocene Green River Formation, Wyoming: Geological Society of America Bulletin, v. 115, p. 549–565.

Smith, M.E., Singer, B.S., Carroll, A.R., and Fournelle, J.H., 2006, High-resolution calibration of Eocene strata: $^{40}Ar/^{39}Ar$ geochronology of biotite in the Green River Formation: Geology, v. 34, p. 393–396.

Smith, M.E., Carroll, A.R., and Singer, B.S., 2008, Synoptic reconstruction of a major ancient lake system: Eocene Green River Formation, western United States: Geological Society of America Bulletin, v. 120, p. 54-84.

Smith, M.E., Chamberlain, K.R., Singer, B.S., and Carroll, A.R., 2010, Eocene clocks agree; coeval $^{40}Ar/^{39}Ar$, U-Pb, and astronomical ages from the Green River Formation: Geology, v. 38, p. 527-530.

Spell, T.L., and McDougall, I., 2003, Characterization and calibration of $^{40}Ar/^{39}Ar$ dating standards: Chemical Geology, v. 198, p. 189-211.

Surdam, R.C., and Stanley, K.O., 1980, Effects on changes in drainage basin boundaries on sedimentation in Eocene Lakes Gosiute and Uinta of Wyoming, Utah, and Colorado: Geology, v. 8, p. 135-139.

Tsukui, K. and Clyde, W.C., 2012, Fine-tuning the calibration of the early to middle Eocene geomagnetic polarity time scale: Paleomagnetism of radioisotopically dated tuffs from Laramide foreland basins: Geological Society of America Bulletin, v. 124, p. 870-885.

Turrin, B.D., Swisher, C.C., III and Deino, A.L., 2010, Mass discrimination monitoring and intercalibration of dual collectors in noble gas mass spectrometer systems, Geochemistry, Geophysics, Geosystems, v. 11, Q0AA09.

Turrin, B.D., Swisher, C.C. III, Hemming, S.R., Renne, P.R., Deino, A.L., Hodges, K.V., Van Soest, M.C., and Heizler, M.T., 2014, Argon Intercalibration Pipette System (APIS): Smoking from the same pipe: Abstract V41A-4786 presented at 2014 Fall Meeting, AGU, San Francisco, Calif., 15-19 Dec.

Villeneuve, M., Sandeman, H.A., and Davis, W.A., 2000, A method for intercalibration of U–Th–Pb and $^{40}Ar–^{39}Ar$ ages in the Phanerozoic: Geochimica et Cosmochimica Acta, v. 64, p. 4017–4030.

Table 4.1. Analysis of monitor standards and calculated J-values.

Pit No.*	Run ID	MSWD	n	Weighted mean J	± SEM
3	20212	0.22	3	1.8022E-03	4.4242E-06
23	20228	0.50	3	1.8057E-03	4.2488E-06
29	20233	0.64	6	1.8092E-03	3.1376E-06
30	20234	0.50	7	1.8015E-03	3.1204E-06
34	20238	4.73	7	1.7983E-03	2.8067E-06
35	20239	0.89	3	1.8053E-03	4.2894E-06
37	20240	0.48	5	1.7974E-03	3.3765E-06

*See Figure 4.1 for the position of the pit.

Table 4.2. J-value for different parts of Irradiation Disk 39C.

	Included Aliquots	n	Weighted mean J	SEM error	MSWD
All disk	20212, 20228, 20233, 20234, 20238, 20239, 20240	34	1.8024E-03	1.3133E-06	1.51
Lower left	20228, 20234, 20239	13	1.8036E-03	2.1696E-06	0.56
Lower right	20233, 20238, 20240	18	1.8015E-03	1.7782E-06	2.49
Upper right	20212	3	1.8022E-03	4.4242E-06	0.22

Table 4.3. Ar isotopic data for Henrys Fork tuff.

Run ID	$^{36}Ar/^{39}Ar$ (x100)	$^{37}Ar/^{39}Ar$ (x100)	Ca/K	$^{38}Ar/^{39}Ar$ (x100)	$^{40}Ar/^{39}Ar$	$^{40}Ar^*/^{39}Ar$	$^{40}Ar^*/^{39}Ar$ Er	$\%^{40}Ar^*$	Age	Age Er with J er	^{39}Ar Moles	^{40}Ar Moles
20215-10A	0.047	0.798	0.0156	1.286	14.779	14.640	0.033	99.1	47.91	0.13	1.17E-15	1.72E-14
20215-08A	0.072	1.081	0.0212	1.278	14.881	14.668	0.032	98.6	48.01	0.12	1.48E-15	2.20E-14
20215-07A	0.071	0.702	0.0138	1.305	14.884	14.675	0.029	98.6	48.03	0.12	2.03E-15	3.02E-14
20215-09A	0.076	0.789	0.0155	1.271	14.901	14.677	0.040	98.5	48.04	0.15	7.86E-16	1.17E-14
20215-12A	0.018	0.832	0.0163	1.243	14.740	14.687	0.042	99.6	48.07	0.15	6.92E-16	1.02E-14
20215-14A	0.040	0.728	0.0143	1.233	14.822	14.703	0.037	99.2	48.12	0.14	9.00E-16	1.33E-14
20215-11A	0.020	0.713	0.0140	1.300	14.802	14.742	0.038	99.6	48.25	0.14	8.47E-16	1.25E-14
20215-15A	0.055	1.179	0.0231	1.248	14.915	14.753	0.055	98.9	48.28	0.19	4.52E-16	6.74E-15
20215-13A	0.020	0.714	0.0140	1.310	14.824	14.765	0.040	99.6	48.32	0.15	7.71E-16	1.14E-14
Irradiation ID: USGS39C												
J = 0.0018385												
J error = 0.0000027213												
20226-11A	0.011	0.699	0.0137	1.270	14.682	14.650	0.028	99.8	47.98	0.12	2.02E-15	2.97E-14
20226-08B	0.100	0.908	0.0178	1.292	14.954	14.657	0.035	98.0	48.01	0.14	1.18E-15	1.77E-14
20226-10A	0.025	1.042	0.0204	1.290	14.734	14.660	0.085	99.5	48.02	0.29	2.62E-16	3.87E-15
20226-09B	0.027	0.773	0.0151	1.290	14.760	14.680	0.028	99.5	48.08	0.12	2.00E-15	2.95E-14
20226-13A	0.062	0.817	0.0160	1.283	14.864	14.681	0.033	98.8	48.08	0.14	1.17E-15	1.74E-14
20226-10B	0.034	0.733	0.0144	1.287	14.782	14.681	0.033	99.3	48.08	0.14	1.09E-15	1.62E-14
20226-08A	0.057	0.955	0.0187	1.254	14.849	14.681	0.045	98.9	48.08	0.17	6.64E-16	9.85E-15
20226-07B	0.074	0.808	0.0158	1.290	14.935	14.715	0.034	98.5	48.20	0.14	1.10E-15	1.64E-14
20226-12A	0.024	0.852	0.0167	1.273	14.789	14.718	0.030	99.5	48.20	0.13	1.73E-15	2.55E-14
20226-14A	0.056	0.986	0.0193	1.283	14.902	14.736	0.037	98.9	48.26	0.15	9.20E-16	1.37E-14
20226-07A	0.282	0.603	0.0118	1.312	15.629	14.794	0.061	94.7	48.45	0.21	4.32E-16	6.75E-15
Irradiation ID: USGS39C												
J = 0.0018399												
J error = 0.0000032739												
20232-10A	0.027	0.811	0.0159	1.282	14.702	14.622	0.029	99.5	47.90	0.11	1.82E-15	2.68E-14
20232-08A	0.030	1.070	0.0210	1.293	14.735	14.645	0.030	99.4	47.98	0.11	1.65E-15	2.42E-14
20232-06A	0.025	0.732	0.0144	1.269	14.722	14.648	0.028	99.5	47.99	0.10	2.32E-15	3.42E-14
20232-12A	0.043	0.732	0.0143	1.260	14.804	14.677	0.038	99.2	48.08	0.13	8.44E-16	1.25E-14
20232-05A	0.068	0.861	0.0169	1.316	14.880	14.678	0.043	98.6	48.08	0.15	6.68E-16	9.95E-15
20232-02A	0.038	0.791	0.0155	1.306	14.796	14.684	0.034	99.2	48.10	0.12	1.10E-15	1.63E-14
20232-01A	0.194	2.277	0.0446	1.330	15.264	14.691	0.034	96.2	48.12	0.12	1.41E-15	2.15E-14
20232-03A	0.111	0.859	0.0168	1.320	15.043	14.716	0.043	97.8	48.21	0.15	6.87E-16	1.03E-14
20232-07A	0.034	0.670	0.0131	1.290	14.840	14.739	0.047	99.3	48.28	0.16	6.24E-16	9.26E-15
20232-11A	0.069	1.443	0.0283	1.271	14.958	14.756	0.037	98.7	48.33	0.13	9.06E-16	1.36E-14
Irradiation ID: USGS39C												
J = 0.0018402												
J error = 0.00000203												

Table 4.4. Ar isotopic data for Fire Clay tonstein.

Run ID	$^{36}Ar/^{39}Ar$ (x100)	$^{37}Ar/^{39}Ar$	Ca/K	$^{38}Ar/^{39}Ar$	$^{40}Ar/^{39}Ar$	$^{40}Ar^*/^{39}Ar$	$^{40}Ar^*/^{39}Ar$ Er	$\%^{40}Ar^*$	Age	Age Er with J Er	^{39}Ar Moles	^{40}Ar Moles
20235-07A	0.058	0.011	0.0224	0.013	103.124	102.9548	0.217	99.8	312.91	0.70	7.52E-16	7.76E-14
20235-03A	0.034	0.015	0.0292	0.013	103.134	103.0335	0.197	99.9	313.13	0.66	1.25E-15	1.29E-13
20235-01A	0.106	0.015	0.0299	0.013	103.385	103.0735	0.241	99.7	313.24	0.76	5.16E-16	5.34E-14
20235-02A	0.071	0.014	0.0283	0.013	103.339	103.1292	0.215	99.8	313.40	0.70	6.90E-16	7.14E-14
20235-05A	0.088	0.014	0.0266	0.013	103.411	103.1506	0.249	99.7	313.45	0.78	5.08E-16	5.25E-14
Irradiation ID: USGS39C												
J = 0.0018396												
J error = 0.0000023145												

Table 4.5. Ar isotopic data for Fish Canyon sanidines.

Run ID	$^{36}Ar/^{39}Ar$ (x100)	$^{37}Ar/^{39}Ar$ (x100)	Ca/K	$^{38}Ar/^{39}Ar$ (x100)	$^{40}Ar/^{39}Ar$	$^{40}Ar^*/^{39}Ar$	$^{40}Ar^*/^{39}Ar$ Er	$\%^{40}Ar^*$	Age	Age Er	Age Er with J Er	^{39}Ar Moles	^{40}Ar Moles
20212-07A	0.091	0.674	0.0132	1.281	8.850	8.579	0.037	97.0	28.08	0.12	0.12	5.84E-16	5.17E-15
20212-08A	0.045	0.701	0.0137	1.290	8.722	8.586	0.031	98.4	28.10	0.10	0.10	7.26E-16	6.33E-15
20212-09A	0.060	0.694	0.0136	1.284	8.793	8.613	0.036	98.0	28.19	0.12	0.12	6.28E-16	5.52E-15
20228-01A	0.007	0.609	0.0119	1.266	8.582	8.560	0.044	99.8	28.02	0.14	0.14	4.72E-16	4.05E-15
20228-02A	0.038	0.671	0.0131	1.276	8.670	8.556	0.033	98.7	28.01	0.11	0.11	6.70E-16	5.81E-15
20228-03A	0.015	0.592	0.0116	1.253	8.643	8.599	0.027	99.5	28.15	0.09	0.09	8.67E-16	7.49E-15
20233-01A	0.082	0.669	0.0131	1.309	8.835	8.589	0.037	97.2	28.12	0.12	0.12	6.04E-16	5.34E-15
20233-02A	0.074	0.661	0.0130	1.293	8.728	8.506	0.036	97.5	27.85	0.12	0.12	6.48E-16	5.65E-15
20233-04A	0.072	0.574	0.0113	1.285	8.767	8.551	0.040	97.5	27.99	0.13	0.13	5.60E-16	4.91E-15
20233-05A	0.073	0.700	0.0137	1.314	8.764	8.546	0.037	97.5	27.98	0.12	0.12	6.04E-16	5.30E-15
20233-06A	0.055	0.667	0.0131	1.289	8.732	8.566	0.038	98.1	28.04	0.12	0.13	5.74E-16	5.01E-15
20233-07A	0.030	0.771	0.0151	1.311	8.668	8.579	0.025	99.0	28.08	0.08	0.08	9.25E-16	8.01E-15
20234-01A	0.047	0.669	0.0131	1.271	8.728	8.586	0.042	98.4	28.11	0.14	0.14	5.08E-16	4.44E-15
20234-02A	0.027	0.615	0.0120	1.192	8.633	8.552	0.044	99.1	27.99	0.14	0.15	4.56E-16	3.94E-15
20234-03A	0.062	0.491	0.0096	1.260	8.753	8.567	0.044	97.9	28.04	0.14	0.14	4.77E-16	4.18E-15
20234-04A	0.026	0.589	0.0116	1.265	8.659	8.583	0.040	99.1	28.09	0.13	0.13	5.34E-16	4.62E-15
20234-05A	0.025	0.631	0.0124	1.243	8.691	8.618	0.030	99.2	28.21	0.10	0.10	7.16E-16	6.22E-15
20234-06A	0.086	0.626	0.0123	1.263	8.895	8.638	0.040	97.1	28.27	0.13	0.13	5.40E-16	4.81E-15
20234-07A	0.056	0.643	0.0126	1.323	8.766	8.600	0.031	98.1	28.15	0.10	0.10	7.04E-16	6.17E-15
20238-01A	0.037	0.687	0.0135	1.277	8.671	8.559	0.029	98.7	28.02	0.09	0.10	7.90E-16	6.85E-15
20238-02A	0.031	0.654	0.0128	1.221	8.807	8.714	0.037	98.9	28.52	0.12	0.12	5.84E-16	5.15E-15
20238-03A	0.002	0.668	0.0131	1.230	8.699	8.692	0.031	99.9	28.45	0.10	0.10	7.08E-16	6.16E-15
20238-04A	0.097	0.695	0.0136	1.293	8.894	8.603	0.029	96.7	28.16	0.10	0.10	7.91E-16	7.03E-15
20238-05A	0.073	0.733	0.0144	1.254	8.730	8.511	0.041	97.5	27.86	0.13	0.14	5.06E-16	4.42E-15
20238-06A	0.020	0.616	0.0121	1.269	8.566	8.505	0.040	99.3	27.84	0.13	0.13	5.33E-16	4.57E-15
20238-07A	0.092	0.553	0.0108	1.294	8.915	8.641	0.032	96.9	28.29	0.11	0.11	6.92E-16	6.17E-15
20239-03A	0.021	0.649	0.0127	1.289	8.632	8.568	0.027	99.3	28.05	0.09	0.09	9.33E-16	8.06E-15
20239-04A	0.032	0.651	0.0128	1.327	8.715	8.619	0.036	98.9	28.21	0.12	0.12	6.03E-16	5.25E-15
20239-06A	0.056	0.801	0.0157	1.348	8.715	8.549	0.041	98.1	27.98	0.13	0.13	5.34E-16	4.65E-15
20240-01A	0.016	0.779	0.0153	1.284	8.667	8.620	0.044	99.5	28.22	0.14	0.14	4.76E-16	4.12E-15
20240-02A	0.014	0.535	0.0105	1.296	8.701	8.658	0.038	99.5	28.34	0.12	0.13	5.45E-16	4.74E-15
20240-04A	0.028	0.792	0.0155	1.258	8.677	8.592	0.028	99.0	28.12	0.09	0.09	8.03E-16	6.97E-15
20240-05A	0.006	0.610	0.0120	1.285	8.646	8.629	0.035	99.8	28.24	0.11	0.11	6.20E-16	5.36E-15
20240-06A	0.024	0.648	0.0127	1.258	8.676	8.604	0.032	99.2	28.17	0.10	0.10	6.89E-16	5.98E-15

Table 4.6. $^{40}Ar/^{39}Ar$ age of Henrys Fork tuff and Fire Clay tonstein according to different decay constant values and Fish Canyon calibration.

Decay constant/FCs age*	$^{40}Ar/^{39}Ar$ age (Ma)		% difference with U-Pb based $^{40}Ar/^{39}Ar$ age	
	Henrys Fork	Fire Clay	Henrys Fork	Fire Clay
(1)/(4)	47.146	307.491	2.31	2.26
(2)/(4)	47.828	311.937	0.90	0.84
(3)/(4)	47.253	308.187	2.09	2.04
(3)/(3)	48.109	313.383	0.31	0.38
U-Pb based $^{40}Ar/^{39}Ar$ age	48.260	314.593	0	0

*1. Steiger and Jäger (1977); 2. Min et al. (2000); 3. Renne et al. (2010, 2011), 4. Kuiper et al. (2008).

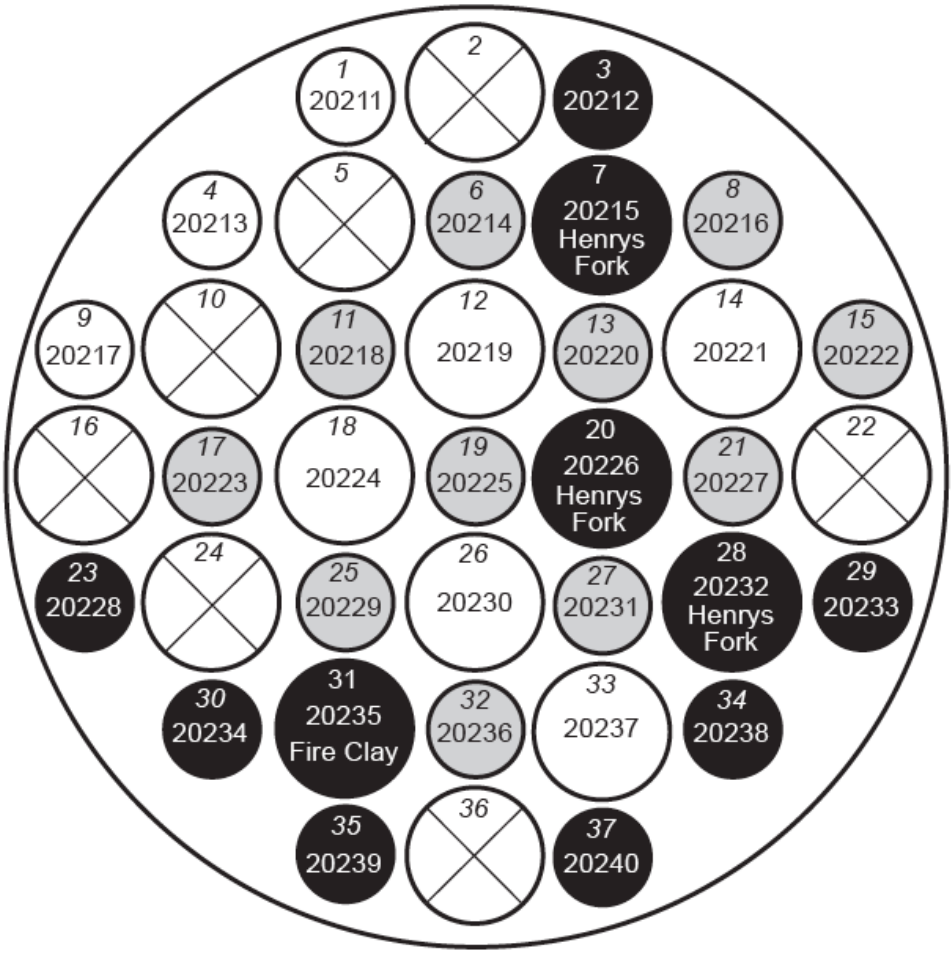

Figure 4.1. Map of Irradiation Disk USGS 39C that contained all of the standards and samples analyzed in this study. Larger pits contained samples whereas smaller pits contained the monitor standards (FCs). This study is based on analyses from those in black pits (samples and standard). The FCs from the pits shaded in gray were run in Disk 673 and not used (see text). Five digit numbers indicate a run number that is specific to each irradiation pit position. The irradiation pits with an "x" were empty. The J-value estimated for each standard pit may be found in Table 4.1.

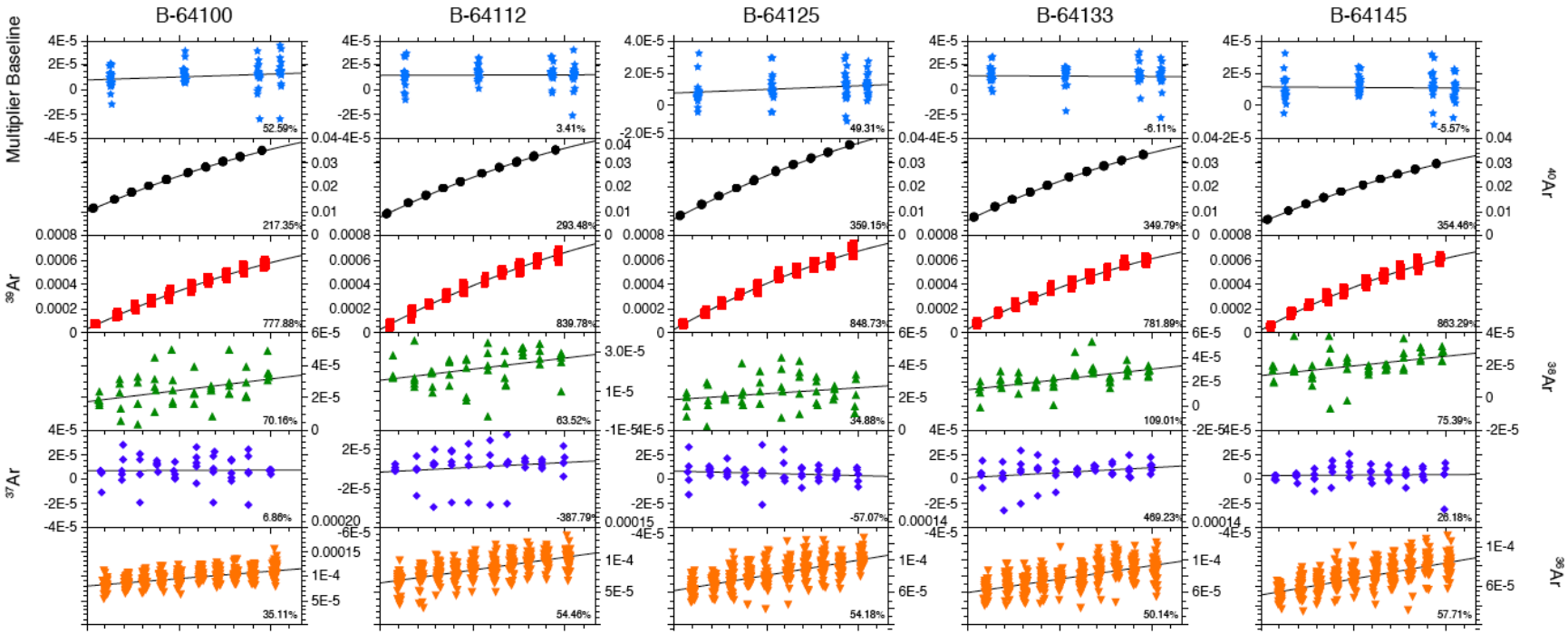
B-64100
B-64112
B-64125
B-64133
B-64145
Multiplier Baseline
39Ar
37Ar
40Ar
36Ar
52.59%
3.41%
49.31%
-6.11%
-5.57%
217.35%
293.48%
359.15%
349.79%
354.46%
777.88%
839.78%
848.73%
781.89%
863.29%
70.16%
63.52%
34.88%
109.01%
75.39%
6.86%
-387.79%
-57.07%
469.23%
26.18%
35.11%
54.46%
54.18%
50.14%
57.71%

Figure 4.2. Representative isotopic evolution of blank runs. ^{40}Ar and ^{39}Ar were fitted with either linear or parabolic fit, while ^{38}Ar, ^{37}Ar, ^{36}Ar, and multiplier baseline were fitted with linear regression. Timing of these analyses is shown in Figure 4.14.

Figure 4.3.A

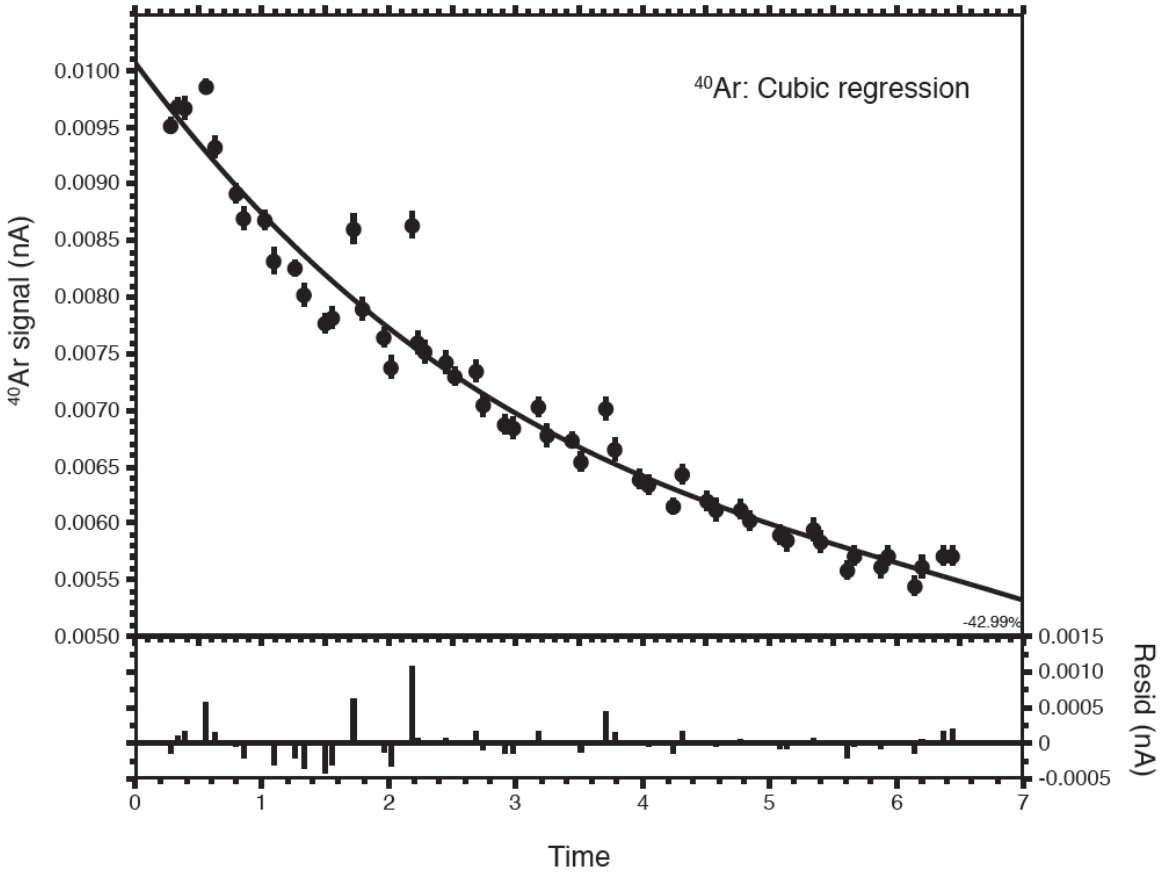
^{40}Ar: Cubic regression
^{40}Ar signal (nA)
0.0100
0.0095
0.0090
0.0085
0.0080
0.0075
0.0070
0.0065
0.0060
0.0055
0.0050
-42.99%
0.0015
0.0010
0.0005
0
-0.0005
Resid (nA)
0
1
2
3
4
5
6
7
Time

Figure 4.3.B

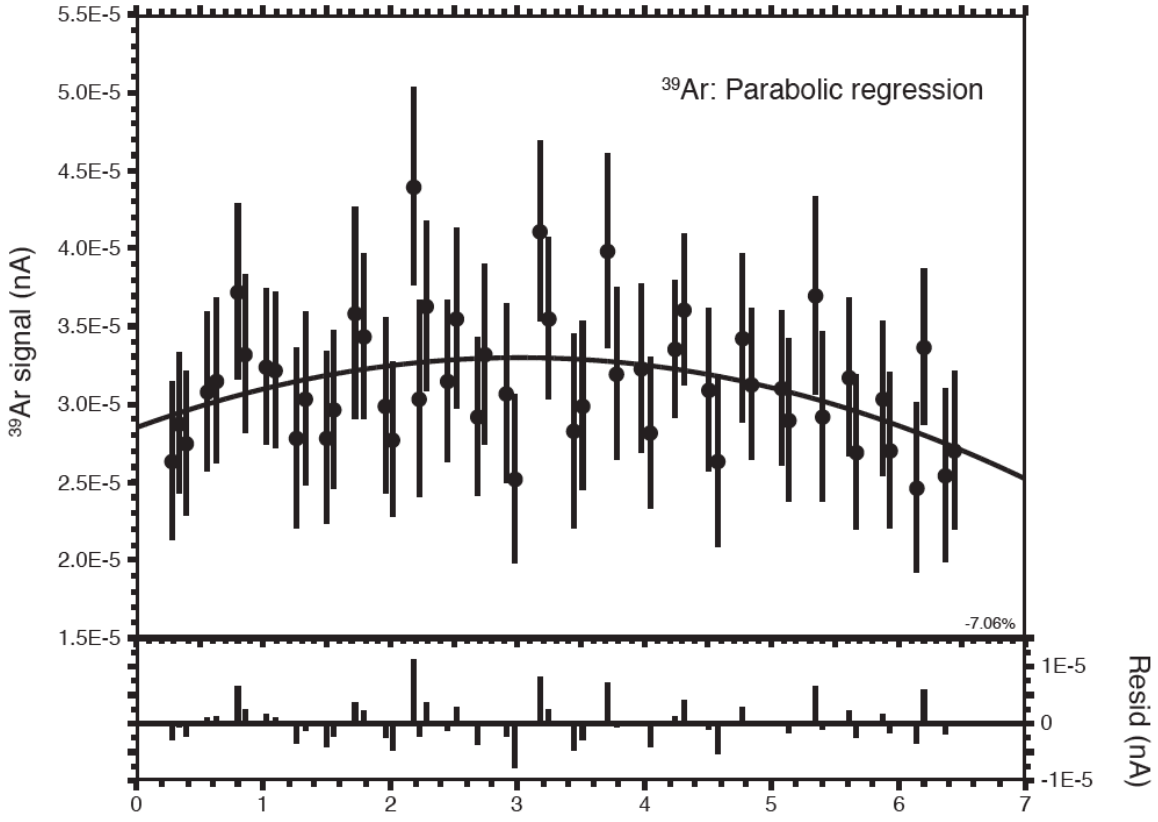
39Ar: Parabolic regression
39Ar signal (nA)
5.5E-5
5.0E-5
4.5E-5
4.0E-5
3.5E-5
3.0E-5
2.5E-5
2.0E-5
1.5E-5
-7.06%
1E-5
0
-1E-5
Resid (nA)
0
1
2
3
4
5
6
7

Figure 4.3.C

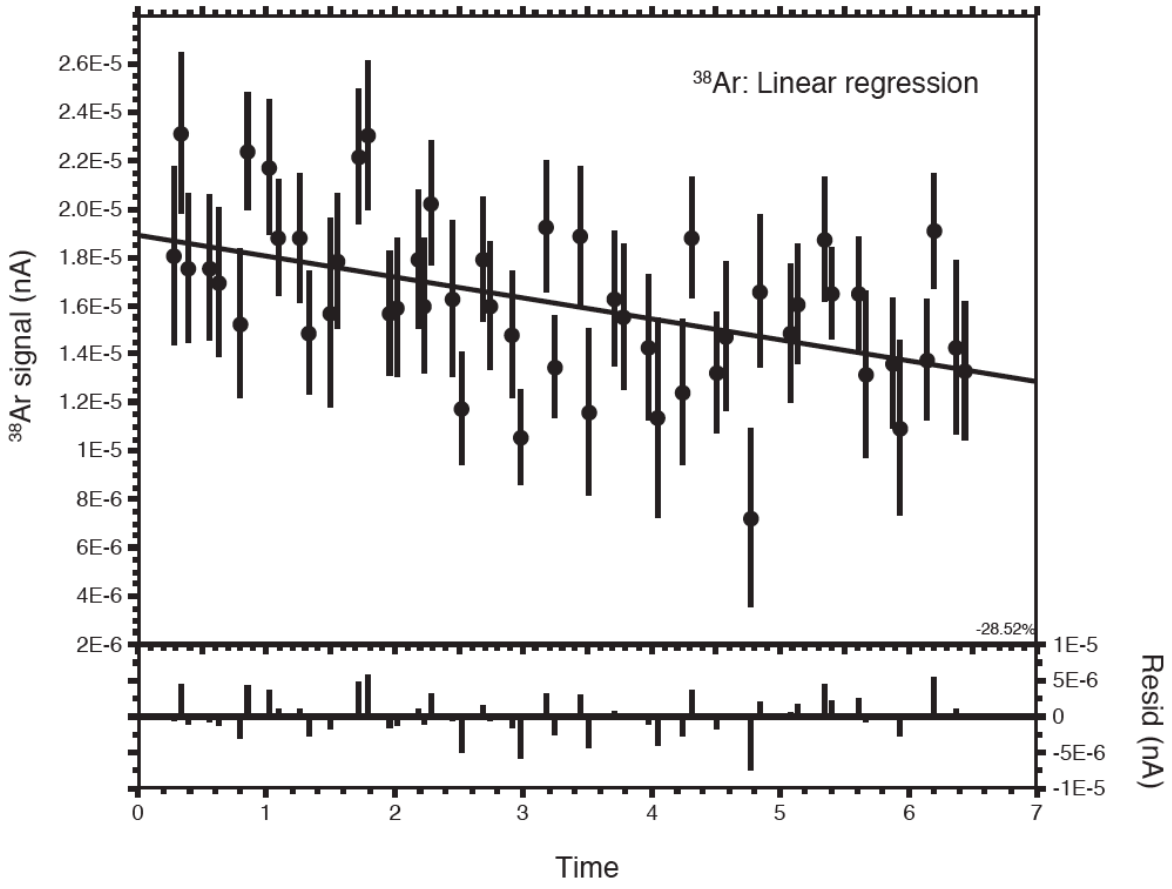
^{38}Ar: Linear regression
^{38}Ar signal (nA)
2.6E-5
2.4E-5
2.2E-5
2.0E-5
1.8E-5
1.6E-5
1.4E-5
1.2E-5
1E-5
8E-6
6E-6
4E-6
2E-6
-28.52%
1E-5
5E-6
0
-5E-6
-1E-5
Resid (nA)
0
1
2
3
4
5
6
7
Time

Figure 4.3.D

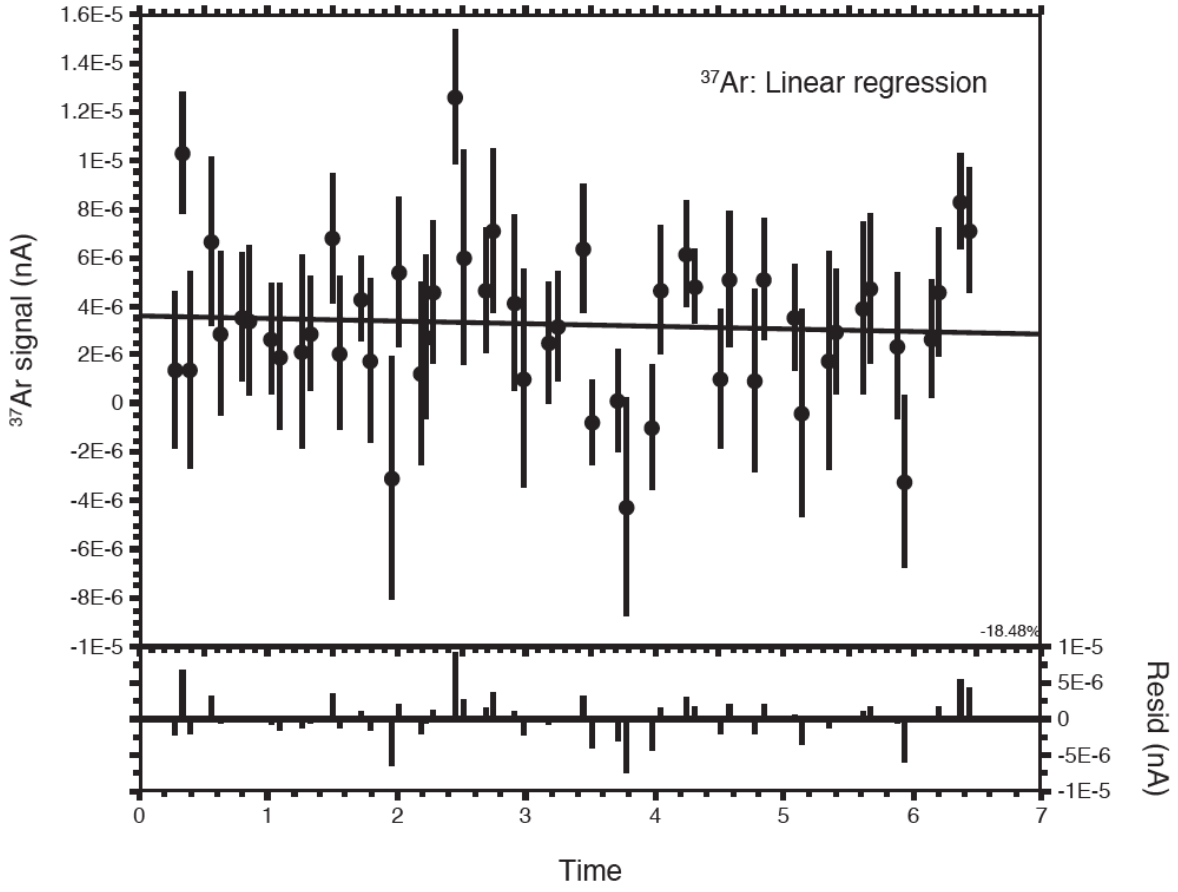
^{37}Ar: Linear regression
^{37}Ar signal (nA)
1.6E-5
1.4E-5
1.2E-5
1E-5
8E-6
6E-6
4E-6
2E-6
0
-2E-6
-4E-6
-6E-6
-8E-6
-1E-5
-18.48%
1E-5
5E-6
0
-5E-6
-1E-5
Resid (nA)
0
1
2
3
4
5
6
7
Time

Figure 4.3.E

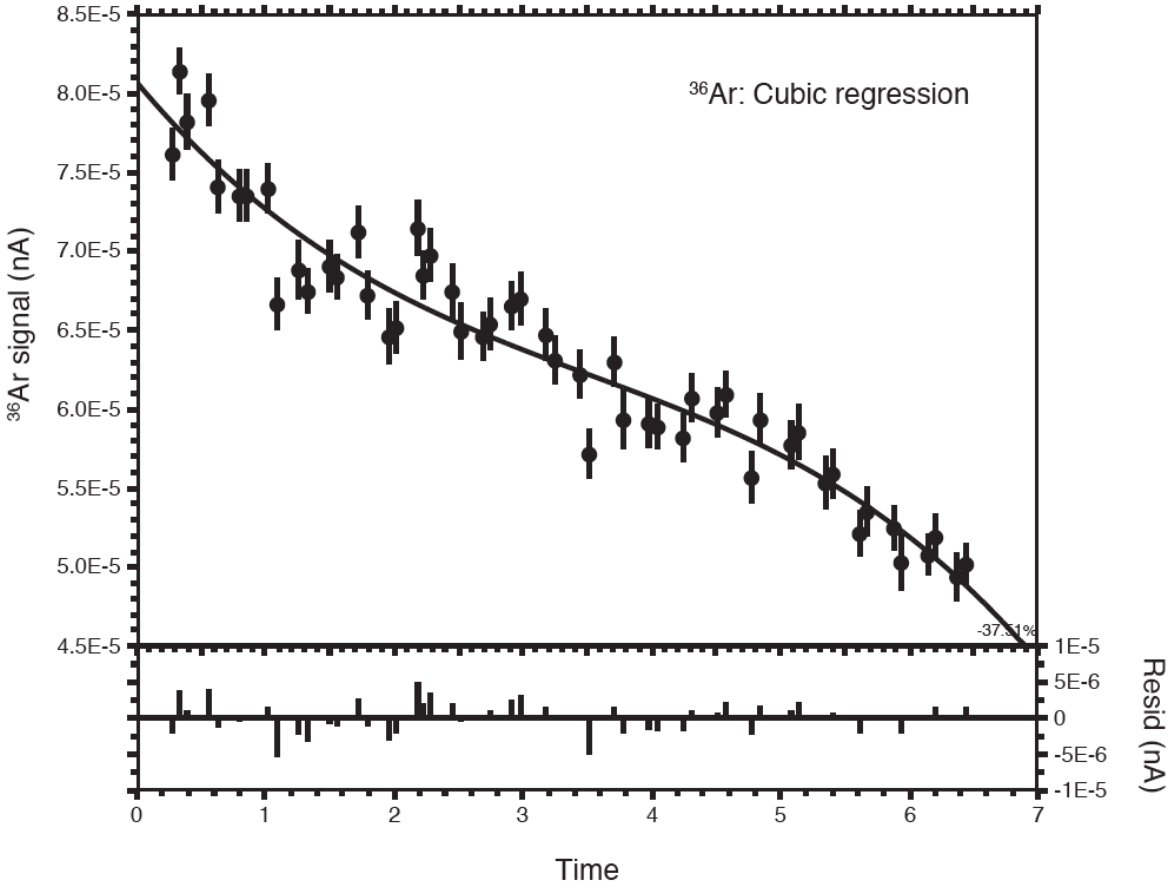
^{36}Ar: Cubic regression
^{36}Ar signal (nA)
8.5E-5
8.0E-5
7.5E-5
7.0E-5
6.5E-5
6.0E-5
5.5E-5
5.0E-5
4.5E-5
1E-5
5E-6
0
-5E-6
-1E-5
Resid (nA)
0
1
2
3
4
5
6
7
Time

Figure 4.3.F

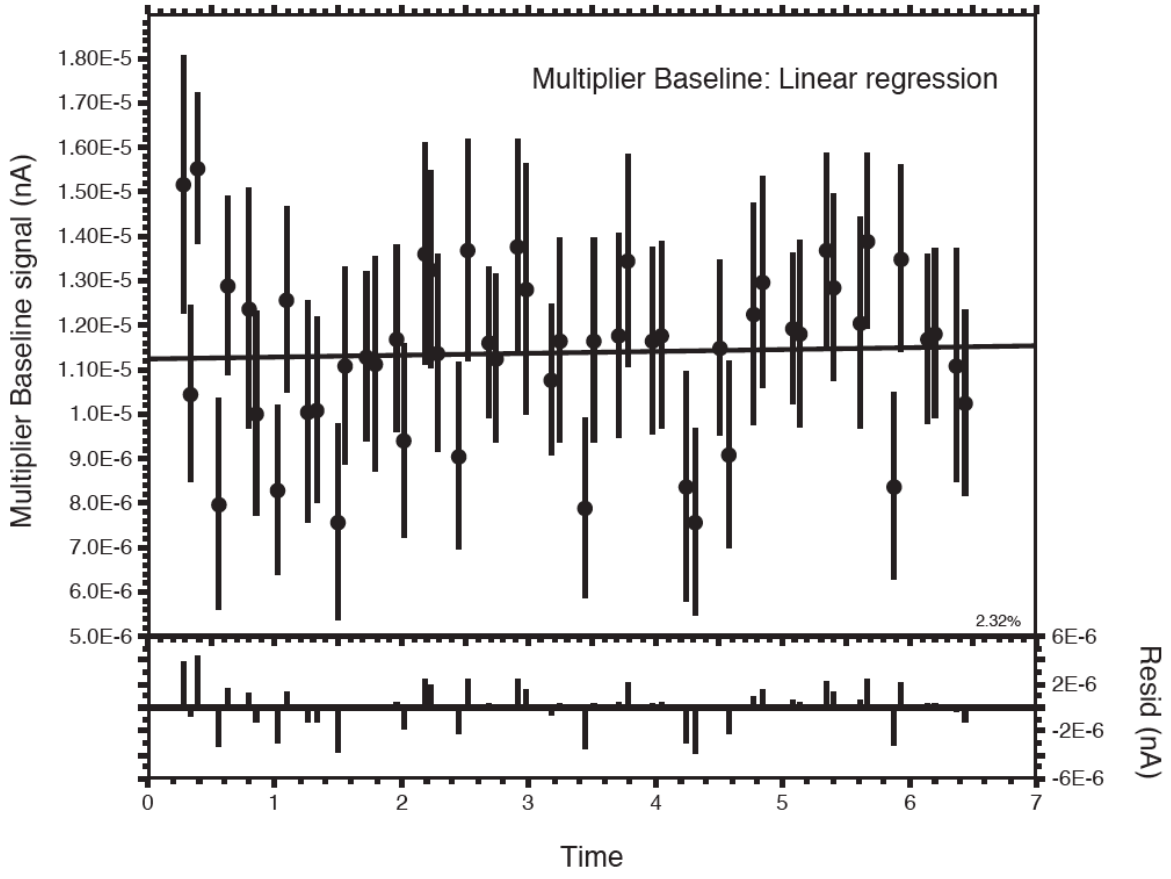

Figure 4.3. Time series of blank runs for (A) ^{40}Ar, (B) ^{39}Ar, (C) ^{38}Ar, (D) ^{37}Ar, (E) ^{36}Ar and (F) multiplier baseline over the course of the analytical period. Type of regression applied to each isotope and multiplier baseline is indicated. Shown at the bottom of each panel is residual signal. Error bars are at 2 sigma.

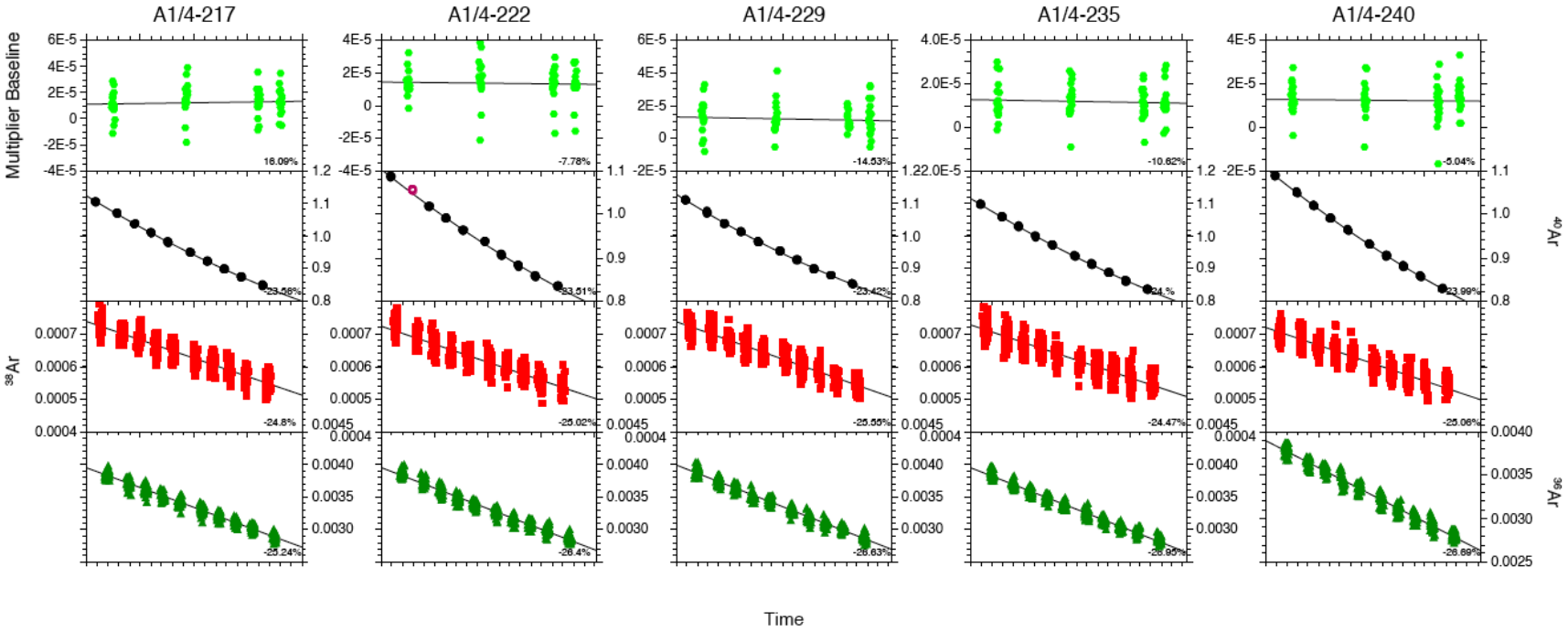
A1/4-217
A1/4-222
A1/4-229
A1/4-235
A1/4-240
Multiplier Baseline
^{38}Ar
^{40}Ar
^{36}Ar
Time

Figure 4.4. Representative isotopic evolution of air pipette analyses at five different times during the period of experiment. ^{40}Ar was fitted with either linear or parabolic fit, while ^{38}Ar, ^{36}Ar and multiplier baseline were fitted with linear regression. Timing of these analyses is shown in Figure 4.14.

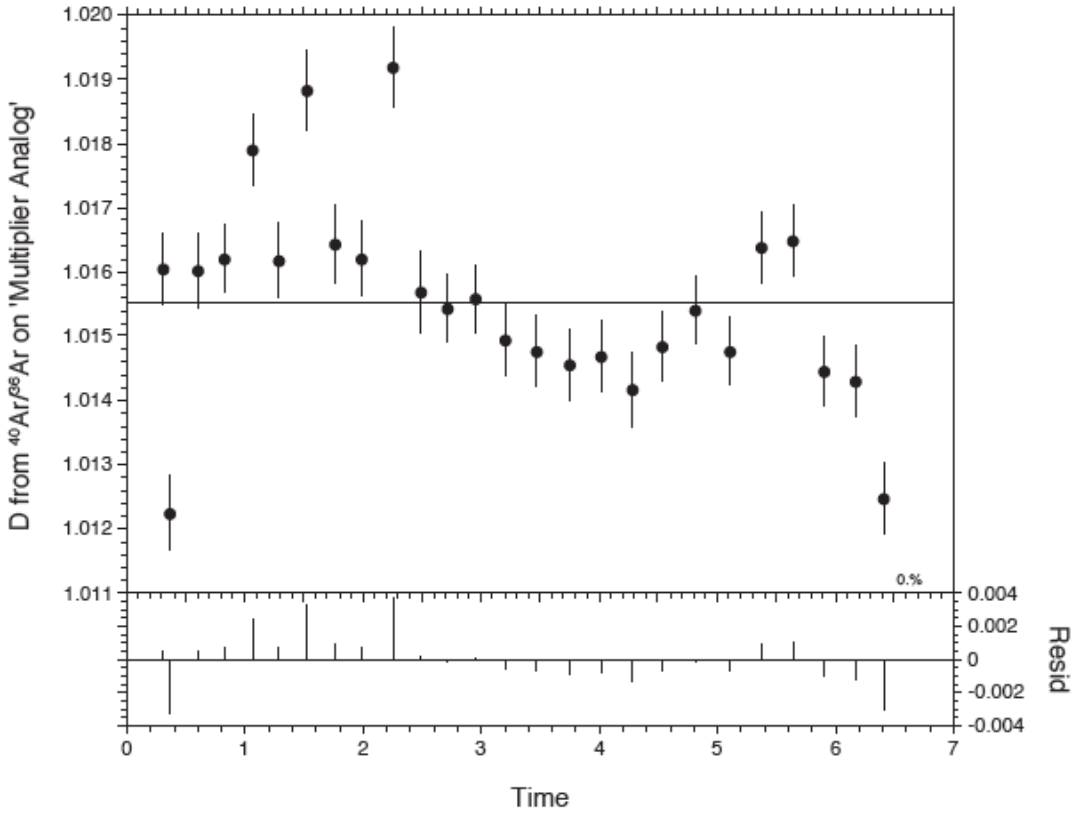

Figure 4.5. Fluctuations of mass discrimination (D) during the period of experiment. It was determined from the $^{40}Ar/^{36}Ar$ values through which an arithmetic mean was fitted. Residual signal is also shown at the bottom. Error bars are at 2 sigma.

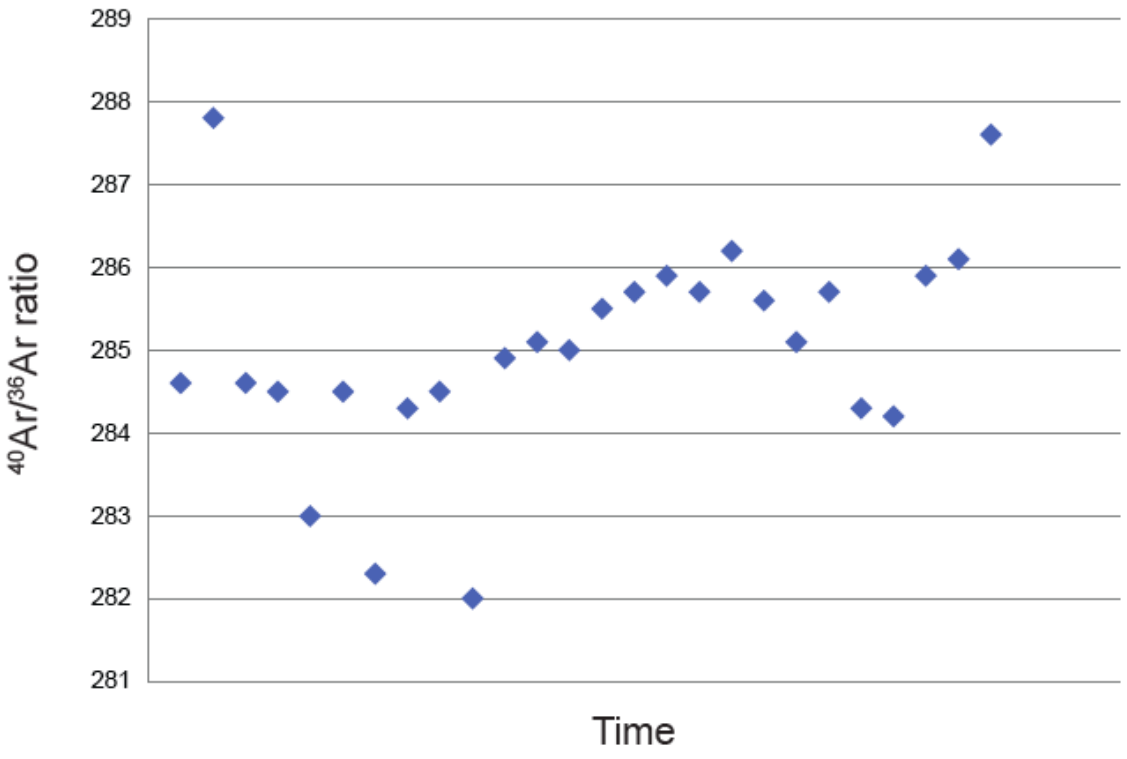

Figure 4.6. Fluctuations in measured $^{40}Ar/^{36}Ar$ values from air pipette runs (A1/4-216 to A1/4-241) during the period of experiment.

Figure 4.7.A

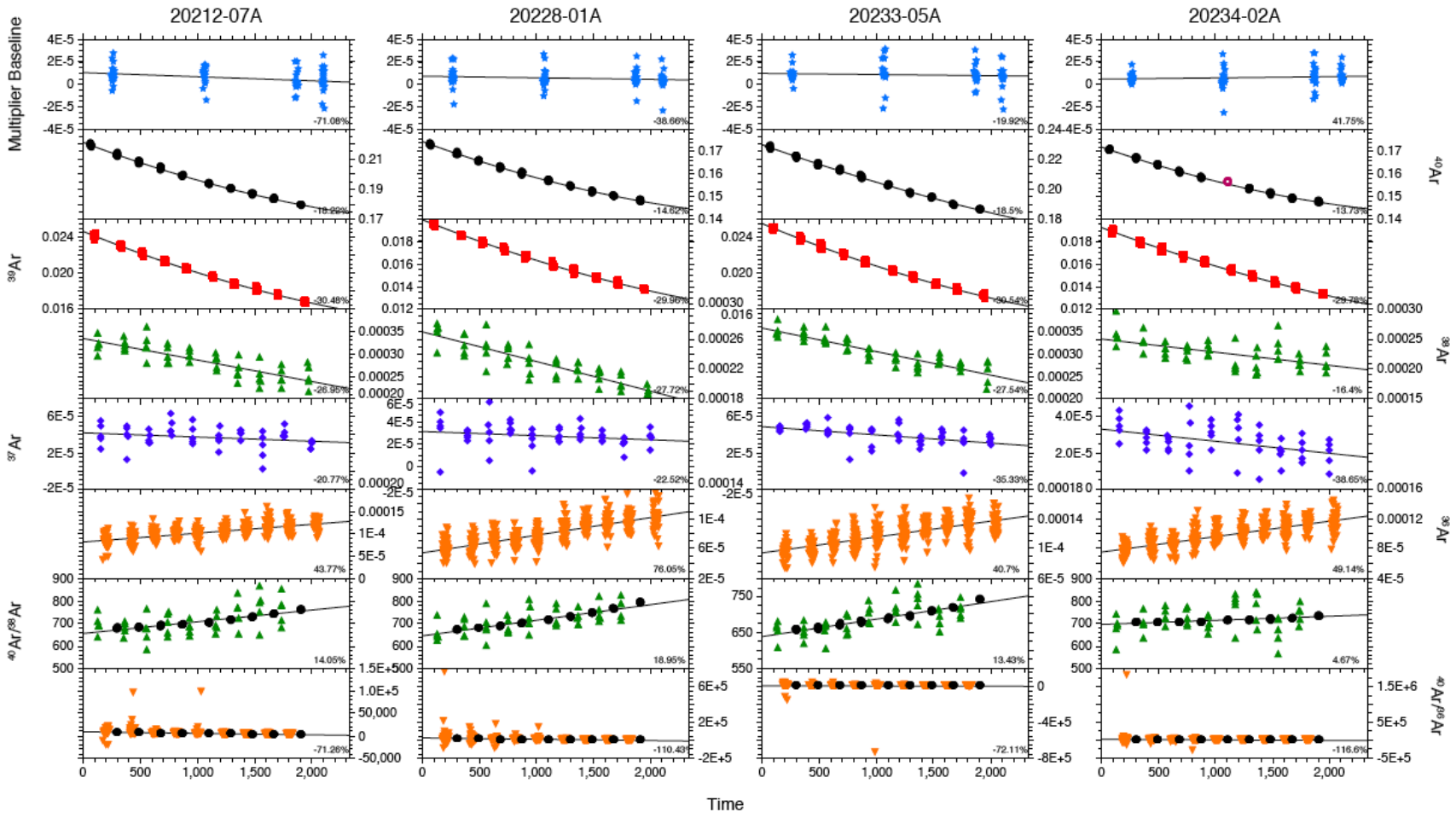
20212-07A
20228-01A
20233-05A
20234-02A
Multiplier Baseline
40Ar
39Ar
38Ar
37Ar
36Ar
40Ar/36Ar
40Ar/39Ar
Time

Figure 4.7.A (*Continued*)

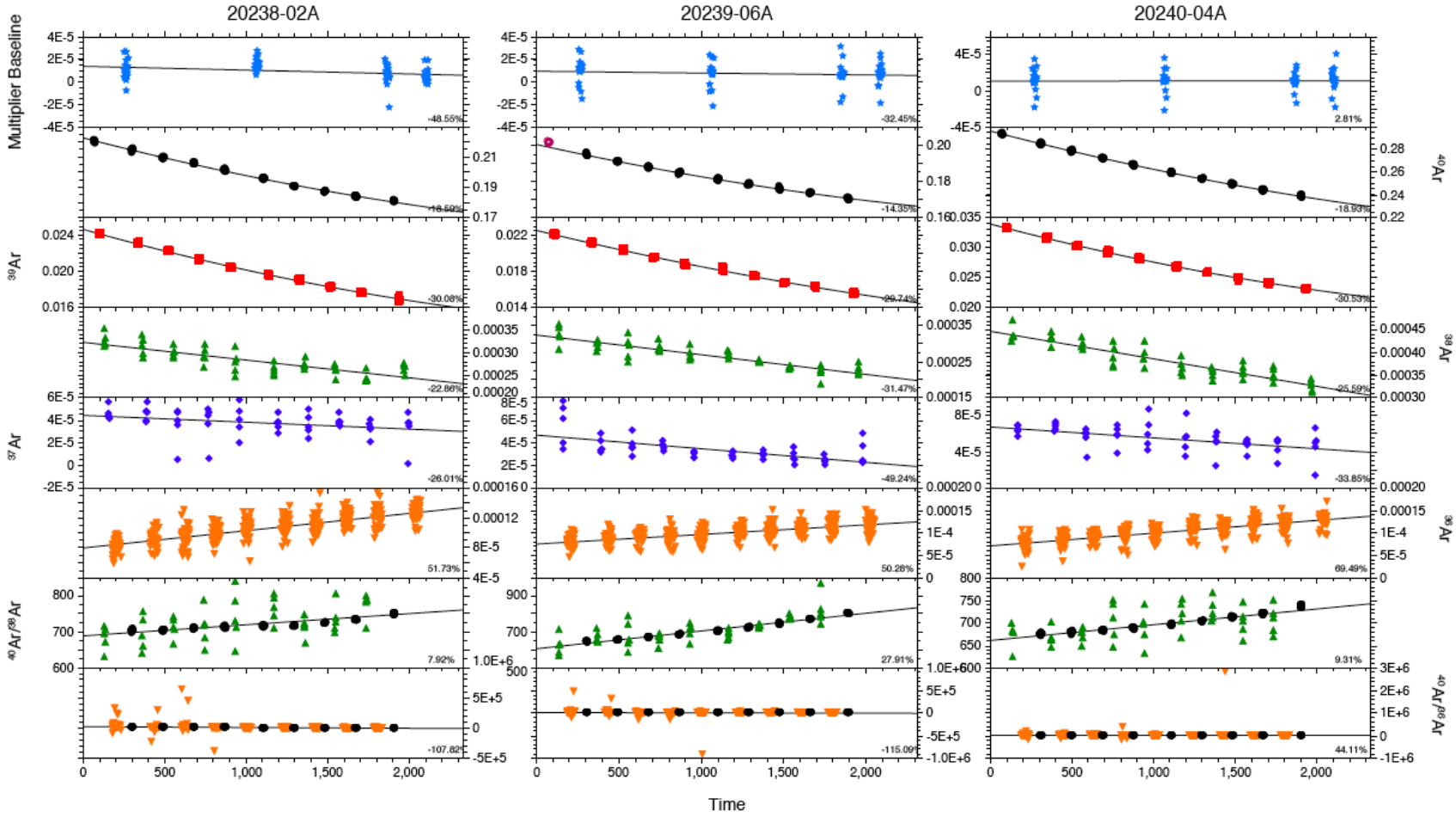

Figure 4.7.B

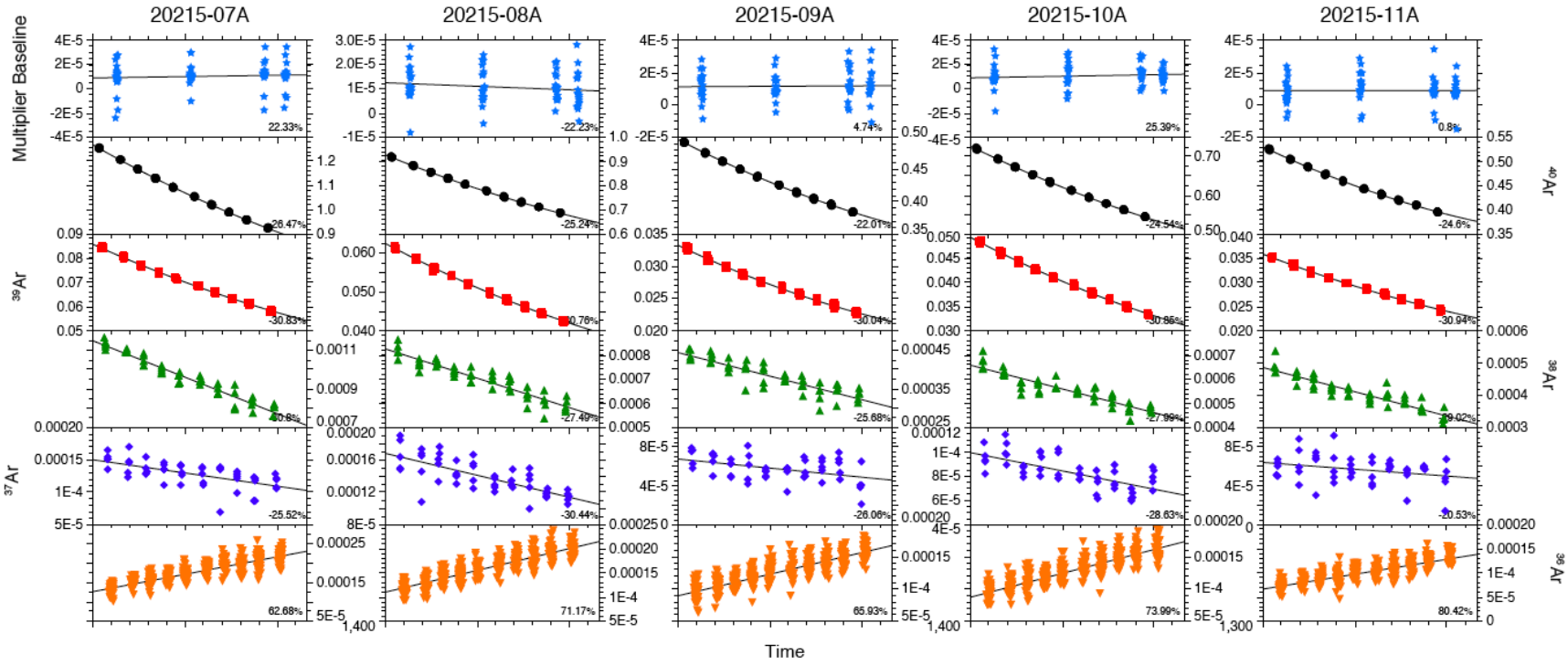
20215-07A
20215-08A
20215-09A
20215-10A
20215-11A
Multiplier Baseline
40Ar
39Ar
38Ar
37Ar
36Ar
Time

Figure 4.7.B (*Continued*)

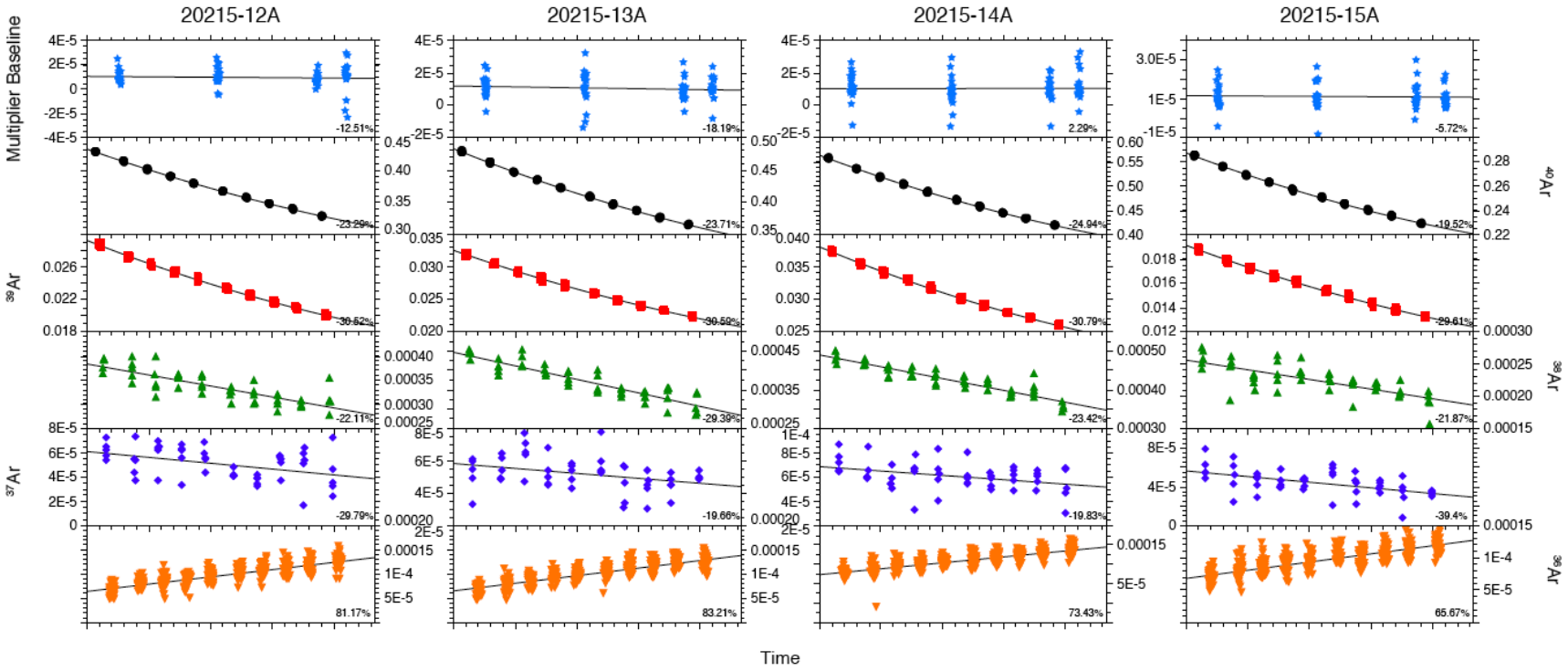

Figure 4.7.B (*Continued*)

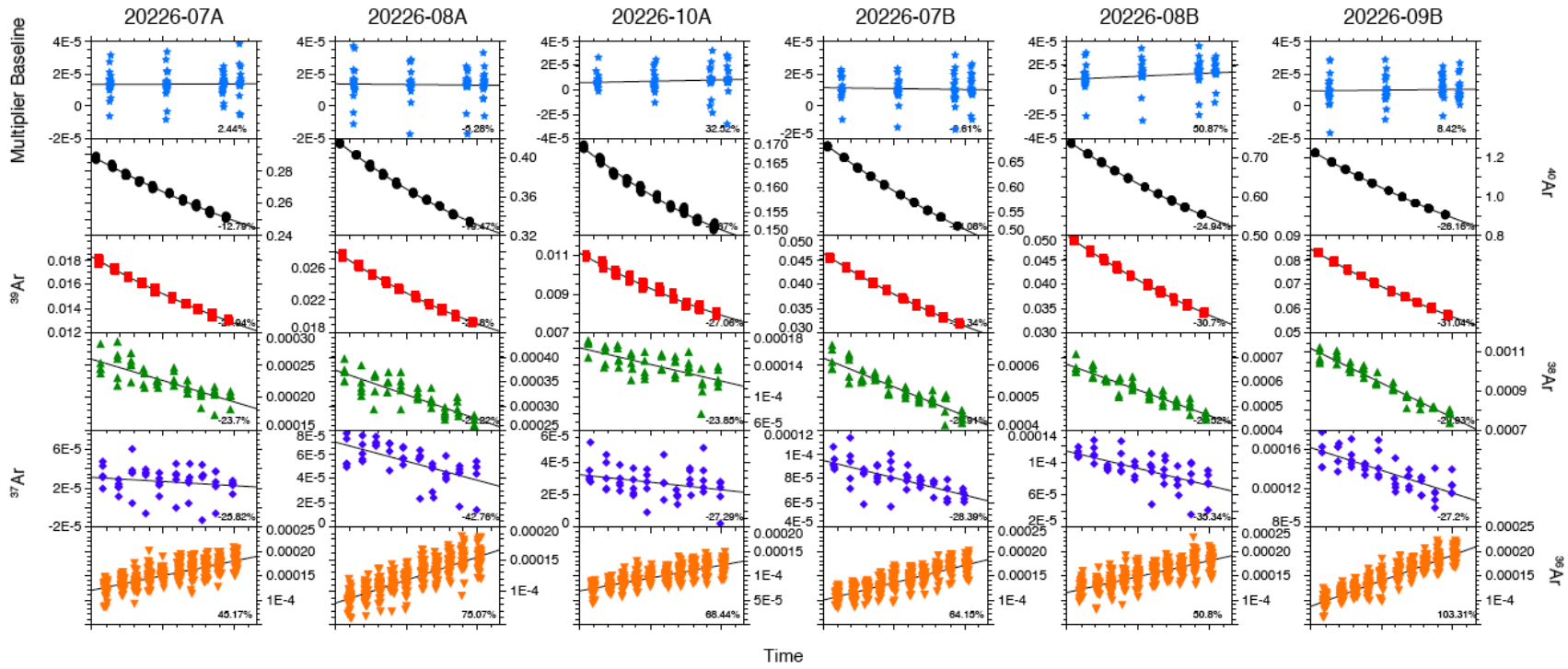

Figure 4.7.B (*Continued*)

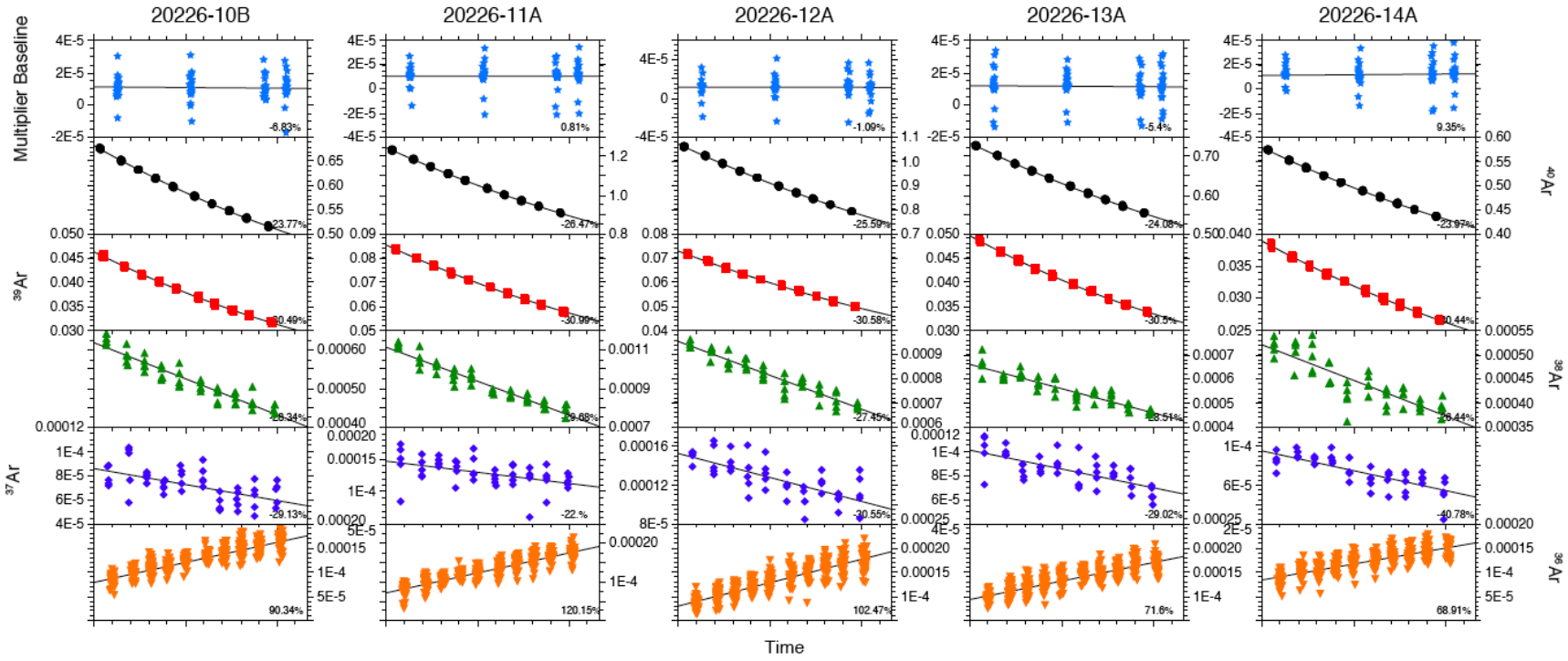

Figure 4.7.B (*Continued*)

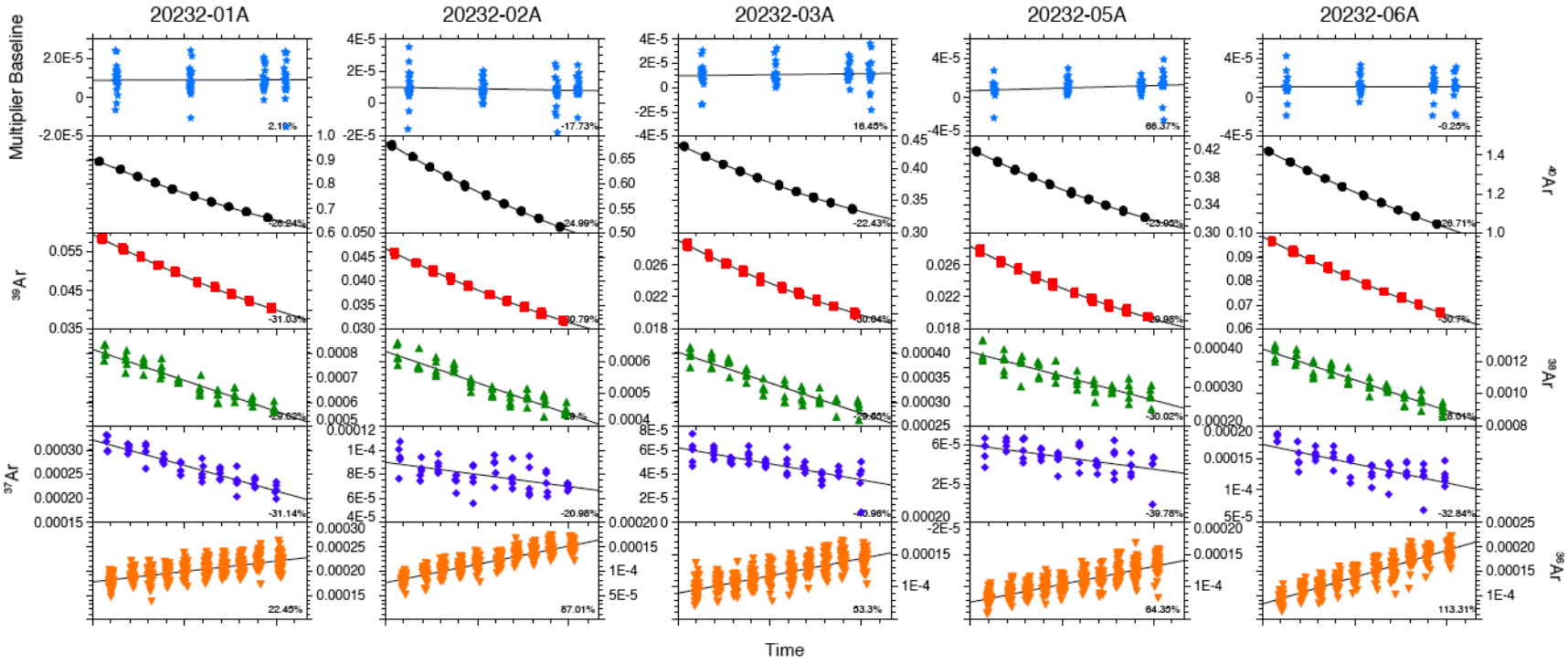

Figure 4.7.B (*Continued*)

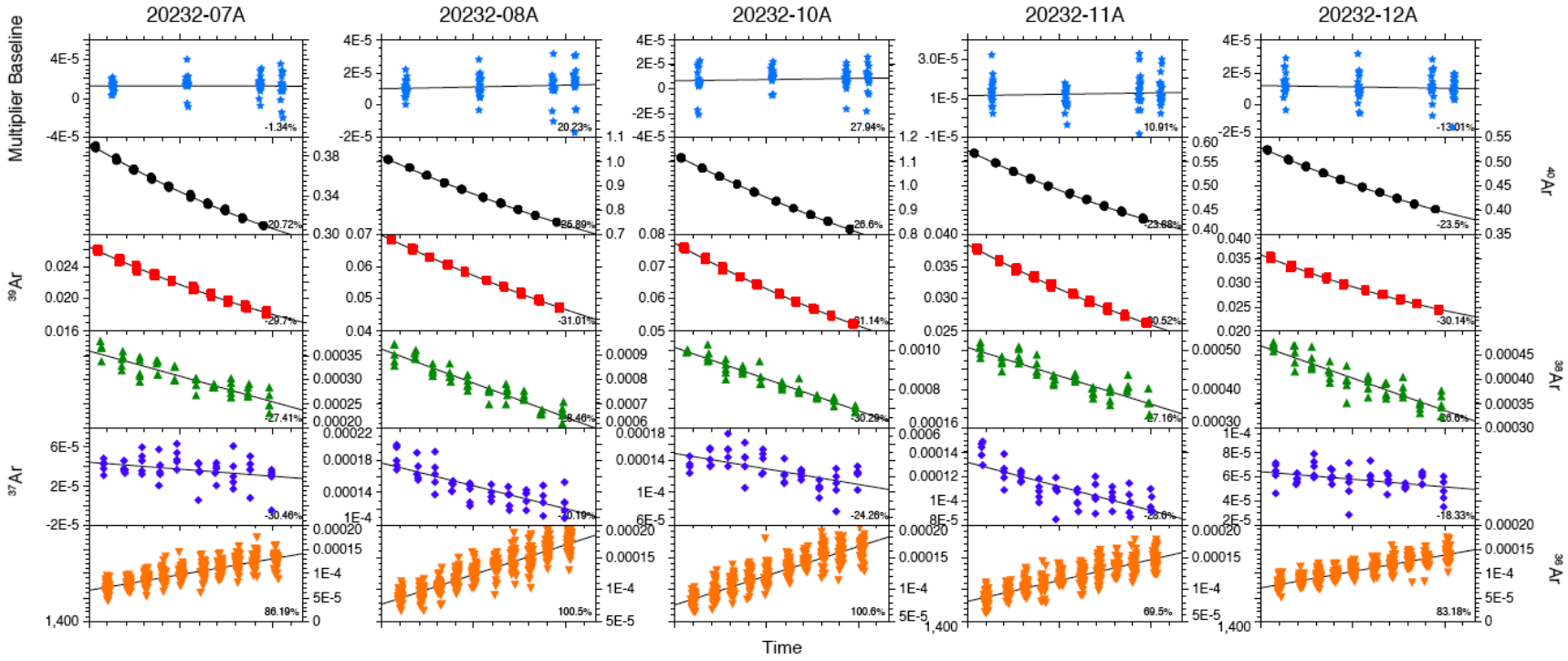

Figure 4.7.C

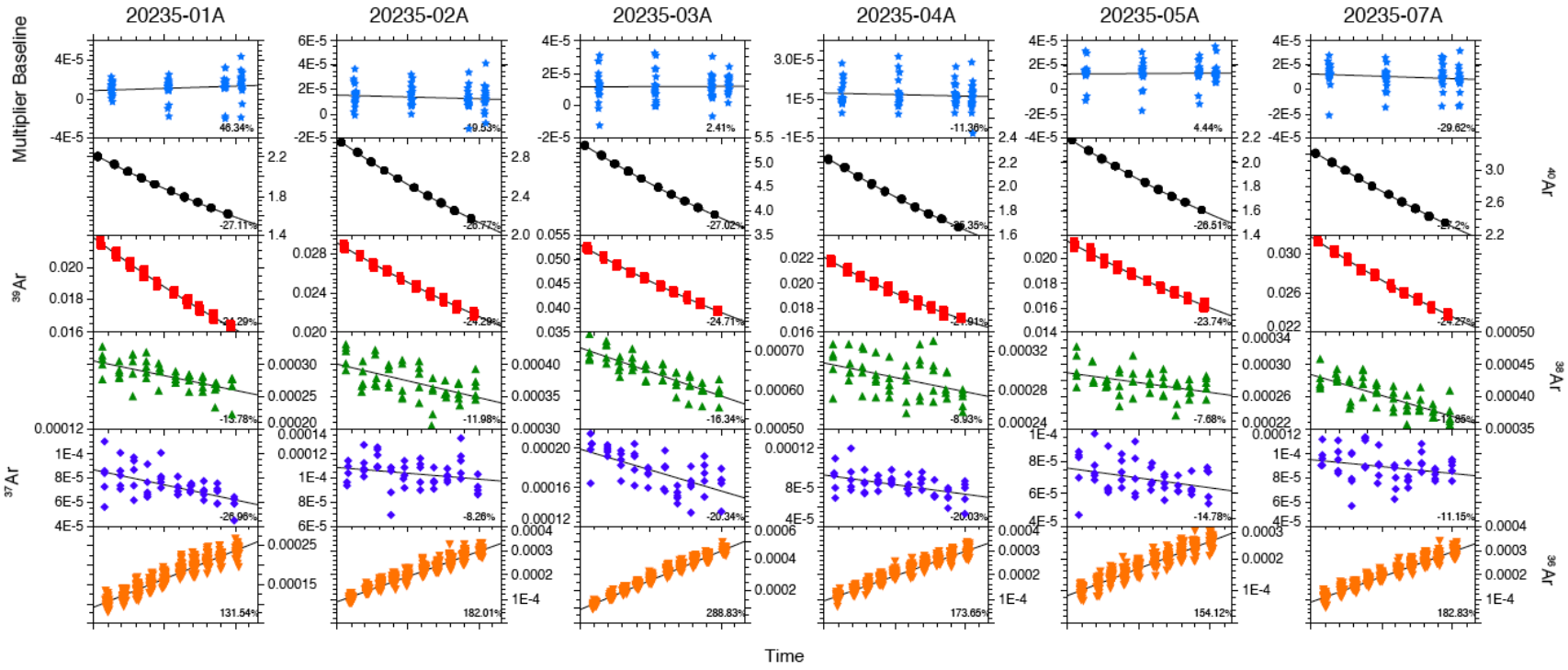
20235-01A
20235-02A
20235-03A
20235-04A
20235-05A
20235-07A
Multiplier Baseline
40Ar
39Ar
38Ar
37Ar
36Ar
Time

Figure 4.7. Isotopic evolution of single-grain sanidine analyses of the (A) Fish Canyon sanidines, (B) Henrys Fork tuff, and (C) Fire Clay tonstein that were included in age calculation. Isotopic evolution of ^{40}Ar and ^{39}Ar was fitted with either linear or parabolic fit, while that of ^{38}Ar, ^{37}Ar, ^{36}Ar, and multiplier baseline was fitted with linear regression. Refer to Figure 4.1 for the position of these alquoits in the irradiation disk.

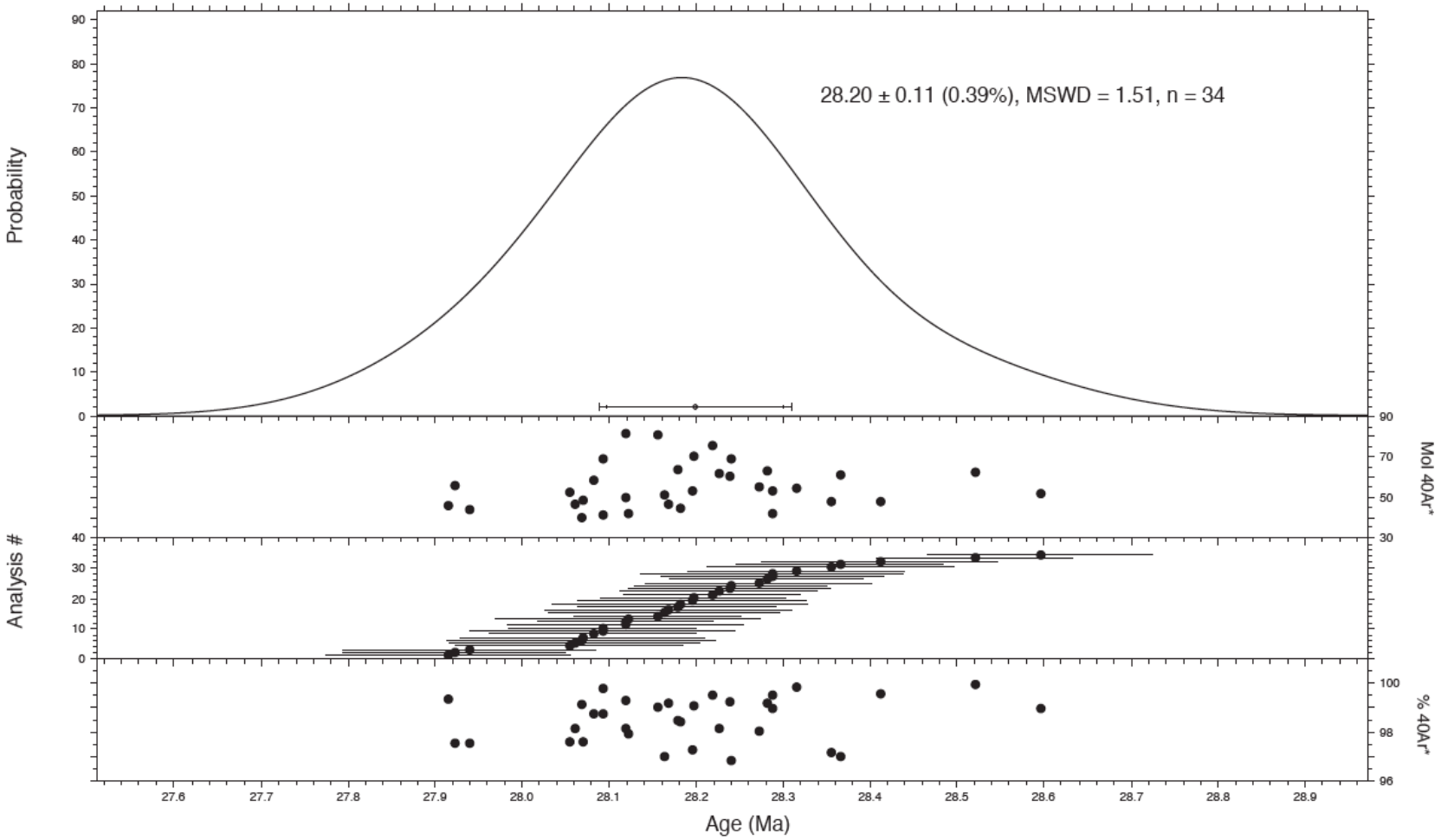

Figure 4.8. Probability plot of the Fish Canyon sanidines used for characterization of J-value for the irradiation disk (USGS 39C).

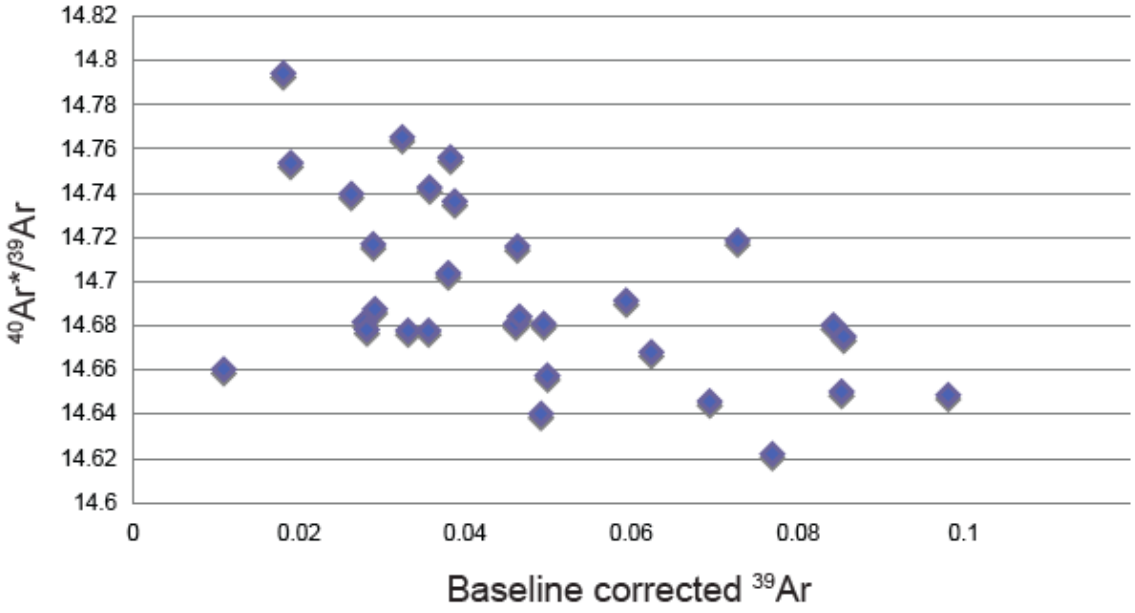

Figure 4.9. Pressure effect during the measurement of the Henrys Fork tuff. R^2 value for all the data is 0.2.

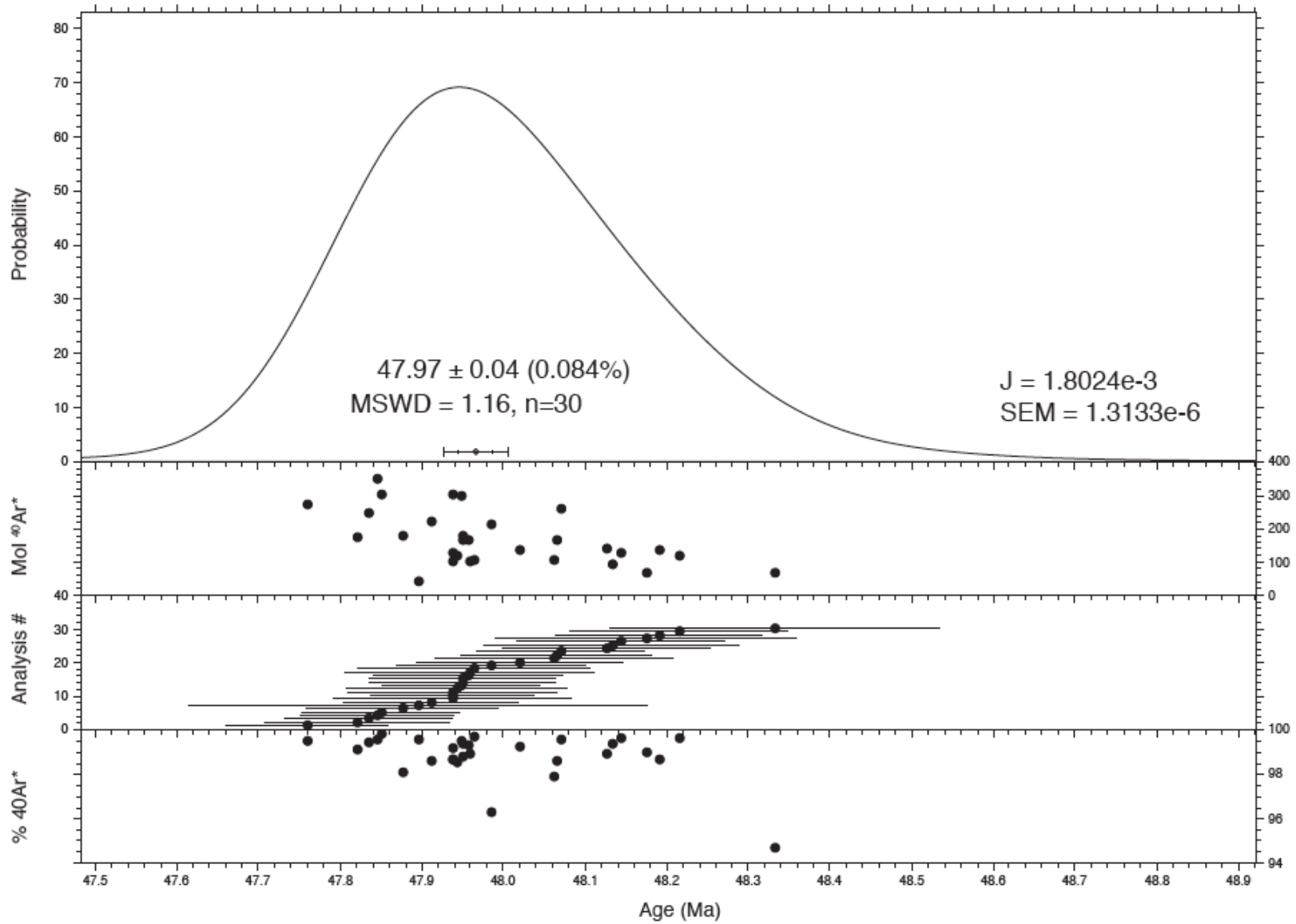
Probability
47.97 ± 0.04 (0.084%)
MSWD = 1.16, n=30
J = 1.8024e-3
SEM = 1.3133e-6
Mol 40Ar*
Analysis #
% 40Ar*
Age (Ma)

Figure 4.10. Probability plot of the Henrys Fork tuff. Also shown are moles of radiogenic ^{40}Ar and percent radiogenic for the single grain analyses. The uncertainty on the age is at 2 sigma and includes uncertainty from J-value calculation. The J-value and its standard error of the mean used in the age calculation are also shown.

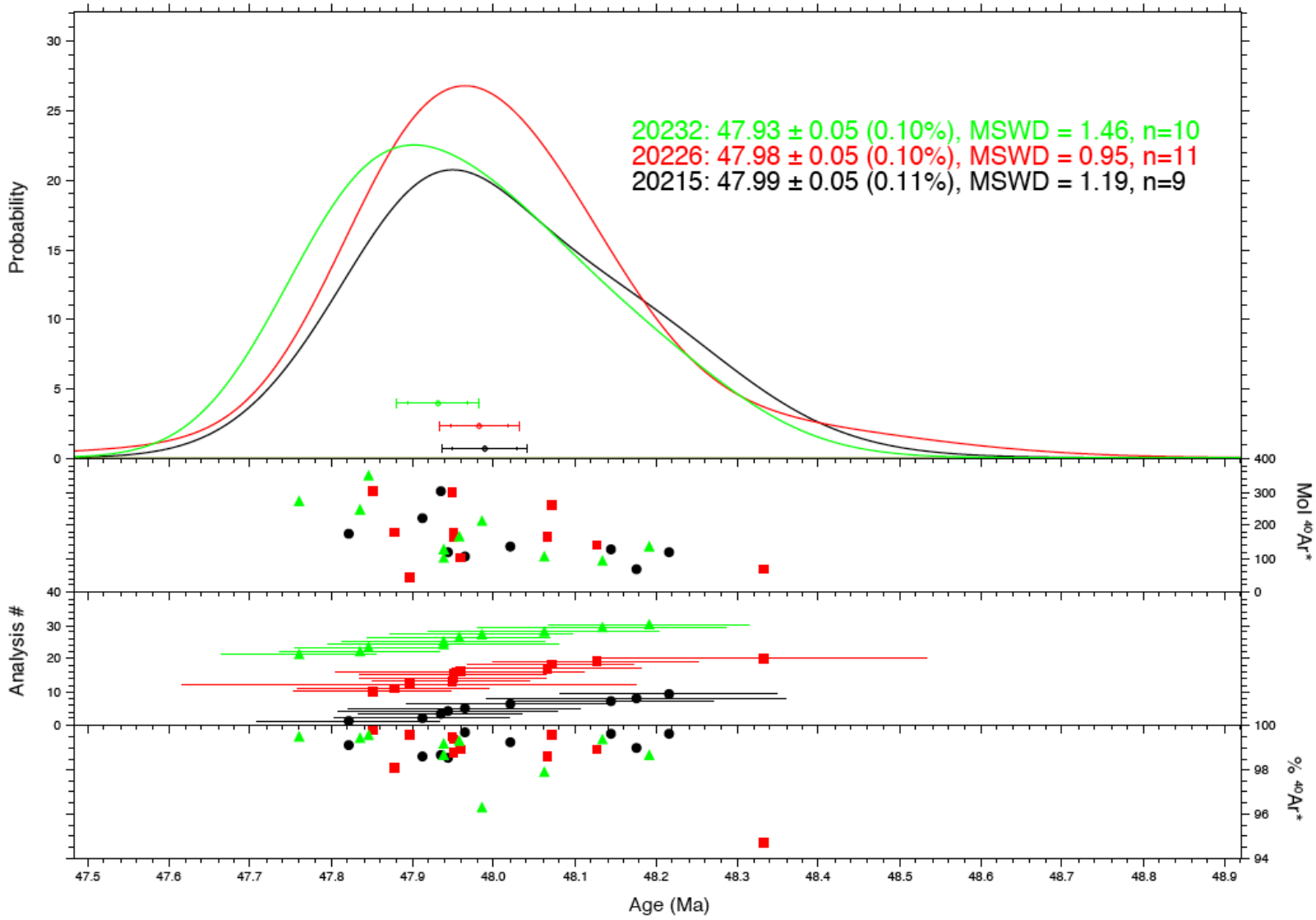
20232: 47.93 ± 0.05 (0.10%), MSWD = 1.46, n=10
20226: 47.98 ± 0.05 (0.10%), MSWD = 0.95, n=11
20215: 47.99 ± 0.05 (0.11%), MSWD = 1.19, n=9
Probability
Analysis #
Mol 40Ar*
% 40Ar*
Age (Ma)

Figure 4.11. Probability plot of the Henrys Fork tuff with analyses from alquiots 20232 (green), 20226 (red), and 20215 (black) are plotted separately.

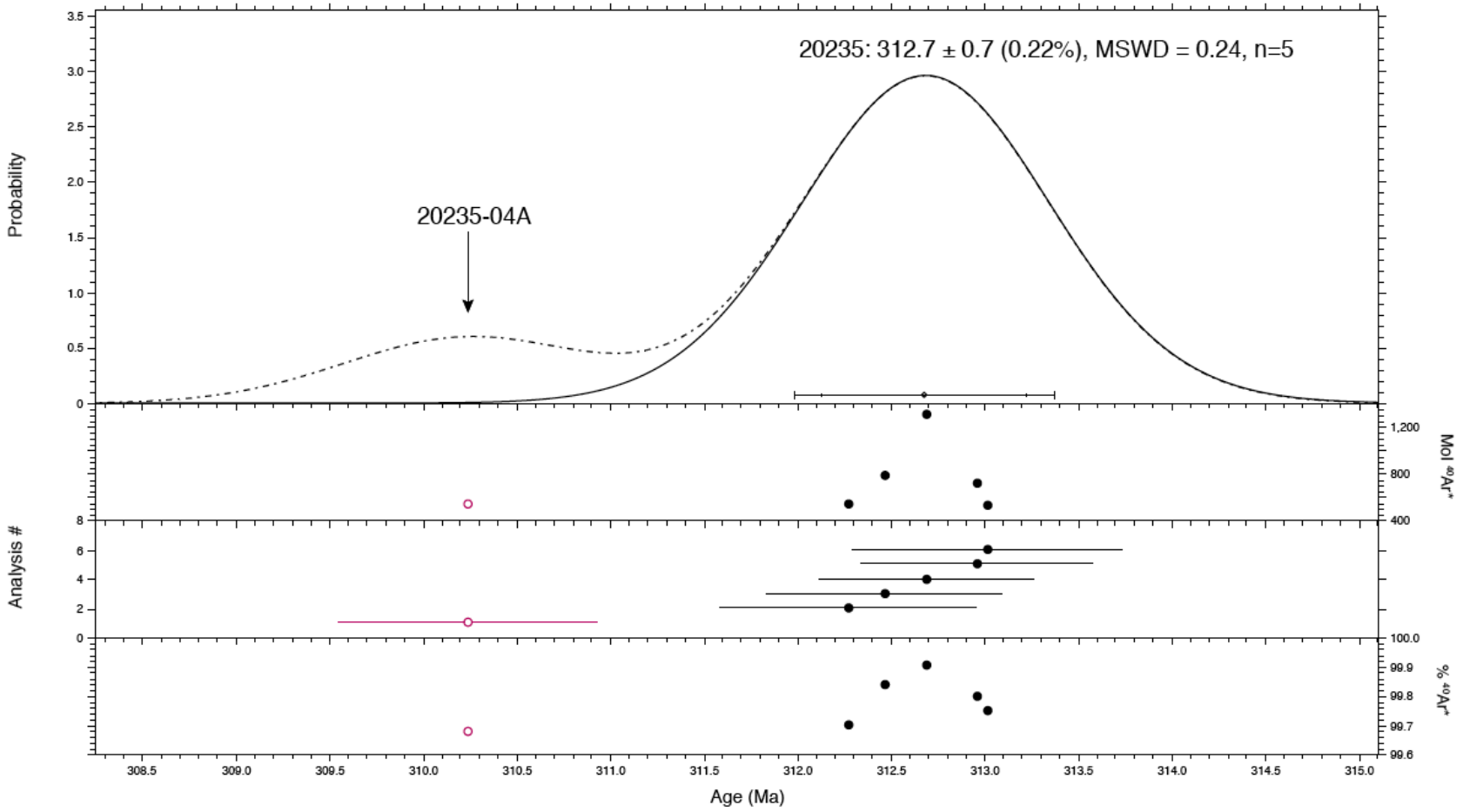

Figure 4.12. Probablity plot of the Fire Clay tonstein shown with 2 sigma errors. Shown in red is 20235-04A and was excluded from age calculation.

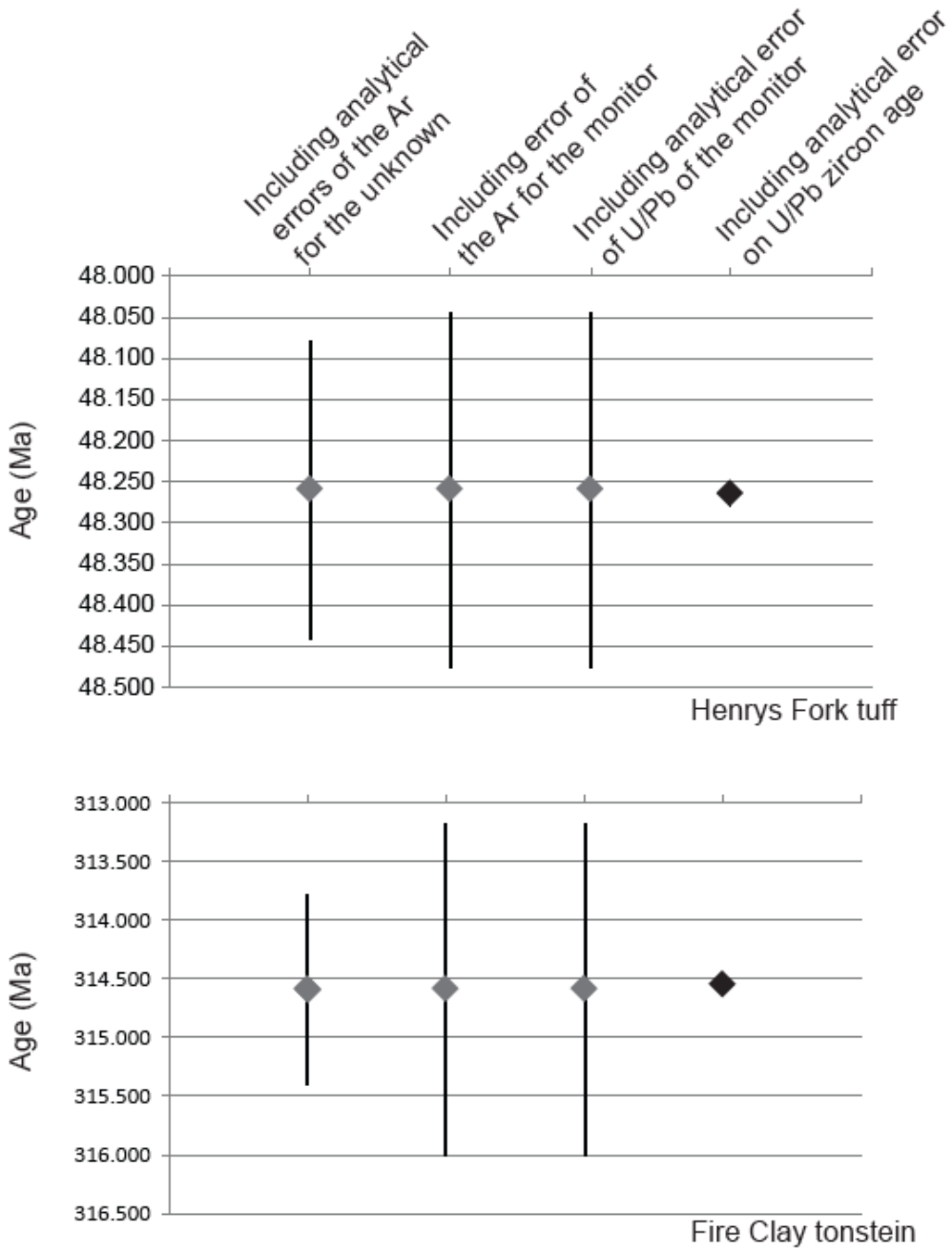

Figure 4.13. Comparison of U-Pb constrained $^{40}Ar/^{39}Ar$ (grey) age estimates and U-Pb zircon (black) estimate of the Henrys Fork tuff (top) and Fire Clay tonstein (bottom). Shown with different uncertainty categories at 1 sigma.

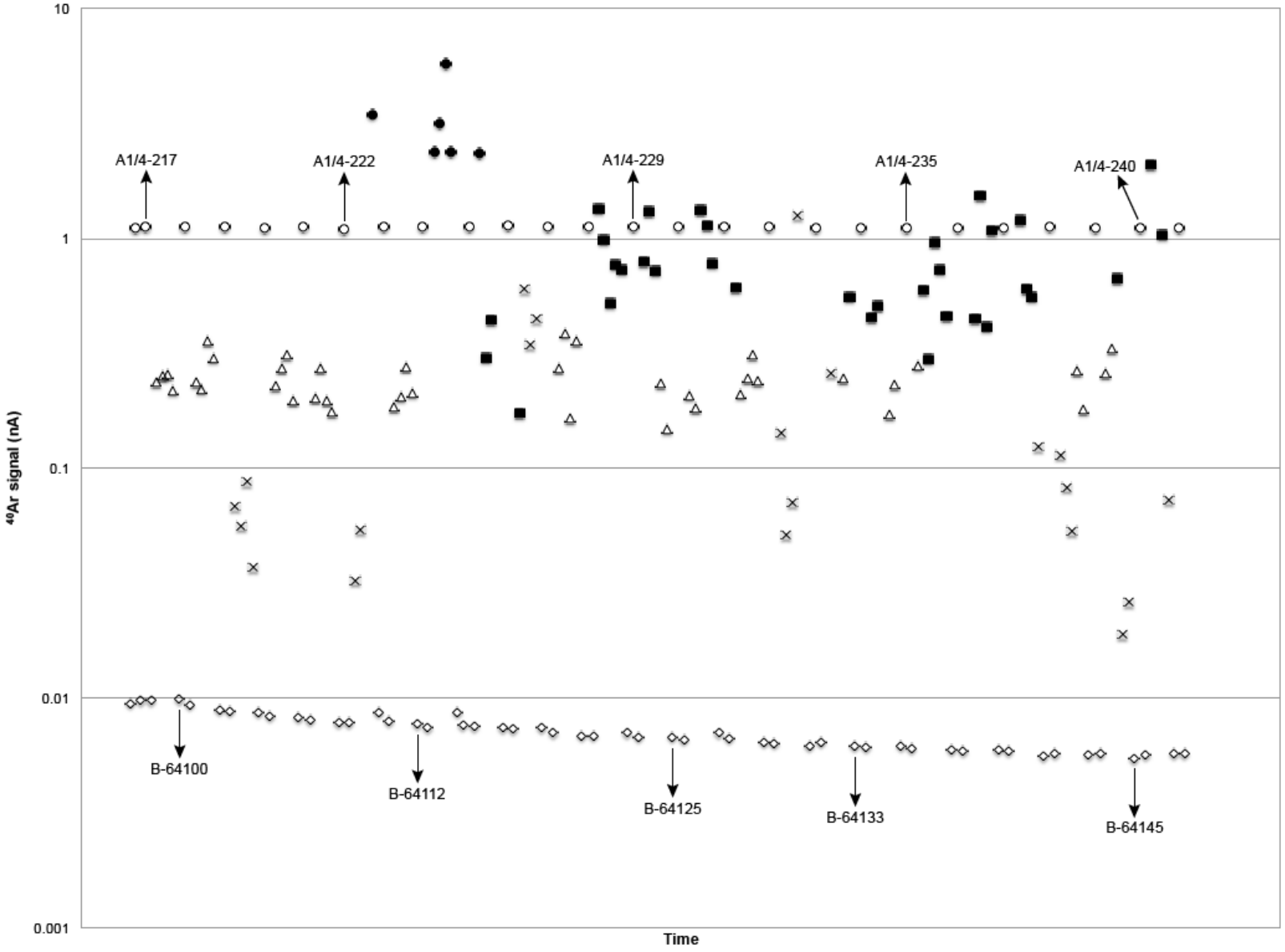
10
1
0.1
0.01
0.001
^{40}Ar signal (nA)
Time
A1/4-217
A1/4-222
A1/4-229
A1/4-235
A1/4-240
B-64100
B-64112
B-64125
B-64133
B-64145

Figure 4.14. ^{40}Ar signal of all of the runs that were measured during the eight-day study period.

Chapter 5

Conclusions

My overarching motivation for this dissertation stems from the fact that a rigorous and high-precision temporal framework is the key to correlate various geological records and ultimately untangle an intricate web of causalities for better understanding of the processes involved. Detailed understanding of the causalities then becomes instrumental in assessing current environmental issues and developing most effective strategies for the future. Guided by the motivation, I mainly focused on the middle Eocene Greater Green River Basin, and in the three content chapters, I presented new chronostratigraphic framework for the middle Eocene (Chapter 2), species-level analysis of body size evolution in the Bridgerian mammals (Chapter 3), and my observations on the current state of $^{40}Ar/^{39}Ar$ geochronology (Chapter 4).

The new magnetostratigraphy of the Bridger Formation provides the fundamental temporal framework for this dissertation. For the first time, the entire Bridger Formation is placed within a magnetostratigraphic context, precisely dated via U-Pb geochronology. The new magnetostratigraphy shows that the Bridger Formation extends from Chrons C22r to C21n, spanning a longer time period than was proposed previously by Smith et al. (2008). The Bridgerian/Uintan boundary was also constrained to Chron C21n. The magnetostratigraphic calibration of the Bridgerian/Uintan boundary allowed re-interpretation of other boundary-bearing magnetostratigraphic sections in the western interior, and the updated inter-basinal correlation showed that the Bridgerian/Uintan boundary is recorded everywhere in Chron C21n. Furthermore, with the integrative (bio-,

magneto- and radioisotopic) chronology applied to the Bridger Formation, I was able to discriminate the best age model for calibration of the early-middle Eocene segment of the Geomagnetic Polarity Time Scale. The combination of the new U-Pb and magnetostratigraphic data suggests that the Option 3 model of Westerhold et al. (2009) shows most agreement with the magnetostratigraphic and radioisotopic constraints for all but one tuff from the Greater Green River Basin. Using the astronomically determined chron durations for the Paleocene, this particular age model estimates the ages of 56.33 Ma and 66.08 Ma for the Paleocene Eocene Thermal Maximum (PETM) and Cretaceous/Paleogene (K/Pg) boundary, respectively. While the PETM age estimate is too old compared to the single U-Pb age determination of Charles et al. (2011), suggesting that age may be somewhat too young and presenting a conflict that is worthy of further investigation, the K/Pg boundary age is in good agreement with the U-Pb data of Bowring et al. (2008) and Renne et al. (2013), as well as the astronomically estimated age by Kuiper et al. (2008). As of the timing of this writing, Westerhold et al. (2015) just published new data to fill in the "middle Eocene gap" in astrochronology and showed promise of calibrating the entire Cenozoic by astronomical chronology. In the same year, Machlus et al. (2015) also published high-precision U-Pb data from the Green River Formation to verify the astronomical solution for the same time interval as Westerhold's (2015) astrochronology. There is now much momentum in resolving the issues of timescale calibration for the Paleogene, and these recent studies will undoubtedly pave the way for new opportunities to investigate further questions. For example, the analysis of body size evolution among the Bridgerian mammals in Chapter 3 of this dissertation was limited to the resolution of biozones, but with development of astrochronology for

the middle Eocene, it may become possible to apply astrochronology to the fluvial Bridger Formation and study the mammalian evolution in light of astronomical forcing as it influences water availability, vegetation and local climate (van Dam et al., 2006; Abdul Aziz et al., 2008). At that resolution of temporal control, it will be possible to examine evolutionary rates of mammalian fauna and ultimately tempo and mode in evolution (Simpson, 1944; Roopnarine, 2003). In any event, all of these potential research opportunities highlight the importance of having a timescale with the highest precision possible. Progress in timescale building inevitably requires better understanding of cross calibration of multiple chronometers and inter-laboratory biases. Now that an increasing number of geological events are dated by more than one geochronological method, the issue of laboratory and chronometer intercalibration is as important as the geological questions themselves. The $^{40}Ar/^{39}Ar$ results on the middle Eocene Henrys Fork tuff and Carboniferous Fire Clay tonstein presented in Chapter 4 indicate that at ~48 Ma and ~315 Ma, the $^{40}Ar/^{39}Ar$ and U-Pb systems are equivalent within error at the community goal of 0.1% precision. However, there was discrepancy between FCs-keyed $^{40}Ar/^{39}Ar$ age and U-Pb based $^{40}Ar/^{39}Ar$ age, and the discrepancy is attributed to the neutron fluence gradient that was not accounted for in these analyses. The experiment highlights the importance of determining the J-value and neutron fluence gradient at the highest possible precision. Variables that are worth exploring further in future $^{40}Ar/^{39}Ar$ experiments include but are not limited to uncertainty in isotope ratio linearity, correlation between signal intensity and $^{40}Ar^*/^{39}Ar$, and better characterization of the J-value by using multiple monitor standards that are close in composition and age to unknowns.

The sedimentary records from the Greater Green River Basin represent merely 0.3% of the Phanerozoic time. However, its basin records hold great promise in improving geochronology, the common currency in the studies of Earth, and its merit will permeate to many disciplines within geosciences and help us understand a variety of planetary and evolutionary processes. It is hoped that the work presented in this dissertation will encourage further studies in the Greater Green River Basin and provide a new intellectual platform for many future studies that will push the limits of the resolution with which we can reconstruct and understand the history of the Earth.

REFERENCES CITED

Abdul Aziz, H., Hilgen, F.J., van Luijk, G.M., Sluijs, A., Kraus, M.J., Pares, J.M., and Gingerich, P.D., 2008, Astronomical climate control on paleosol stacking patterns in the upper Paleocene–lower Eocene Willwood Formation, Bighorn Basin, Wyoming: Geology, v. 36, p. 531-534.

Bowring, S.A., Johnson, K.R., Clyde, W, Ramezani, J., Miller, I., and Peppe, D., 2008, A Paleocene timescale for the Rocky Mountains: status and potential: Geological Society of America Abstracts with Programs, v. 40, no. 6, p. 322.

Charles, A.J., Condon, D.J., Harding, I.C., Pälike, H., Marshall, J.E.A., Cui, Y., Kump, L., and Croudace, I.W., 2011, Constraints on the numerical age of the Paleocene-Eocene boundary: Geochemistry, Geophysics, Geosystems, v. 12, Q0AA17, doi:10.1029/2010GC003426.

Kuiper, K.F., Deino, A., Hilgen, F.J., Krijgsman, W., Renne, P.R., and Wijbrans, J.R., 2008, Synchronizing rock clocks of Earth history: Science, v. 320, no. 5875, p. 500-504.

Machlus, M.L., Ramezani, J., Bowring, S.A., Hemming, S.R., Tsukui, K., and Clyde, W.C., 2015, A strategy for cross-calibrating U-Pb chronology and astrochronology of sedimentary sequences: an example from the Green River Formation, Wyoming, USA, Earth and Planetary Science Letters, v. 413, p. 70-78, doi:10.1016/j.epsl.2014.12.009.

Renne, P.R., Deino, A.L., Hilgen, F.J., Kuiper, K.F., Mark, D.F., Mitchell, W.S., Morgan, L.E., Mundil, R., and Smit, J., 2013, Time scales of critical events around the Cretaceous-Paleogene boundary: Science, v. 339, p. 684–687, doi:10.1126/science.1230492.

Roopnarine, P.D., 2003, Analysis of rates of morphologic evolution: Annual Review of Ecology, Evolution and Systematics, v. 34, p. 605-632.

Smith, M.E., Carroll, A.R., and Singer, B.S., 2008, Synoptic reconstruction of a major ancient lake system: Eocene Green River Formation, western United States: Geological Society of America Bulletin, v. 120, no. 1-2, p. 54-84.

Simpson, G.G., 1944, Tempo and Mode in Evolution: New York, Columbia University Press, 237 p.

van Dam, J.A., Abdul Aziz, H., Álvarez Sierra, M.Á., Hilgen, F.J., van den Hoek Ostende, L.W., Lourens, L.J., Mein, P., van der Meulen, A.J., and Pelaez-Campomanes, P., 2006, Long-period astronomical forcing of mammal turnover: Nature, v. 443, p. 687-691.

Westerhold, T., Röhl, U., McCarren, H.K., and Zachos, J.C., 2009, Latest on the absolute age of the Paleocene–Eocene Thermal Maximum (PETM): New insights from exact stratigraphic position of key ash layers +19 and −17: Earth and Planetary Science Letters, v. 287 p. 412–419.

Westerhold, T., Röhl, U., Frederichs, T., Bohaty, S. M., and Zachos, J.C., 2015, Astronomical calibration of the geological timescale: closing the middle Eocene gap: Climate of the Past, v. 11, p. 1665–1699.